WIRE-GRID ANALYSIS OF ANTENNAS NEAR CONDUCTING SURFACES

Woldemariam Wolde-Ghiorgis, B.S. (M.I.T.), M.S. (Lehigh U.)

WIRE-GRID ANALYSIS OF ANTENNAS NEAR CONDUCTING SURFACES

by

Woldemariam Wolde-Ghiorgis, B.S. (M.I.T.), M.S. (Lehigh U.)

A thesis submitted to the Faculty of Graduate Studies and Research
in partial fulfillment of the requirements for the degree of
Doctor of Philosophy.

Department of Electrical Engineering,
McGill University,
Montreal, Quebec.

March, 1972.

ABSTRACT

This thesis is a comprehensive and systematic examination of the wire-grid modeling technique applied to radiating antennas mounted on or near conducting bodies. The central objective is to seek general guidelines both for the grid model formulation and for the computational process structure. The study is carried out in terms of closely coordinated and parallel numerical and experimental analysis of eight progressively more complicated antenna structures ranging from a simple monopole on a finite ground plane to a complex aircraft structure.

The computational and experimental results are compared and evaluated in terms of far field patterns. The study establishes the relative influence and significance of, and indicates guidelines for, the following essential features of the wire-grid modeling technique :

(i) the numerical formulation of the basic integral equation,

(ii) the computational modeling of the excitation source,

(iii) the kind of basis function used for segment current approximation,

(iv) computational details regarding geometrical data accuracy and exploitation of symmetry features,

(v) the use of the 'stationary lines of flow' concept,

(vi) the geometry of the wire-grid model,

(vii) the numbers of grid wires used and their segmentation,

(viii) the cross-section geometry and dimensions of modeling wires, and

(ix) the continuing importance of experimental measurements.

The conclusions suggest the eventual possibility of formulating wire-grid modeling procedures from basic canonic forms and indicate the need to examine the influence of additional features such as grid-wire junctions and wire element peripheral current distribution.

ACKNOWLEDGEMENTS

Dr. T.J.F. Pavlasek supervised and directed the project reported in this thesis. The author would like to record his sincere thanks for his guidance and encouragement.

The author is also greatly indebted to his research colleague, Associate Professor S.J. Kubina of Loyola College, Montreal, for many useful discussions and for his help in developing and testing experimental procedures for pattern measurements. Special thanks are due to Mr. J. Foldvari and his colleagues who built the antenna models, probes and mechanical supports ; to Mr. I. Borissov for providing technical advice on photography ; to Mr. S. Henry for his help in the maintenance of electronic instrumentation; to Mr. A. Skalina for his invaluable aid in obtaining experimental results and also for drawing expertly the diagrams for the antenna structures ; to Mr. T. Bayou for his kind help in preparing the radiation pattern plots ; and to the author's colleagues, Messrs R.C. Murphy and C.C. Huang for many hours of free discussion and general assistance.

Particular thanks are due to Mrs. P. Hyland for her patience and expert typing of the thesis. The author's wife has been a constant source of encouragement during the period of study. Thanks are also due to Mrs. M. Brown for the printing of the thesis.

Finally, the author wishes to express his gratitude to the Canadian International Development Agency for a three-year Fellowship from 1969 to 1972, which enabled him to undertake this work at McGill University, and to Haile Sellassie I University (Addis Ababa, Ethiopia) for special leave of absence.

TABLE OF CONTENTS

Page

Page

CHAPTER I

INTRODUCTION

1.1 Background : The Linear Antenna in Unbounded Space

This thesis considers the general problem of wire antennas mounted near conducting surfaces. In order to introduce the subject, a review of thin wire antennas in unbounded space is necessary. The fundamental concepts of linear antenna theory form an essential foundation to this study, and the introduction therefore begins with a survey of classical and numerical methods of linear antenna analysis.

1.1.1 Classical - Analytical Studies

The thin wire antenna in free space (μ_o, ϵ_o) has been studied as a boundary-value problem for quite a long time. The basic problem is to determine the current distribution along the antenna due to a known time-harmonic ($e^{j\omega t}$) excitation, and to evaluate the resultant electromagnetic field and the driving-point impedance. When the antenna takes the usual thin and uniform cylindrical shape as shown in Figure 1.1 (a), the field equations, derived from Maxwell's equations, can be formulated directly in terms of cylindrical coordinates. The required solutions, however, have never been easy to obtain because a finite cylindrical surface does not belong to any set of regular coordinates for which the separation of variables technique is possible. Consequently, the solutions to this antenna problem have been sought generally by introducing some geometric approximation, or by seeking completely different methods. In broad terms, as discussed more fully by Aharoni [1], and Schelkunoff [2], three

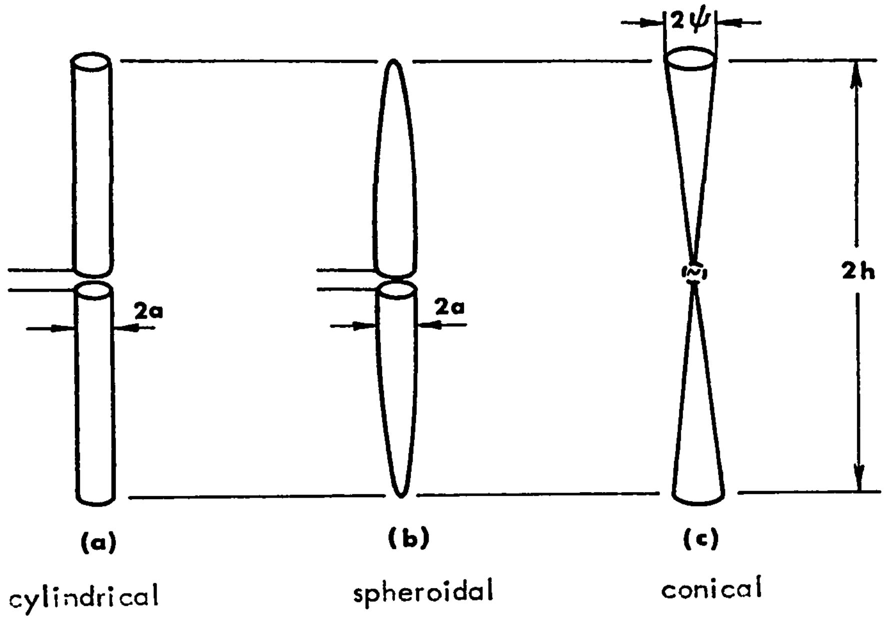

Figure 1.1. Three Basic Mathematical Models of the Straight Thin Wire Antenna.

different mathematical methods have been used :

(1) the antenna is treated as a boundary-value problem ;

(2) the antenna is considered to be a transmission-line-like waveguide, and

(3) the antenna is described as a circuit problem defined by an integral equation.

As radio communications technology developed, engineering approximations were also introduced to improve the design of broadcast towers and high frequency antennas. The three mathematical methods assume that the antenna surface is a perfect conductor. Aside from this common assumption, the approximations used in each method are radically different. The exact boundary-value type of solution first obtained by Chu and Stratton [3] was based on prolate spheroidal geometry shown in Figure 1.1 (b). A prolate spheroid coordinate system is one of the few for which boundary conditions can be matched directly and separation of variables carried out [4]. Although in practice antennas were not (and are not) designed as spheroids, the complete oscillatory solutions obtained were nevertheless found useful by providing results which could be compared with other solutions. When the spheroid is elongated and the ratio $h/a \gg 1$, it approximates a thin cylindrical antenna very closely, and thus the important antenna parameters can be deduced. Starting with a different approach, Schelkunoff [5] arrived at similar results. The antenna was approximated by a wide-angled conical transmission line with a source between the apexes of the conical arms as in Figure 1.1 (c). It was postulated that the arms of the transmission line act as a waveguide, launching the radiated energy into space. From transmission-line-like equations for the electric vector $\overline{E}$ (in place of voltage V) and the magnetic field vector $\overline{H}$ (in place of current I), field solutions were derived. The unknown coefficients were determined by matching boundary conditions at different regions. If the cone angles 2ψ were taken to be narrow, it was argued, the conical configuration approximated a cylindrical antenna, and once again important antenna parameters were evaluated.

While the fundamental antenna problem was being studied mathematically, more practical attempts were being made to arrive at some useful engineering models and approximations. The earliest successful studies were made by Carter [6] on short monopoles, and Brown [7] on long antennas. The thin wire antenna was compared to an open-ended transmission line, and some basic similarities noted. Despite structural differences, field solutions applicable to a coaxial transmission line were directly extended to the center-fed wire antenna. This led to one of the most important approximations in antenna engineering – namely that the current distribution along the antenna could be approximated by simple sinusoidal functions with constant phase. Actually this result was proposed earlier by Pocklington [8] in a mathematical study of electrical oscillations in a thin wire. It is significant to note that the whole foundation of linear antenna engineering has been largely based on the assumption of trigonometric-function current distribution [9], [10], [11].

The main limitation of the classical "sinusoidal" theory is that it predicts fields inaccurately near the antenna surface and consequently cannot be relied upon for the determination of input impedance. Various other methods have been proposed therefore for determining the current distribution analytically. A major starting point has been the one-dimensional integral equation first formulated by Hallén [12], which he solved asymptotically. Most subsequent investigations for solving Hallén's integral equation are described in King's definitive book [14]. More recent techniques along similar lines are surveyed by Collin and Zucker [15], and King and Harrison [16]. In addition to Schelkunoff's and Hallén's work, significant contributions have been made also by Albert and Synge [17], whose rigorous integral equation was shown to be equivalent to Hallén's and has provided useful insight into the physical and mathematical modeling for the excitation source of the wire antenna.

1.1.2 Recent Numerical Techniques for Thin Wire Antennas in Free Space

As in the case of many other electromagnetic problems, the wire antenna problem has been analyzed by recently developed computational techniques. Hallén's integral equation, though difficult to solve analytically, has been easily discretized by Mei [18]. The collocation technique which he used was later improved by Yeh and Mei [19], and the procedure has been extended to thin wire antennas of arbitrary shape. The moment method exploited by Harrington [20], [21] in simplifying the study of many electromagnetic problems has also been applied to the thin wire antenna. A more recent attempt has been made by Popović [22] to solve Hallén's equation using polynomial approximations. Significant numerical contributions have also been made by Harrington and Mautz [23], and Thiele [24].

1.2 Wire Antennas Near Conducting Surfaces : A Survey of Theoretical and Experimental Studies

For the purpose of this thesis, a conducting surface may be a disk, a cylinder, a plane sheet, any curved surface, or any combination and intersection of such surfaces. The surface may be closed or open ; it can be partially or totally formed by a wire-grid, or meshed structure, but it must have finite electrical dimensions. By a wire antenna is meant a monopole or dipole fed against a conducting surface or any straight wire antenna placed near a conducting surface. (The terms "electric dipole (s)," "dipole (s)" or monopole are used frequently in the text instead of the term "wire antenna (s)").

If the problem of the isolated wire antenna in unbounded space is quite difficult, the problem of the wire antenna mounted on or near a conducting surface is considerably more formidable. The fundamental questions are still the same as in the case of the simple isolated antenna : "How to determine the impressed or induced current distribution on the complex antenna structure, and thence how to find the resulting fields and driving-point impedance ?" The basic departure from the simple antenna situation is the presence of impressed or induced currents on the neighbouring conducting surfaces which will most likely modify the radiation pattern of the isolated antenna.

The simplest wire antenna – conducting surface system which has received considerable attention consists of a monopole on a conducting disk. One prominent contribution to this problem is that by Leitner and Spence [25] who calculated the radiation pattern of a quarter-wave monopole above a disk by formulating the scalar wave equation in spheroidal coordinates. The current distribution on the disk was computed and the radiation pattern obtained for various disk radii. Another important solution was made by Storer [26] who applied variational methods to an electric field integral equation. His method removed the restrictions on the length of the monopole, but its range of validity is limited to angles above and beyond the plane of the disk. In addition to the above radiation pattern studies, extensive experimental and theoretical investigations concerning the impedance characteristics of the monopole antenna on a disk have been made by Meir and Summers [27], Storer [28], and Bekefi [29], to name a few. The next complex structure is probably the corner reflector antenna which was first studied by Kraus [30], and later more extensively by Moulin [31] using the image theory technique. The same problem has been treated by Wait [32] by means of potential equation formulations. Still another study of the corner reflector has been made by Ohba [33] who obtained radiation patterns for finite reflectors by applying the geometrical theory of diffraction. Progressing to other shapes, the case of an electric dipole antenna mounted on or near a sphere has been studied by Pappas and King [34], and Harrington [35]. The general problem of wire antennas near cylinders was first investigated by Carter [36] using diffraction theory and the reciprocity principle. Sinclair [37] later extended the same method to dipole and loop antennas mounted near cylinders of elliptic cross section. Lucke [38] also obtained similar results for electric dipoles near cylinders of circular and elliptic cross sections using a Green's function method. A further simplification of Carter's method has been attempted by Knight [39]. Wait's treatise [40], which is mainly devoted to studies of radiation from conducting surfaces excited by slots, also describes the corner reflector, axial dipoles near conducting cylinders, and radial dipoles near cylindrical surfaces.

For most radiating structures consisting of wire antennas and conducting surfaces, especially those with complex or irregular shapes, radiation patterns have been determined in practice by experimental measurements on actual systems or scaled models. One basic reference for the modeling technique is the work of Sinclair and others [41] who also formulated the theory for scale model measurements [42]. Direct determination of current distribution on aircraft frames has been made by Granger and Morita [43], but in practice such measurements are far more difficult to perform than the direct determination of radiation patterns. The scale model technique has been applied to antennas mounted on ship structures by Wong and Barnes [44], and there have been similar numerous measurements of radiation patterns made for aircraft and helicopters [45].

1.3 Computational Techniques for Wire Antennas near Conducting Surfaces

One inherent problem in the scaled-model measurement technique has always been the excessive time and cost involved in the design and construction of equipment and the antenna models. Recent advances in numerical and computational techniques show a definite promise for overcoming this difficulty. Research in the computational methods is currently in three or four areas. Balanis [46] has considered the problem of a dipole near a relatively large cylinder of circular or rectangular cross-section. His method resolves the problem into two components - in the first part, rigorous solutions for a radial current element near an infinite ground plane are applied, and in the second part, diffraction contributions from the edges of the large but finite cylinder are added. The method essentially follows well-known diffraction techniques. More exact numerical techniques have, however, been applied only to surfaces with electrical dimensions of the order of a wavelength and half (or smaller). Two equivalent but different techniques have been used.

One method divides the conducting surface into a discrete number of small surface current elements. The second method involves the modeling of the complete antenna structure by an equivalent grid of thin wires. Both techniques follow the same numerical and computing procedures. Integral equations are formulated in which the unknowns are either surface currents in the case of the surface element method, or line currents in the wire-grid modeling method. Using point-matching techniques, the integral equations are transformed into a system of algebraic equations which are solved by standard matrix methods. The surface element method has been formalized into a magnetic field integral equation by Poggio and Miller [47] . A variation of the same method known as the surface distribution technique, has been applied by Oshiro and Metzner [48] to scattering problems. Tesche and Neurether [49] have used magnetic field and electric field integral equations with Green's functions to determine the current distribution and radiation patterns of one or two monopole antennas mounted on a conducting sphere. In a more complete form, the surface element technique has been used by Goldhirsh and others [50] to obtain the radiation pattern of a short radial electric dipole near a finite conducting cylinder. The wire-modeling technique, which appears to be more efficient both from the modeling and computational points of view, was first developed by Richmond [51] for the study of scattering by conducting surfaces. This can be considered as the dual of the surface modeling technique in that the integral equation defines an electric field. The technique has been successfully applied by Miller and others [52] to the analysis of helicopter antennas, and by Thiele and others [53] to a monopole mounted on the base of a cone.

The basic approach of Miller and his co-workers has been to solve a scattering problem, and then to deduce radiation patterns by using the induced current method . Thiele and others assumed a current distribution on the monopole, and then proceeded to determine the unknown currents on the surface of the cone.

Besides the above two equivalent methods, there have been attempts made to combine classical and computational techniques. Bolle and Morganstern [54] have studied the radiation pattern of a monopole on a sphere by applying Schelkunoff's method for conical antennas. A more extensive study of a monopole mounted on a sphere or a cylinder has been made by Tai [55], who employed image theory and transform techniques.

1.4 The Present Work

Despite the progress made in computational techniques to reduce complex antenna structures to surface elements or wire grids, previous work has been usually directed to isolated problems. With the exception of the wire-grid method which is beginning to show practical application, the other methods (e.g. Tesche and Neurether, Bolle and Morganstern, Tai) emphasize mainly the mathematical and numerical aspects of the techniques. The use of the wire-grid method by other investigators for scattering by conducting bodies has laid a foundation for its application to energized radiating arbitrarily shaped conducting bodies. However, at this time the principal gaps in the technique are : (a) the lack of systematic procedures for establishing the wire-grid models of complex structures, and (b) the lack of comprehensive methods for the segmentation of the wire-grid model and the subsequent discretization details necessary for practical computation. A major long-range goal of research in this area therefore should be an attempt to formulate definitive methods for wire-grid modeling - methods which might be described as canonic forms of modeling and computation. A basic objective of this present thesis therefore is to undertake a series of systematic coordinated studies of antenna systems to seek some indication how such canonic forms might be established in the future. To substantiate the accuracy of computed patterns, and hence to provide an independent validation of the modeling procedures, there also exists a need to obtain experimental results.

The thesis is thus aimed at determining radiation patterns by applying the wire-grid method of analysis to a number of finite antenna structures, and thereby prepare a foundation for the general goal mentioned above. The specific objectives of the study are as follows :

(i) To develop a more systematic method for arriving at a wire-grid model for a given antenna configuration.

(ii) To apply the wire-grid technique to structures which to date have not been considered or have only been examined partially.

(iii) To complement most of the computed patterns by experimental measurements. The experimental investigation is an integral part of the study because

(a) it indicates the degree of equivalence of continuous conducting surfaces and their wire-grid models,

(b) it provides an insight to significant parameters that affect the accuracy of the computed patterns.

(iv) From a comparison of the computed and experimental patterns, to draw conclusions regarding the general applicability, accuracy, and limitations of the technique, and to seek a set of criteria for the determination of the number and the distribution of wire elements needed for a given antenna structure.

In realizing the above objectives, and in testing the computer programs, the computed patterns are also compared whenever possible with results based on other techniques such as :

(a) Classical analytical approximations.

(b) Equivalent numerical techniques.

(c) Experimental measurements by other investigators.

The basic features of some patterns have also been compared with those available from commercial data.

It should be pointed out that no claim is made about the originality of either the numerical techniques used or the experimental procedures followed. However, the following claims are made :

(i) The wire-grid modeling technique is applied in a comprehensive and systematic way to a wide range of radiating antenna systems.

(ii) Unlike previous work, notably that of Miller [52] where scattering techniques and induced-current method have been used, or Thiele [53] where the source currents have been assumed, the antenna structures in this study have been treated as active radiating systems with the excitation voltage specified and the resulting impressed current distribution on the complete antenna system as the unknown. The approach has required a representation of the coaxially-fed excitation point either by a finite-width gap with a uniform electric field or a magnetic frill source sufficiently accurate for radiation pattern calculations. These source models have been studied before in the treatment of balanced dipole antennas or ground-based monopoles by King [14], Harrington [20], Albert and Synge [17], and Tai [55]. However, as far as it could be established, they have not been used previously in the study of complex radiating structure.

(iii) An attempt has been made to establish the effect of the thinness of the wire models on the accuracy of the patterns. This step has been found to be important especially in applying the computation programs to antenna systems in which wires of different radii or thin strips of different widths are part of the structure.

(iv) Extensive effort has been made to substantiate the computed patterns experimentally for most of the antenna configurations investigated in the study.

The numerical-computational part of the thesis begins in Chapter II where the basic equations and numerical techniques are described. Starting with Pocklington's integral equation, the field interactions of neighbouring current segments are formulated. The numerical analysis essentially involves the use of pulse basis functions and impulse weighting functions. In transforming the equations into "Kirchhoff-like network equations," a slight but significant departure is made from the basic methods formulated by Harrington [20], Poggio and Miller [47], and Thiele [56]. Approximations for radiation pattern computations are also established.

In Chapter III, the wire-grid analysis method is described, and its application to calculation of current distribution of specific antenna configurations is developed. It is shown that the use of the technique is dependent to a large extent on the type of source feeding, and the geometry of the radiating structure. The method is applied in two steps. First, simple structures are considered, and these are then followed by more complex radiating structures. The simple structures consist of a monopole on a disk, a monopole on a sphere, a dipole mounted on the side of cylindrical towers (or masts) of different diameters, and a corner reflector antenna for different corner angles. The most complicated structure approximates a monopole mounted on the tail section of a helicopter. But before this structure is analyzed, intermediate configurations are modeled. First a radial dipole mounted on the side of a finite cylinder, next a dipole on the end of the cylinder, and finally a dipole on the large end of a truncated cone are considered. The technique is finally applied to determine the elliptically polarized radiation pattern of a monopole placed on a helicopter tail section. The effect of a variable geometry is also investigated partly by considering the effect of different positions of the helicopter rotor blades. The appropriate segmentation schemes and the particular computational procedures followed are discussed in some detail.

Chapter IV outlines a description of the experimental antenna models used and the experimental procedure followed.

A discussion of the computed and measured far-field radiation patterns is given in Chapter V . Plots of radiation patterns for principal plane cuts and polarization components are presented.

Finally, the significant results, conclusions and contributions are summarized in Chapter VI. The main observation drawn from comparisons of computed and measured patterns is that the wire-grid method of analysis is an effective practical and flexible technique, capable of wide application provided certain basic modeling steps are followed in obtaining wire models of antenna structures. Guidelines for these steps form an important contribution to this investigation.

CHAPTER II

EQUATION FORMULATION, NUMERICAL TECHNIQUE, AND RESPRESENTATION OF EXCITATION SOURCE

2.1 Introduction

The field of an isolated current element is first formulated in terms of its current distribution. The current element is assumed to be a perfectly conducting wire, and its radius and length are taken as parameters. The method of equation formulation is then extended to a finite number of neighbouring current elements. The basic numerical technique for transforming the integral equations into a system of linear equations which can be referred to as "Kirchhoff-like network equations" is then outlined. The solution of these network equations yields the unknown current distribution on the wire elements. Since the representation of the source is essential to the setting up of the equations, an extensive consideration of excitation source models is presented. Finally the radiation field equations, which are needed for pattern computation, are derived.

2.2 Integral Equation Formulation

2.2.1 Fields of a Cylindrical Current Element

Consider the cylindrical element of finite length s and radius $a \ll \lambda$, where λ denotes wavelength. As shown in Figure 2.1, the element is oriented along the z-axis. A time-harmonic current $I(z') \exp(j \omega t)$ is assumed. The current at any point along the element is considered to be uniform around its periphery.

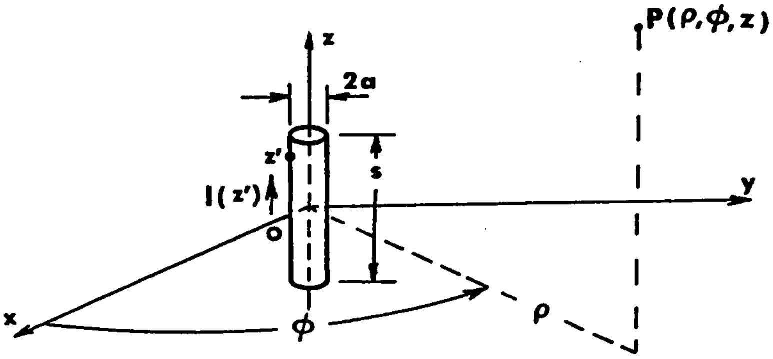

Figure 2.1. A Cylindrical Current Element of Length s and Radius a .

The electric field at an observation point P (ρ , φ , z) near the current element is sought, where ρ , φ , z are cylindrical coordinates. The time exponential will be hereafter omitted in the derivations, and the medium surrounding the current element is assumed to be free space (μ_o , ϵ_o) . Since the current I (z') is taken to be uniform around the element periphery, the fields will be independent of φ , and hence the observation point can be taken in the y - z plane. The z - component of the vector potential $\overline{A}$ and the scalar potential Φ can be written, respectively, in the form

$$A_z (\rho , \pi/2 , z) = \frac{\mu_o}{4\pi} \int_{-s/2}^{s/2} i (z') G (z , z') d z' \tag{2.1}$$

and

$$\Phi (\rho , \pi/2, z) = \frac{1}{4 \pi \epsilon_o} \int_{-s/2}^{s/2} q (z') G (z, z') d z' \tag{2.2}$$

where $I(z')$ has been defined above, and $q(z')$ is the charge per unit length of the element. The Green's function $G(z, z')$ is given by

$$G(z, z') = \frac{1}{2\pi} \int_0^{2\pi} \frac{e^{-jkR}}{R} \, d\varphi' \tag{2.3}$$

with

$$R = [(z - z')^2 + \rho^2 + a^2 - 2\rho a \cos\varphi']^{1/2} \tag{2.4}$$

where $j = \sqrt{-1}$ and $k = \omega \sqrt{\mu_o \epsilon_o}$ is the wave number for radian frequency ω. The coordinates of the source point on the surface of the current element are taken to be (a, φ', z'). Since the current element is assumed to be perfectly conducting, then because of skin effect the current is concentrated on the surface of the cylinder. Thus the element can be solid or a hollow cylinder provided the condition $a << \lambda$ is satisfied.

The electric field $\overline{E}^s$ due to the current and charge on the element can be obtained from the potentials by

$$\overline{E}^s = -j\omega \overline{A} - \nabla \Phi \tag{2.5}$$

where the superscript s is used to distinguish this field from an impressed (or incident) electric field $\overline{E}^i$. The vector and scalar potentials satisfy the condition

$$\nabla \cdot \overline{A} + j\omega \mu_o \epsilon_o \Phi = 0 \tag{2.6}$$

The line current $I(z')$ and the charge density $q(z')$ also satisfy the continuity relation

$$\frac{d\, I(z')}{d z'} + j \omega \epsilon_o q(z') = 0 \tag{2.7}$$

Thus with Equations (2.5), (2.6), and (2.7), it can be shown that

$$\overline{E}^s = -\frac{j\omega}{k^2} [\nabla (\nabla \cdot \overline{A}) + k^2 \overline{A}] \tag{2.8}$$

Because of the φ - symmetry, the vector $\overline{E}^s$ will have radial and axial components only, i.e.,

$$\overline{E}^s = \overline{i}_z E_z^s + \overline{i}_\rho E_\rho^s \tag{2.9}$$

where $\overline{i}_z$ and $\overline{i}_\rho$ are unit vectors in the axial and radial directions. Thus from Equations (2.1), (2.8), and (2.9), the z-component of the electric field can be written in the form

$$E_z^s = \frac{-j}{4\pi\omega\epsilon_o} \int_{-s/2}^{s/2} I(z') \left[\frac{\partial^2 G(z,z')}{\partial z^2} + k^2 G(z,z') \right] dz' \tag{2.10}$$

Similarly, the radial component becomes

$$E_\rho^s = \frac{-j}{4\pi\omega\epsilon_o} \int_{-s/2}^{s/2} I(z') \frac{\partial^2 G(z,z')}{\partial z\, \partial \rho} dz' \tag{2.11}$$

Equations (2.10) and (2.11) give the complete field, and they are valid for regions near and including the surface of the wire element. If in addition an impressed field $\overline{E}_z^i$ is applied parallel to the axis of the element, and is also uniformly distributed around its periphery, then the boundary condition

$$E_z^s + E_z^i = 0 \tag{2.12}$$

must be satisfied on the wire surface since it has been assumed to be perfectly conducting. Re-writing (2.12) in the form

$$E_z^s = - E_z^i \tag{2.13}$$

and substituting (2.13) in (2.12), the integral equation

$$- \frac{j}{4 \pi \omega \epsilon_o} \int_{-s/2}^{s/2} I(z') \left[\frac{\partial^2 G(z, z')}{\partial z^2} + k^2 G(z, z') \right] dz' = - E_z^i \tag{2.14}$$

is obtained. If $\overline{E}_z^i$ is known or given, then (2.14) is an equation for the current distribution $I(z')$. The equation is commonly referred to as Pocklington's integral equation, and it has been used as the starting point in formulating equations for straight wire antennas [14]. The Green's function $G(z, z')$ can be integrated numerically, but it is also frequently approximated by [16]

$$G(z, z') \approx \frac{e^{-jkr}}{r} \tag{2.15}$$

where

$$r = [(z - z')^2 + \rho^2 + a^2]^{1/2} \tag{2.16}$$

With this approximation, the differentiations in (2.10) and (2.11) can be carried out inside the integral signs. The resulting relations are

$$\begin{aligned} E_z^s &= - E_z^i \\ &= - \frac{j}{4 \pi \omega \epsilon_o} \int_{-s/2}^{s/2} I(z') \left[2 r^2 (1 + jkr) - (\rho^2 + a^2)(3 + 3jkr - k^2 r^2) \right] \frac{e^{-jkr}}{r^5} dz' \end{aligned} \tag{2.17}$$

and,

$$E_{\rho}^{s} = -\frac{j}{4\pi\omega\epsilon_o}\int_{-s/2}^{s/2} I(z')\,[(z-z')(3+3jkr-k^2r^2]\frac{e^{-jkr}}{r^5}\,dz' \tag{2.18}$$

Equations (2.17) and (2.18) are the fundamental relations used in the wire-grid analysis method.

2.2.2 Field Equations for N Interacting Current Elements

The formulations given in (2.17) and (2.18) can be easily applied to a system of N (≥ 2) arbitrarily oriented cylindrical current elements. First consider the two current elements shown in Figure 2.2a. Each element is specified by its length s_m and s_n, radius a_m and a_n, and centre coordinates (x_m, y_m, z_m), and (x_n, y_n, z_n), respectively, with respect to the origin 0.

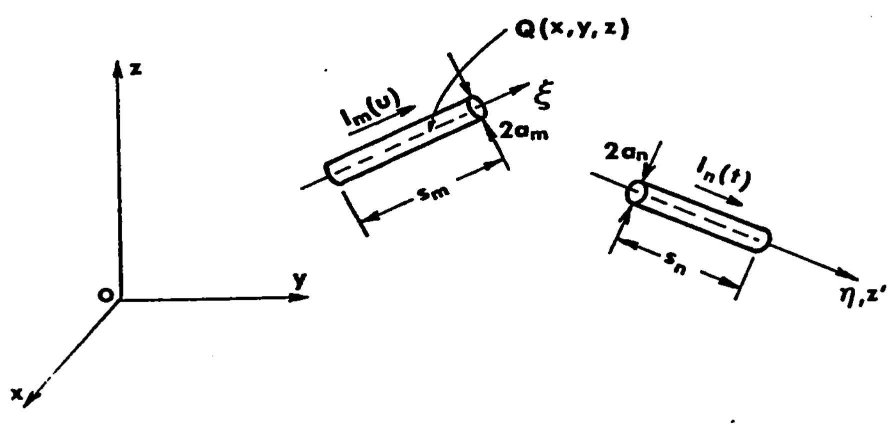

Figure 2.2a. Two Arbitrarily Oriented Cylindrical Current Elements.

Axial coordinates ξ and η are defined in the direction of current flow in each element, and the respective current distributions are

$$I_m\ (u) \qquad\qquad -s_m/2 \le u \le s_m/2$$

and

$$I_n\ (t) \qquad\qquad -s_n/2 \le t \le s_n/2$$

for elements s_m and s_n, respectively. Let the impressed field along the axis of s_m be E^i_ξ. It is required to express the total axial electric field along the axis of s_m. The total field consists of two components : one part is the given impressed field E^i_ξ, and the other component is the field due to the self-current $I_m\ (u)$ plus the field due to the current $I_n\ (v)$ on element s_n. The total field, by (2.12), must be zero on the surface of s_m. This boundary condition can, however, be matched at any point inside s_m, and this will be done along the axis of s_m. Thus at any point inside s_m and along its axis, there exists the condition

$$E^i_\xi + E^s_\xi = 0 \tag{2.19}$$

where E^i_ξ is given, and

$$E^s_\xi = (E^s_m)_m + (E^s_n)_m \tag{2.20}$$

In (2.20), $(E^s_m)_m$ is the axial field due to the self-current $I_m\ (u)$, and $(E^s_n)_m$

is the field component* due to the current $I_n(t)$ on segment s_n. The $(E^s_m)_m$ component can be deduced from (2.17) provided new coordinate axes are defined with the ξ - axis replacing the z - axis of Figure 2.1 . To evaluate $(E^s_n)_m$, a coordinate transformation is required, and it should be noted that Richmond's main contribution [51] in the development of the wire-grid technique probably lies in simplifying this coordinate transformation.

An approach which is partially different is presented below. The direction of the current flow in each element has already been specified, but further information about the angular orientation is also needed. Using Richmond's notation, each element lies an angle α below a plane parallel to the x - y plane, and its projection in the x - y plane makes an angle β with the x - axis. The angles are shown in Figure 2.2 b, with the arrow indicating the direction of current flow.

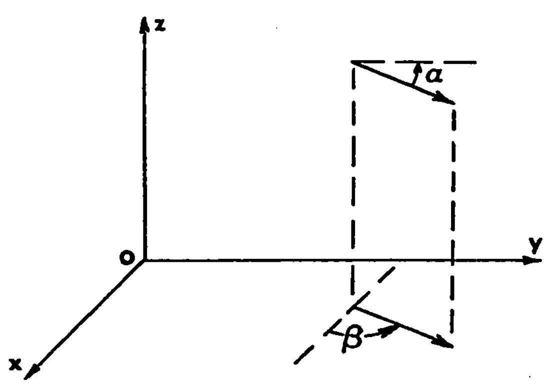

Figure 2.2 b. Direction of Current Flow in a Wire Element Specified by Angles α and β .

---

* Some additional explanation about the superscripts and subscripts is needed here. The superscript " s " has been defined on page 19 . The internal subscript denotes the source current, and the external subscript refers to the point of observation.

Referring again to the two elements in Figure 2.2 a, it is seen that element s_m, a_m, is defined by its centre-coordinates (x_m, y_m, z_m) with respect to a chosen reference system centred at 0, and orientation angles α_m and β_m. Similarly current element s_n is defined by (s_n, a_n, x_n, y_n, z_n, α_n, β_n). To simplify the derivation, it can be assumed that $a_m = a_n = a$. The next step is to define a new coordinate system (x', y', z',) centred at (x_n, y_n, z_n), with the z' - axis coinciding with the z - axis, i.e. the axis of element s_n. The following unit vectors are also defined :

$\bar{i}_x$, $\bar{i}_y$, $\bar{i}_z$: in the (x, y, z) coordinate system.

$\bar{i}_{x'}$, $\bar{i}_{y'}$, $\bar{i}_{z'}$: in the new (x', y', z') system.

$\bar{i}_\xi$: in the direction of current flow in element s_m.

$\bar{i}_\eta = \bar{i}_{z'}$: in the direction of current flow in element s_n.

$\bar{i}_\rho$: radial unit vector in the (x, y, z) system.

$\bar{i}_{\rho'}$: radial unit vector in the (x', y', z') system.

In terms of the orientation angles, it can be shown that

$$\bar{i}_\xi = \bar{i}_x \cos\alpha_m \cos\beta_m + \bar{i}_y \cos\alpha_m \sin\beta_m - \bar{i}_z \sin\alpha_m \tag{2.21}$$

Similarly

$$\bar{i}_\eta = \bar{i}_{z'} = \bar{i}_x \cos\alpha_n \cos\beta_n + \bar{i}_y \cos\alpha_n \sin\beta_n - \bar{i}_z \sin\alpha_n \tag{2.22}$$

If the direction cosines $(\lambda_1, \mu_1, \nu_1)$, $(\lambda_2, \mu_2, \nu_2)$, and $(\lambda_3, \mu_3, \nu_3)$ are defined for each of the new x', y', z' axes with respect to the fixed reference system of axes [57], then the new coordinates will be given by the following relations :

$$x' = \lambda_1 x + \mu_1 y + \nu_1 z \tag{2.23a}$$

$$y' = \lambda_2 x + \mu_2 y + \nu_2 z \tag{2.23b}$$

$$z' = \lambda_3 x + \mu_3 y + \nu_3 z \tag{2.23c}$$

with $$\lambda_1 = \sin\beta_n \; , \; \mu_1 = -\cos\beta_n \; , \; \nu_1 = 0 \; , \tag{2.24a}$$

$$\lambda_2 = -\sin\alpha_n \cos\beta_n \; , \; \mu_2 = -\sin\alpha_n \sin\beta_n \; , \; \nu_3 = -\cos\alpha_n \; , \tag{2.24b}$$

and $$\lambda_3 = \cos\alpha_n \cos\beta_n \; , \; \mu_3 = \cos\alpha_n \sin\beta_n \; , \; \nu_3 = -\sin\alpha_n \; . \tag{2.24c}$$

Knowing the transformation coefficients, the coordinates of element s_m can be referred to the new system of axes. A point Q is chosen on the axis of element s_m, and its coordinates can be specified by $Q(x, y, z)$ or $Q(x', y', z')$. If the distance from the origin of the new system (i.e. x_n, y_n, z_n) to the point Q is defined by $\bar{r}'$, it can be expressed either in the form

$$\bar{r}' = \bar{i}_x (x - x_n) + \bar{i}_y (y - y_n) + \bar{i}_z (y - z_n) \tag{2.25a}$$

or $$\bar{r}' = \bar{i}_{x'} x' + \bar{i}_{y'} y' + \bar{i}_{z'} z' \tag{2.25b}$$

Then the cylindrical radial distance is given by

$$\rho' = [\,|\bar{r}'|^2 - z'^2\,]^{1/2} \tag{2.26}$$

Thus the radial unit vector $\bar{i}_{\rho'}$ is given by

$$\bar{i}_{\rho'} = \bar{i}_{x'}\, x' / \rho' + \bar{i}_{y'}\, y' / \rho' \tag{2.27a}$$

or equivalently by,

$$\bar{i}_{\rho'} = (\bar{r}' - \bar{i}_{z'}\, z') / \rho' \tag{2.27b}$$

Once the unit vectors $\bar{i}_\xi$, $\bar{i}_\eta$ (or $\bar{i}_{z'}$) and $\bar{i}_{\rho'}$ are described in terms of the unit vectors $\bar{i}_x$, $\bar{i}_y$, $\bar{i}_z$, the field component $(E_n^s)_m$ can be evaluated by

$$(E_n^s)_m = \bar{i}_\xi \cdot \bar{i}_{z'}\, E^s_{z'_m} + \bar{i}_\xi \cdot \bar{i}_{\rho'}\, E^s_{\rho'_m} \tag{2.28}$$

where, once again, $(E_n^s)_m$ is the field at s_m due to the current on s_n. The components $E^s_{z'_m}$ and $E^s_{\rho'_m}$, are to be determined using (2.17) and (2.18), respectively.

When there are $N > 2$ neighbouring elements, the above procedure can be repeated. This will be illustrated by considering the four elements shown in Figure 2.3. Consider the case where it is required to find the total field due to the four current elements inside and along the axis of s_4. Then, with (2.20), the field at

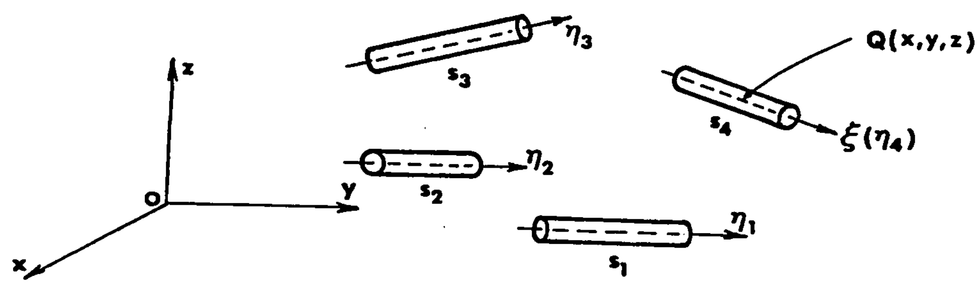

Figure 2.3. Four Arbitrarily Oriented Current Elements.

Q would be given by

$$E^s_\xi = (E^s_4)_4 + \sum_{n=1}^{3} (E^s_n)_4 \tag{2.29}$$

where $(E^s_4)_4$ will be the self-field, and $(E^s_n)_4$ represents the contribution from each of the neighbouring elements, and is to be evaluated by (2.28). Thus for N arbitrarily oriented current elements, all assumed to be perfectly conducting and thin cylindrical wires, the field inside and along the axis of the m^{th} element can be expressed in the form

$$E^s_\xi = (E^s_m)_m + \sum_{\substack{n=1 \\ n\neq m}}^{N-1} (E^s_n)_m \tag{2.30}$$

It should be noted that the point $Q(x, y, z)$ at which E^s_ξ is to be evaluated has not yet been specified. This will be done after the numerical method for solving the approximate current values is outlined in the following section.

2.3 Numerical Technique

The numerical method used in this study is essentially the generalized method of moments described by Harrington [20], [21]. However, the wire-grid analysis method was formulated earlier by Richmond [51] without any recourse to the moment method, and the "network equations" for the unknown current distribution were established by Aharoni [1], Schelkunoff [2], and Schelkunoff and Friis [58], long before high-speed digital computers became generally available. The numerical technique, however, contributes a firm mathematical foundation for the approximations needed to transform the integral equations into a system of algebraic equations similar to Kirchhoff's network equations.

2.3.1 Generalized Moment Method

Integro-differential or integral equations of the types of (2.5) or (2.10) can be formulated in the form [20]

$$L\,B(z) = h(z) \tag{2.31}$$

where L is defined as a linear integro-differential operator, $B(z)$ is the unknown function or response, and $h(z)$ is the known function or excitation. In general, $B(z)$ and $h(z)$ are complex functions. The first step in the moment method requires an approximation of $B(z)$ by a finite series of basis or expansion functions such that

$$B(z) \approx \sum_{n=1}^{N} b_n f_n(z) . \tag{2.32}$$

The b_n' s are undetermined coefficients, and the $f_n(z)$'s are independently defined over the domain of L , i.e. the space of functions on which L is defined and permitted to operate. The function $h(z)$ is said to be in the range of L , i.e., the space of all functions that L can generate by operating on $B(z)$. The operator has been defined to be linear, and therefore it satisfies the condition

$$L\,[a_k f_k(z) + a_z f_z(z) + \ldots + a_k f_k(z)] = a_1 L f_1(z) + \ldots + a_k f_k(z) \tag{2.33}$$

where $a_1 , a_2 , \ldots a_k$ are constant coefficients.

Thus if (2.32) is substituted into (2.31) , the resulting relation would be

$$\sum_{h=1}^{N} b_n L f_n(z) \approx h(z) \tag{2.34}$$

where L, because of (2.33) , operates over each basis function. The approximate equality sign should be noted, because of the finite sum representation of $B(z)$ as indicated by (2.32). It is required that a residual error $\epsilon(z)$ defined by

$$\epsilon(z) = L B(z) - \sum_{n=1}^{N} b_n L f_n(z) \tag{2.35}$$

converges to zero as the number of basis functions tends to infinity. In practice, the summation in (2.32) is finite, and consequently the residual error will not be zero [21]. In general, the f_n's can be defined as being non-zero over the entire domain of L, and in such cases they are referred to as entire-domain basis functions. However, in most applications, especially in wire antenna studies, they are defined in the domain of L, but exist only over parts or subsections of the domain. Hence they are denoted sub-domain or piecewise bases.

The next important step in the moment method is to introduce a set of weighting or testing functions $W_m(z)$, and to define an inner product [59]

$$< W_m(z) \, , \, Lf(z) > \; = \; < W_m(z) \, , \, h(z) > \tag{2.36a}$$

or in integral form,

$$\int W_m(z) \, [L f(z)]^* \, dz = \int W_m(z) \, h^*(z) \, dz \tag{2.36b}$$

where the asterisk denotes conjugation. Using (2.34), Equation (2.36a) can be put into the form

$$\sum_{n=1}^{N} < W_m \, , \, L f_n > b_n \approx < W_m \, , h > \tag{2.37}$$

where the coefficients b_n have been factored out by (2.33). Using network equation notation (2.37) can be stated in matrix form

$$[Z_{mn}] [I_n] = [V_m] \tag{2.38}$$

where the "impedance" coefficient Z_{mn} is given by

$$\begin{aligned} Z_{mn} &= \langle W_m , L f_n \rangle \\ &= \int W_m (z) [L f_n (z)]^* \, dz \end{aligned} \tag{2.39}$$

and the "voltage" V_m by

$$\begin{aligned} V_m &= \langle W_m , h \rangle \\ &= \int W_m (z) \, h^* (z) \, dz \end{aligned} \tag{2.40}$$

The column "current" matrix $[I_n]$ defined by

$$[I_n] = [b_n] \tag{2.41}$$

represents the unknown coefficients.

Two special cases of the moment method are :

(i) Galerkin's method in which the weighting functions W_m are chosen from the same class of basis functions, i.e.,

$$W_m(z) = f_m(z) \tag{2.42}$$

and

(ii) <u>The collocation or point-matching</u> method in which the weighting functions are delta - functions,

$$W_m(z) = \delta(z - z_m) \tag{2.43}$$

which are applied at $z = z_m$. A distinction is usually made between collocation and point-matching methods [47]. In the former case, triangular, sinusoidal and polynomial functions can be employed, whereas in the latter only rectangular piece-wise pulses are used as basis functions.

The choice of basis functions depends on the complexity of the problem and the degree of accuracy required. The functions commonly used as mentioned above in the analysis of wire antennas are the following three sub-domain approximations [56] :

Rectangular Pulses :

$$f_n = \begin{cases} b_n & \text{for } z \text{ in } \Delta z_n \\ 0 & \text{otherwise} \end{cases} \tag{2.44}$$

Triangular Functions :

$$f_n = \begin{cases} \dfrac{b_n (z_{n+1} - z) + b_{n+1} (z - z_n)}{\Delta z_n} & \text{for } z \text{ in } \Delta z_n \\ 0 & \text{otherwise} \end{cases} \tag{2.45}$$

Sinusoidal Interpolation Functions :

$$f_n = \begin{cases} a'_n + b'_n \sin k(z - z_n) + c'_n \cos k(z - z_n)^* & \text{for } z \text{ in } \Delta z_n \\ 0 & \text{otherwise} \end{cases} \qquad (2.46)$$

In Equations (2.44), (2.45) and (2.46), Δz_n denotes the length of a current element centred about z_n, and it is equivalent to the symbol s_n introduced earlier in the chapter.

When the moment method is applied to equation formulation of the type in (2.14), L represents a combined integration-differentiation operation, B (z) is the element current distribution I (z), and h (z) is the impressed field E_z^i along the axis of each element. The approximations involved in the discretization process are discussed in the next section.

2.3.2 Formulation of Network Equations

The network equations, a system of algebraic equations resulting from Pocklington's integral equations, are to be solved numerically for the current distribution on the arbitrary set of thin conducting cylinders as discussed in Section 2.2.2. The accuracy of the current values is directly related to the order of the basis functions. Higher order functions, for example triangular or sinusoidal functions, have been shown to yield better accuracy with faster convergence than the simple rectangular basis function [19], [60]. Unfortunately the determination of the unknown coefficients in (2.45) or

---

* A prime notation is used here to avoid confusion with b_n coefficients elsewhere.

(2.46) is quite lengthy even for the simplest geometric shape – namely the straight wire antenna.* Consequently, in many applications, the general practice is to use pulse basis functions with impulse weighting functions. Such an approximate point-matching method cannot be relied upon to give accurate near field or impedance values. Nevertheless, it has proved to give reasonably accurate radiation patterns if the condition $s \leq 0.1\,\lambda$ is satisfied by the length of each current element [56].

The wire elements discussed in Section 2.2.2 could be small sections of one long straight or curved wire, or they could be sections of a number of closely arranged wires. Provided the radius of each element $<< \lambda$, and its length $\leq 0.1\,\lambda$, then the current in the s_n th element can be approximated by

$$I_n(t) = \begin{cases} I_n & \text{for } t \text{ in } s_n \\ 0 & \text{otherwise} \end{cases} \qquad (2.47)$$

Hence, I_n can be taken outside the integral sign in (2.14). Next the boundary condition (2.19) must be matched at the centre point $Q\,(x_m, y_m, z_m)$. Thus if E^i_m is substituted for E^i_ξ, then with E^s_ξ obtained from (2.28), the point-matching method would yield, with N neighbouring elements, the relations

$$\sum_{n=1}^{N} Z'_{mn}\, I_n = -\,E^i_m \qquad (2.48a)$$

or in matrix notation,

---

* To illustrate the computational complexities involved when higher order basic functions are used, additional details on the sinusoidal interpolation functions (see Equation (2.46)) are given in Appendix A.

$$[Z'_{mn}]\,[I_n] = [-E^i_m] \tag{2.48b}$$

where

$$Z'_{mn} = (\bar{i}_\xi \cdot \bar{i}_{z'})\,E_{z'} + (\bar{i}_\xi \cdot \bar{i}_{\rho'})\,E_{\rho'} \tag{2.49}$$

It should be noted that $E_{z'}$ and $E_{\rho'}$ are different * from $E^s_{z'_m}$ and $E^s_{\rho'_m}$, and are defined by

$$E_{z'} = E^s_{z'_m} / I_n \tag{2.50}$$

$$E_{\rho'} = E^s_{\rho'_m} / I_n \tag{2.51}$$

The subscripts z'_m , and ρ'_m refer to the axial and radial components of the electric field due to current element s_n at the z'_m and ρ'_m coordinates of $Q\,(x_m, y_m, z_m)$ with respect to the new coordinate system, centred at (x_n, y_n, z_n). More explicitly, $E_{z'}$ and $E_{\rho'}$, can be expressed, respectively, by

$$E_{z'} = -\frac{i}{4\pi\omega\epsilon_o}\int_{-s_n/2}^{s_n/2}\left[\frac{\partial^2 G(z,t)}{\partial z^2}\bigg|_{z=z'_m} + k^2 G(z'_m, t)\right]dt \tag{2.52}$$

---

* The symbols $E_{z'}$ and $E_{\rho'}$ used here follow Richmond's notations [51] with the exception that in his case the $E_{z'}$ and $E_{\rho'}$ electric field components appear to correspond to $E^s_{z'_m}$ and $E^s_{\rho'_m}$ used above in (2.50) and (2.51).

and

$$E_{\rho'} = -\frac{j}{4\pi\omega\epsilon_o} \int_{-s_n/2}^{s_n/2} \left[\frac{\partial^2 G(z, t)}{\partial z \ \partial t} \Big|_{\substack{z = z_{m'} \\ \rho = \rho_{m'}}} \right] dt \tag{2.53}$$

where ρ'_m and z'_m will be expressed below in terms of angles of orientation and centre coordinates of the current elements. It is important to note that the integrations in both (2.52) and (2.53) are carried out with respect to the dummy variable t along the z' (or η) axis of element s_n. If the approximate kernel of (2.15) is used, the integration in (2.53) can be evaluated analytically. For $m \neq n$, i.e. non-diagonal terms of Z'_{mn}, (2.52) has to be determined numerically, and it has been shown [56] that either a fifth or ninth order Newton-Cotes integration scheme [61] would give good results. The choice between the fifth or ninth order is made depending on whether the distance between (x_n, y_n, z_n) and (x_m, y_m, z_m) is greater or less than about five times the radius of element s_n. The self-impedance terms, i.e. the case when $m = n$, can be approximated by analytical integrations of finite series expansions, as described in Appendix C.

The Z'_{mn} "impedance" parameters of (2.52) are direct measures of the field interaction of elements s_m and s_n. The following derivations will show how they are related to the angles of orientation (α_m, β_m) and (α_n, β_n), and their separation distances. Using (2.21) and (2.22) gives the dot product

$$\bar{i}_\xi \cdot \bar{i}_\eta = \cos\alpha_m \cos\beta_m \cos\alpha_n \cos\beta_n + \cos\alpha_m \sin\beta_m \cos\alpha_n \sin\beta_n + \sin\alpha_m \sin\alpha_n \tag{2.54}$$

To determine the product $\bar{i}_\xi \cdot \bar{i}_{\rho'}$, the unit vector $\bar{i}_{\rho'}$ has to be described more explicitly. From Equation (2.25a), the vector $\bar{r}'$ is given by

$$\bar{r}' = \bar{i}_x x_{mn} + \bar{i}_y y_{mn} + \bar{i}_z z_{mn} \tag{2.55}$$

where

$$x_{mn} = x_m - x_n , \quad y_{mn} = y_m - y_n , \quad z_{mn} = z_m - z_n \tag{2.56}$$

The cylindrical coordinates z'_m and ρ'_m, are given by

$$z'_m = x_{mn} \cos \alpha_n \cos \beta_n + y_{mn} \cos \alpha_n \sin \beta_n - z_{mn} \sin \alpha_n \tag{2.57}$$

and

$$\rho'_m = [\, |\bar{r}'|^2 - z'^{\,2}_m \,]^{1/2} \tag{2.58}$$

From (2.22), (2.27b), (2.57) and (2.58), the unit vector $\bar{i}_{\rho'}$ is given by

$$\begin{aligned} \bar{i}_{\rho'} = {} & \bar{i}_x (x_{mn} - z'_m \cos \alpha_n \cos \beta_n) / \rho'_m \\ & + \bar{i}_y (y_{mn} - z'_m \cos \alpha_n \sin \beta_n) / \rho'_m \\ & + \bar{i}_z (z_{mn} + z'_m \sin \alpha_n) / \rho'_m \end{aligned} \tag{2.59}$$

Therefore the dot product $\bar{i}_\xi \cdot \bar{i}_{\rho'}$ gives

$$\overline{i}_{\xi} \cdot \overline{i}_{\rho'} = \cos\alpha_m \cos\beta_m (x_{mn} - z_{m'} \cos\alpha_n \cos\beta_n) / \rho_{m'}$$

$$+ \cos\alpha_m \sin\beta_m (y_{mn} - z'_m \cos\alpha_n \sin\beta_n) / \rho_{m'} \tag{2.60}$$

$$- \sin\alpha_m (z_{mn} + z'_m \sin\alpha_n) / \rho_{m'}$$

In summary the non-diagonal Z'_{mn} parameters can be expressed in terms of space co-ordinates and angles of orientation of s_m and s_n, and also in terms of the values of $E_{z'}$ and $E_{\rho'}$ as defined by (2.52) and (2.53) in the form :

$$Z'_{mn} = (E_{z'} - z'_m E_{\rho'} / \rho'_m)(\cos\alpha_m \cos\beta_m \cos\alpha_n \cos\beta_n$$

$$+ \cos\alpha_m \sin\beta_m \cos\alpha_n \sin\beta_n + \sin\alpha_m \sin\alpha_n)$$

$$\tag{2.61}$$

$$+ E_{\rho'} (x_{mn} \cos\alpha_m \cos\beta_m + y_{mn} \cos\alpha_m \sin\beta_m$$

$$- z_{mn} \sin\alpha_m) / \rho'_m$$

This completes the formulation of the "network equations", and the problem that now remains is to determine how the $[- E^i_m]$ excitation matrix is to be filled.

2.4 Representation of the Source of Excitation

As mentioned in the introductory outline of this study, one major area which has not been fully covered in previous wire-grid analysis applications is a computational representation of an actual excitation source located on or near a finite conducting surface. In the following discussion an appraisal of source field representation for wire antennas is given and then the numerical evaluation of the source fields is formulated.

2.4.1 Physical and Mathematical Models of the Field Source for Wire Antennas

Very difficult and crucial questions that have been raised about the source in cylindrical antenna studies can be re-stated as follows :
What is the source of radiation ? Where exactly is it located ? How can it be modeled mathematically ? These problems have been considered by many antenna engineers and applied mathematicians, notably by Hallén [12], King [14], Schelkunoff [2], Infeld [62], Albert and Synge [17], and recently by Chen and Keller [63], King and Wu [64], and Otto [65], [66]. The basic field considerations used for reference are usually the coaxial feed arrangement of Figure 2.4 (a) or the balanced dipole feed shown in Figure (2.4 (b). An obvious observation is of course that the source is really a dielectric gap across which a time harmonic excitation voltage $V \exp(j \omega t)$ is maintained, V being the complex voltage amplitude, and ω is radian frequency. The general location of the source is also easily identified. In the case of the coaxial feed, it is at the base of the monopole, and in the symmetrical dipole case it must be between the arms of the antenna.

While higher modes may also exist [65], the principal excitation wave

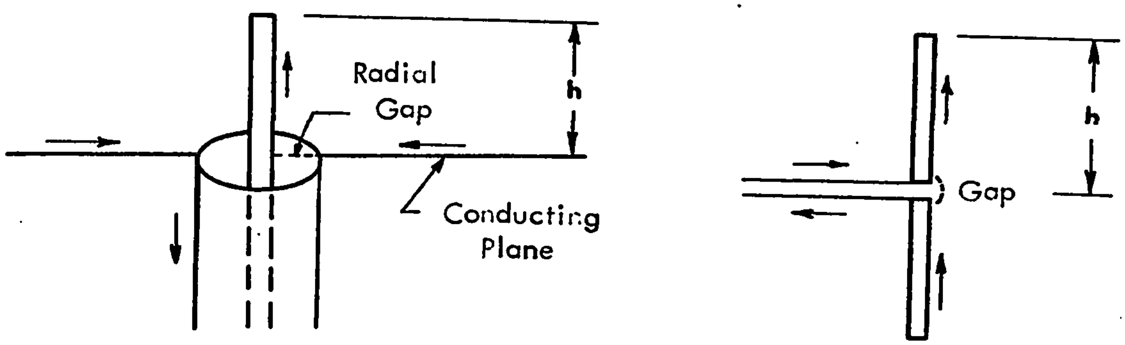

(a) Coaxially-Fed Monopole

(b) Centre-Fed Dipole

Figure 2.4. Basic Source Feeds.

in both types of gaps is a TEM-mode. Thus the mathematical model for both antennas * is usually the well-known delta-gap model (Figure 2.5) which is used in evaluating current distribution, input impedance, and near and far fields. The delta-gap model, which assumes an infinitesimal gap of width 2 g across which the voltage V is maintained, has greatly influenced the theoretical analysis of linear antennas. The representation was first introduced by Hallén to simplify the formulation of his integral equation for the centre-fed dipole by imposing on the impressed field the condition

---

* It is assumed that the conducting plane against which the monopole is fed, is infinitely large, and hence an image of the monopole is formed below the plane as indicated in Figure 2.5 (a).

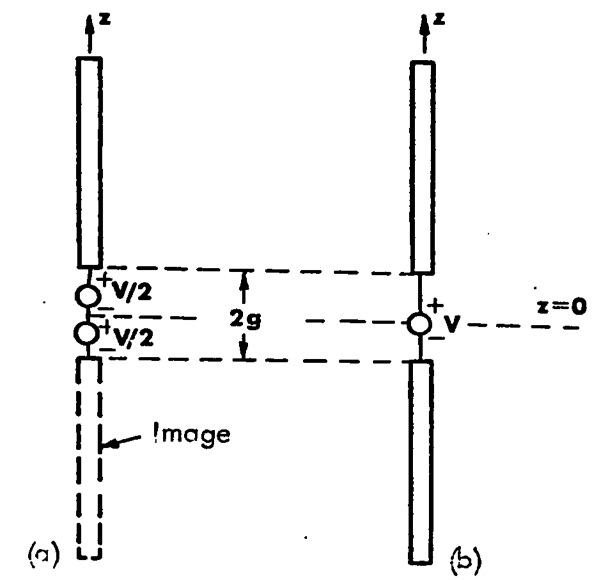

Figure 2.5. Delta-Gap Generator Models for (a) Base-Fed Monopole, (b) Centre-Fed Dipole. (Note : Source Region Expanded to show details of Modeling).

$$E_z^i = \begin{cases} -V\,\delta(z) & |z| < g \\ 0 & g < |z| \end{cases} \tag{2.62}$$

That is, the impressed electric field is zero on the surface of the perfectly conducting antenna except across the infinitesimal gap at the feed point. It can be easily seen that the simplifications made to arrive at this mathematical model are drastic, and yet the idealized approximations have proved to be effective and extremely useful.

Despite its immense success, especially in the hands of King and his research associates [14], [64], the delta-gap generator has been criticized on many occasions, mainly on physical grounds. One persistent doubt has been raised about the fact that a very narrow gap idealization, besides being artificial, leads to zero impedance or infinite admittance values. To clear this difficulty, a number of different assumptions and formulations have been tried. In Schelkunoff's work [2], the source was treated as a singularity enclosed within a spherical aperture of small radius as indicated in Figure 1 (c). This fitted very well with his conical theory of antennas, but the associated mathematics was very complex. Perhaps the only working model which has come to be regarded as an alternative to the delta - gap model, especially in recent computational applications, is the magnetic frill source shown in Figure 2.6 (a). This model was proposed by Albert and Synge [17] to represent the coaxial feed of Figure 2.4 (a). They also argued that in the case of the center - fed dipole, a more accurate model would be the finite width gap of Figure 2.6 (b).

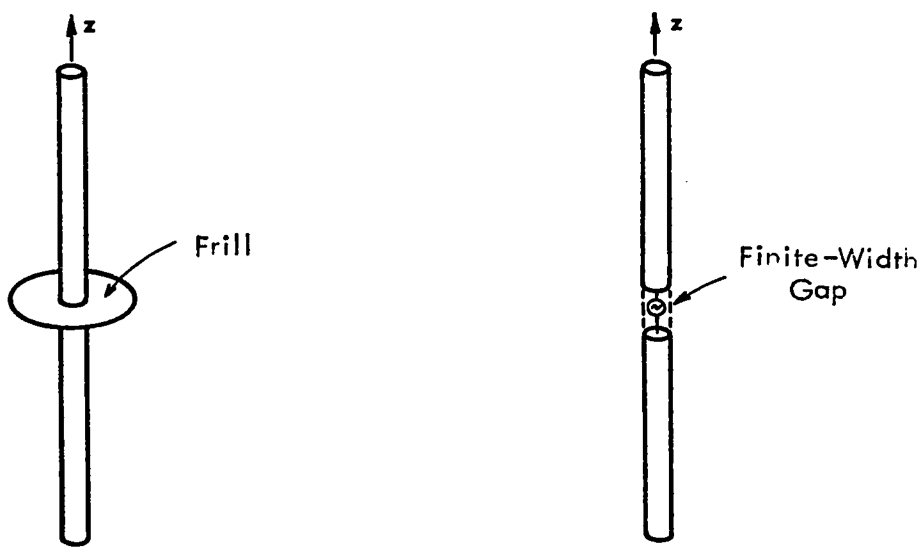

(a) Magnetic Frill Source

(b) Finite-Width Gap

Figure 2.6. Alternative Mathematical Models of Antenna Feeds.

For a delta - gap source, they observed, with the electric field along the surface of the antenna being almost everywhere zero, the existence of radiation could not be explained. To avoid this difficulty, the inclusion of an actual gap of finite width was therefore recommended. Similar observations have been made by Infeld [62], and Chen and Keller [63]. In defining the approximate gap width, Albert and Synge postulated the condition,

wavelength >> length of gap >> radius of antenna.

The requirement "length of gap >> radius of antenna" is somewhat stringent, but on the whole the finite - width gap and the frill model are nearer to physical situations than the idealized delta - gap model. Mathematically, the frill excitation source is a radial electric field given by [65]

$$E^i_\rho = \begin{cases} \dfrac{V}{\rho' \ln\left(\frac{b}{a}\right)}, & a < \rho' < b \\ 0, & \rho' > b. \end{cases} \tag{2.63}$$

where V is the voltage amplitude, a and b are the inner and outer radii of the frill as shown in Figure 2.7.

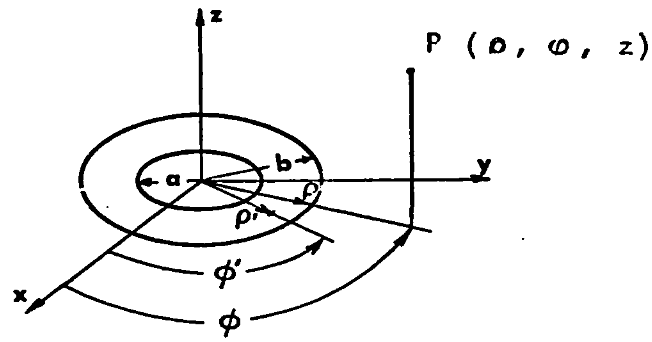

Figure 2.7. Details of the Frill Source.

Equivalently, from the relationship [35]

$$\bar{M} = \bar{E} \times \bar{n} \tag{2.64}$$

where $\bar{M}$ is magnetic surface current density and $\bar{n}$ is a unit vector normal to the plane of the frill, the source can be put in the form

$$M^{i}_{\varphi'} = \begin{cases} -\dfrac{V}{\rho' \ln \dfrac{b}{a}} , & a < \rho' < b \\ 0 , & \rho' > b \end{cases} \tag{2.65}$$

The field equations can be formulated using either (2.63), or (2.64) as the excitation source.

Other recent investigations have tended to establish the equivalence of the frill and delta - gap models [67], [68]. Still the basic feature of the various models remains essentially the same : the source of radiation in wire antennas is the large electric field (or equivalently, magnetic surface current) that is excited in the gap irrespective of whether it is assumed to be a frill, or a circumferential gap of finite width. On the surface of the perfectly conducting antenna, the same boundary conditions are postulated, and in the far field, the same radiation relationships are assumed. Consequently, the derived solutions give close agreement in predicting basic antenna characteristics and patterns.

The above brief summary of the mathematical representation of the source of electromagnetic radiation fields in linear antennas is not intended to be exhaustive and complete, nor is it intended to verify the different methods of highly involved mathematical formulations and derivations. It provides a firm perspective for the computational source models used in this work. It will be seen in the next section that modified versions of the finite-width gap or frill model can represent the source adequately for far field pattern computations.

2.4.2 Computational Source Models

In seeking computational source models, the essential objective is to evaluate numerically the source terms on the right hand side of (2.48b) or for an equivalent form to be derived below. With reference to Figure 2.8, the problem can be stated in two parts :

(a) Given a balanced dipole antenna mounted near an arbitrary conducting surface, how can the excitation field be determined ?

(b) Given a coaxially-fed wire antenna mounted on an arbitrary structure what source representation is adequate for far field computations ?

In both types of feed-arrangements, the radiating structures have finite electrical dimensions, and consequently image theory methods cannot be applied directly. Instead, the source models in Figure 2.8 are postulated. The model for the balanced dipole seems obvious, and the only point to be stressed is that it is a gap with finite width. On the other hand, the representations of the coaxial feed cannot be explained simply. A possible justification for the frill model is that, intuitively, it appears to be a nearer approximation to the actual source as in the case of an infinite plane structure. To justify the axial gap model, one has to resort probably to Schelkunoff's contention that the source of TEM and TM waves in linear antennas is a "spherical input boundary" of small radius concentrated around the feed point [2]. This suggests that the radial electric field can be approximated by an equivalent axial field within the radius of the "input boundary". However, the only strong justification for the finite width gap in place of the frill appears at this stage to depend mainly on its usefulness. Within computational accuracy, it predicts the far field patterns that would be obtained with a frill source model as demonstrated in Chapter III where current values computed with the two excitation representations are compared.

Having proposed the required models, attention can now be given to the numerical procedures. The frill source will be considered first. If the magnetic current density $\overline{M}$ in (2.64) is known, then the electrical vector potential $\overline{F}$ is given by [35]

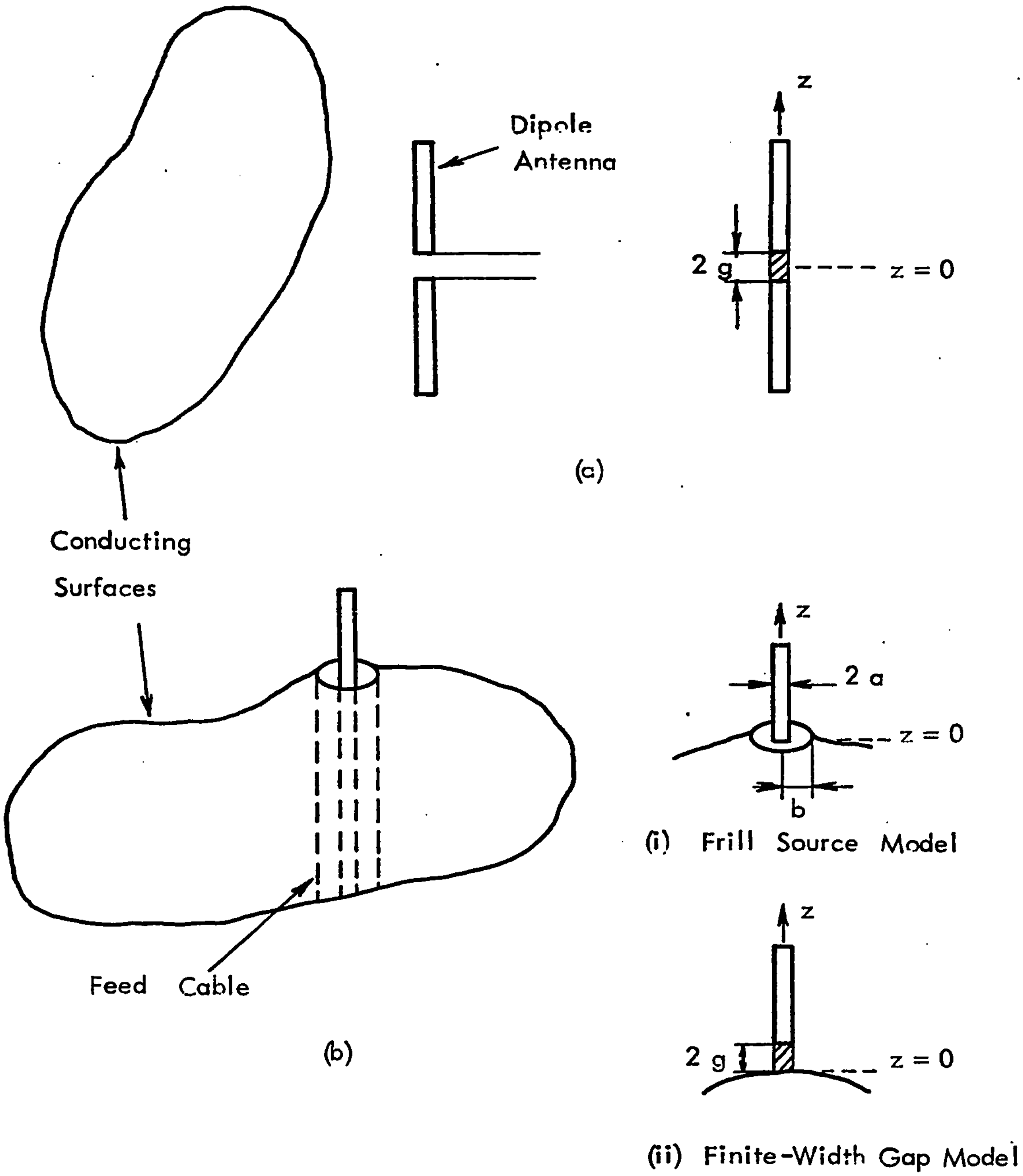

Figure 2.8. Physical Feed Arrangements and their Source Models :

(a) Dipole mounted near a Conducting Surface.

(b) Monopole mounted on a Conducting Surface.

$$\overline{F} = \frac{\epsilon_o}{4\pi} \iint\limits_{\substack{\text{Frill} \\ \text{Surface}}} \frac{\overline{M}\, e^{-jkr_o}}{r_o}\, dS' \tag{2.66}$$

where r_o with reference to Figure 2.7 is given by

$$r_o = \sqrt{z^2 + \rho^2 + \rho'^2 - 2\rho\rho' \cos(\varphi - \varphi')} \tag{2.67}$$

The primes indicate the source coordinates, and the observation point is at (ρ, φ, z). To simplify the derivations, it is assumed, without loss of generality, that the frill is centred at the origin of the coordinate system in, Figure 2.3 . Since $\overline{M}$ has only one component, $M_{\varphi'}$, $\overline{F}$ also has an F_φ component, and from axial symmetry, F_φ will be independent of φ. Thus the observation point can be taken in the $x - z$ plane, and from (2.66) ,

$$F_\varphi = \frac{\epsilon_o}{4\pi} \int_a^b \int_0^{2\pi} \frac{-V}{\ln(b/a)} \left(\frac{e^{-jkr_o}}{r_o} \right) \cos\varphi'\, d\varphi'\, d\rho' \tag{2.68}$$

The electric field $\overline{E}$ is related to $\overline{F}$ by [35]

$$\overline{E} = \frac{1}{\epsilon_o} \nabla \times \overline{F} \tag{2.69}$$

and hence

$$\overline{E}^i = \overline{i}_z E_z^i + \overline{i}_\rho E_\rho^i \tag{2.70}$$

where

$$E_z^i = -\frac{1}{\epsilon_o}\frac{1}{\rho}\frac{\partial}{\partial\rho}(\rho F_\varphi) \tag{2.71}$$

and

$$E_\rho^i = \frac{1}{\epsilon_o}\frac{\partial}{\partial z}(F_\varphi) \tag{2.72}$$

The excitation column in (2.48b) can now be determined from

$$E_m^i = \bar{i}_\xi \cdot \bar{E}^i \tag{2.73}$$

where $\bar{i}_\xi$, as defined by (2.21) is a unit vector parallel to the direction of current flow in element s_m, and (2.71) and (2.72) are evaluated at the centre of s_m. It can be shown that the expression of F_φ in (2.68) involves the determination of a complete elliptical integral of the first kind [55], [56]. The integrations and differentiations can readily be carried out numerically, and further details of derivations and analytical approximations are outlined in Appendix B.

The corresponding formulations for the finite-width gap involve much less computation. To begin with, the boundary conditions on the impressed field for the source model of Figure 2.8 (a), can be stated in the form

$$E_z^i = \begin{cases} -\dfrac{V}{2g} , & |z| < g \\ 0 , & |z| > g \end{cases} \tag{2.74}$$

and for the axial-gap model of Figure 2.8 (b) by

$$E_z^i = \begin{cases} -\dfrac{V}{2g} & , \quad 0 \leq z < 2g \\ 0 & , \quad z > 2g \end{cases} \tag{2.75}$$

In each case, 2 g is the total gap width. The only difference between (2.62) and (2.74) is that instead of an impulse function impressed over a delta-gap, there is now a uniform field over the finite-width gap.

Suppose now that the excitation gap is surrounded by a number of cylindrical current elements. The gap can be considered as a typical current element over which current is flowing, and at whose centre the boundary condition postulated by (2.12) is also to be satisfied. First, from (2.75) , provided the gap width $2g \leq 0.1\lambda$, the relationship

$$V = \begin{cases} -2g\,E_z^i & \text{over source element} \\ 0 & \text{all other elements} \end{cases} \tag{2.76}$$

is obtained. To generalize this result, if the m^{th} element of length s_m is taken and if (2.45a) is multiplied by $-s_m$, then

$$\sum_{n=1}^{N} Z_{mn}\, I_n = V_m^i \tag{2.77}$$

where

$$Z_{mn} = (-s_m)\, Z'_{mn} \tag{2.78}$$

Z'_{mn} has been defined previously, and

$$V^i_m = (-s_m)\, E^i_m \,. \tag{2.79}$$

If the total number of current elements including the source gap is N , and if the excitation "element" is identified as the lth element, then (2.76) , (2.77) and (2.79) yield the N by N matrix *

$$[Z_{mn}]\,[I_n] = [V^i_m] \tag{2.80}$$

where

$$[V^i_m] = \begin{array}{cl} \begin{bmatrix} 0 \\ \cdot \\ \cdot \\ \cdot \\ 1 \\ \cdot \\ \cdot \\ \cdot \\ 0 \end{bmatrix} & \begin{array}{l} \\ \\ \\ \\ \leftarrow l^{th} \text{ row} \\ \\ \\ \\ \\ \end{array} \end{array} \tag{2.81}$$

and the excitation voltage has been normalized to 1 volt. Equation (2.81) states that the excitation voltage is zero at the centre of every element except the lth element across which a uniform field is impressed. This type of approximation was first

---

* Only square coefficient matrices have been considered in this work.

shown by Harrington [20] to yield good results for current distribution computations on straight wire antennas * , **. However, as far as the author could determine, this is the first time that the method has been extended to arbitrary three dimensional structures.

Thus two approximate but alternative methods are available for determining the excitation fields, without which the element current distributions cannot be determined. Most of the computations made in this study have been based on the finite-width gap source model. Although programming and computational details have yet to be outlined, it is easy to see that (2.81) is simpler to handle than (2.73) , because the latter requires separate subprograms for integration and differentiation. However, it appears that the frill representation is probably more accurate than the artificially introduced gap with finite width [56] .

2.5 Radiation Fields

Once the current distribution on a given system of N neighbouring current elements is known, the radiated far field can be evaluated by a simple superposition of

---

* Mei [18] bypassed the problem of source modeling, since he applied the collocation method to Hallén's integral equation directly. Popović [22] also essentially followed a similar procedure except that in his method the antenna current distribution is approximated by 'entire-domain' polynomials.

** One other noteworthy attempt has been made by Thiele [24] to model the excitation source of a linear antenna by means of a current generator. However, this formulation suffers from a basic disadvantage in that it cannot be used easily to determine input impedance.

contributions from each element. Consider the element s_m (with $s_m \leq 0.1\,\lambda$) shown in Figure 2.9.

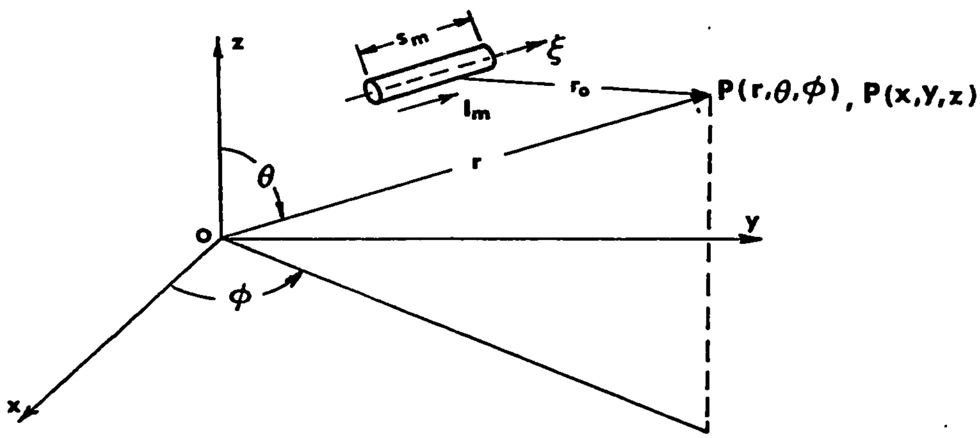

Figure 2.9. Coordinate System for Radiation Field of Current Element s_m.

The thin element is uniquely specified by the already defined parameters : length s_m, coordinates x_m, y_m, z_m, and angles of orientation α_m and β_m. Let the constant current distribution be I_m. Then the vector potential at the observation point is

$$
\begin{aligned}
\bar{A}_m &= \bar{i}_\xi\, A_m \\
&= \bar{i}_\xi\, \frac{\mu_o\, I_m\, s_m}{4\,\pi\, r_o'}\, e^{-j k r_o'}
\end{aligned}
\tag{2.82}
$$

where the unit vector $\bar{i}_\xi$ is in the direction of current flow, and has been defined by (2.21), and

$$r_o' = [(x - x_m)^2 + (y - y_m)^2 + (z - z_m)^2]^{1/2} \tag{2.83}$$

If the rectangular coordinates (x, y, z) are expressed in terms of the spherical coordinates (r, θ, φ), then

$$r_o' \approx r[1 - \frac{2}{r}(x_m \sin\theta \cos\varphi + y_m \sin\theta \sin\varphi + z_m \cos\theta)]^{1/2} \tag{2.84}$$

$$\approx r - (x_m \sin\theta \cos\varphi + y_m \sin\theta \sin\varphi + z_m \cos\theta) \tag{2.85}$$

For the denominator of (2.82), following Schelkunoff's formulation [69], the standard far field approximation is to set $r_o' \approx r$; for the phase exponential, however, the more complete expression given in (2.85) is retained, because the phase changes involved can be significantly large. Hence, the far field vector potential takes the form

$$\bar{A}_m = \bar{i}_\xi A_m$$
$$\approx i_\xi \mu_o \frac{I_m s_m}{4\pi r} e^{-jkr} e^{jk[x_m \sin\theta \cos\varphi + y_m \sin\theta \sin\varphi + z_m \cos\theta]} \tag{2.86}$$

The electric field has been expressed in terms of the vector potential by (2.8). Because of $1/r^2$ dependence, the component $-j\omega(\nabla(\nabla \cdot \bar{A}))/k^2$

is mainly localized in the near field region, and it can therefore be neglected in the far field region. Thus the radiation field is given by

$$\bar{E}_m \approx -j\omega \bar{A}_m \tag{2.87}$$

This field can be resolved into two components such that

$$\bar{E}_m = \bar{i}_\theta E_{\theta_m} + \bar{i}_\varphi E_{\varphi_m} \tag{2.88}$$

where

$$E_{\theta_m} = \bar{i}_\theta \cdot \bar{i}_\xi (-j\omega A_m) \tag{2.89}$$

$$E_{\varphi_m} = \bar{i}_\varphi \cdot \bar{i}_\xi (-j\omega A_m) \tag{2.90}$$

and $\bar{i}_\theta$, $\bar{i}_\varphi$ are spherical unit vectors given by the transformations

$$\bar{i}_\theta = \bar{i}_x \cos\theta \cos\varphi + \bar{i}_y \cos\theta \sin\varphi - \bar{i}_z \sin\theta \tag{2.91}$$

and

$$\bar{i}_\varphi = -\bar{i}_x \sin\varphi + \bar{i}_y \cos\varphi \tag{2.92}$$

Thus the total radiated field due to N neighbouring current elements will have an E_θ component of the form

$$E_\theta = -j\omega \sum_{n=1}^{N} (\cos\theta \cos\varphi \cos\alpha_m \cos\beta_m + \cos\theta \sin\varphi \cos\alpha_m \sin\beta_m + \sin\theta \sin\alpha_m) A_m \tag{2.93}$$

and an $\bar{E}_\varphi$ component of the form

$$E_\varphi = j\omega \sum_{n=1}^{N} (\sin\varphi \cos\alpha_m \cos\beta_m - \cos\varphi \cos\alpha_m \sin\beta_m) A_m \tag{2.94}$$

In general E_θ and E_φ are not in phase ; i.e., the radiation field is elliptically polarized.

It is important to emphasize an observation made earlier about the location of the current elements. They could be small sections of an arbitrarily shaped thin wire, or they could be just short wire elements distributed in some fashion over a three-dimensional configuration, and as stated in the introductory chapter, the nature of their distribution forms one of the basic problems of this study.

In summary, this chapter outlines the integral equation formulation and numerical methods for transforming these equations into a system of network equations. Physical and mathematical models of coaxially-fed sources have been discussed and the general expressions for the radiation fields described. The material as a whole forms a more complete basis for the wire-grid analysis method for radiating bodies with continuous surfaces, or with wire-grid structures. It is claimed to be more complete because a solution to the problem of excitation source representation has been proposed without any recourse to such methods as image theory or the use of the specialized delta-gap model. In the next chapter, the technique is applied to specific antenna systems for which the wire-grid model process and computer programming details are described.

CHAPTER III

WIRE-GRID ANALYSIS OF WIRE ANTENNAS NEAR CONDUCTING BODIES

3.1 Introduction

The task of this chapter is to apply the "network" equation formulations just presented to wire antennas mounted near finite conducting bodies which, as mentioned earlier, may be continuous surfaces or thin wire structures. The main emphasis is laid, however, on continuous surfaces. In formulating the equation, it is assumed that each element is uniquely specified by its dimension parameters and space coordinates with respect to a fixed reference system. It is also assumed that the current flow direction in each wire element is pre-assigned. The problem therefore is to attempt relating the current elements to the actual induced or impressed surface current distribution on a given conducting body excited by a nearby wire antenna. Specifically, the aim is to replace the continuous surface by a thin wire structure, not arbitrarily, but by following intuitive, heuristic but physically valid procedures. The resulting wire model segmented into small elements then allows the derivation of specific "network" equations. The equations are then solved for the approximate current distribution on the continuous body which is simulated by the wire model. The chapter is divided into four major topics, namely :

(i) Basic Wire-Grid Modeling and Analysis,

(ii) Programming Aspects of Current Distribution Computations,

(iii) Application to Simple Radiating Surfaces, and

(iv) Application to a number of increasingly more complex thin wire structures, commencing with a radial dipole on a cylinder and progressing to a dipole on a helicopter tail section.

The surfaces studied in this work are assumed to be perfectly conducting. Considerable effort is made to justify the models used by resorting to physical considerations of source-feed arrangement and the shape of each antenna structure. One major objective of the segmentation schemes in the case of the simple radiating structures is to improve the programming efficiency by exploiting the symmetry of the radiating body. Only the current distributions are considered here and the resulting radiation patterns are discussed in Chapter V .

3.2 Basic Wire-Grid Modeling and Analysis of a Conducting Body with a Wire Antenna near its Vicinity

3.2.1 Problem Formulation

The use of wire-grids or meshes in place of metal plates or surfaces has been known for quite a long time in antenna engineering design. In the case of the corner reflector antenna, extended reflecting sheets that would be normally used are replaced by parasitic conducting rods. Another standard design procedure is the replacement of a conducting disk by a grid of radial wires for a 'ground plane' antenna. Similarly the conducting ground planes of broadcast tower antennas are normally constructed from a mesh of buried copper conductors [10] . Not only are these practices well-established, but they also have good theoretical and experimental basis. For example, Maley and King [70] have made a theoretical-experimental study to support design criteria for radial wires. Kraus [30] and Moulin [31] have been able to derive design parameters for the corner reflector antenna from theoretical-experimental investigations. In general, grids or meshes have been found to act essentially the same as the continuous metal surfaces which they replace, without significant alteration to the results provided that the mesh gauge is small relative to the wavelength used. Thus the basic problem, as far as this work is concerned is not whether wire grids can be substituted for conducting surfaces, but whether the wire-grid modeling method can be formalized to simple rules or procedures. Such procedures would make the technique applicable to any arbitrary wire antenna in the vicinity of any conducting body while making the wire grid model as simple as possible in order to make it amenable to computational techniques. Therefore to formulate the problem more broadly, the following four questions are considered :

(a) Given a continuous conducting surface with a wire antenna mounted near its surface, how should its wire-grid model be established ?

(b) For a given thin wire structure which may have been obtained by modeling a continuous surface, or which may already be in a grid form, how are the one-dimensional integral equation formulations and the derived "network" equations applied ?

(c) How significant is the thinness of the wires in a given model ?

(d) Are there direct or indirect criteria for establishing whether the wire-grid model is "correct" or not ?

It will be shown that the answer to question (a) hinges on an intuitive appraisal of the physics of the particular antenna problem. The answer to question (b) involves essentially known techniques, but more emphasis is laid on how it can be related to the first and third questions. The question of the thinness of wires used in grid modeling has not been fully considered in recent computational works. Its influence is first qualitatively established, and then later verified in Section 3.4 by examining computed current distributions for a simple structure. The final question implies one of the following three possibilities : (i) knowing beforehand what the 'correct' model should be, (ii) going through a trial computational procedure to arrive at the final model, and (iii) working from experimentally measured radiation patterns for the continuous surface and / or its wire-grid model. The third possibility has been found to be very important to this study, and it will be examined later. Here it will be indicated that it is still difficult to formulate precise rules which would lead to a final 'correct' model. Still, it is possible to set heuristic guidelines based on source location and antenna configuration.

A fifth question can also be raised. How are currents at the junctions in a wire-grid model to be handled ? This problem is not considered in this investigation because of the greatly increased complexity which would be added to the computational procedures. A possible approach to this problem however might be based on a method proposed by Schelkunoff and Friis [58], which attempts to satisfy Kirchhoff's junction law and assumes a continuous potential distribution.

The remainder of this thesis shows how the above questions can be approached, and the results suggest the degree to which they can be answered at this stage of development.

3.2.2 Stationary Lines of Flow and Wire Grid Modeling

In Figure 3.1 are shown three general cases of antenna mountings and conducting surfaces which are representative of the structures investigated in this work. Figure 3.1 (a) illustrates an antenna near an arbitrarily shaped thick cylinder;* in Figure 3.1 (b) is a monopole centrally located on an essentially symmetrical shape; and Figure 3.1 (c) represents a radial dipole mounted on an arbitrarily shaped cylinder in an unsymmetrical manner. In each case, the dotted lines suggest the directions of flow for the induced (Figure 3.1 (a)), or impressed surface currents. If it is assumed that the surface current at any point can change in value, (i.e. depending on the strength of excitation) but not in the path along which it flows, then such lines may be described as stationary lines of flow [1]. This concept of stationary lines is central to the wire-grid analysis method as applied in this study.

The important question is how to establish these stationary flow lines. Here one might rely on a heuristic approach by resorting to the wave function type of solutions that would be obtained by classical methods. For time harmonic fields, the usual formulation of the partial differential equations derived from Maxwell's equations can be made in terms of the Hertz potentials $\bar{\pi}$ which are written in the form [40], [71]

$$\nabla^2 \bar{\pi} + k^2 \bar{\pi} = - \bar{J}^i / j \omega \epsilon_o \tag{3.1}$$

where $\bar{J}^i$ is the impressed current density. Each vector component of (3.1) is then treated as a scalar Helmholtz wave equation for which solutions, when permitted by the surface geometry, are found by separation of variables. This is followed by derivation of the electric field $\bar{E}$ and magnetic field $\bar{H}$ from the relations

$$\bar{E} = \omega^2 \mu \epsilon \bar{\pi} + \nabla (\nabla \cdot \bar{\pi}) \tag{3.2}$$

and

$$\bar{H} = j \omega \mu \nabla \times \bar{\pi} \tag{3.3}$$

---

* By a "thick cylinder" is meant here a circumference of the order of $0.1 \times \pi$ wavelength at any sectional plane [67].

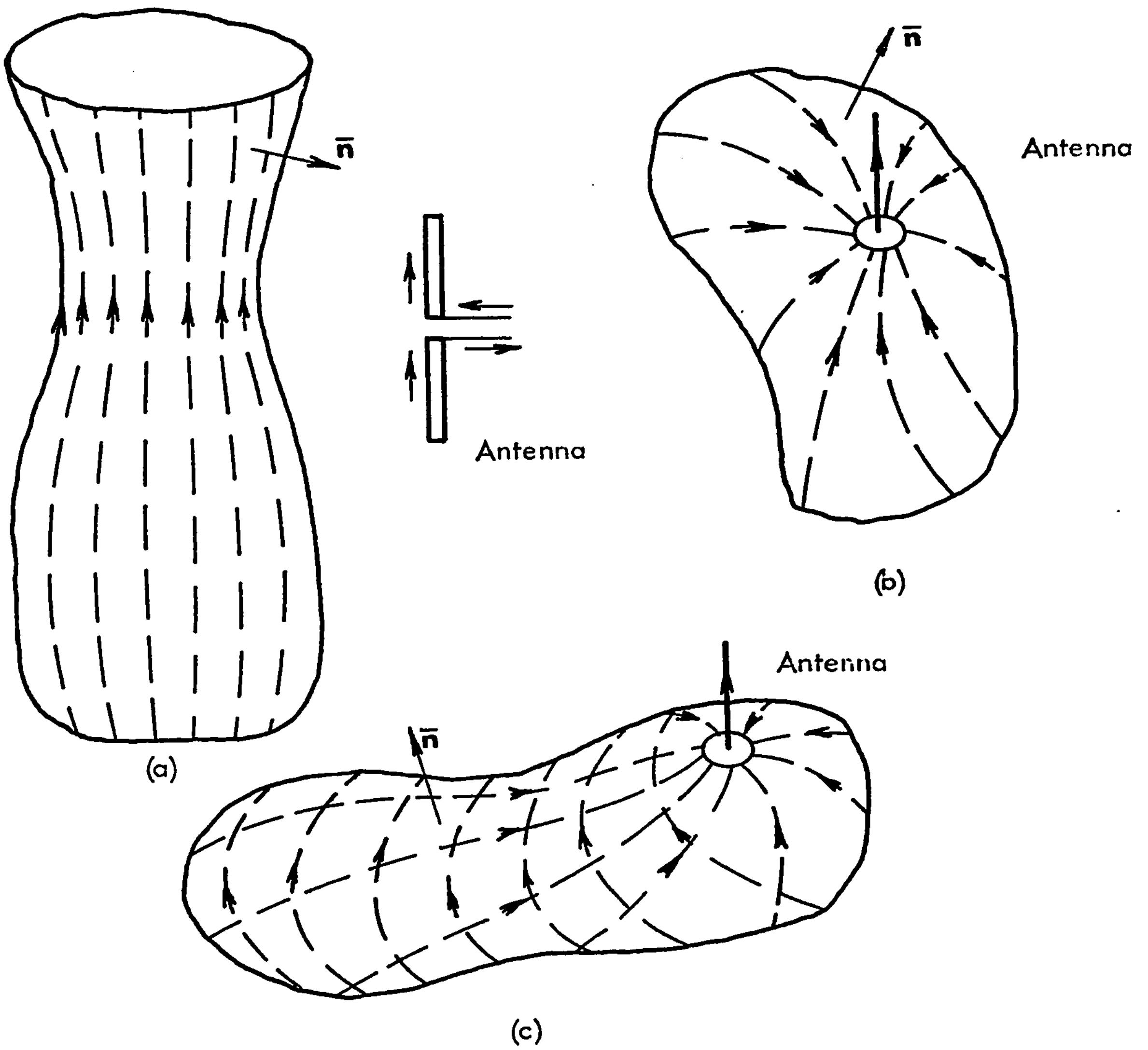

Figure 3.1. Radiating Antennas mounted near or on Conducting Surfaces.

(a) Antenna near a Cylinder.

(b) Antenna on a rounded surface with some degree of symmetry.

(c) Antenna on an arbitrary, largely unsymmetrical surface.

If $\overline{E}$ and $\overline{H}$ are known just outside the conducting surfaces of Figure 3.1, then, in principle, the surface current density $\overline{J}_s$ can be determined by imposing the tangential boundary conditions

$$\overline{n} \times \overline{E} = 0 \tag{3.4}$$

and

$$\overline{n} \times \overline{H} = \overline{J}_s \tag{3.5}$$

where $\overline{n}$ is a normal unit vector directed outwardly from the surface.* In practice, the main difficulty is that most conductor surface geometries, even if regular, are such that the boundary conditions (3.4) and (3.5) cannot be matched directly to the possible separable solutions of scalar wave equations. Fortunately, the direction of $\overline{J}_s$ can be deduced for many situations without undergoing the difficult formal solutions by examining carefully the feed arrangement, the antenna structure, and the polarization of the impressed or radiated fields. Going back to Figure 3.1 (a), the stationary lines are indicated in the general direction of the dipole field polarization, whereas for Figure 3.1 (b), the lines are shown to be essentially radial. However, it is to be noted that in Figure 3.1 (c) crossed stationary lines are postulated. It is well-known that cylindrical conductors with radial dipoles near their surfaces give rise to elliptically polarized radiation patterns [40]. This fact therefore suggests that the surface current density on the cylinder in Figure 3.1 (c) must have different vectorial components, and hence the need to assign to this particular configuration orthogonal stationary flow lines.

Despite the stated reasons for the chosen distribution of stationary lines of flow in the above three examples, it must be pointed out that these cannot possibly cover all

---

* In determining experimentally the current distribution on aircraft structures, Granger and Morita [43] measured the magnetic field H by mounting an exploring loop near the conductor surface, and then by (3.5), they were able to obtain maps of current distribution. It should also be mentioned that the data was interpreted qualitatively using results obtained from quasi-static arguments which are somewhat similar to the concept of stationary lines of flow.

cases of wire antennas near conducting surfaces. In fact, it should be mentioned that their choice is dictated by the types of specific structures which are to be discussed in Sections 3.4 and 3.5 below. Nevertheless, the basic steps would remain essentially the same, except that other problems might contain increasingly greater complexity. The main observation, whether one uses mathematical analysis or depends on a heuristic process, is that the orientation and distribution of the stationary lines of flow should serve as the point of departure for wire-grid modeling of any antenna system.

3.2.3 Wire-Grid Modeling and Analysis

The method of wire-grid analysis as used in this work follows generally known techniques. However, two important fundamental aspects are emphasized here for the first time. One refers to the excitation source representation, which has already been considered in the previous chapter. The second relates the location of the thin wires directly to the distribution of stationary lines of flow on the conducting body, as was concluded above. The thin wires, which may be straight or curved depending on whether the stationary lines of flow are straight or curved, are then segmented into small elements whose orientation is established from the lines of flow, and whose normalized coordinates (i.e. with respect to wavelength) are defined with reference to a chosen system of axes. The standard segmentation scheme for straight wires is simply to make equal lengths, but in certain cases it may be convenient to vary the segment lengths depending on the location of the wire members with respect to the feed region. Curved wires are first divided into small arcs, and then the arcs are approximated by chords. For simple surfaces of revolution, the whole segmentation scheme can be handled by a subroutine. On the other hand, for an arbitrary structure it may not be so easy to generate the segments, and it may therefore be required that coordinate data be supplied. This has to be done especially for arbitrary structures that are already in wire grid form. In the end, each wire element has to be specified by the parameters introduced in Chapter II, namely : its centre coordinates, its length and radius, and its angle of orientation.

In the integral equation formulation, it was assumed that the element length s was smaller than a wavelength, and its radius a was much smaller than a wavelength.

The more specific conditions

$$a << \lambda \quad \text{or} \quad k a << 1 \tag{3.6}$$

and

$$2a < s \leq 0.1\,\lambda \tag{3.7}$$

are now stated. But it should be pointed out that the grid wires are not necessarily restricted to be of circular cross section. Possible examples are wires with elliptical cross section or flat strips. King [14] has shown that if an arbitrary wire has a maximum cross-sectional dimension of $2u$, and length s satisfying the conditions

$$k u << 1 \tag{3.8a}$$

and

$$2u < s \leq 0.1\,\lambda \tag{3.8b}$$

then it can be treated as a cylindrical wire of equivalent radius a_e and length s. For the flat strip of Figure 3.2 (a), the equivalent radius a_e is given by

$$a_e = W/4 \tag{3.9}$$

where W is the width of the strip.

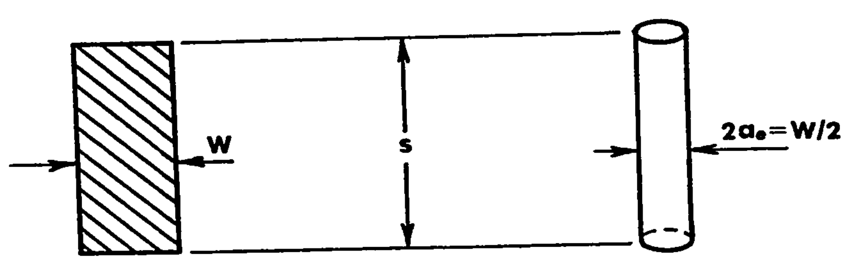

Figure 3.2. Equivalent Circular Wire of Radius a_e for a Flat Strip of Width W.

In the experimental part of this study, both wires with circular cross section and flat strips have been used in constructing wire-grid models, and hence the technique was applied to either type or a combination of both types of structures. It well may be argued that a flat strip is the more meaningful wire element to use when the modeling attempts to represent a surface situation. This argument, however, might necessitate the re-examination of the assumption made at the very beginning that the current distribution is uniform around the circumference of the wire element. This would particularly affect the formulation of the kernel of the integral equation in (2.14).

3.2.4 Significance of Wire Radius Parameter in Wire-Grid Modeling

The significance of the element length s has been emphasized in the derivation of the network equations in Section 2.3.2, and also by condition (3.7). It has been pointed out that because of computational difficulties, one is forced to consider only pulse - type basis functions. This would yield current distributions that are accurate enough for radiation pattern computations, but perhaps not for near field or impedance evaluations. The next question that arises is whether the wire thinness would also have much influence on the computed current distributions, and hence on the radiation patterns. In replacing a continuous surface by wire grids, one tends to assume that the wires, which are put on the stationary lines of flow, must be vanishingly thin. Certainly (3.6) and (3.7) have to be satisfied for each wire element in a given model, for otherwise the one-dimensional integral equations of (2.1) and (2.2) would not be valid [14], [72]. But in formulating, the electric field integral equations (2.17) and (2.18) and then in deriving the system of algebraic equations (2.77) for the unknown current distributions, it was stipulated that the tangential electric boundary condition was to be matched along the axis of each element. It was also assumed that the current would be uniform around the circumference of each wire element. Thus the wire radius, or the equivalent wire radius in the case of flat filaments or strips, from purely physical arguments, should be expected to affect the results of the wire modeling.

Assuming that it does, one is then led to ask why or how. In the recent discussions of numerical techniques in the literature, except in the case of the straight wire antenna [73], the influence of the wire radius has not received detailed study. However, its significance has been established experimentally and theoretically by Moullin [31] for wire-grid models of some conducting surfaces. He showed that the effectiveness of a grid of parasitic rods replacing metallic reflectors depended, in addition to the number of rods and their spacings, on critical values of the diameters of the rods. With this background, the influence of the wire radius on the numerical evaluation of (2.48b) and (2.77) was investigated. The impedance matrices $[Z'_{mn}]$ and $[Z_{mn}]$ are diagonally dominated by the self-impedance elements [18]. These terms being functions of the wire radius parameter are strongly affected by the value of a chosen, both in their real and imaginary parts. A strong dependence on a is thus to be expected.

Looking ahead to the experimental part of this study, it should be stressed that this awareness of the influence of the radius parameter was reached only after repeated computations failed to match adequately well with measured patterns. Current distributions computed for one of the simple grid models for different radius values will be examined in Section 3.4. It will be indicated there how the results have been interpreted for specifying the wire radii of an arbitrary thin wire structure for current computations.

3.2.5 Accuracy of Modeling

The fourth important question is whether the wire-grid representation used in a current (and pattern) computation is actually a 'correct' model, and also whether the number of elements obtained by segmentation is adequate. By a 'correct' model is meant here that the distribution and number of wire segments have been chosen to give as accurate results as possible. Obviously the question is directly related to the three previous questions in the problem formulation set. Since the 'correct' model cannot in general be known beforehand, it implies that either one has to proceed through an iterative process until convergence in current values or preferably in radiation pattern is achieved, or else one has to depend on experimental results for reference. While measured patterns are indeed the best tests for accuracy, the problem is of course that they are not always readily obtainable. Besides, the desired aim is to arrive at reasonably accurate patterns by wire grid analysis without resorting to scaled model or full scale measurements. However, from the computational point of view, an iterative procedure would be unnecessarily expensive. It is here that a fundamental set of "canonic " rules would be extremely useful. If such rules were available, they could be applied both in the modeling and segmenting procedures. As yet unfortunately, it has not been possible to formulate such rules precisely.

In similar related studies, practical figures of merit have been derived to serve as guidelines for determining the necessary grid wires and their spacing. In designing wire-grid lenses, Tanner and Andreasen [74] have calculated values for the ratio of square root of surface area to wavelength. More closely related to the problem at hand, Miller and others [52] have evaluated, from extensive scattering studies the sizes of wire grid openings which would adequately model radar cross sections of solid conducting surfaces. In a recent appraisal, Miller and others [75] have concluded however, that it is impossible to establish a complete set of guidelines for the modeling or segmentation requirements of an arbitrary conducting body. While the results of the present study as will be shown seem to suggest that there might be a set of "canonic" rules, still it should be stated that the fundamental approach has been largely intuitive and based essentially on heuristic arguments. One general observation that appears to be evident for the particular radiating surfaces studied is to put as many segments as possible near the source area. Although not applied to all the structures studied, it also appears that more segments might be placed on the side facing the wire antenna than on the "shadow" area of the conducting surface.

In seeking an accurate wire grid model, it should also be remembered that the segmentation is to be made as simple as possible. If the desired 'correct' model is more refined, then a relatively complex segmentation subprogram has to be prepared. Thus quite often a compromise has to be made between programming simplicity, and the need for more accurate wire grid modeling requirements. In summary, such a compromise would necessarily have to depend on simple heuristic approaches, depending on the antenna configuration and on experience.

3.3. Computation of Current Distributions : Basic Programming Aspects

3.3.1 Flow Chart of Current Computation Program

The organization of the basic program for the computation of current distribution on a given wire grid structure is shown in Figure 3.3. The program has been adopted from Thiele's work [56] with some minor and major changes. Blocks with (*) marks have been retained essentially in the same form as in Thiele's program. Blocks with (* *) marks have either been modified to suit particular applications or have been added and extended. Those blocks in double frame have been newly developed to handle structures that have not been solved previously by wire modeling method. The dimension list consists of both complex (impedance and current distributions) and real arrays. Generally, the segmentation subprogram reads in space coordinates in length units (e.g. centimeters), and these are then normalized with respect to wavelength. For simple geometries, the segmentations are carried inside the subprograms using a few data inputs, e.g. number of segments, wire antenna lengths and wire diameters.

The choice of source model can be made using two IF statements ; one IF leads to the evaluation of either the $[Z'_{mn}]$ of (2.48b) or the $[Z_{mn}]$ of (2.77) . The other IF statement selects, for the source column, either the impressed voltages of $[V^i_m]$ in (2.80) or the impressed electric fields at the points of matching. The latter column, i.e. the E^i_m of (2.73), are computed from the magnetic frill source model. A Gaussian elimination scheme which can handle systems of equations with complex coefficients has been adopted from McCracken [76] . Because the impedance $[Z'_{mn}]$ or $[Z_{mn}]$ matrices are characterized by large self-impedance terms as mentioned above, the elimination scheme used pivots directly on the diagonal elements without any further search for positioning [61] .

The excitation voltage in both source representations is set at one volt, and the computed current output is in amperes per volt. Further details on the computational structuring followed will emerge in the applications.

3.3.2 Validity and Accuracy Test

It will be shown (Chapter V) that the soundness of the computed patterns in this study has been established for most cases by comparison with measured or known

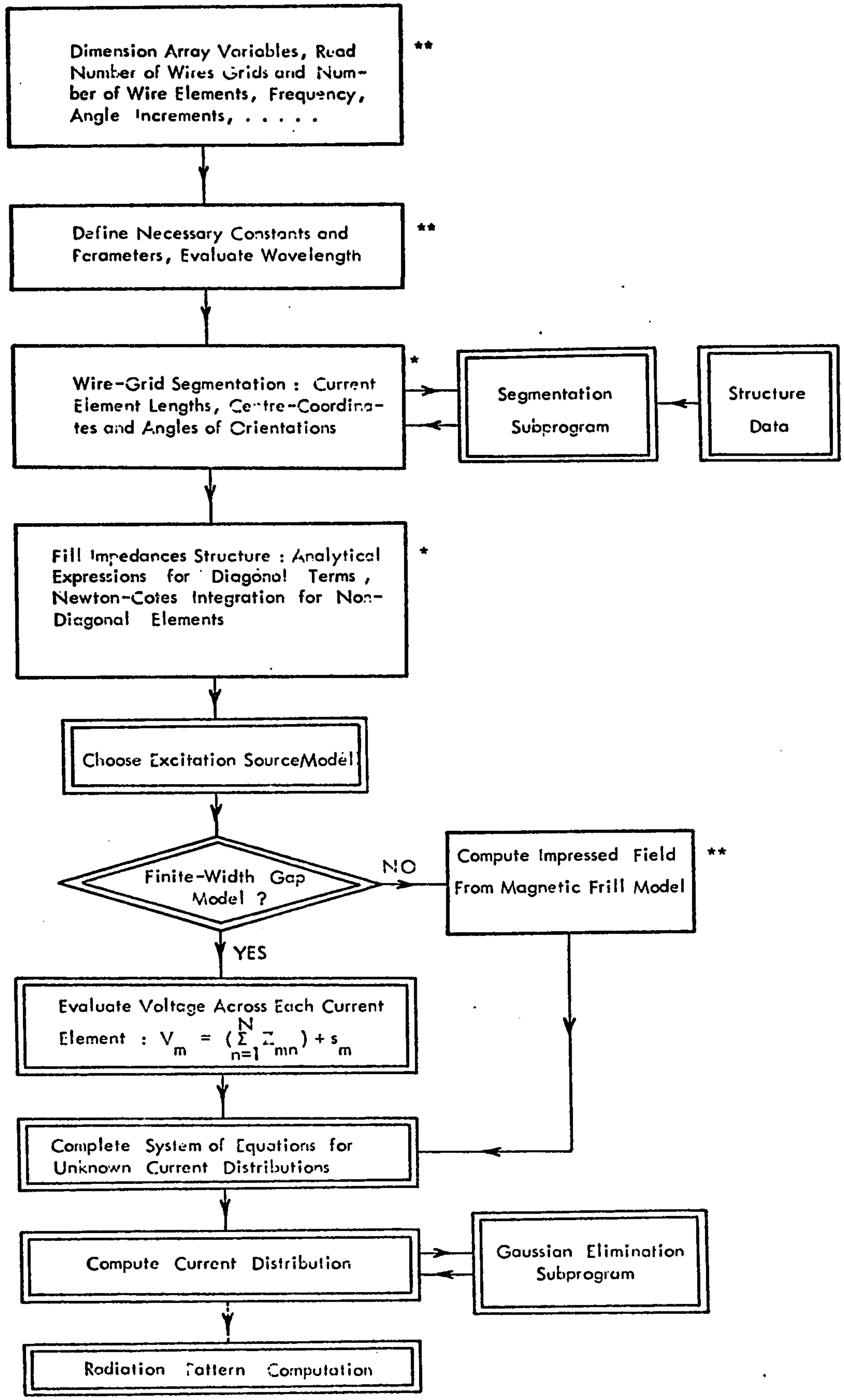

Figure 3.3. Flow Chart for Basic Current Computation Program.

patterns. It has already been pointed out that the significance of the wire radius parameter has been suggested by the experimental results. However, before being used in this study, some of the basic programming routines had to be tested. The two outstanding routines are the Gaussian elimination subprogram that is referred in Figure 3.3 and the source modeling representations discussed earlier. The validity and accuracy of their use was tested by computing current distributions on centre-fed dipole antennas by the moment method using sinusoidal basis functions. Both source models (i.e. the finite-width gap and the magnetic frill) have been attempted, and computed current values have been found to agree with known results.

As to the accuracy or rather the precision of computation, test runs have shown that Single Precision (SP) computations are sufficient for the purposes of this study. Besides the obvious saving in core memory storage, the gain in using Double Precision (DP) was found to be marginal, and this was established in the early phases of the investigation. Differences between SP and DP calculations appeared only in the sixth or seventh decimal places. Consequently, practically all final computations except for one limited use of DP in one segmentation subprogram, have been carried out in SP.

Up to this point, the foundations of the wire grid analysis method have been outlined. Equation formulations, and numerical techniques were covered in Chapter II. The first half of this chapter has been devoted to a closer examination of the wire grid modeling procedure and general programming aspects. The remainder of this chapter addresses itself to an application of the techniques to specific structures in considerable detail.

3.4 Wire Grid Analysis of Antennas near Simple Conducting Surfaces

The lines of stationary flow for simple conducting surfaces can be easily established, and hence their wire grid models determined using a physical and intuitive approach. Four basic geometries are considered here : a monopole on a sphere, a monopole on a disk, a dipole near a cylindrical tower or mast, and a dipole in a corner reflector. Because the sphere and disk are the simplest shapes and also share common programming details, they will be taken first together. The dipole near the cylinder is then considered next, and the corner reflector last.

3.4.1 Monopole on Sphere or on Plane Disk

Figure 3.4 (a) shows a monopole of height h mounted on a sphere. The monopole current distribution is denoted by $I_z(z')$ where $z' = 0$ corresponds to $z = R_s$. The current $I_s(\theta)$ on the sphere is assumed to flow on the meridian lines, and thus the wire-grid model of Figure 3.4 (b) is obtained. For the case of a monopole

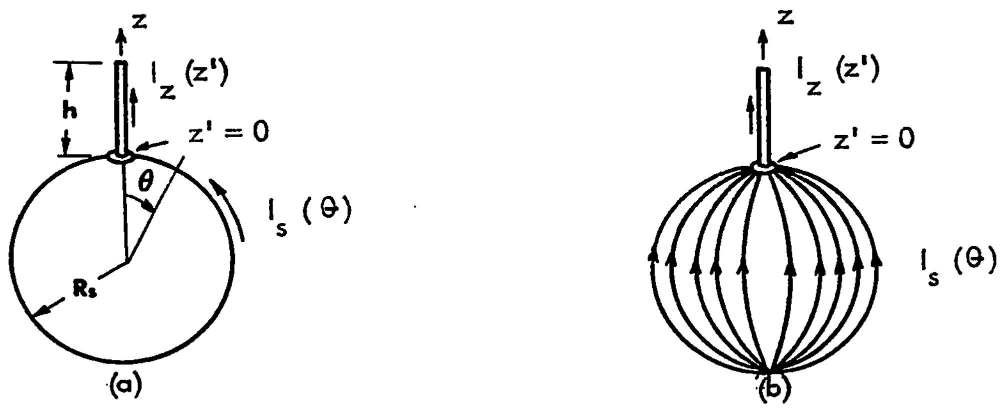

Figure 3.4. Wire-Grid Modeling of a Conducting Sphere.

of height h mounted on a disk of finite radius R_d (Figure 3.5 (a)), the model is the well-known grid of radial wires, shown in Figure 3.5 (b). In both cases the arrows indicate the directions of current flow on the stationary lines.

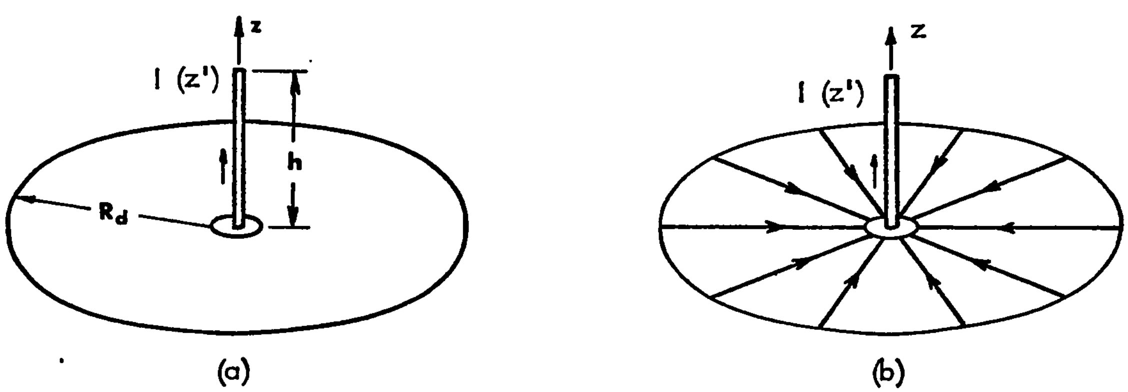

Figure 3.5. Modeling of a Conducting Disk by Radial Wires.

3.4.1 (a) Segmentation Scheme for the Disk Radial Wires

Although the sphere was modeled before the disk, it is easier to consider the segmentation scheme for the latter structure first. As indicated in Figures 3.6 (a) and 3.6 (b) the monopole, and one typical radial wire are segmented into short wire elements. The segmentation scheme proposed, at this stage, is heuristic and arbitrary but conforms to conditions (3.6) and (3.7). The source (shaded region) is also re-

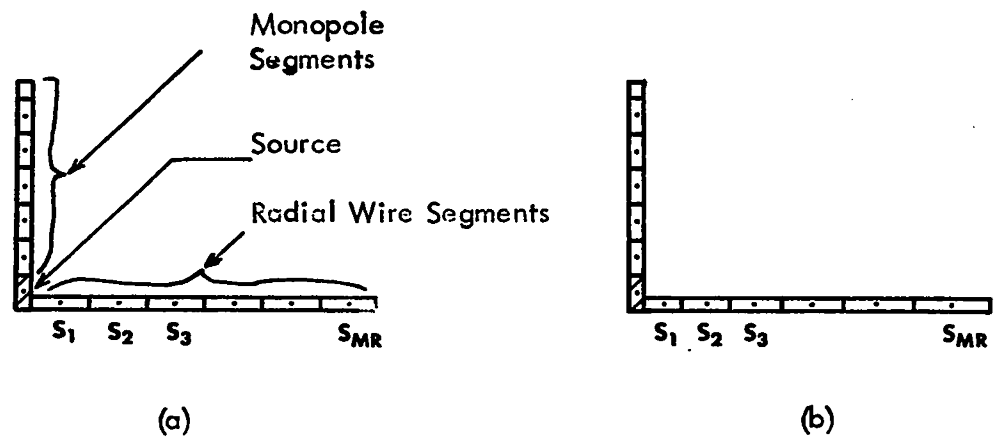

Figure 3.6. Details of Segmentation for Monopole Mounted on a Conducting Disk. (a) Uniform Segmentation. (b) Linearly increasing Segmentation.

presented by one segment. In Figure 3.6 (a), the segments are such that the lengths are equal, i.e.

$$s_1 = s_2 = \ldots\ldots\ldots s_{MR} \tag{3.10}$$

whereas in Figure 3.6 (b), the segment lengths are such that

$$s_2 - s_1 = \Delta, \quad s_3 - s_2 = \Delta, \ \ldots \tag{3.11a}$$

or

$$s_2 = s_1 + \Delta, \quad s_3 = s_2 + \Delta, \quad s_4 = s_3 + \Delta, \ \ldots\ldots \tag{3.11b}$$

where Δ is a small increment, and the segmentation length is said to be linearly increasing.

This has been introduced to place as many short segments as possible near the source region where the current is stronger than near the disk edge region. If the total number of segments n per radial wire is known, and the first segment length s_1 are known, the increment can be easily determined from the relation

$$\Delta = \frac{2 R_d}{n(n-1)} - \frac{2 s_1}{(n-1)} \tag{3.12}$$

The monopole segments can be taken very small or relatively long. If one is interested in improving the current values, segments lengths as small as 0.01λ would provide reasonably accurate distribution. For far field pattern calculations, the monopole segments can be safely taken as large as 0.05λ. Since the current at the end of the monopole should go to zero, a half - segment is normally left near the top end [20], but again for far field approximations this is not a crucial point. The value of s_1 in (3.12) can be set equal to the length of a monopole segment or any other value can be chosen provided the condition

$$s_n \leq 0.1 \lambda \tag{3.13}$$

is satisfied. The increment Δ can also be chosen judiciously, and if $\Delta = 0$, then

$$s_1 = s_2 = \ldots\ldots\ldots = s_n = \frac{R_d}{n} \tag{3.14}$$

The dots in Figure 3.6 represent the centre points of the wire elements. The other radial wires are segmented similarly, and this is followed by specifying the x, y, z coordinates of the centre points, and their angular orientation.

3.4.1 (b) Segmentation Scheme for Meridian Lines on Sphere

In the segmentation of curved wires there is, along with the "electrical" approximation problem, the additional problem of piecewise linear geometric approximation of a curve. Consider the arc AB and chord AB in Figure 3.7. The error difference Δ_s between the arc and chord lengths is given by

$$\Delta_s = R_c \theta - 2 R_c \sin\left(\frac{\theta}{2}\right) \tag{3.15a}$$

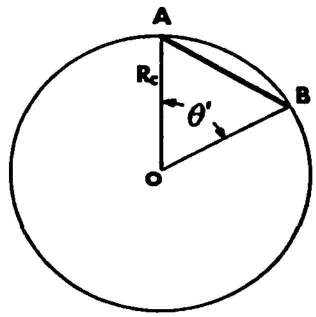

Figure 3.7. Approximating an Arc by a Chord.

where R_c is the radius of the circle A B C and θ is the angle subtended by AB. This can be approximated by

$$\Delta_s \approx \frac{R_c\ \theta^3}{24}\ , \qquad (\theta/2) < 1 \tag{3.15b}$$

$$\approx \frac{25\,\theta^3}{6}\ \%\ , \qquad (\theta/2) < 1 \tag{3.15c}$$

It is easy to see that provided $\theta \le \pi/3$, the error will be less than 5 % . Thus following this example, the meridans in Figure 3.4 (b) are first divided into arcs, and then the arcs are represented by chords as shown in Figure 3.8 (a) with constant segmentation, or in Figure 3.8 (b) with linearly increasing segmentation. The determination of the centre co-

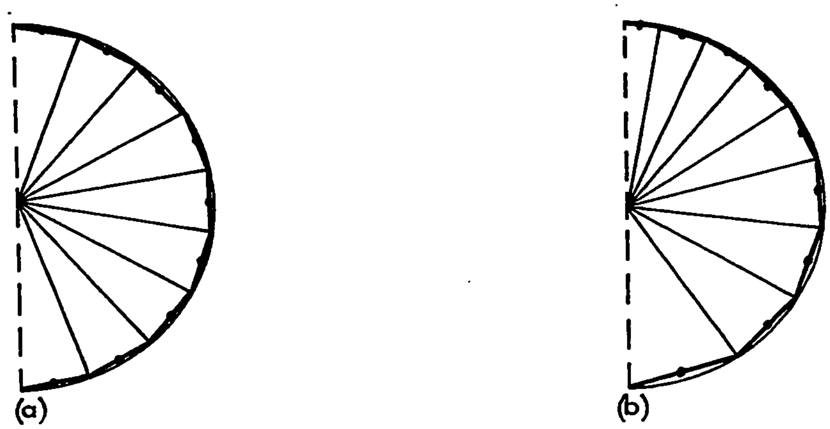

Figure 3.8. Segmentation of a Typical Semi-Circular Wire from the Sphere's Wire-Grid Model :
(a) Unifrom Segmentation, (b) Linearly increasing Segmentation.

ordinates and the angular parameters is obviously somewhat complicated, and this is especially true if linearly increasing segmentation is employed. If the one full meridian

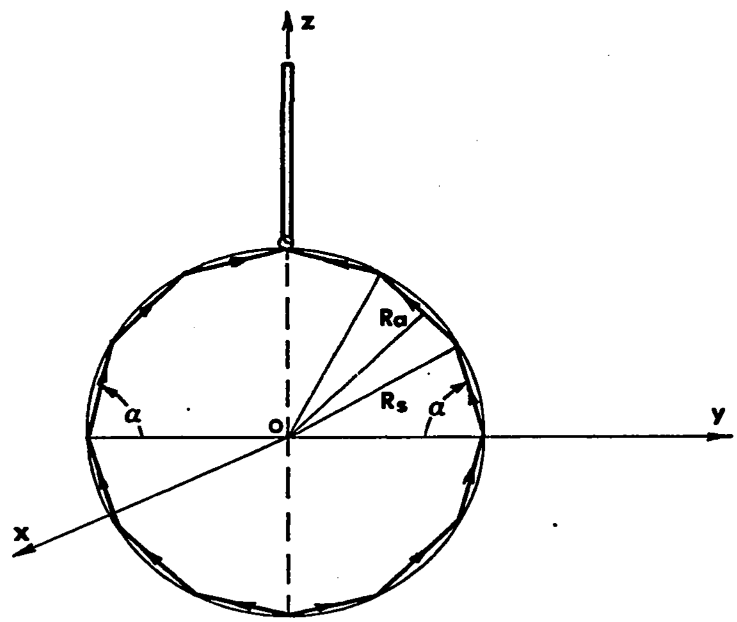

Figure 3.9. Details of Segmentation for the Sphere Grids.

circle in Figure 3.9 is considered, it can be concluded that symmetric segments will have identical α angles (i.e. with respect to the $x - y$ plane) but their β angles will be different by π radians. It is also important to note that for the assumed flow of current distribution, the α angles are all negative, since α is defined as shown in Figure 3.10(a) with the limits indicated in Figure 3.10 (b). These physical details of the segmentation

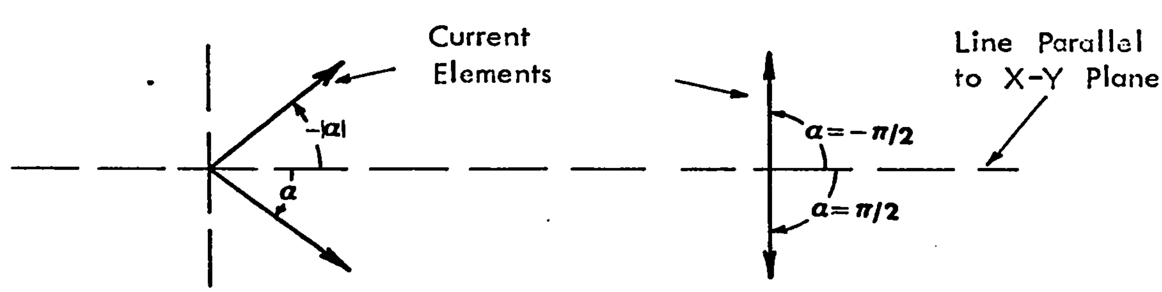

Figure 3.10. Maximum and Minimum Ranges of the Current Direction Angle α .

procedure involve elementary operations in three-dimensional geometry, but it should be mentioned that this was recognized only after the problem had been successfully solved. For a more complete description of the grid model segmentation for the sphere, reference may be made to Appendix D.

3.4.1 (c) Evaluation of the Impedance Matrix Elements

Not only are the above grid models obvious, but because of structural symmetry, the current distribution at corresponding points on the meridians or radials must be the same. This fact has been exploited in reducing the dimensions of the impedance matrix arrays, and the essential steps are examined as follows.

Let

NM = number of segments on monopole,

MR = number of segments on meridian or radial lines,

L = number of meridians or radial lines,

where it is assumed that L is even. If the total number of current elements is denoted by NWS, then

$$NWS = NM + L \times MR \tag{3.16}$$

Of these, however, the number of unique current elements is given by

$$MW = NM + MR \tag{3.17}$$

Obviously an impedance matrix which is MW x MW will be far less costly to operate on than an impedance matrix which is NWS x NWS. Hence in evaluating the impedance elements a reduced matrix is desirable and the next problem is to fill the reduced matrix. The dimensions of the impedance matrix array are shown in Figure 3.11. where all the lengths have been defined except for MKS and MLS, which are given by

$$MKS = L \times MR/2 \tag{3.18a}$$

and

$$MLS = MKS + MR \tag{3.18b}$$

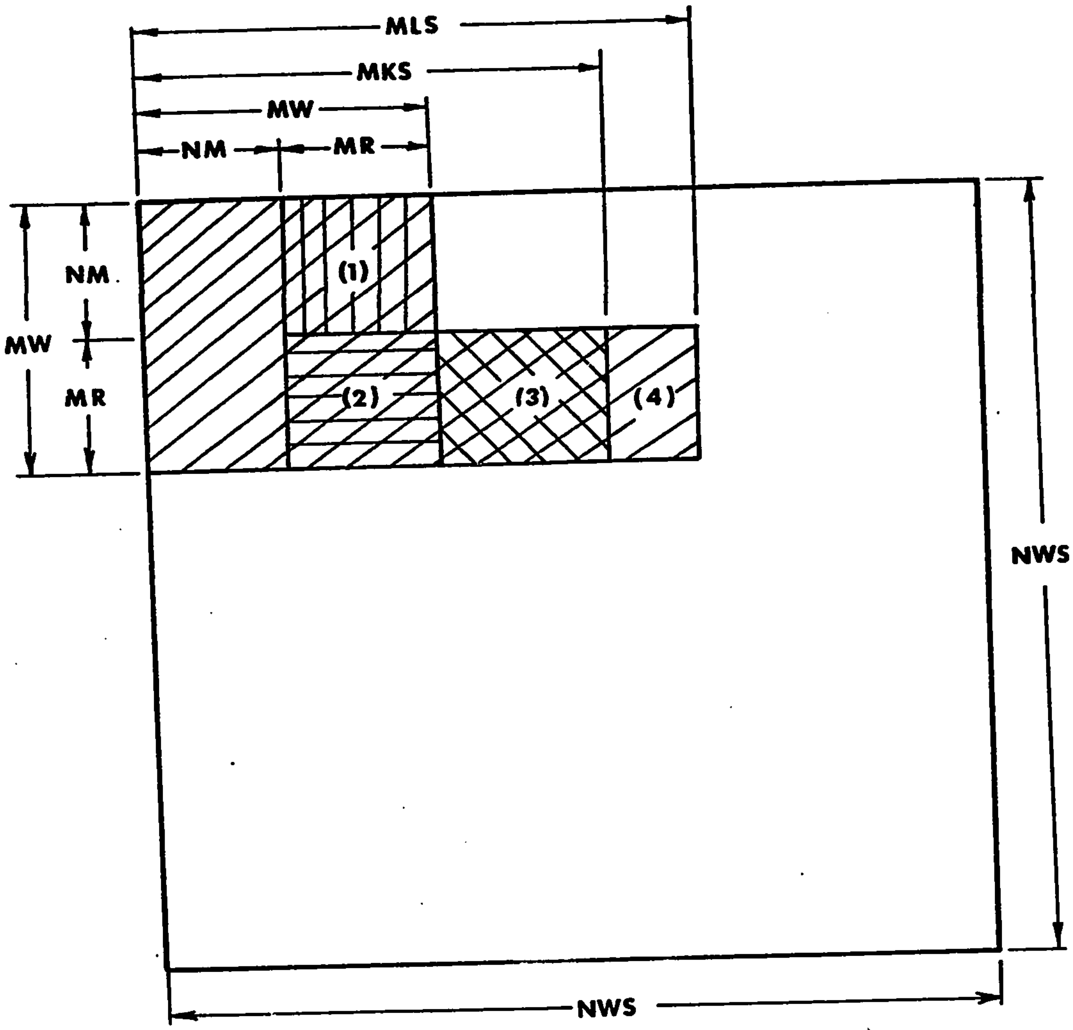

Figure 3.11. Impedance Matrix Evaluation for Monopole on Conducting Sphere or on Disk.

To understand the different shaded regions, consider the impedance equations given by (2.77) with Z_{ij} and I_j replacing Z_{mn} and I_n, respectively. First, it can be seen that

$$\sum_{j=1}^{MW} Z_{ij} I_j + \sum_{j=NM+1}^{NWS} Z_{ij} I_j = V_i^i , \qquad 1 \le i \le NM \tag{3.19}$$

But

$$\sum_{j=NM+1}^{NWS} Z_{ij} I_j = L \times \left(\sum_{j=NM+1}^{MW} Z_{ij} I_j \right) , \qquad 1 \le i \le NM \tag{3.20}$$

since the contributions from segments at a fixed distance from a point on the monopole are the same. Thus the region (1) in Figure 3.11 represents the left-hand side of (3.20). Continuing with additional MR rows, one would obtain

$$\sum_{j=1}^{NM} Z_{ij} I_j + \sum_{j=NM+1}^{NWS} Z_{ij} I_j = V_i^i \quad , \quad NM + 1 \le i \le MW \tag{3.21}$$

The first summation in (3.21) is represented by region (2) in Figure 3.11. Now the second summation on the right hand side of (3.21) can be replaced by

$$\sum_{j=NM+1}^{NWS} Z_{ij} I_j = 2 \times \underbrace{\sum_{j=NM+1}^{MKS} Z_{ij} I_j}_{\text{Region (3)}} + \underbrace{\sum_{j=MKS+1}^{MLS} Z_{ij} I_j}_{\text{Region (4)}} \quad , \quad \begin{array}{l} NM+1 \le i \le MW \\ NM+1 \le j \le MW \end{array} \tag{3.22}$$

The multiplication by the factor 2 is based on symmetry considerations, but the second sum on the right hand side determines the contributions from radial segments on the same diameter or meridian segments lying on the same circle. The next step in the reduction process requires identifying the symmetrically located segments. Such segments carry equal currents such that

$$I_k = I_{k1} = I_{k2} = \dots\dots\dots \quad , \quad NM+1 \le k \le MW \tag{3.23}$$

with $k1 = k + MR$, $k2 = k + 2\,MR$, . . . and so on. Thus (3.22) can be rewritten in the form

$$\sum_{j=NM+1}^{NWS} Z_{ij} I_j = \sum_{k=NM+1}^{MW} (Z_{i,k} + Z_{i,k1} + Z_{i,k2} + \dots\dots)\, I_k \quad , \quad NM+1 \le i \le MW \tag{3.24}$$

where regions (2), (3) and (4) are now compressed into region (2). Hence using (2.80) and (2.81), the final reduced matrix equation to be solved takes the form

$$\begin{bmatrix} Z_{i,1} & \cdots\cdots\cdots & Z_{1,MW} \\ \vdots & & \\ Z_{MI,1} & \cdots\cdots\cdots & Z_{MI,MW} \\ & & \\ Z_{MW,1} & \cdots\cdots\cdots & Z_{MW,MW} \end{bmatrix} \begin{bmatrix} I_1 \\ \vdots \\ I_{MI} \\ \vdots \\ I_{MW} \end{bmatrix} = \begin{bmatrix} 0 \\ \vdots \\ 1 \\ \vdots \\ 0 \end{bmatrix} \tag{3.25}$$

where MI signifies the source excitation segment. The excitation column in (3.25) could also be filled with impressed electric field values computed with a frill source, and then each ith row in the impedance matrix of (3.25) would have to be divided by s_i , i.e. the length of the ith segment, as discussed earlier in Section 2.3.

Once the MW current values are determined, the corresponding symmetrical elements are evaluated by (3.23), and therefore the approximate but complete current distribution on the monopole and on either the disk or the sphere is known.

3.4.1 (d) Significant Results from Current Computations for the Sphere Grid Models

The sphere was chosen in this study as a test model for the many basic assumptions and approximations involved in the wire grid analysis method. Consequently, somewhat extensive computations were carried out, and these are summarized in Table 3.1. Five different values of sphere radius ($\lambda/8$, $3\lambda/16$, $\lambda/4$, $5\lambda/16$, and $3\lambda/8$) were considered, and the number of meridians replacing the continuous surface was varied from 8 to 32 , with the total number of current segments, including the monopole segments, ranging from 125 to 825. The computed radiation patterns will be discussed later, and at this point more attention will be paid to : (i) the influence of sphere radius and the number of grids on the current distribution, and (ii) the equivalence of the excitation source models. Except for one trial computation, the wire radius a for all the elements in the spherical grid structure was determined from the well-known antenna parameter [14]

TABLE 3.1

SUMMARY OF COMPUTATIONS WITH WIRE-GRID MODELS OF CONDUCTING SPHERE (HEIGHT OF MONOPOLE SET AT 0.25 λ)

	SPHERE RADIUS R_s	SEGMENTATION					MAIN PURPOSE(S) OF COMPUTATION (S)
		L	MR	NM	MW	NWS	
1	$\lambda/8$	16	16	25	41	281	A
2	$\lambda/4$	16	16	25	41	281	A, B
3	$\lambda/4$	24	16	25	41	409	B
4	$\lambda/4$	24	25	25	50	625	B, D
5	$\lambda/4$	32	25	25	50	825	A, B, C, D
6	$3\lambda/16$	32	25	25	50	825	D
7	$5\lambda/16$	32	25	25	50	825	D
8	$3\lambda/8$	32	25	25	50	825	D
9	$\lambda/4$	16	15	5	20	245	E

Key of symbols used in "Main Purpose(s) of Computation (s)"

A : Testing of validity and accuracy of wire grid model by comparison with known results.

B : Computations made to arrive at an "optimum" grid model.

C : Study of source modeling : Finite-width gap model versus frill current source.

D : Pattern computations for comparison with measured patterns.

E : Testing of coarse segmentation for pattern computation.

$$\Omega = 2 \ln (2h/a) \tag{3.26}$$

where h is the height of the monopole.* The value of Ω was chosen to be 9.6, which for $h = \lambda/4$, yields **

$$a \approx 0.00412\,\lambda \tag{3.27}$$

The problem of determining the current distribution on the surface of a perfectly conducting sphere has been studied in some detail by Pappas and King [34]. However, in that work, the current on the monopole was assumed to be a sinusoidal distribution. Thus direct comparison cannot be made because in the results shown below, the real and imaginary components of the monopole current are seen to be influenced by the radius of the sphere. The plots shown in Figures 3.12 to 3.19 indicate the normalized computed currents $I_z(z')$ versus z' for the monopole, and $I_s(\theta)$ versus θ for a typical meridan line on the surface of the sphere. The parameters are R_s (radius of sphere), and the segmentation variables L and MR. Comparing Figures 3.12 and 3.13, there appears to be very little change introduced by the increase in sphere radius despite the fact that L is also doubled for $R_s = 3\lambda/16$. In Figures 3.14 and 3.15, it can be seen that for a fixed sphere radius of $R_s = \lambda/4$, there are significant variations in the real and imaginary components, although the current magnitudes appear to remain essentially of the same shape. For larger values of R_s both real and imaginary components of $I_s(\theta)$ begin to exhibit oscillatory variations, as indicated in Figure 3.19.

The equivalence of the finite-width gap model and the frill current source was established for $R_s = \lambda/4$ with $L = 32$ and $MR = 25$. The computed current results are compared as shown in Table 3.2 where it can be seen that an essentially fixed ratio exists between the two values. The discrepancy arises because the inner and outer radii of the frill in Figure 2.7 have to be approximated from physical dimensions. Thus the ratio b/a is very critical in that it scales down or up the impressed field by the factor $1/\ln(b/a)$ according to (2.63). Although this does not affect the far field pattern, it does change the magnitude of the computed current values.

---

* A more concise definition of the antenna parameter is $\Omega = 2 \ln$ (total antenna length / conductor radius).

** This value of Ω was also chosen by Tesche and Neurether [49].

3.4.1 (e) Important Results from Computations with the Disk Radial Wires

Most of the sphere computations listed in Table 3.1 were also repeated with a 0.166 λ monopole mounted on a disk with $R_d = 0.5\,\lambda$. However, the segmentation used was quite coarse because by the time the disk was successfully modeled (including the source), enough experience had been accumulated for the wire grid modeling procedure. During the course of the investigation, it was found that as long as the two conditions in (3.6) and (3.7), were satisfied, the segmentation as fine as used for the sphere was not necessary if far field patterns only were required. The disk was modeled with $L = 8$, 12, 16 and 24 radials. For the monopole, the number of segments was kept constant at $NM = 3$, and for each radial wire, $MR = 9$ was also kept constant. The important results obtained were : (i) the equivalence of the source models was again established, and (ii) the significance of the wire radius parameter, as indicated in Tables 3.3 (a) and 3.3 (b), was shown. The current results in the latter tables demonstrate that the wire radius is indeed a significant parameter, and the obvious conclusion drawn is that its value should be chosen judiciously. More specifically, if one were to apply the wire grid analysis method to actual thin wire structures, then the wire radius dimensions must be taken into consideration as accurately as possible. This interpretation has influenced significantly the relative accuracy of computed patterns in comparison with measured patterns for antenna structures studied in this work.

Figures 3.12 to 3.19. Normalized Current Distribution for Monopole (Height $h = \lambda/4$) Mounted on Spheres of Different Radii.

(a) Monopole Current Distribution

(b) Current Distribution on One Typical Meridian.

Current Components : —o—o— Imaginary, —x— Real, —•—•— Magnitude.

Parameters : R_s = Sphere Radius, L = Number of Meridians for Sphere Modeling, MR = Number of Segments in Each Meridian.

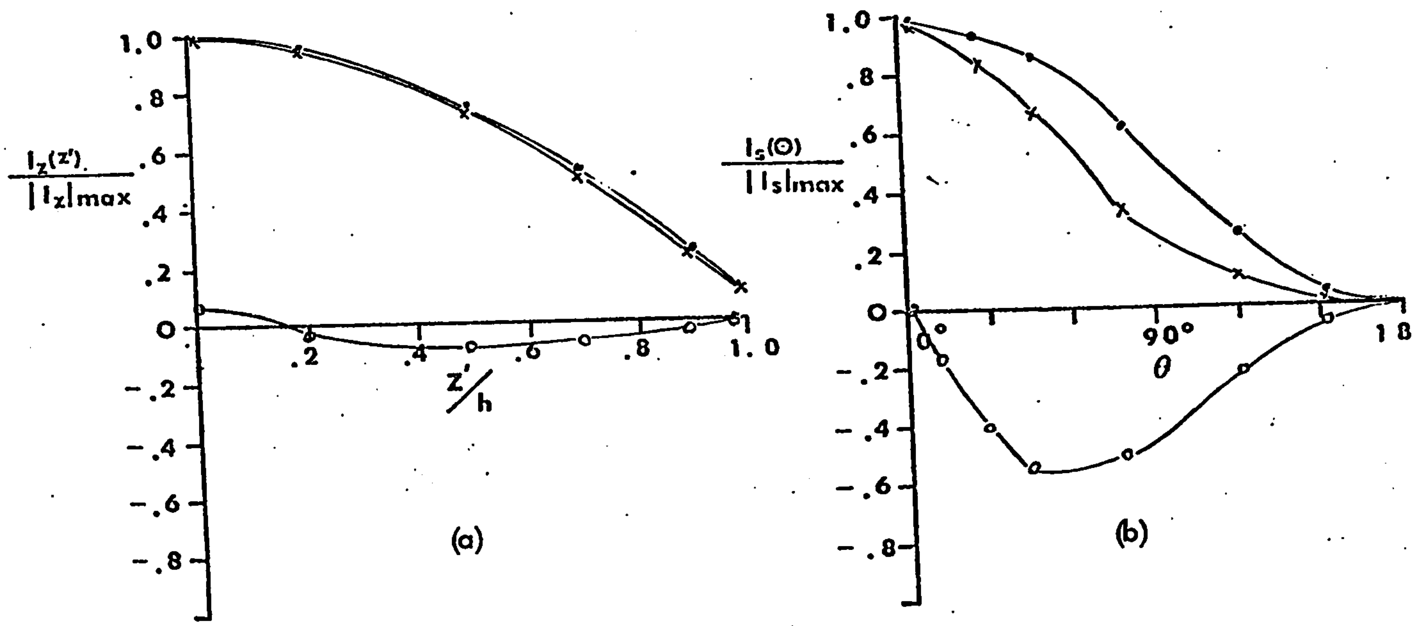

Figure 3.12. $R_s = \lambda/8$, L = 16, MR = 16.

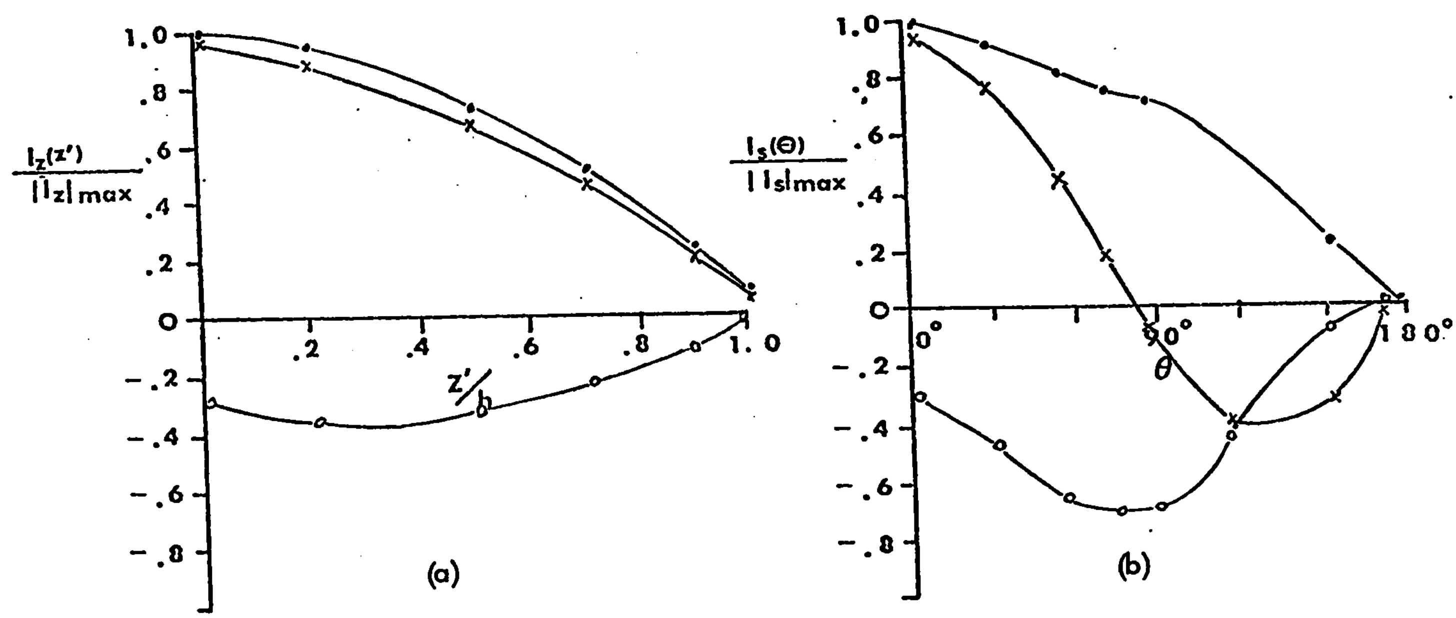

Figure 3.13. $3\lambda/16$, L = 32, MR = 25.

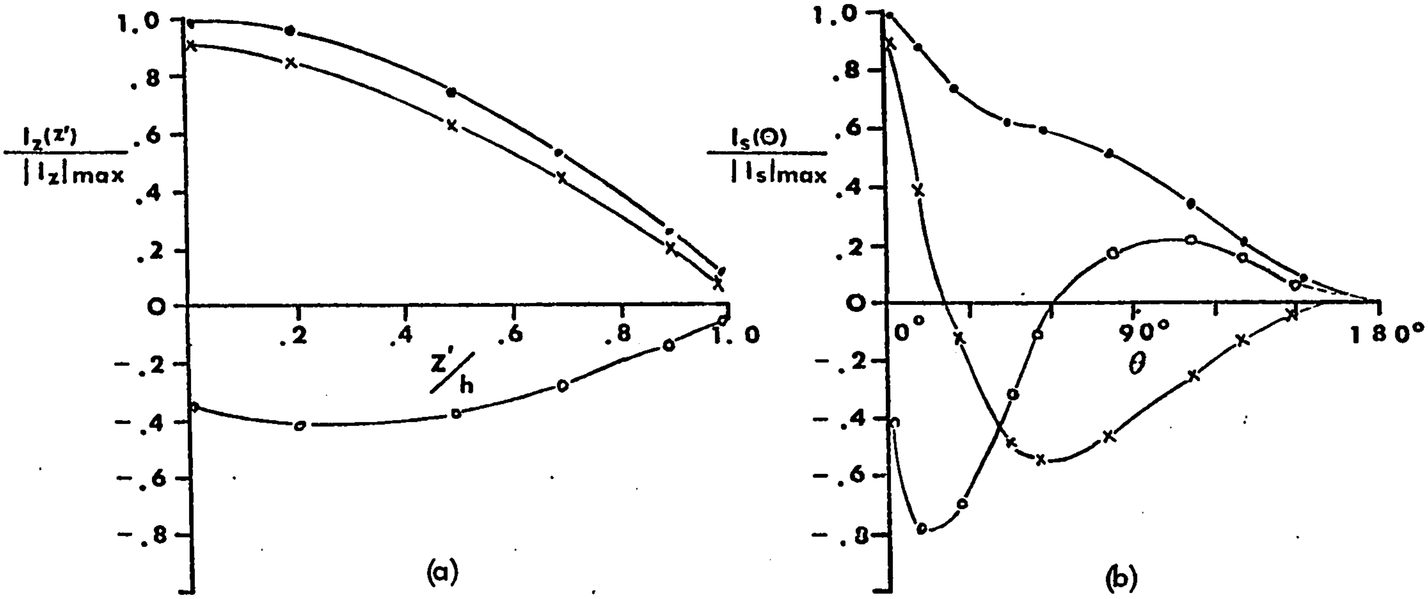

Figure 3.14. $R_s = \lambda/4$, $L = 16$, $MR = 16$.

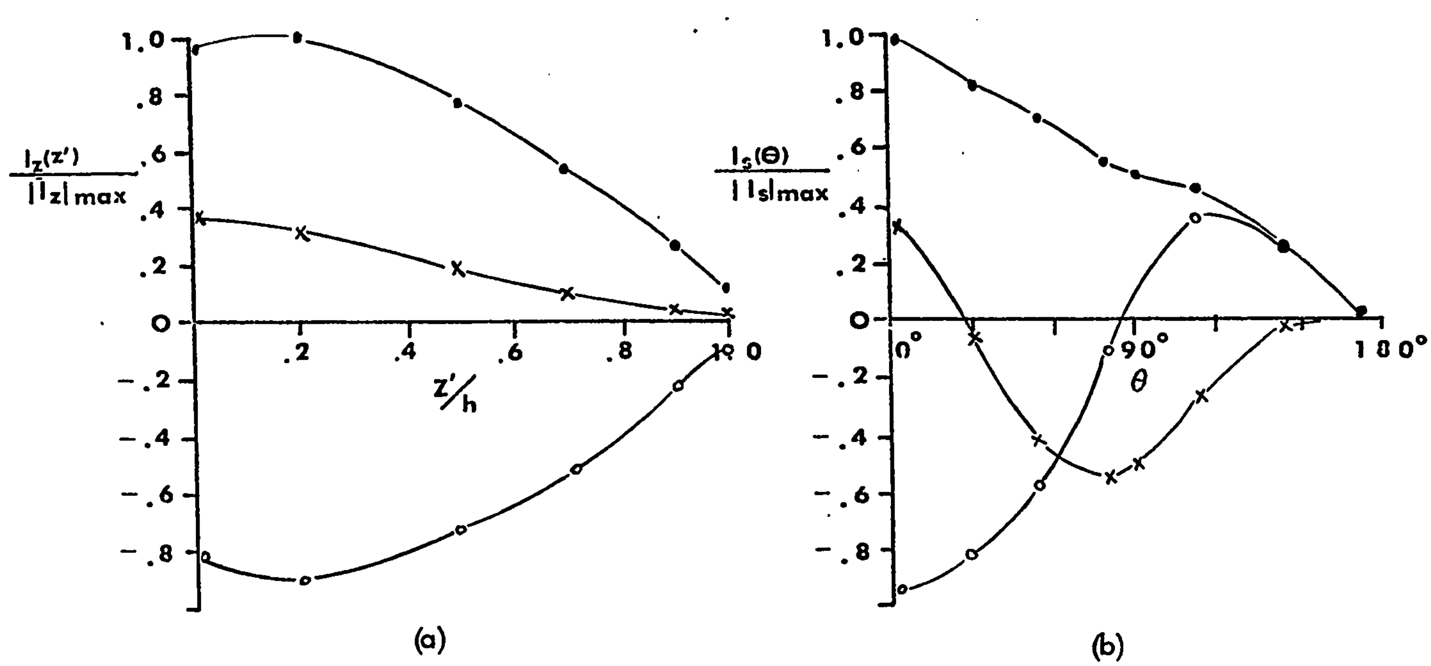

Figure 3.15. $R_s = \lambda/4$, $L = 24$, $MR = 16$.

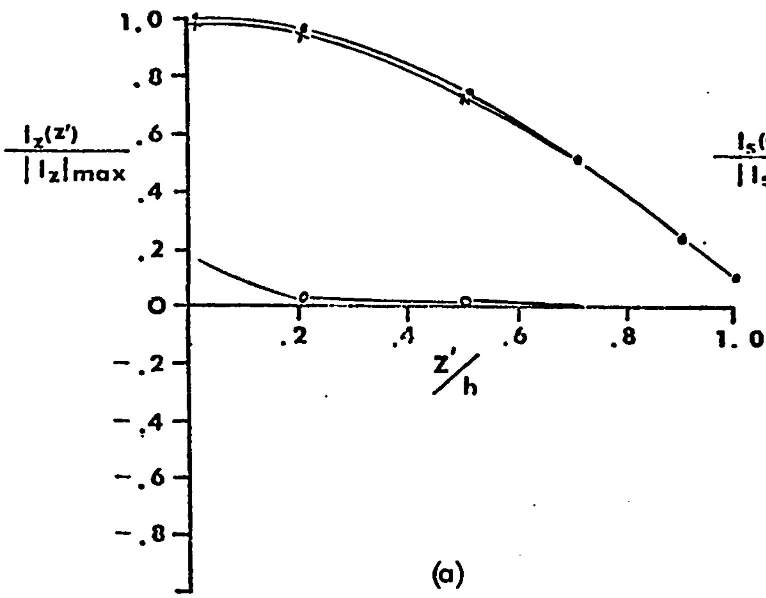

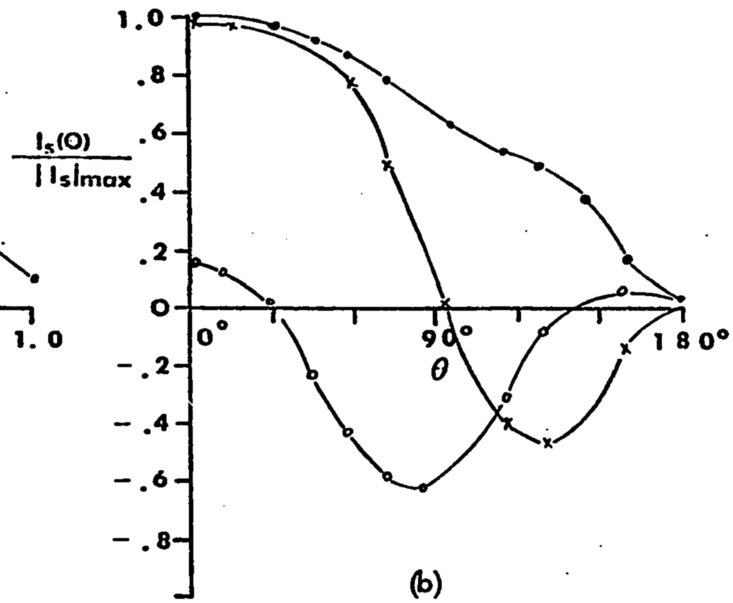

Figure 3.16. $R_s = \lambda / 4$, L = 24, MR = 25 .

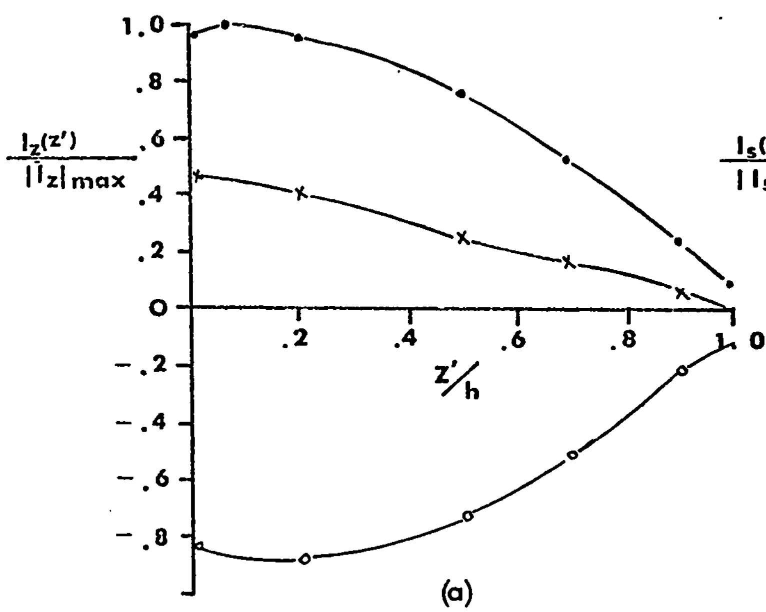

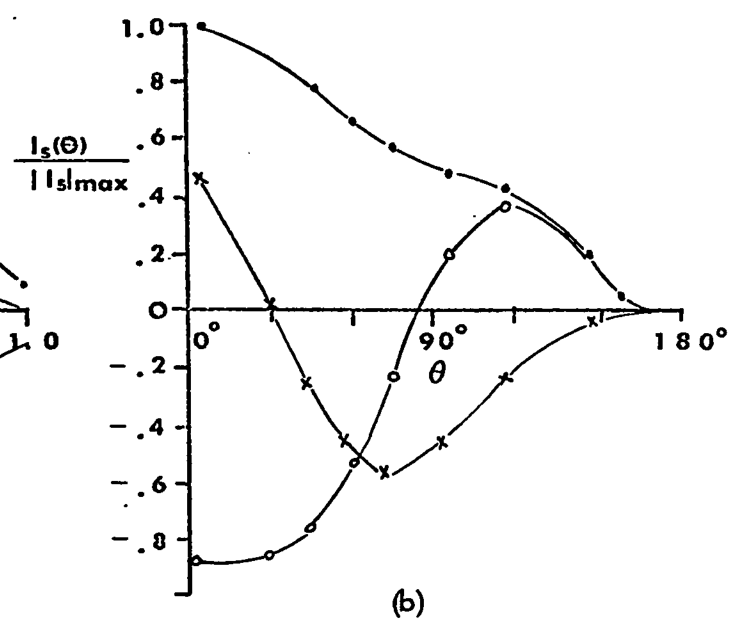

Figure 3.17. $R_s = \lambda / 4$, L = 32, MR = 25 .

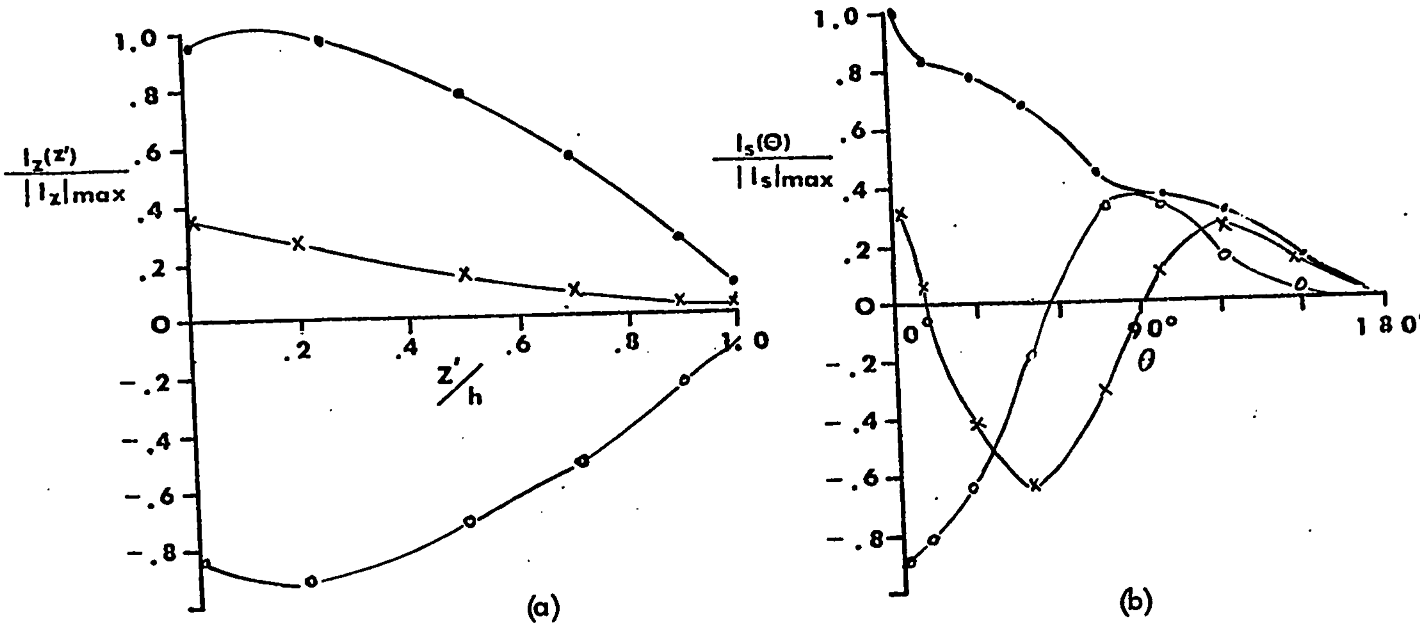

Figure 3.18. $R_s = 5\lambda/16$, L = 32, MR = 25.

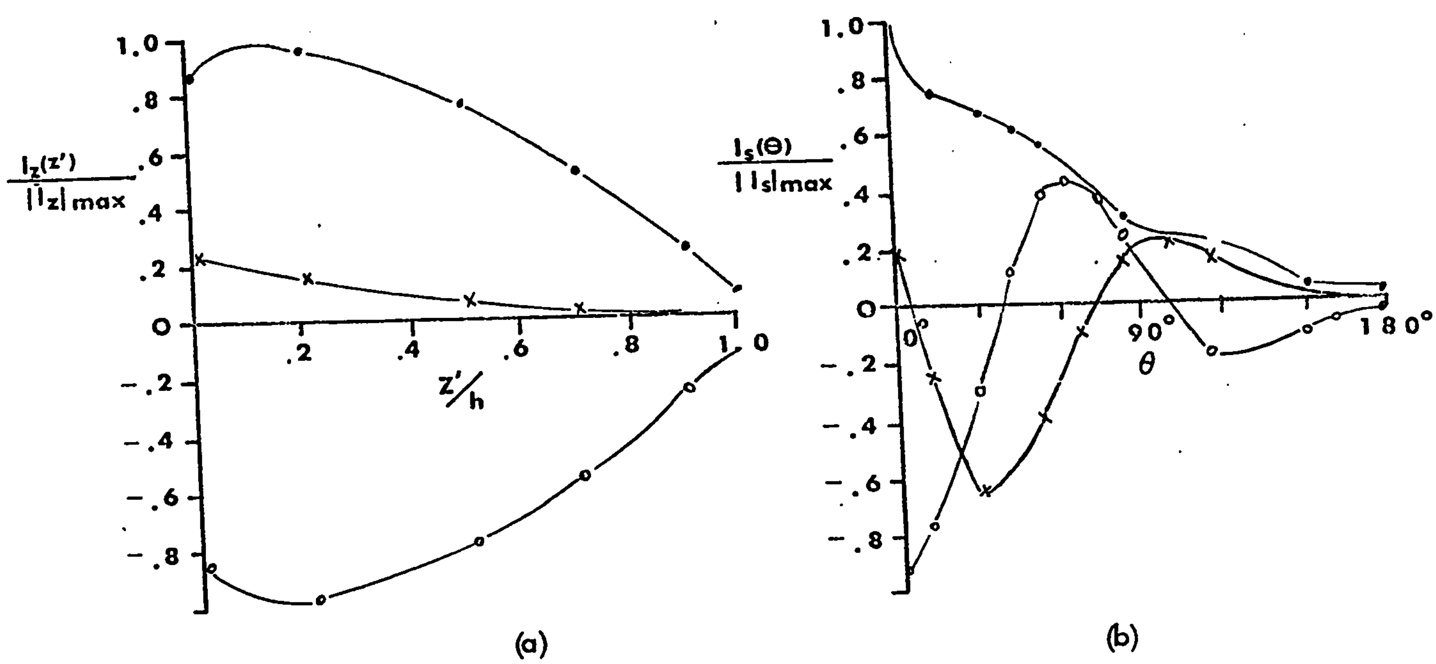

Figure 3.19. $R_s = 3\lambda/8$, L = 32, MR = 25 .

TABLE 3.2.

EQUIVALENCE OF MAGNETIC FRILL AND FINITE-WIDTH GAP SOURCE MODELS

CURRENT DISTRIBUTION FOR 1/4λ MONOPOLE MOUNTED ON SPHERE OF RADIUS = 1/4 λ. (APPROXIMATE CURRENT VALUES, I, IN MA/VOLT)

N*	FRILL SOURCE: $I = I_1 + j\, I_2$		FINITE GAP : $I = I_3 + j\, I_4$		RATIOS	
	I_1	I_2	I_3	I_4	I_3/I_1	I_4/I_2
1	2.7240	-4.8640	2.9658	-5.0295	1.0888	1.0340
2	2.6032	-4.8808	2.8342	-5.2883	1.0887	1.0835
3	2.4956	-4.9004	2.7171	-5.3285	1.0888	1.0874
4	2.3950	-4.8926	2.6075	-5.3255	1.0887	1.0885
5	2.2982	-4.8612	2.5020	-5.2935	1.0887	1.0889
6	2.2030	-4.8084	2.3985	-5.2371	1.0887	1.0892
7	2.1084	-4.7358	2.2955	-5.1584	1.0887	1.0892
8	2.0136	-4.6440	2.1922	-5.0587	1.0887	1.0893
9	1.9178	-4.5338	2.0879	-4.9389	1.0887	1.0894
10	1.8208	-4.4058	1.9824	-4.7995	1.0888	1.0894
11	1.7226	-4.2604	1.8755	-4.6412	1.0888	1.0894
12	1.6228	-4.0982	1.7669	-4.4646	1.0888	1.0894
13	1.5216	-3.9196	1.6566	-4.2701	1.0887	1.0894
14	1.4188	-3.7252	1.5447	-4.0583	1.0887	1.0894
15	1.3146	-3.5152	1.4312	-3.8297	1.0887	1.0895
16	1.2090	-3.2904	1.3162	-3.5846	1.0887	1.0894
17	1.1018	-3.0508	1.1996	-3.3236	1.0888	1.0894
18	0.9934	-2.7968	1.0816	-3.0469	1.0888	1.0894
19	0.8838	-2.5286	0.9622	-2.7548	1.0887	1.0895
20	0.7728	-2.2462	0.8413	-2.4471	1.0886	1.0894
21	0.6602	-1.9492	0.7188	-2.1235	1.0888	1.0894
22	0.5458	-1.6364	0.5943	-1.7828	1.0889	1.0895
23	0.4290	-1.3056	0.4670	-1.4225	1.0886	1.0895
24	0.3080	-0.9516	0.3352	-1.0366	1.0883	1.0893
25	0.1782	-0.5592	0.1940	-0.6092	1.0887	1.0894
26	0.0900	-0.1718	0.0981	-0.1829	1.0900	1.0646
27	0.0712	-0.1636	0.0775	-0.1763	1.0885	1.0776
28	0.0536	-0.1664	0.0583	-0.1800	1.0877	1.0817
29	0.0316	-0.1686	0.0345	-0.1826	1.0918	1.0830
30	0.0064	-0.1670	0.0070	-0.1810	1.0938	1.0838
31	-0.0204	-0.1596	-0.0222	-0.1731	1.0882	1.0846
32	-0.0464	-0.1458	-0.0504	-0.1582	1.0862	1.0850
33	-0.0694	-0.1256	-0.0753	-0.1363	1.0850	1.0852
34	-0.0876	-0.1002	-0.0951	-0.1087	1.0856	1.0848
35	-0.0998	-0.0712	-0.1083	-0.0771	1.0852	1.0829
36	-0.1054	-0.0404	-0.1145	-0.0437	1.0863	1.0817
37	-0.1048	-0.0100	-0.1137	-0.0108	1.0849	1.0800
38	-0.0984	0.0178	-0.1067	0.0194	1.0843	1.0899
39	-0.0874	0.0412	-0.0948	0.0448	1.0847	1.0874
40	-0.0734	0.0590	-0.0797	0.0641	1.0858	1.0864
41	-0.0580	0.0704	-0.0630	0.0765	1.0862	1.0866
42	-0.0428	0.0750	-0.0464	0.0816	1.0841	1.0880
43	-0.0290	0.0736	-0.0314	0.0799	1.0828	1.0856
44	-0.0176	0.0666	-0.0191	0.0723	1.0852	1.0856
45	-0.0092	0.0556	-0.0099	0.0603	1.0761	1.0845
46	-0.0038	0.0420	-0.0040	0.0457	1.0526	1.0881
47	-0.0008	0.0280	-0.0008	0.0305	-	-

* Current Distribution on Monopole : N = 1 (source element at base of monopole) to N = 25 (near top end of monopole). (See Figure 3.4 (a)).
Current Distribution on a Typical Meridian : N = 26 (near θ = 0) to N = 47 (θ → 180°)
Note : the sphere was modeled by 32 meridians.

TABLE 3.3.

INFLUENCE OF WIRE RADIUS PARAMETER "a" ON COMPUTED CURRENT DISTRIBUTION FOR 0.166 λ MONOPOLE MOUNTED ON RADIAL GROUND WIRES (RADIUS ≈ 0.5λ).

$I = I' + j\,I''$.

(a) MONOPOLE MOUNTED ON 12 RADIAL WIRES

N	a = 0.00104 λ		a = 0.00182 λ		a = 0.00564 λ		a = 0.00728 λ	
	I'	I"	I'	I"	I'	I"	I'	I"
1	7.9045	16.3462	3.3605	13.0106	1.2842	9.5309	1.2197	9.4491
2	6.5990	12.5173	2.8210	9.7787	1.0896	6.8549	1.0374	6.7397
3	4.0112	7.1978	1.7323	5.5891	0.6835	3.8606	0.6546	3.7943
4	0.6578	1.3199	0.2797	1.0466	0.1068	0.7601	0.1014	0.7528
5	0.7396	1.1981	0.3165	0.9381	0.1187	0.6470	0.1120	0.6351
6	0.9298	1.1327	0.4021	0.8836	0.1492	0.5763	0.1400	0.5609
7	1.1666	1.0929	0.5092	0.8575	0.1883	0.5318	0.1762	0.5135
8	1.3788	1.0365	0.6068	0.8246	0.2245	0.4911	0.2100	0.4709
9	1.4966	0.9355	0.6642	0.7599	0.2470	0.4394	0.2310	0.4191
10	1.4578	0.7766	0.6536	0.6483	0.2453	0.3683	0.2297	0.3498
11	1.2162	0.5602	0.5523	0.4845	0.2106	0.2735	0.1976	0.2591
12	0.7474	0.2991	0.3454	0.2708	0.1351	0.1541	0.1273	0.1461

(b) MONOPOLE MOUNTED ON 16 RADIAL WIRES

N	a = 0.00104 λ		a = 0.00182 λ		a = 0.00564 λ		a = 0.00728 λ	
	I'	I"	I'	I"	I'	I"	I'	I"
1	18.8890	21.8326	6.7071	17.7710	1.6028	10.4566	1.3035	9.9321
2	15.2957	16.5441	5.4707	13.3511	1.3437	7.5337	1.1775	7.0931
3	9.1108	9.4224	3.2960	7.6115	0.8364	4.2429	0.7399	3.9941
4	1.2403	1.4031	0.4397	1.1372	0.1023	0.6421	0.0881	0.6024
5	1.2070	1.1683	0.4419	0.9672	0.1096	0.5399	0.0956	0.5063
6	1.3507	1.0047	0.5178	0.8797	0.1364	0.4791	0.1199	0.4469
7	1.5743	0.8586	0.6292	0.8244	0.1738	0.4407	0.1535	0.4090
8	1.7363	0.7042	0.7376	0.7675	0.2107	0.4065	0.1869	0.3755
9	1.8989	0.5332	0.8050	0.6867	0.2360	0.3638	0.2100	0.3349
10	1.8330	0.3533	0.7956	0.5698	0.2389	0.3052	0.2132	0.2802
11	1.5263	0.1846	0.6783	0.4142	0.2090	0.2270	0.1873	0.2083
12	0.9397	0.0555	0.4287	0.2248	0.1365	0.1281	0.1231	0.1177

Note : (i) The above approximate current values are in milliamperes per volt.

(ii) N = 1 - 3 correspond to current elements on monopole, and
N = 4 - 12 correspond to current elements on one radial wire (in both Tables).

3.4.2 Dipole Antenna Mounted on the Side of a Cylindrical Support

The next case that can be modeled readily is an isolated thick cylindrical structure (e.g. a tower or mast) supporting a dipole antenna on its side with the dipole oriented parallel to the axis of the cylinder. Side and top views of the antenna mounting are shown in Figure 3.20 with cylindrical coordinates z and φ.

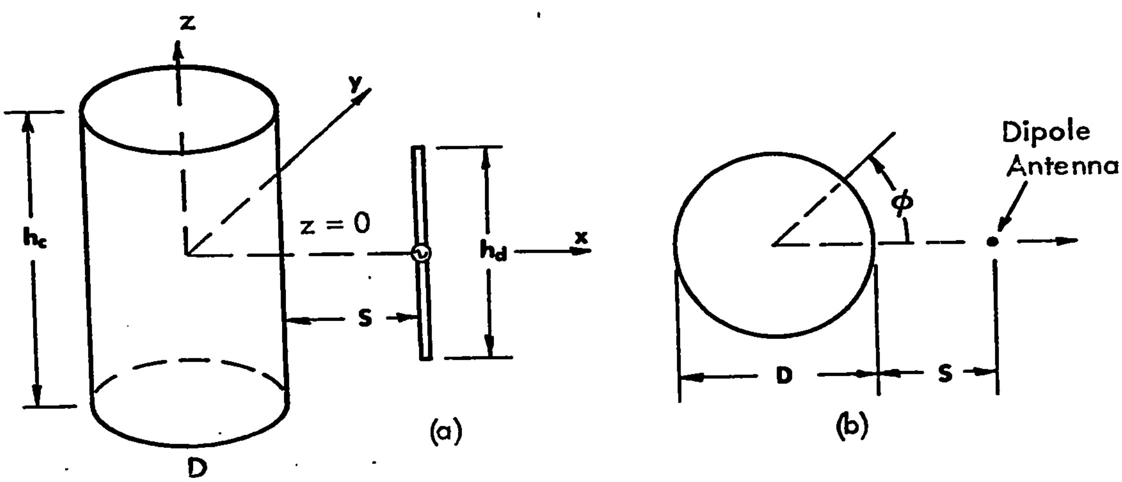

Figure 3.20. Dipole Mounted on the Side of a Cylindrical Conductor. (a) Side View, (b) Top View.

The cylindrical support modifies the pattern of the dipole depending on its diameter D, and the separation distance S. The height of the cylinder, h_c, is not too critical provided it is longer than the height of the dipole, h_d. Because the thickness of the cylinder is likely to be significant, i.e. ($D \geq 0.1\,\lambda$), the induced surface current distribution, with stationary lines of flow parallel to the cylinder axis, can no longer be assumed to be uniformly distributed around its circumference. Still, it is physically apparent that the cylinder may be replaced by a set of thin wires as shown in Figure 3.21.

The real problem then is how to choose a sufficient number of thin wires which would simulate the continuous surface. If it is assumed that the induced surface current density is an arbitrary function of φ, but independent of z, it would be possible to relate the required number of current lines to the order of a wave function of solution [35].

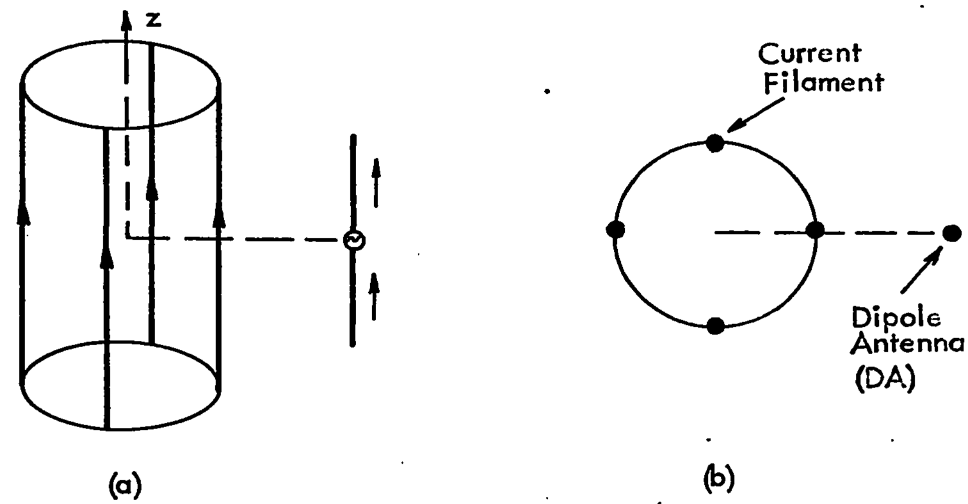

Figure 3.21. Cylinder Replaced by Four Thin Wires.
(a) Side View, (b) Top View.

One might express the vector potential as a series summation of cylindrical Bessel functions, truncate the series by a finite sum, and hence obtain the order number. The number may turn out to be related directly to the number of symmetrically located current filaments. However, the problem under consideration is a finite cylinder, and the current distribution cannot be assumed to be independent of z. In fact, intuitively the current on each filament may be expected to be maximum near the dipole region and then vanish toward the cylinder ends. The only remaining course to follow is a simple modeling procedure using four, six and eight current lines. The computed patterns may then be compared qualitatively with patterns obtained by other methods [37], [38], or available from commercial data [77]. The comparisons are repeated for different combinations of D and S, and also with experimental models, discussed later. Repeated computations suggest the following modeling procedure :

Cylinder Diameter	Number of Current Lines or Filaments
$D \approx \lambda/8$ to $3\lambda/16$	4
$D \approx \lambda/4$ to $3\lambda/8$	6
$D \approx \lambda/2$ to $3\lambda/4$	8

These guidelines have been followed in making final computations for experimental comparisons, and it will be shown that the results obtained have been on the whole satisfactory. Although not quite as efficient as the sphere-disk matrix reduction or the corner reflector program (to be discussed in the next subsection), an attempt has also been made to reduce the size of the impedance matrix using symmetry considerations.

3.4.2 (a) Significant Parameters for Modeling the Cylindrical Conductor with an Axial Dipole

The significant parameters for computation used in modeling the mast-mounted dipole antenna are shown in the following table :

1.	Dipole Mounting :		Symmetrical about centre of Cylinder
2.	Source Model :		Finite-Width Gap Source
3.	Cylinder Height :		$0.75\,\lambda$ to $1.0\,\lambda$ in Trial Computations
	h_c	=	$0.6\,\lambda$ to $1.0\,\lambda$ for Experimental models
4.	Cylinder Diameter :		
	D	=	$0.125\,\lambda$ to $0.5\,\lambda$
5.	Dipole Antenna Height :		$0.5\,\lambda$ in Trial Computations
	h_d	=	$0.3\,\lambda$ to $0.5\,\lambda$ for Experimental Models
6.	Dipole Separation Distance :		
	S	$\approx$	$0.25\,\lambda$ to $1.0\,\lambda$
7.	Number of Current Filaments :		
	NC	=	4 to 8
8.	Number of Segments per current Filament :		
	NT	=	11 to 15
9.	Number of Segments for Dipole Antenna :		
	NM	=	7 to 11
10.	Wire Radius :		
	a	=	$0.002\,\lambda$ in Trial Computations and for the experimental models,
	a	=	$0.001\,\lambda$ to $0.0017\,\lambda$ for Dipole Antenna
		=	$0.0015\,\lambda$ to $0.0025\,\lambda$ for Current Filaments
11.	Total Number of Segments or Current Elements :		
	NWS	=	NM + NC x NT
12.	Total Number of segments for which current is computed :		
	NA	=	NM + (NC / 2 + 1) x NT

3.4.2 (b) Typical Computed Current Distributions

In Figures 3.22 to 3.27 are shown representative results of the current computations. For each antenna mounting, the diameter of the conducting cylinder, the separation distance S, and the number of segments used in modeling the cylindrical surface are indicated in the top left side corner. The height of the cylinder was kept at 1.0λ and the dipole height was a half-wavelength. It is interesting to note that except for changes in magnitudes, the current distribution on the dipole antenna remains essentially similar to the distribution on an isolated half-wavelength antenna. As predicted, the currents on the filaments modeling the cylinder are symmetrical functions of z which tend to vanish at the two cylinder ends. Close examination of the current plots from (b) to (d), or (b) to (e), or (b) to (f) reveals the fact that the induced current, in addition to being z - dependent, is also φ - dependent. Again, this was one of the initial assumptions made in specifying the modeling procedure for the cylinder. By comparing Figures 3.22 and 3.23, Figures 3.24 and 3.25, and Figures 3.26 and 3.27, (and also the corresponding radiation patterns), the guidelines stated earlier for determining the number of current filaments were reached.

3.4.3 Wire-Grid Analysis of the Corner Reflector Antenna

The corner reflector antenna as used in practice is in a wire grid form. Its radiation patterns have been documented from extensive experimental measurement by Wilson and Cottony [78], and earlier by Harris [79]. However, it has always been a difficult boundary-value problem to tackle. References have already been made to the work of Kraus [30], Moulin [31], and Wait [32]. Kraus derived practical design figures for wire spacings and corner angles ; Moullin, using image theory methods, obtained more extensive radiation patterns for special corner angles which are submultiples of 180°. Wait introduced a method which can be applied to arbitrary corner angles. However, both Moullin and Wait considered reflecting surfaces with infinite dimensions. The only treatment of a corner reflector with finite dimensions that has been reported so far is that of Ohba [33] who used the geometrical theory of diffraction approach. Thus the analysis of a finite corner reflector using the grid modeling approach

Figures 3.22 to 3.27. Computed Current Distribution, $I = I' + j\,I''$, for Dipole Antenna (DA) of Height $h_d = \lambda/2$, and Supporting Conducting Cylinder (Height $h_c = 1.0\,\lambda$).

(a) Current Distribution on Half-Wavelength Dipole.

(b), (c), (d), (e), (f) - Current Distributions on Filaments used for Cylinder Modeling. —x—x— I', —o—o— I'', —•—•— $|I|$.

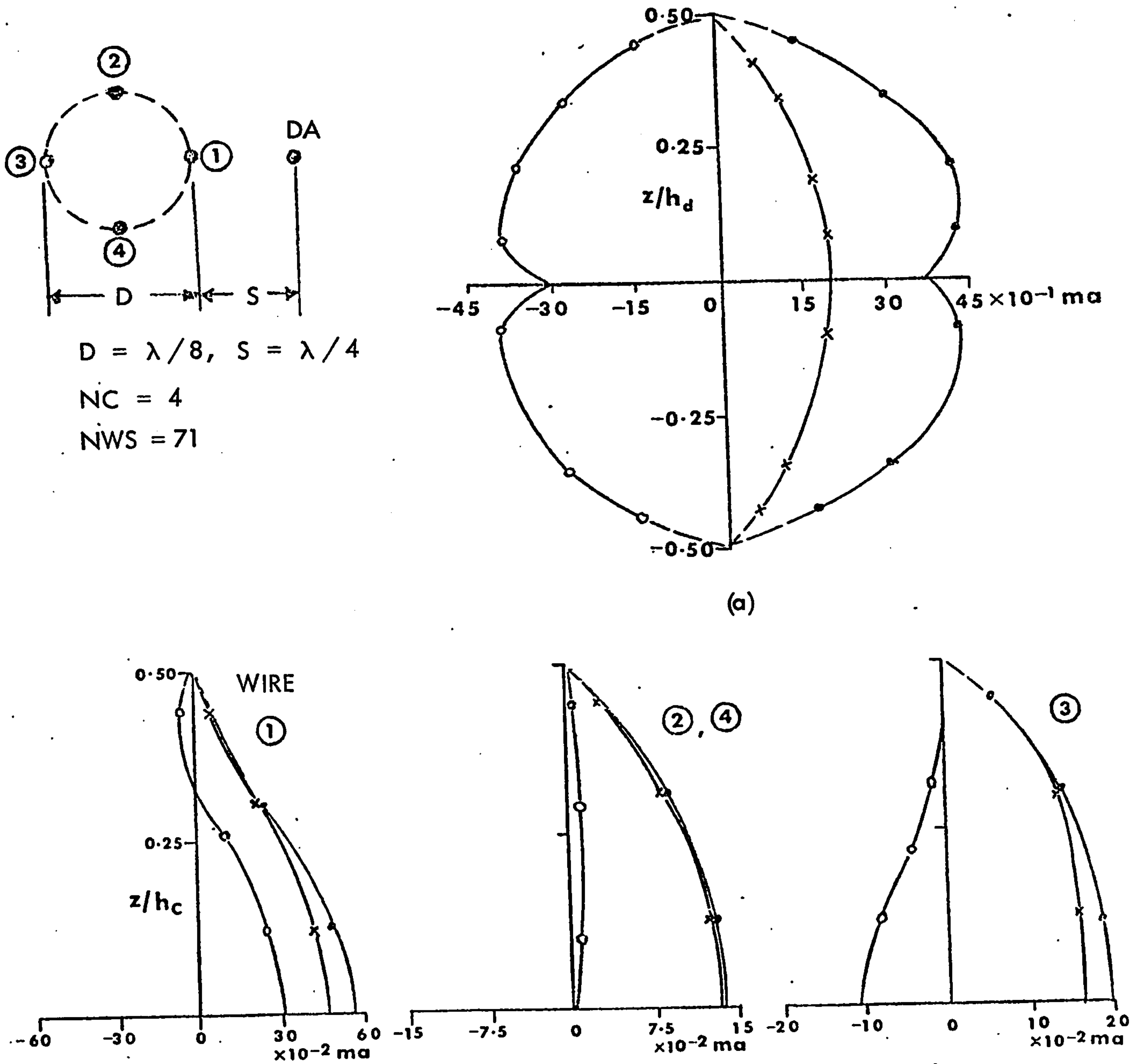

(a) (b) (c) (d)

Figure 3.22.

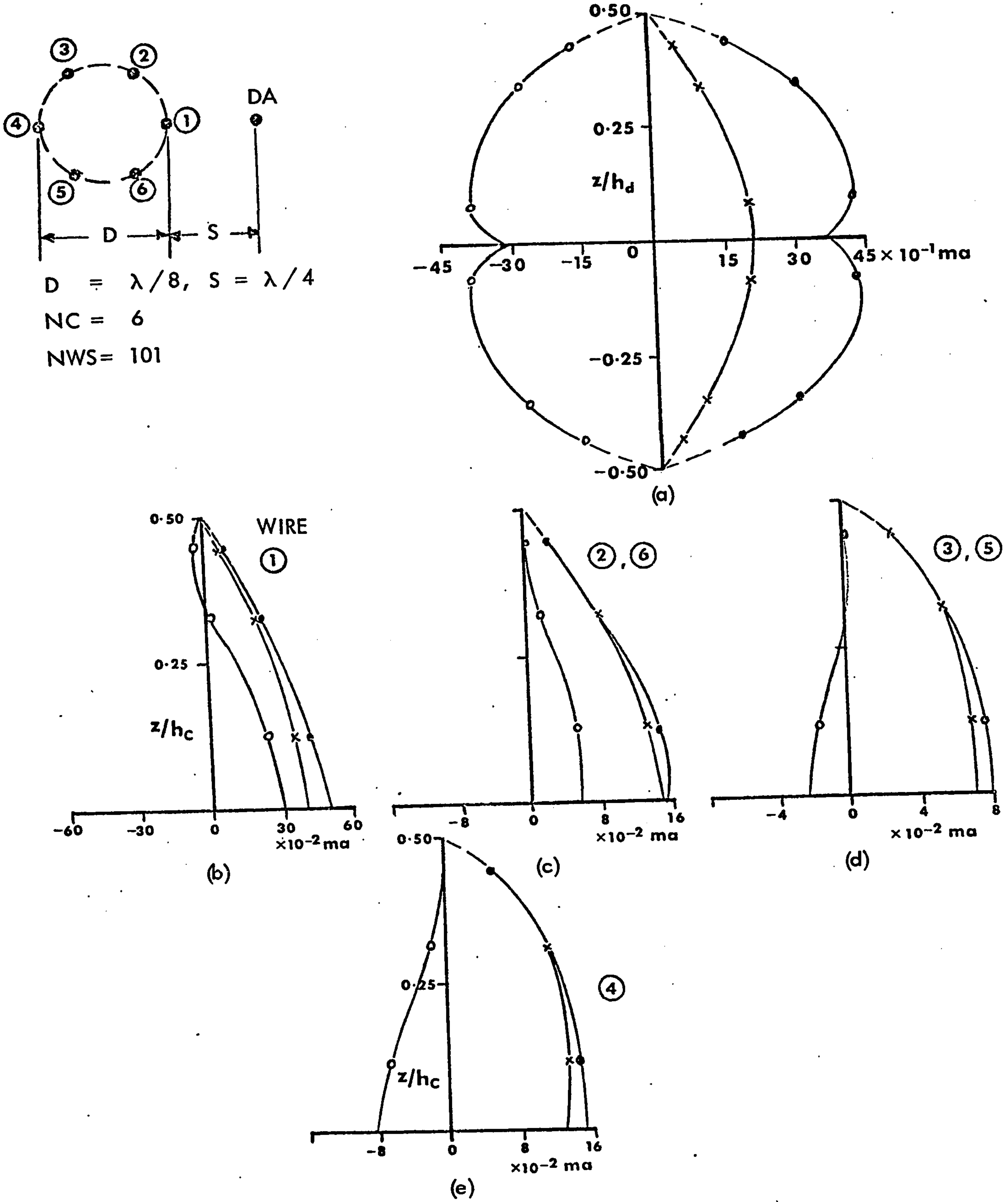

③ ②
DA
④ ①
⑤ ⑥
D
S
D = λ/8, S = λ/4
NC = 6
NWS= 101
0·50
0·25
z/h_d
−45 −30 −15 0 15 30 45 × 10⁻¹ma
−0·25
−0·50
(a)
0·50
WIRE ①
0·25
z/h_c
−60 −30 0 30 60
×10⁻² ma
(b)
②, ⑥
−8 0 8 16
×10⁻² ma
(c)
③, ⑤
−4 0 4 8
×10⁻² ma
(d)
0·50
0·25
④
z/h_c
−8 0 8 16
×10⁻² ma
(e)

Figure 3.23.

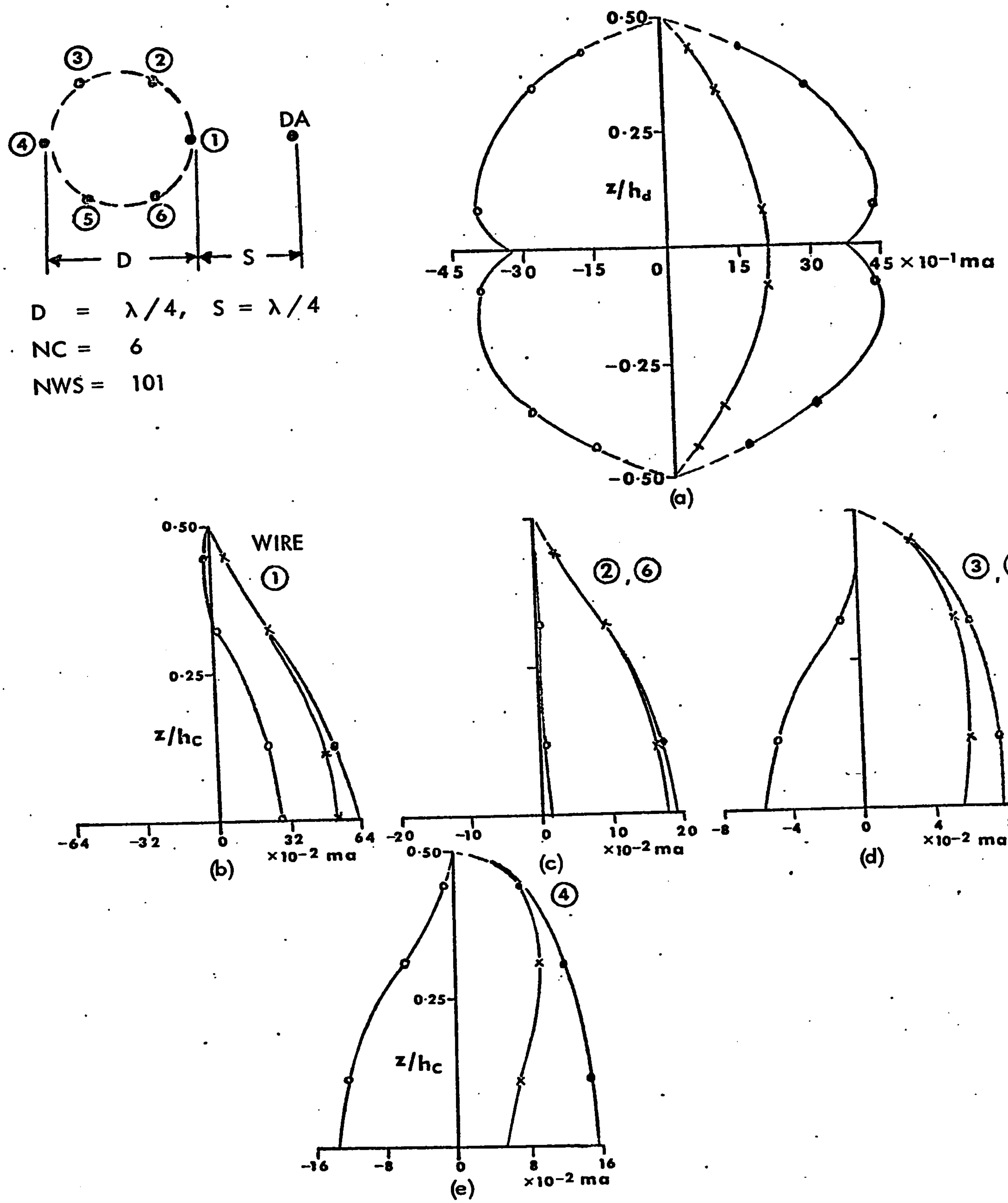

③
②
DA
④
①
⑤
⑥
D
S
D = λ / 4, S = λ / 4
NC = 6
NWS = 101
0·50
0·25
z/hd
-45
-30
-15
0
15
30
45 × 10⁻¹ ma
-0·25
-0·50
(a)
0·50
WIRE
①
0·25
z/hc
-64
-32
0
32
64
×10⁻² ma
(b)
②, ⑥
-20
-10
0
10
20
×10⁻² ma
(c)
③, ⑤
-8
-4
0
4
8
×10⁻² ma
(d)
0·50
④
0·25
z/hc
-16
-8
0
8
16
×10⁻² ma
(e)

Figure 3.24.

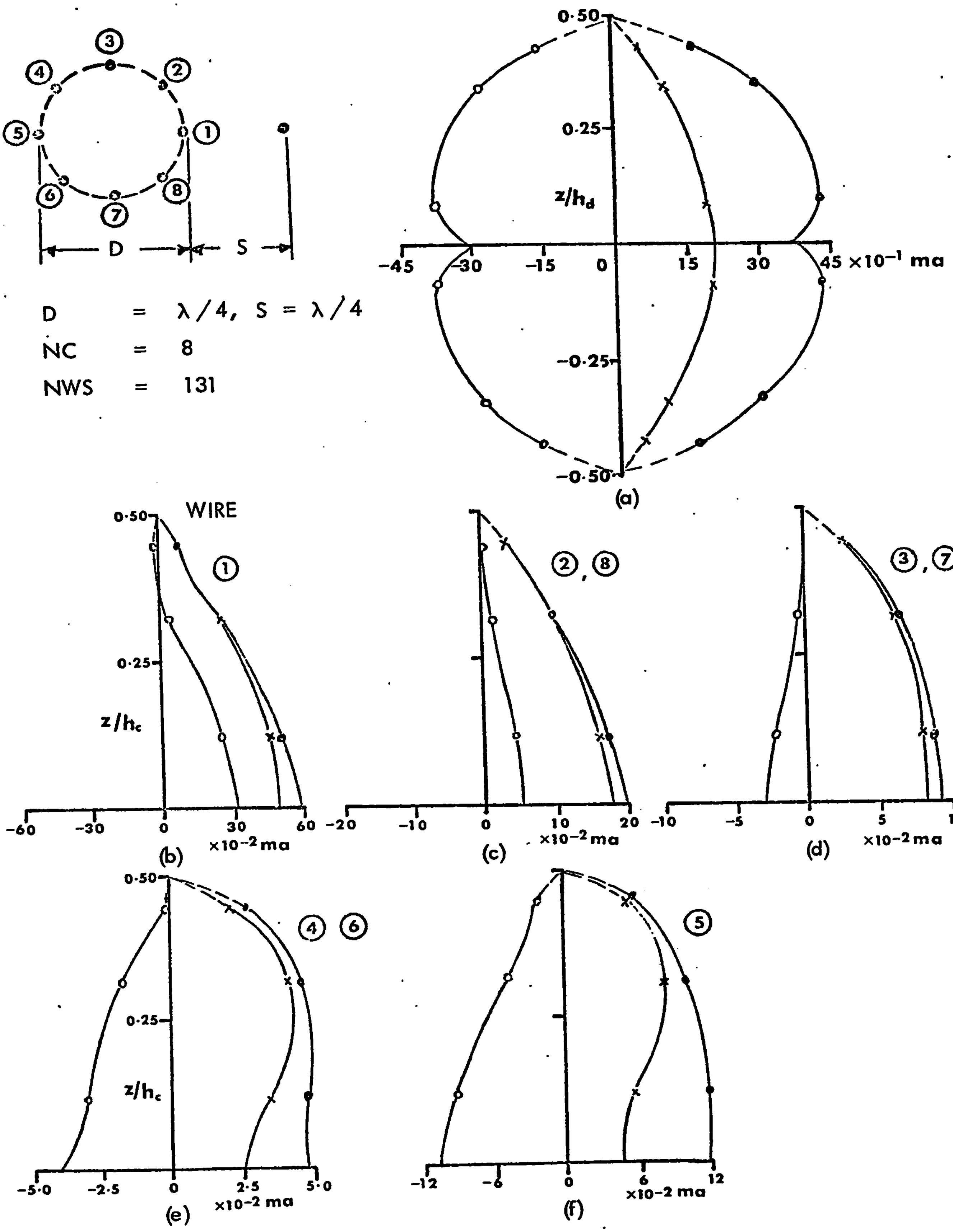

D
S
D = λ/4, S = λ/4
NC = 8
NWS = 131
0.50
0.25
z/h_d
-45
-30
-15
0
15
30
45 ×10^-1 ma
-0.25
-0.50
(a)
WIRE
0.50
0.25
z/h_c
-60
-30
0
30
60
×10^-2 ma
(b)
-20
-10
0
10
20
×10^-2 ma
(c)
-10
-5
0
5
10
×10^-2 ma
(d)
0.50
0.25
z/h_c
-5.0
-2.5
0
2.5
5.0
×10^-2 ma
(e)
-12
-6
0
6
12
×10^-2 ma
(f)

Figure 3.25.

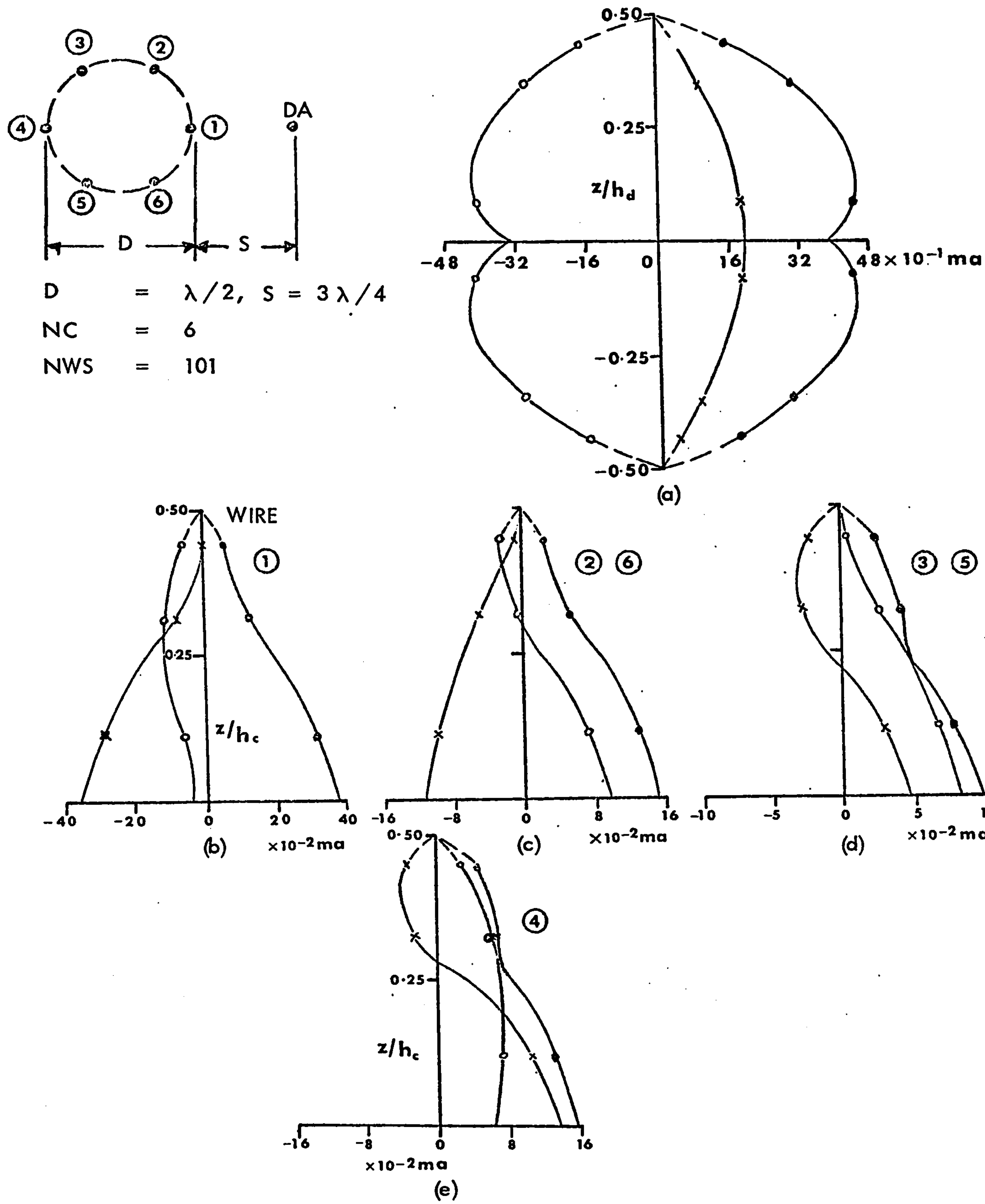

③
②
④
①
DA
⑤
⑥
D
S
D = λ/2, S = 3λ/4
NC = 6
NWS = 101
0·50
0·25
z/h_d
-48
-32
-16
0
16
32
48×10⁻¹ma
-0·25
-0·50
(a)
0·50
WIRE
①
0·25
z/h_c
-40
-20
0
20
40
(b)
×10⁻²ma
② ⑥
-16
-8
0
8
16
(c)
×10⁻²ma
③ ⑤
-10
-5
0
5
10
(d)
×10⁻²ma
0·50
④
0·25
z/h_c
-16
-8
0
8
16
×10⁻²ma
(e)

Figure 3.26.

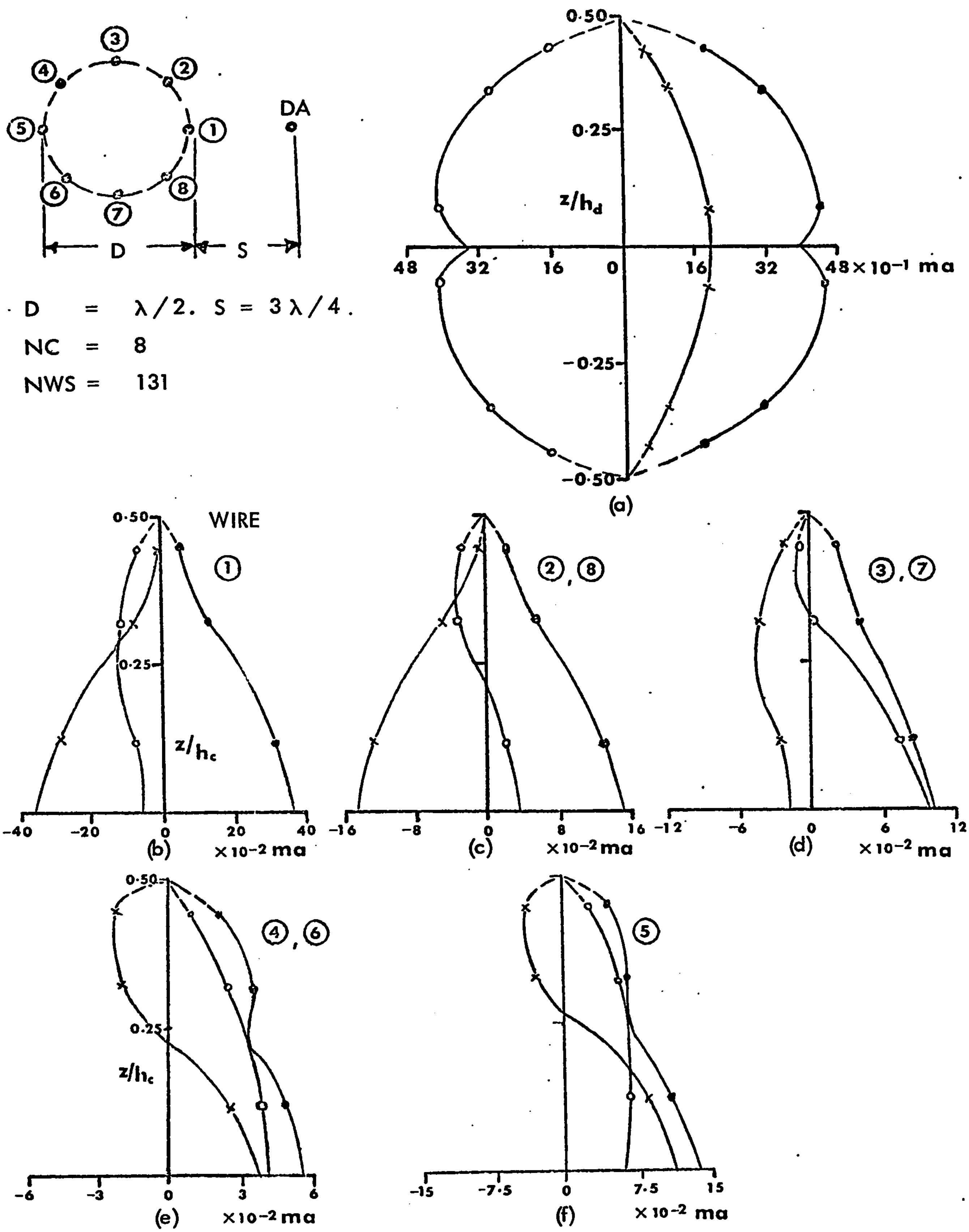

Figure 3.27.

serves several special purposes. It provides more detailed understanding of a well-known antenna form which helps to validate some of the modeling assumptions mentioned earlier and it is useful in improving programming efficiency in the light of the symmetrical structure. As indicated below the programming scheme turns out to be very challenging and differs significantly from the programs for the previous three cases.

The coordinates and notations used are illustrated in Figure 3.28. The z-axis is made to coincide with the corner edge, but the x - and y - axes could have

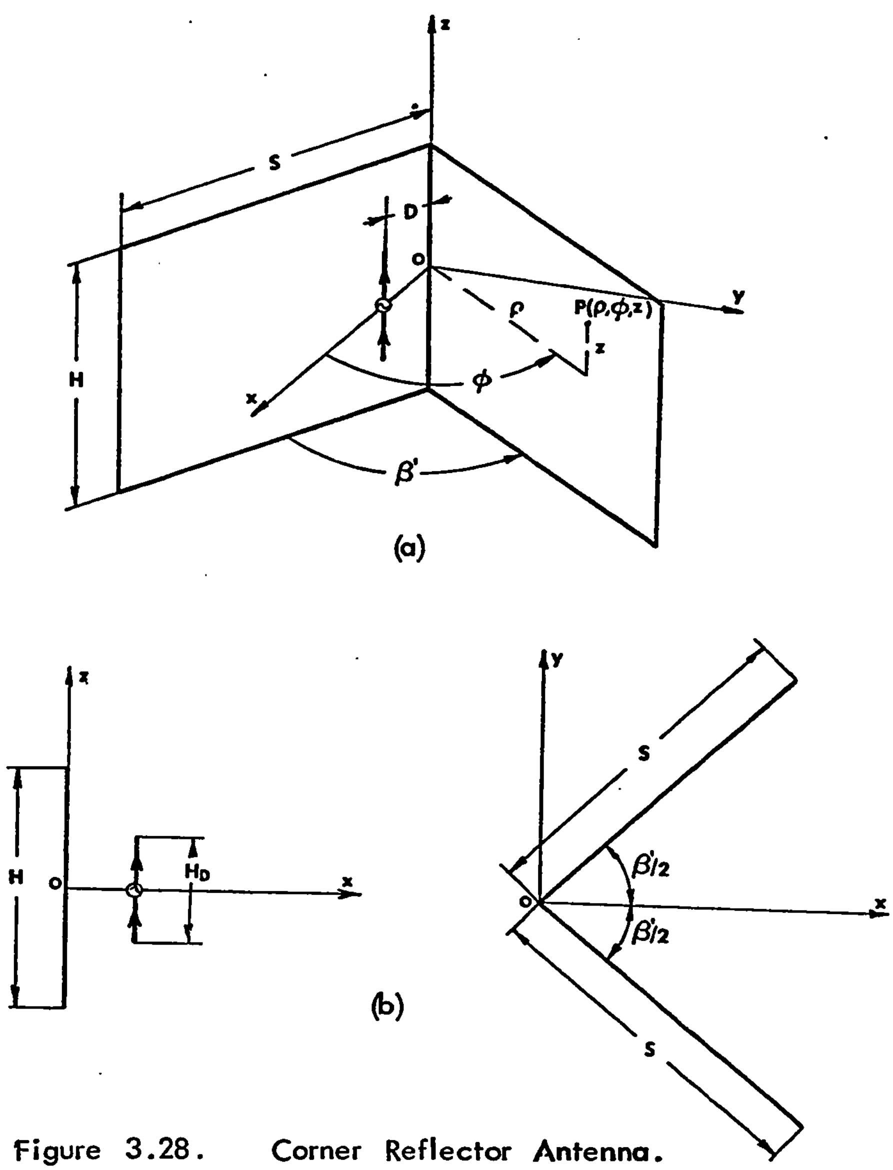

Figure 3.28. Corner Reflector Antenna.

been rotated so as to include the corner angle within the axes for $\beta' < 90^{o}$, or to have the axes contained within the corner aperture for $\beta' > 90^{o}$. The width and height of one reflector side are denoted by S and H , respectively. As indicated in Figures 3.28 (a) and (b), the dipole antenna is placed at a distance D from the corner edge, has a height $H_d < H$, and lies in the z - x plane parallel to the z - axis. Its centre is in line with the centre of the corner edge at z = 0 .

The continuous reflecting surfaces are replaced by an array of wires as shown in Figure 3.29. The separation distance d between the wires is about 0.1 λ, and the total number of wires is therefore determined by the S dimension. The wires are located symmetrically relative to the corner (the z - axis) .

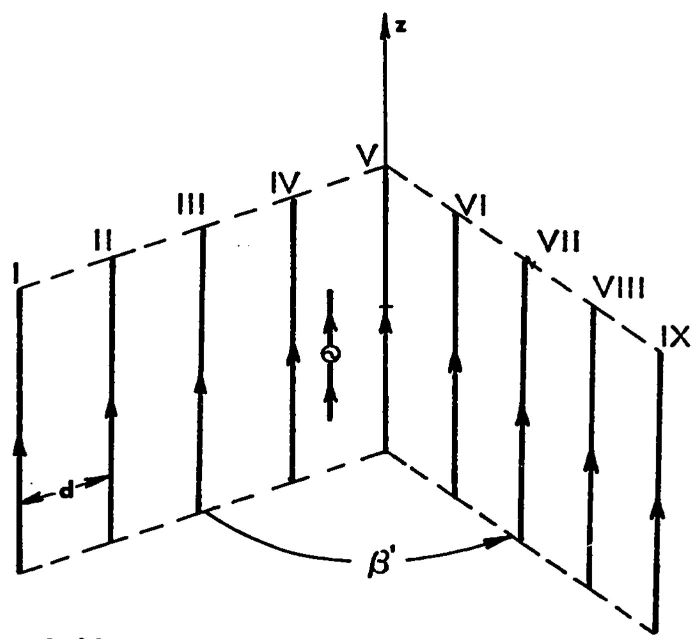

Figure 3.29. Wire-Grid Modeling of Corner Reflector Antenna with Vertical Dipole.

3.4.3 (a) Segmentation and Current Computation Schemes

A simple generalized segmentation scheme for arbitrary values of H, S, β' and H_d is possible, but the segment parameters must be carefully specified. To determine the total number of wire elements, the following parameters can be proposed :

1. NC = Total number of parallel wires modeling the corner reflector (e.g. 7, 9, 11, 17)

2. MR = Number of segments into which each parasitic wire is to be divided (e.g. 9, 11, 13)

3. ND = Total number of segments into which the dipole antenna is to be divided (e.g. 5, 7, 9)

Thus, the total number of current elements would be given by

$$NRS = NC \times MR + ND \tag{3.28}$$

It is important to note that NC, MR and ND are all odd numbers. NC specifies the number of wire lines which simulate both reflecting surfaces plus the line replacing the corner edge. ND and MR are odd because the current distribution must be a symmetrical function of z in the dipole and in the passive elements. The antenna is a half-wave dipole, and although the segmentation scheme that has been worked out is in no way restricted, the value of H has been set at $1.0\,\lambda$, and two values ($0.5\,\lambda$ and $1.0\,\lambda$) have been chosen for S. The corner angle has been varied between 60° and 130°.

The development of a compact current computation program, which again is not restricted in any way except by the available computer memory, has required a great deal of re-arrangement of the segments into which the current lines are divided. The basic approach is to make use of the fact that the current distribution is not only symmetrical on each current line, but is also identically the same on the image line in the second surface. Consider filaments I and IX of Figure 3.29. The current lines are re-drawn including the corner line in Figure 3.30 with new notations. Filament I is divided into MR elements, and these can be identified as 1, 2, . . . M2, . . . MR. Similarly filament IX is divided into MR elements which are numbered N1, ...N2....N3. If the voltage equation from (2.77) is to be written for segment 1 on filament I, one would obtain

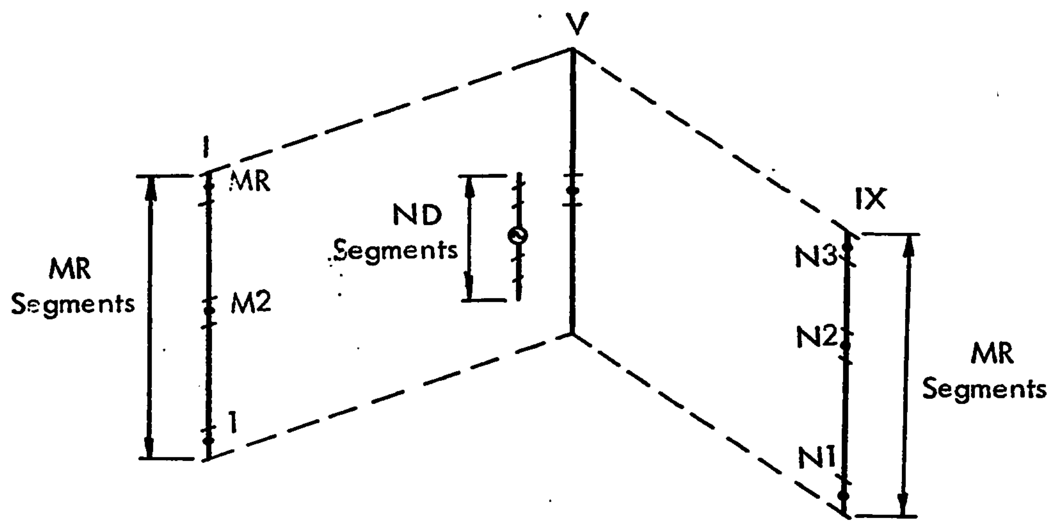

Figure 3.30. Corner Reflector Antenna : Segmentation of Symmetrically Located Wires.

$$Z_{1,1}\, I_1 + Z_{1,2}\, I_2 + \cdots + Z_{1,MR}\, I_{MR} + \cdots + Z_{1,NRS}\, I_{NRS} = V_1^i \tag{3.29}$$

where MR and NRS have already been defined, and $I_1, I_2, \ldots I_{NRS}$ are element currents. But from symmetry considerations

$$I_1 = I_{MR} = I_{N1} = I_{N2} \tag{3.30}$$

$$I_{M2} = I_{N2} \tag{3.31}$$

$$I_{N4} = I_{NRS} \tag{3.32}$$

where

$$N1 = MR \times (NC - 1) + 1 \tag{3.33}$$

$$M2 = (MR + 1)/2 \tag{3.34}$$

$$N2 = MR \times (NC - 1) + M_2 \tag{3.35}$$

$$N3 = MR \times NC \tag{3.36}$$

$$N4 = MR \times NC + 1 \tag{3.37}$$

Similar identities can be expressed for current elements (Figure 3.29) on filaments II and VIII, III and VII, and so on. When this is done, equation (3.29) can be rewritten in the form

$$(Z_{1,1} + Z_{1,MR} + Z_{1,N1} + Z_{1,N2}) I_1 + (Z_{1,2} + Z_{1,MR-1} + \ldots) I_2 + \ldots\ldots + (Z_{1,N4} + Z_{1,NRS}) I_{NRS} = V_1 \tag{3.38}$$

If (3.38) is generalized, it becomes

$$\sum_{j=1}^{NRW} Z_{i,j} I_j = V_i \quad , \qquad 1 \leq i \leq NRW \tag{3.39}$$

where

$$NRW = ((MR + 1)/2) \times (NC + 1)/2 + (ND + 1)/2 \tag{3.40}$$

and Z_{ij} now represents, except for two current elements, sums of either four or two impedance values in the NRS rows similar to (3.29). The two exceptions are the centre currents of the corner filament, and the dipole antenna. For the other current lines the equivalent Z_{ij} in (3.39) is given by two sums for the centre currents, and by four impedance sums for the non-centre current elements.

After establishing the general procedure, the real difficulty arises when one tries to keep track of the rows and columns of the NRW x NRW reduced matrix from which the unknown element currents are to be determined. This could be best seen from an examination of a complete computation program, however for the sake of brevity programming details are not presented in this thesis since the procedures are of a routine nature.

3.4.4 Summary of Wire Grid Analysis of the Simple Conducting Surfaces

From the current computations made for the four simple surfaces, the following observations have been deduced.

(i) The assumed source models are valid.

(ii) In working towards a 'correct' wire grid model, the current results confirm the validity of putting the thin wires along the "stationary lines of flow" in the modeling procedure.

(iii) The wire radius parameter affects appreciably the computed current distribution for a given wire grid model, and its effect on the corresponding radiation pattern will be discussed. As will be shown in the next section, this result has also helped in tackling wire-grid structures built with wire segments that may have different radius values.

(iv) The segmentation schemes and procedures apply equally well to straight and curved wires as long as conditions (3.6) and (3.7) are satisfied, and adequate piece-wise linear approximation of curved wires is achieved.

(v) A coarse segmentation scheme has been found to be sufficient for far field computations. This conclusion was reached as progress was made from the sphere where very fine segmentation was used, to the cylinder with axial dipole, and then to the corner reflector.

(vi) Provided the physics of the problem is clearly understood - that is the source is properly modeled, and the "stationary lines of flow" are correctly established, the results have shown that one can achieve computational efficiency by taking into consideration the geometrical symmetry of a given conducting surface [47], [56].

In Table 3.4, the reductions that have been obtained are summarized. The possible electrical dimensions of the individual surfaces which might be handled by the modeling and programming schemes within a 300 k core memory of an 0 / S 360 computer are also indicated.

TABLE 3.4.

SUMMARY OF WIRE-GRID COMPUTATIONS FOR THE SIMPLE ANTENNA SYSTEMS

	WIRE SEGMENTS			ELECTRICAL DIMENSIONS	
ANTENNA STRUCTURE	NUMBER OF ELEMENTS	REDUCED NUMBER OF ELEMENTS	APPROXIMATE RATIO OF REDUCED MATRIX TO ACTUAL STRUCTURE MATRIX	COMPUTATIONS MADE	POSSIBLE RANGES
Monopole of height h mounted on sphere of radius R_s	245 - 825	20 - 50	5 % - 3 %	$h = 0.25\lambda$ $R_s = \lambda/8$ to $R_s = 3\lambda/8$	$h \leq 0.5\lambda$ $R_s \leq 1.0\lambda$
Monopole of height h mounted on disk of radius R_d	75 - 219	12	3 %	$h = 0.166\lambda$ $R_d = 0.5\lambda$	$h \leq 0.5\lambda$ $R_d \leq 2.5\lambda$
Axial dipole antenna mounted near a cylindrical mast of diameter D and height h_c	71 - 131	56 - 86	29 % - 44 %	$h_c = 0.75\lambda$ to $h_c = 1.0\lambda$ $D = \lambda/8 - \lambda/2$	$D \leq 1.5\lambda$ $h_c \leq 2.0\lambda$
Corner reflector of width S and height H	104 - 236	33 - 69	10 % - 9 %	$S = 0.5\lambda$ $H = 1.0\lambda$ — $S = 1.0\lambda$ $H = 1.0\lambda$	$S \leq 2.5\lambda$ $H \leq 2.5\lambda$

3.5 Wire Grid Analysis of a Thin Wire Structure

The structure considered in this section is a more complicated three dimensional one consisting of a truss-like body, shown in Figure 3.31, resembling the tail section of a Bell 47G-2A helicopter. At 675 MHZ, the 1 : 20 scale model is about 1.1 λ long, and its front face (plane containing line A-B) which is shown in detail, is a rectangle 0.11 λ by 0.14 λ. A coaxial feed is connected to the radially oriented dipole antenna through the rod A-B. Although most of the truss members are made from the same kind of uniform thin wire (about 0.0017 λ in radius), there are segments in the structure (e.g. the rod A-B) which have different radius values. Outside the frame itself, the line C-D, which models the rotor blades of the helicopter, is a thin strip with a width of about 0.0032 λ. Thus although the problem of determining the stationary line of current flow is solved a priori, one still has to take into consideration the different wire radii in a current computation program. To arrive at an accurate segmentation of the structure into smaller elements, one is also required to supply the geometrical coordinates correctly [56]. Provided these precautions are taken, the equation formulations completed, and the source properly chosen, there is no reason in principle why the analysis should not yield satisfactory results.

During the course of the actual computations, however, difficulties were encountered. The most persistent source of error was due to insufficiently accurate source data about the coordinate position of individual segments. As indicated below, each segment needs to be identified by six coordinates. One, two, or three errors in a deck of one hundred and seventy or so data cards may completely nullify the results of a computation program that has been painstakingly assembled. There was also the more serious problem of appreciating the physical structure of the thin wire body such as its asymmetrical and three-dimensional aspects, identifying the locations of segments which could affect significantly the current distribution, and identifying also segments which might be ignored in the current and / or pattern computations. It was therefore seen that if the results of the wire grid analysis of this particular problem were to be reliable and satisfactory, a novel and more fundamental approach would have to be attempted.

The approach chosen was essentially simple. The thin wire structure was to be evolved gradually from known surfaces of revolution. The steps taken are pictorially

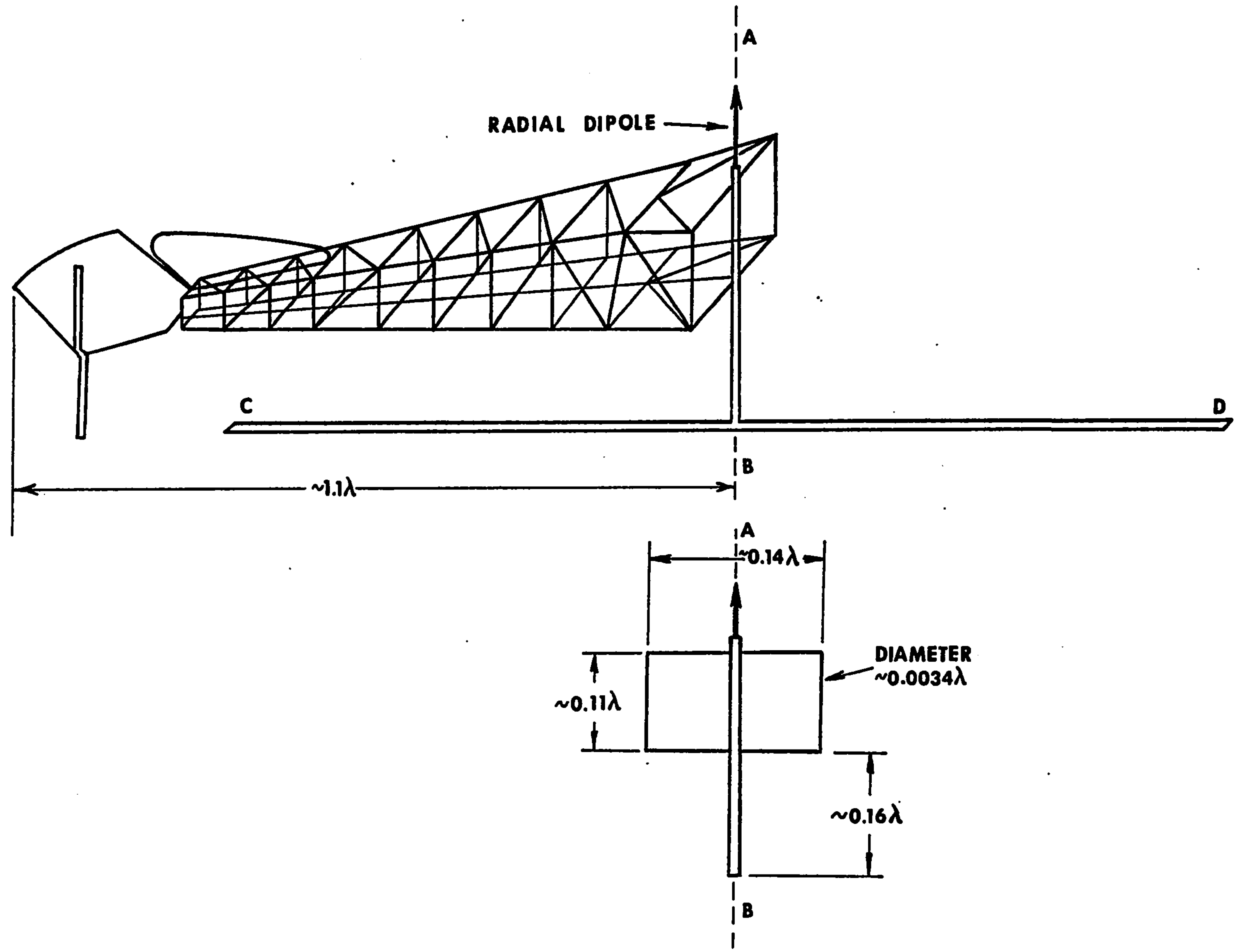

Figure 3.31. Thin Wire Body which Approximates the Tail Section of a Bell 479-2A Helicopter.

Note : The model was set upside-down for mounting on an Antenna Rotator for Pattern Measurements as described in Chapter IV.

illustrated in Figure 3.32. Starting with a radial dipole near the centre of a finite cylinder, and then proceeding through a number of intermediate antenna mountings, the situation of a radial dipole side-mounted at the base end of a cone is reached. In the approximation process, it was implicitly assumed that the thin wire body of Figure 3.31 could be replaced by an equivalent continuous surface shown in Figure 3.32 (g). The exact shape of this conducting surface is a compromise between the cylinder of Figure 3.32 (e) and the cone of Figure 3.32 (f). The radiating systems in Figures 3.32 (a) and (b) not only helped in starting the modeling procedure, but also served as direct and independent checks of the applicability of the wire grid technique according to the formulations and assumptions used in this study. Of these two configurations the first problem has been studied by Wait [40] and Kuel [80] by classical methods, and recently by Goldhirsh and others [50] by numerical methods using the surface element technique. As far as the author could determine, the case of two diametrically opposite radial dipoles was first studied by Wait and Okashimo [81], also later discussed by Wait [40], although Sinclair and others [41] had considered two radial dipoles mounted 120° apart on the surface of a cylinder. The other dipole mountings with the parasitic stub have been introduced in the study to make the modeling procedure more complete, and it seems that they have not been studied before.

In the following sub-sections, the wire models of the surfaces of revolution are treated first, and then segmentation scheme for the thin wire structure will be outlined. The computed patterns are once again to be discussed later in Chapter V.

3.5.1 Wire Grid Modeling of a Cylinder with Radial Dipole

The wire modeling of the surfaces given in Figure 3.32 begins by establishing the stationary lines of flow on a finite perfectly conducting cylinder with a radial dipole mounted on its centre. The cylinder has a length l and diameter d, and the coordinate systems are shown in Figure 3.33. The surface current distribution is not restricted to lines of flow parallel to the axis of the cylinder, but at least near the feed region, the currents must also flow along circular paths around the circumference of the cylinder towards the feed point. An attempt is made in Figure 3.34 to show the assumed current distribution. However, it would be quite difficult to base a wire grid model on such flow lines. Instead

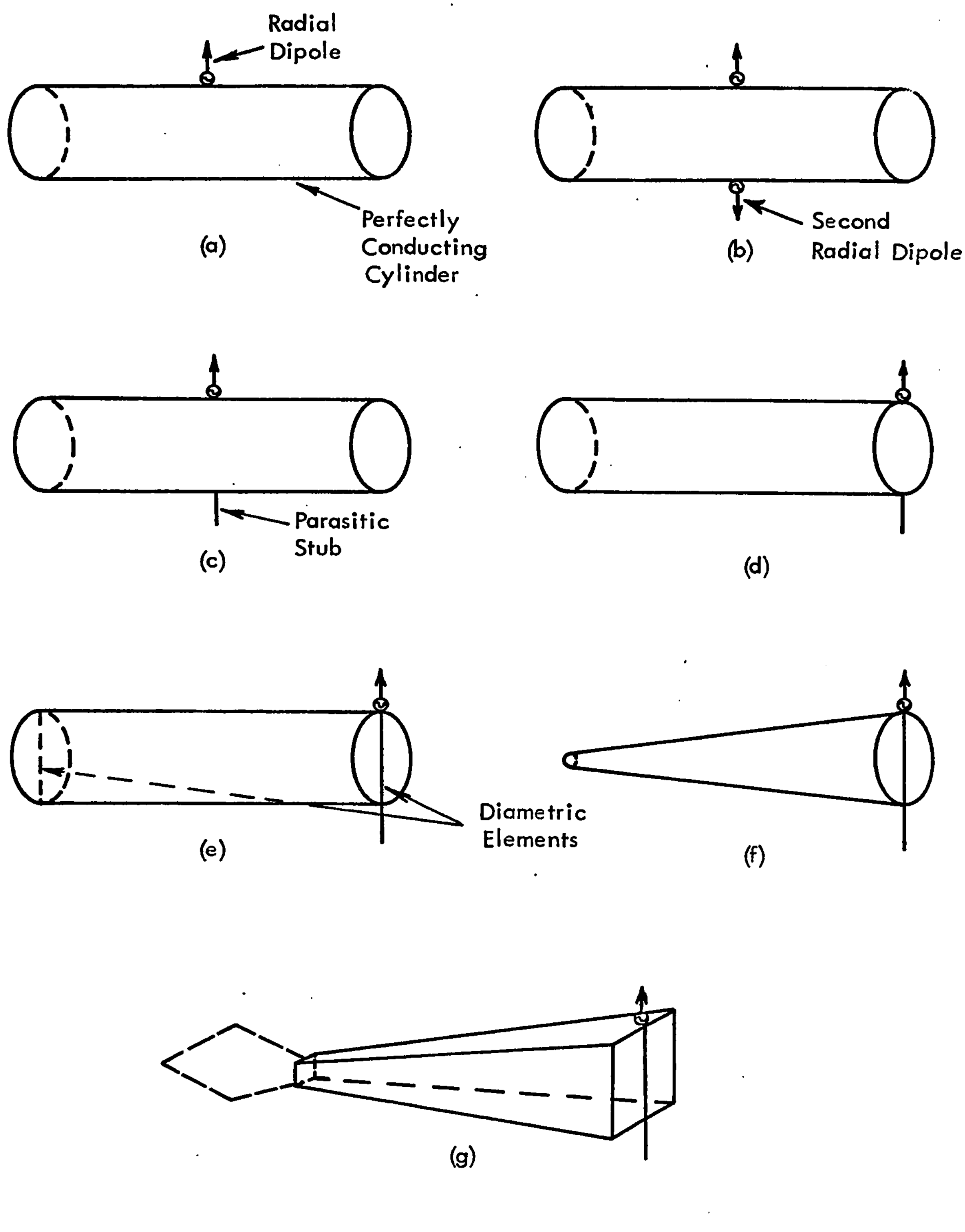

Figure 3.32. Development of the Thin Wire Body from Simple Surfaces of Revolution.

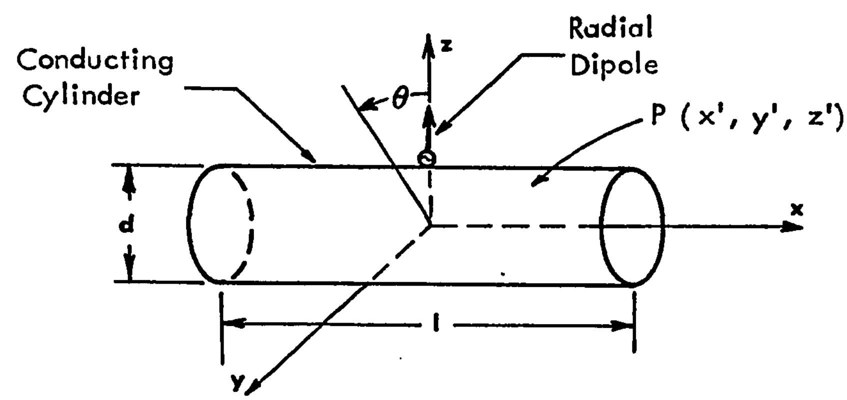

Figure 3.33. Radial Dipole Mounted on the Centre of a Finite Cylinder.

it is postulated that a reasonably accurate model can be achieved by putting on the surface

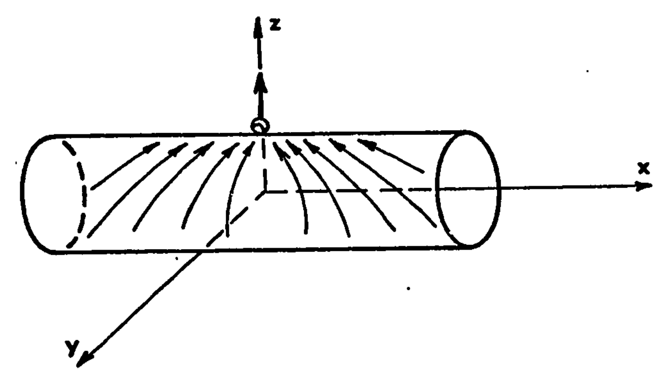

Figure 3.34. Assumed Directions of Stationary Lines of Flow for the Antenna Structure shown in Figure 3.33.

of the cylinder, lines of flow parallel to its axis, and circumferential lines of flow in the planes perpendicular to the axis, as shown in Figure 3.35. There is a sound physical argument behind this modeling scheme. At any point P (x', y', z') on the surface of the cylinder, the current distribution vector $\overline{J}_s$ can be resolved into two components such that

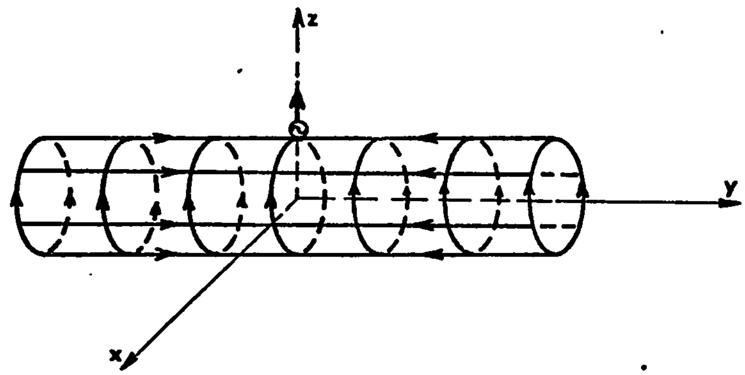

Figure 3.35. Simplified Stationary Flow Lines.

$$\bar{J}_s = \bar{i}_y J_y + \bar{i}_{\theta'} J_{\theta'} \tag{3.41}$$

where $\bar{i}_{\theta'}$ is a unit vector tangential to the cylinder surface and given by

$$\bar{i}_{\theta'} = \bar{i}_x \cos\theta - \bar{i}_z \sin\theta \tag{3.42}$$

and $\bar{i}_x$, $\bar{i}_z$ are unit vectors in the x -, and z - directions, respectively. Obviously, $J_{\theta'}$ is the current component flowing circularly in a plane perpendicular to the axis of the cylinder. Thus in effect, the wire model shown in Figure 3.35 has been achieved by making separate models for the two current components, and then combining them together on the surface of the cylinder with fixed junctions at the points of crossings of stationery lines of flow. Intuitively, one is led to conclude that the fixed junctions must be part of the complete model, for otherwise the $J_{\theta'}$ component outside the z - x plane would not be flowing towards the feed point. More specifically, the junctions represent the points at which the current vector $\bar{J}$, is to be satisfied according to (3.41) .

The number of axial lines and circular loops for a given cylinder will of course be determined by the electrical dimensions of the cylinder, i.e. its diameter d and its length l . For large d, more axial lines will be needed, and for a longer l , more circular flow lines will be needed to make the wire model a good simulation of the cylindrical surface.

3.5.1 (a) Segmentation Procedure

Once the wire model is established, the next step is to determine the number of segments required for current computation. The segmentation of the axial lines is straightforward as long as condition (3.7) is met. In segmenting the rings, experience from the sphere grid model suggests that they should first be divided into arcs, and then the arcs replaced by chords. The number of chords required to model each circle would depend on the value of d. The largest diameter that has been tested in the study is $0.25\,\lambda$, and the circumference which is about $0.8\,\lambda$ is modeled adequately by six chords.* As shown in Figure 3.36 (a), each ring in Figure 3.35 is approximated by a regular hexagon. The axial lines are then drawn along the corners of the hexagons as illustrated in Figure 3.36 (b). In the modeling process, the value of l was chosen to range between $0.48\,\lambda$ and $0.64\,\lambda$. Since the current is more concentrated near the feed region, one of the guidelines discussed earlier (Section 3.1.5) suggests that more rings be placed near the centre and fewer near the cylinder ends.

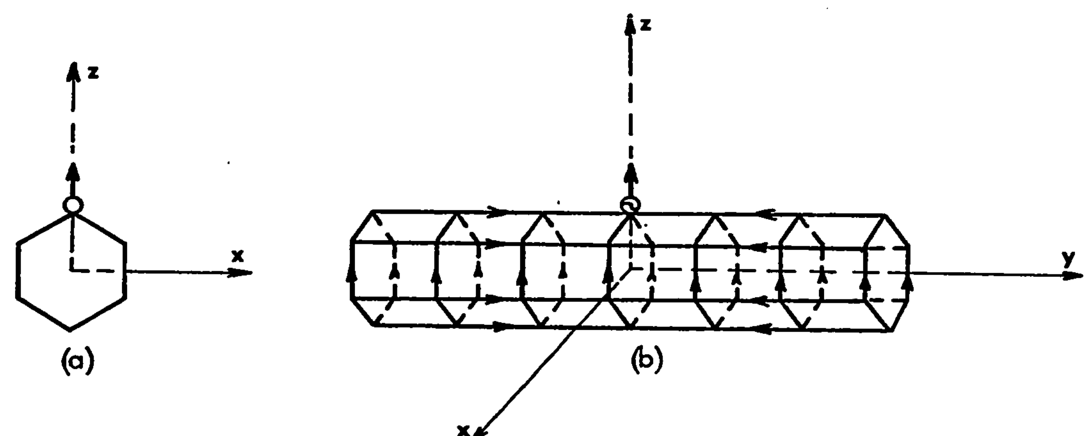

Figure 3.36. Details of Segmentation for Cylinder with $d \leq 0.25\,\lambda$, and $l \approx 0.48\,\lambda$.
(a) a hexagonal model for a ring, (b) final wire modeling and segmentation scheme for Antenna Structure shown in Figure 3.33.

Although this was attempted in experimental pattern measurements, the procedure was not followed in the computations for two reasons : (1) it was found (from an examina-

---

* The largest diameter chosen is well within the $\lambda/3$ limit established by Miller and others [52] in similar studies.

tion of the computed patterns) that equal segmentation was sufficient ; and (2) as mentioned earlier, it would have required the preparation of a segment coordinate subprogram which would manage the varying spacing between the rings. Thus for a given value of l , the spacing between the circular lines (i.e. the length of each element in the axial direction) was fixed at a $0.08\ \lambda$. Therefore the number of segments along the axial lines varied from six to eight equal divisions.

To make direct comparisons with the results of other workers [50] , the radial dipole was also located at different distances from the surface of the cylinder. In such cases, there will only be an induced current distribution on the surface of the cylinder. However, the same wire model shown in Figure 3.35 has been found to be adequate.

3.5.1 (b) Modeling and Segmentation of the Remaining Surfaces

The above modeling procedure can now be extended successively to treat the source locations and the conducting surfaces in Figures 3.32 (b) to 3.32 (f). The final models, where again $d \leq 0.25\ \lambda$ and $0.48\ \lambda \leq l \leq 0.64\ \lambda$, are shown in Figures 3.37 (a) to (e) . It is important to observe the differences introduced at each step. For example, in Figure 3.37 (a) , two equally phased sources are considered, whereas in Figure 3.37 (b) , there is only one active source, and a parasitic stub has been added. In Figure 3.37 (c), the dipole and the parasitic stub have been moved to the right end of the cylinder. The presence of elements along a diameter at each end should be noted in Figure 3.37 (d). The radial stub has also been increased in length to stimulate the rod A - B in Figure 3.31. The diametric element at the left end is placed to approximate the loop section (shown in a dotted line in Figure 3.32 (g)) of the surface replacing the thin wire body. Finally, the conical surface, for which a separate segmentation subprogram had to be written, was modeled as shown in Figure 3.37 (e) .

The line representing the rotor blades (C - D in Figure 3.31) can be easily added to the final cylindrical model of Figure 3.37 (d) as shown in Figure 3.38. The position of rotor blades parallel to the axis of the tail structure is simulated, but the line can be placed in any direction (in a plane parallel to the x - y plane). Thus the effect of rotor position can be examined.

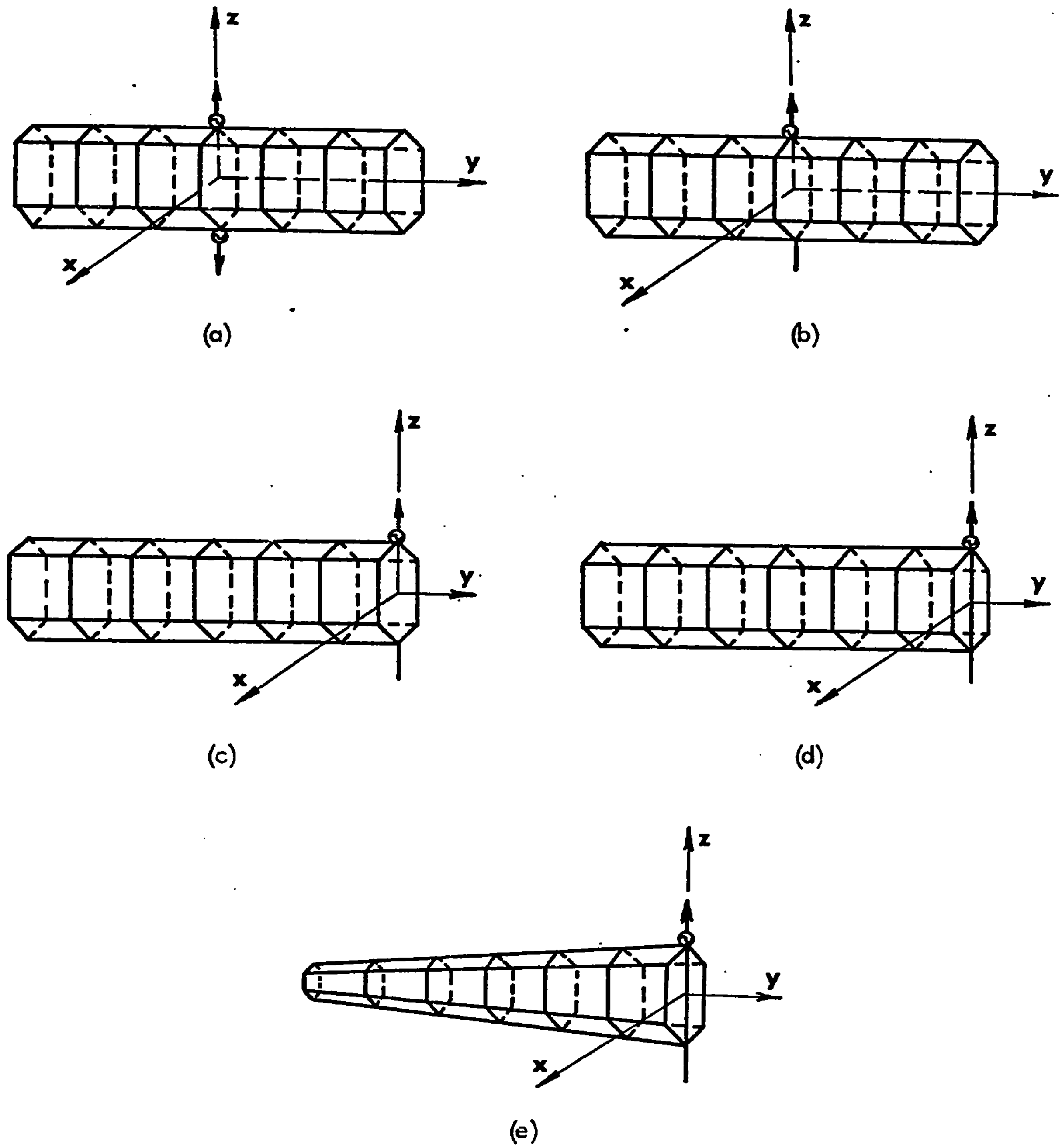

Figure 3.37. Wire-Grid Models and Segmentations of the conducting Surfaces with Radial Dipole shown in Figures 3.32 (b) to 3.32 (f) .

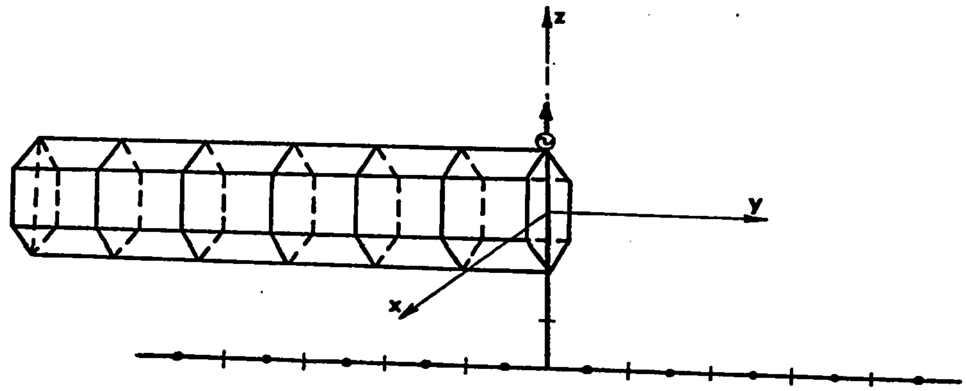

Figure 3.38. Simulation of "Rotor Blades".

So far, nothing has been said about structural symmetry in the development of the wire models illustrated in Figures 3.36 and 3.37. Although the current distribution in the various segments is obviously symmetrical about the z - y plane, no attempt has been made to reduce the number of unknown elements. That this can be done has already been demonstrated for the simple radiating surfaces. However, the main objective with the structures just considered has been to move through the modeling sequences towards the thin wire body. It is clear that except for two orientations (i.e. in the z - y and z - x planes) the horizontal line in Figure 3.38 will disturb the symmetry of the structure. Consequently symmetry considerations were set aside.

The final current and pattern computations made for the above structures are summarized in a condensed form in Table 3.5 where the electrical dimensions used and the corresponding numbers of wire elements are indicated. The symbols used in the table are defined as follows :

d = diameter of cylinder or cone base,

l = length of cylinder or cone,

dp = distance from centre of radial dipole to nearest surface of cylinder,

L = number of circular wires on structure,

TABLE 3.5.

SUMMARY OF CURRENT AND PATTERN COMPUTATIONS MADE FOR SURFACES OF REVOLUTION WITH RADIAL DIPOLE(S) AND PARASITIC STUB

		ELECTRICAL DIMENSIONS			SEGMENTATION AND NUMBER OF WIRE ELEMENTS			
RADIATING STRUCTURE		d	l	d p	AXIAL LINES (MR)	CIRCULAR LINES (L)	TOTAL (NWS)	REMARKS OR DETAILS
	IA	0.112 λ	0.48 λ	0.625 λ	6	7	79	One Radial Dipole located
	IB	0.112 λ	0.48 λ	0.125 λ	6	7	79	at three different distances
Fig. 3.36(b)	IC	0.112 λ	0.48 λ	0.25 λ	6	7	79	from surface of cylinder.
	ID	0.25 λ	0.48 λ	0.05 λ	6	7	79	Pattern computed for comparison.
Fig. 3.37(a)	II	0.25 λ	0.48 λ	0.05 λ	6	7	80	Two Radial Dipoles.
Fig. 3.37(b)	III	0.25 λ	0.48 λ	0.05 λ	6	7	80	One Radial Dipole and one stub.
Fig. 3.37(c)	IV	0.25 λ	0.48 λ	0.05 λ	6	7	80	Dipole and stub at one end of cylinder.
Fig. 3.37 (d)	V	0.16 λ	0.64 λ	0.04 λ	6	9	109	Radial stub 0.16 λ long.
Fig. 3.37(e)	VI	0.16 λ	0.64 λ	0.04 λ	6	9	95	Truncated cone.
Fig. 3.38	VII	0.16 λ	0.64 λ	0.04 λ	6	9	121	" Rotor " line 0.92 λ long.

Note : The symbols d, l, dp, MR, L and NWS, are defined in the text.

MR	=	number of chords modeling one circular wire,
NWS	=	total number of wire segments.

As shown below, the values of NWS listed in Table 3.5 vary slightly from structure to structure.

STRUCTURE (S)	NWS
IA, IB, IC, ID	MR × (2 × L − 1) + 1
II, III, IV	MR × (2 × L − 1) + 2
V	MR × (2 × L − 1) + 7
VI	MR × (2 × L − 3) + 5
VII	MR × (2 × L − 1) + 12

3.5.2 Segmentation of the Thin Wire Structure

Segmenting a given thin wire structure into small wire elements involves essentially two steps [56]. First the directions of current flow on the various wires in the structure are assigned. Then for each wire element, the coordinates of the current-inflow point and the current-outflow point are specified with respect to a fixed coordinate system. Thus, from six x, y, z coordinates, the parameters needed for current computation - i.e. length of element, its centre coordinates, and its angular orientation are determined using simple trignometric relations. The wire radii have, however, to be supplied separately. If wires which are continuous between junctions are too long, they must be divided into smaller segments. However a limit to the total number of wire elements that can be used is the size of the core memory available and the cost of computation. This may also require finding those wire members which are situated far from the source relative to other segments, or members that are located in a "shadow" region with respect to the source, if their influence on the current distributions may be neglected so that they can be omitted. It is imperative that this be done judiciously, and it is clear that considerable guess work is involved.

The above general method can now be applied to the structure shown in Figure 3.31. A section of the body near the feed region is re-drawn in Figure 3.39 where

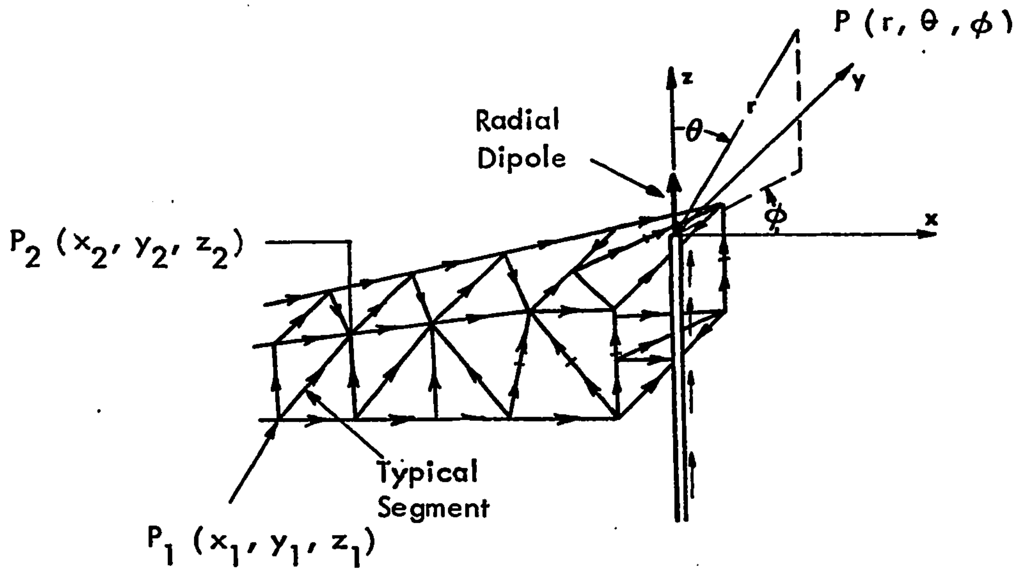

Figure 3.39. Coordinate System for the Thin Wire Structure.

coordinates are also defined with the origin at the source point. To specify uniquely the typical segment shown, the coordinates of its end points, $P(x_1, y_1, z_1)$ and $P(x_2, y_2, z_2)$, were determined from a detailed drawing, and the procedure extended to all the other segments identified for current computation. The six coordinates were then used to evaluate the segmentation parameters for each wire element, namely : centre coordinates, length and angular orientation. As noted earlier, the wire radii were also supplied to the current computation program.

Two forms of the thin wire structure were considered, namely, with and without the rotor blades. For the latter case, only two rotor positions were considered. However more extensive applications to more complex structures or configurations have been studied and refined as reported by Kubina and others [82], Pavlasek and others [83], Kubina [84].

3.6 Summary

The material presented in this chapter represents about one half of the original contribution reported in this study. The second half is related to the efforts made to obtain experimental radiation patterns, and the procedures followed will be outlined in the next chapter. But it is essential to take stock of what was contributed in the realm of current distribution computation. The aim was to demonstrate how the wire grid analysis technique might be applied systematically to simple and complex radiating conducting surfaces excited by wire antennas. The central idea, it has been shown, is the method of establishing a computational wire model. It has been suggested that there could well be some "canonical rules" to follow in order to arrive at a 'correct" model. Although it is still not possible to state generalized rules precisely, the concept of "stationary lines of flow" has been applied to provide a starting point for the modeling process. It has been discussed qualitatively that the distribution and orientation of the lines are dependent on the geometry of the structure and the location of the source. Equally important, the two source representations which were described in Chapter II have been shown to be equally useful. Attempts have been made to show the effects of electrical dimensions and / or of varying the number of wire grids on the computed current distribution on a sphere with a monopole or a cylinder with an axial dipole near its surface. Computational efficiency was achieved for the simple surfaces by exploiting symmetry. The significance of the wire radius has been investigated in some detail. The awareness of its influence on computed current distribution has greatly simplified the application of the technique to a structure with non-uniform wire members. Finally, it has been shown that a complex conducting body with a wire antenna mounted on or near its surface can be evolved gradually from simple surfaces of revolution.

CHAPTER IV

METHOD OF RADIATION PATTERN MEASUREMENT

4.1 Significance of Experimental Patterns in this Work

One of the objectives of the present investigation from the start has been to complement the computed radiation patterns by experimental measurement. The experimental study followed the numerical modeling very closely. After some experience with computations for straight wire antennas, it was seen that it would be far more important to test the validity of computed patterns by direct comparison with measured patterns rather than to devote too much time to refining the numerical technique still further. In any case, even if such refinements were developed, they would have applied only to specialized configurations such as those referred to in Section 2.3.2, but would not have contributed much to the structures modeled in the previous chapter.

As it turned out, the experimental work was very beneficial to the improvement of the computational procedures. A number of minor but subtle approximations in the current distribution computations could not have been made at all without the physical insight obtained from the actual antenna models, and their measured patterns. The important approximations which influenced the current computation schemes directly or indirectly were : (i) the location of the source and its representation, (ii) the significance of the wire radius parameter, (iii) the testing of various grid models for a given antenna structure, and most importantly, (iv) the ability to compare directly wire grid structures and their continuous surface equivalences, or vice versa.

The measured patterns, which are presented in the next chapter, were obtained for structures whose largest dimensions (length, width, or radius) varied from about $0.5\,\lambda$ to about $1.25\,\lambda$. Although most of the measurements were made between 600 and 1000 MHZ, radiation patterns were also measured at 2600 MHZ. In the following sections, the facilities, the construction of the antenna models, and the experimental pattern measurement technique are discussed separately.

4.2 Experimental Facility

The measurement of radiation patterns other than on an outdoor range requires the use of an anechoic room, instrumentation for measurement and recording and the field sensing probe with its positioning mechanism. The pattern measurements reported have made use of an available experimental facility that was specially developed to allow a wide variety of different measurement. It has been described elsewhere by Pavlasek and Kubina [85] , [86] , [87] , and Kubina [84] . Only the essential components are listed here.

4.2 (a) UHF Anechoic Chamber

A broadband (500 MHZ and up) UHF, free-space environment has been simulated by a roofless polygonal, fourteen-sided chamber whose inscribed circle is 2.25 m and wall height is 3 m . The floor and walls of the chamber are covered with Type BB16 and BP24 McMillan absorber, respectively. The BB material, which is in the shape of "building blocks" was also used as a "walkway" path in the floor. The BP is a standard absorbing material in pyramidal blocks. Both absorbers are enclosed in black polyethylene (5 mils thickness) sheeting as a protection against the weather. As shown in Figure 4.1, the important features inside the chamber are a rotatable antenna mount located at the centre of the floor, an inner polystyrene and an outer plywood circular arch for probe mounting. The outer arch is about 2 m in radius, and has angle markings at five degree intervals, and a span of 110 degrees. The inner arch is 1.2 m in radius, and has one degree markings over a span of 130 degrees on two sides of a centre vertical line. A movable probe carriage with a vernier scale is attached to the inner arch. A number of HPY - 24 Eccosorb (Emerson and Cumming) absorbers have also been spread on the floor to fill holes and cover exposed metallic surfaces that are part of the inner arch assembly. The centre point of the anechoic chamber is about 8 m away from an indoor control room.

4.2 (b) Instrumentation

The signal source, power monitoring, signal strength measuring and recording arrangement is shown in Figure 4.2. The assembly consists of the following units :

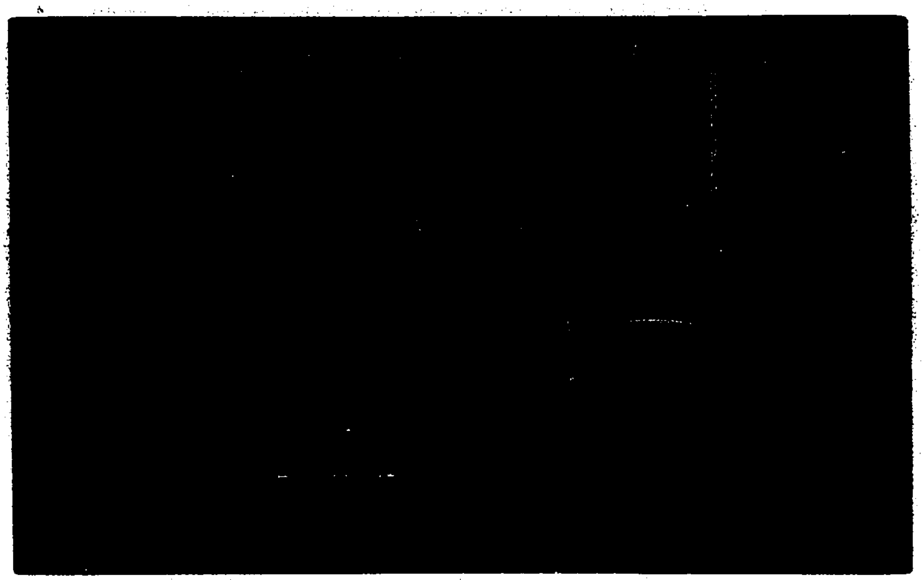

Figure 4.1. UHF Anechoic Chamber with the Antenna Mount at the Centre and the Two Arches Used for Probe Mounting.

Figure 4.2. Signal Source, Measuring and Recording System.

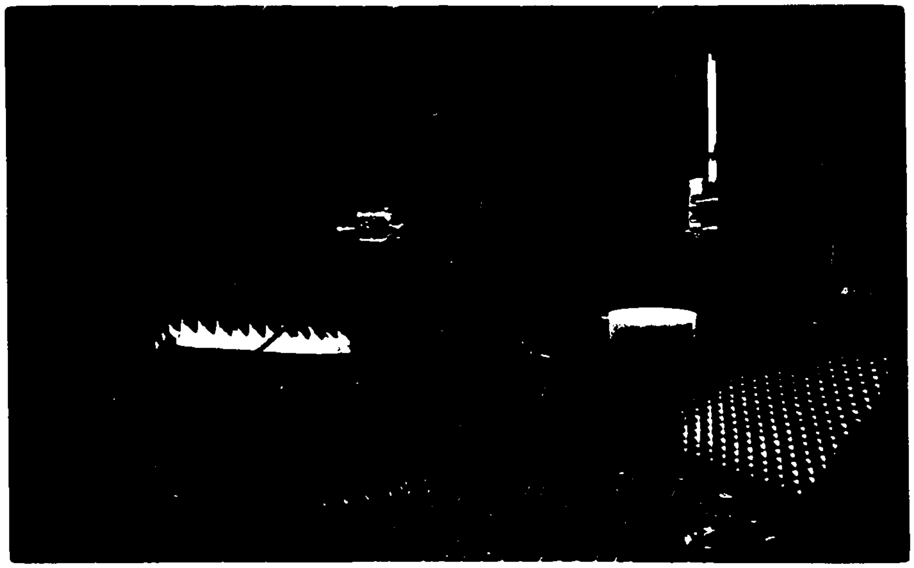

Figure 4.1. UHF Anechoic Chamber with the Antenna Mount at the Centre and the Two Arches Used for Probe Mounting.

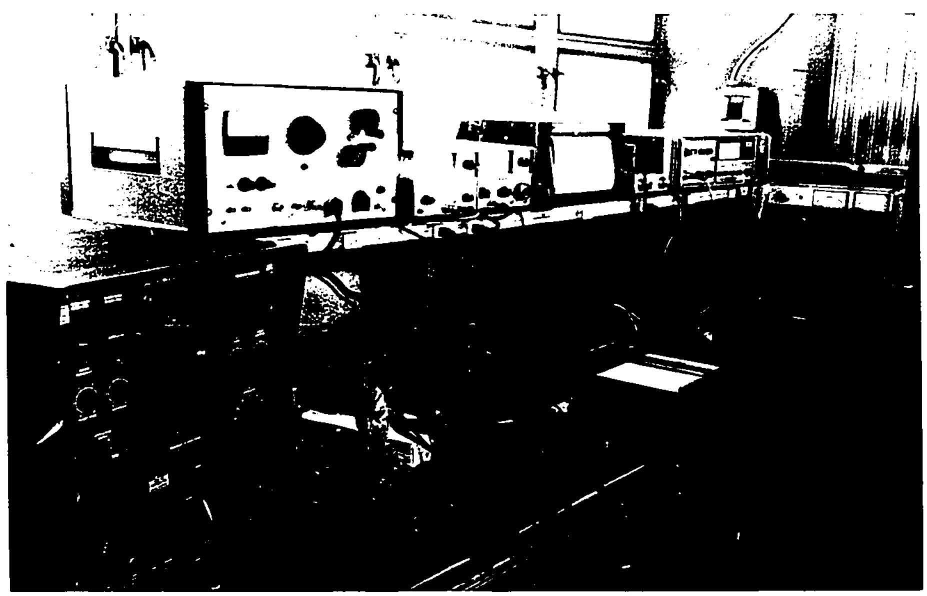

Figure 4.2. Signal Source, Measuring and Recording System.

1	AIL	125 C	Signal Source
1	HP	8410 A	Network Analyzer
1	HP	8405 A	Vector Voltmeter
1	HP	431 B	Power Meter
1	Polaroid	DUI	Spectrum Analyzer
1	HP	7035 B	x-y Recorder
1	HP	7100 B	Strip Chart Recorder
1	HP	393 A	Variable A
1	Siera	137 A	Directional Coupler
1	Philco	640 A	Directional Coupler
1	RL14		Sine-Cosine Potentiometer
1	HP	350 A	Attenuator Set
1	Speed Control Circuitry which also includes two selsyns (run in parallel with two other sylsens inside the anechoic chamber driving an EEL azimuth rotator), compass to indicate azimuth position of antenna.		

The complete equipment schematic is shown in Figure 4.3.

4.3 Experimental Models of Conducting Bodies and Wire Antennas

The experimental models for which radiation pattern measurements were made are the following :

(a) 1/4 λ monopole on spheres,

(b) a short monopole on finite disks,

(c) axial dipoles mounted on the sides of conducting cylinders,

(d) corner reflector antenna,

(e) short radial dipole mounted on a cylinder,

(f) short radial dipole on a simulated helicopter tail structure.

The list follows the wire-grid models for which current computations were made as described in the previous chapter. The significant features of each structure will now be examined.

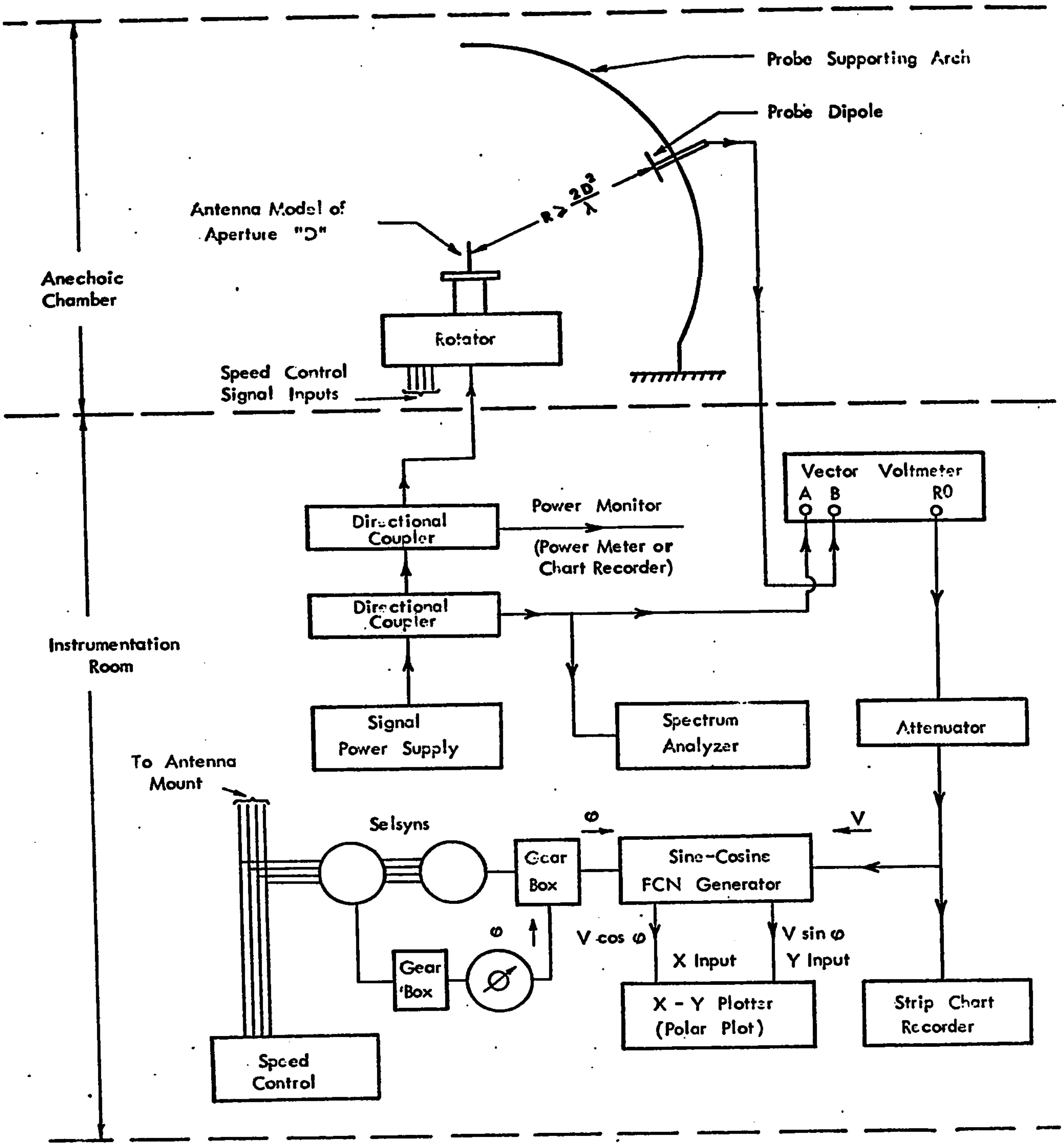

A	Channel "A" of Vector Voltmeter (Reference Signal Input) .
B	Channel "B" of Vector Voltmeter (Received Signal Input) .
RO	Recorder Output.
Ø	Azimuth Position Indicator for Rotator.

Figure 4.3. Equipment Schematic for Instrumentation used in Pattern Measurement.

4.3 (a) 1/4 λ Monopole on Spheres

Although the spherical surface was relatively simple in the mathematical modeling, the construction of its physical models was more challenging. As shown in Figure 4.4, one sphere with a continuous surface and three spherical grids were prepared. Each sphere has a radius of 12.7 cm, and at 600 MHZ, 750 MHZ and 900 MHZ, the corresponding electrical radii would be $\lambda/4$, $5\lambda/16$, and $3\lambda/8$, respectively. The material used for the continuous spherical surface is bronze. It was first sand-cast in two halves, and these were then machined to a polished surface. The three spherical grids (with 32, 24, and 16 lines each), and three monopoles were prepared from brass wire of 1/16" diameter. To hold the grid structure firmly, a hollow plexiglass tube was placed across the ends of the wires. The height of the monopole had to be kept constant at three different frequencies (i.e., 600 MHZ, 750 MHZ and 900 MHZ), and thus three different monopole lengths were chosen : 12.7 cm, 12.2 cm and 8.4 cm. The mounting of a monopole was simply done at one end of the plexiglass, but as described later in the method of measurement, the feed cable for the spherical grids was not run directly through the plexiglass tube.

4.3 (b) Short Monopole On A Disk

Each of the continuous surface and radial disk models shown in Figure 4.5, has a radius of 5.7 cm which corresponds to about 0.5λ near 2600 MHZ. The short monopole used was a Type SM 204 CC Omni Spectra probe antenna with a height of about 0.16λ. It can be noted that one radial wire structure has a bonding ring, and this was designed to test its effect on the measured patterns. The number of radial wires was varied from four to twenty four. The monopole was fed coaxially at the centre of each disk.

4.3 (c) Dipole Antenna Axially Mounted on Side of Cylindrical Support

The models were made of two styrofoam cylinders with diameters of 5 cm and 10.2 cm, respectively, and both about 30 cm high. When continuous surfaces

Figure 4.4. Solid Sphere and Three Wire Grid (32, 24, 16) Meridians with Mounted Monopoles.

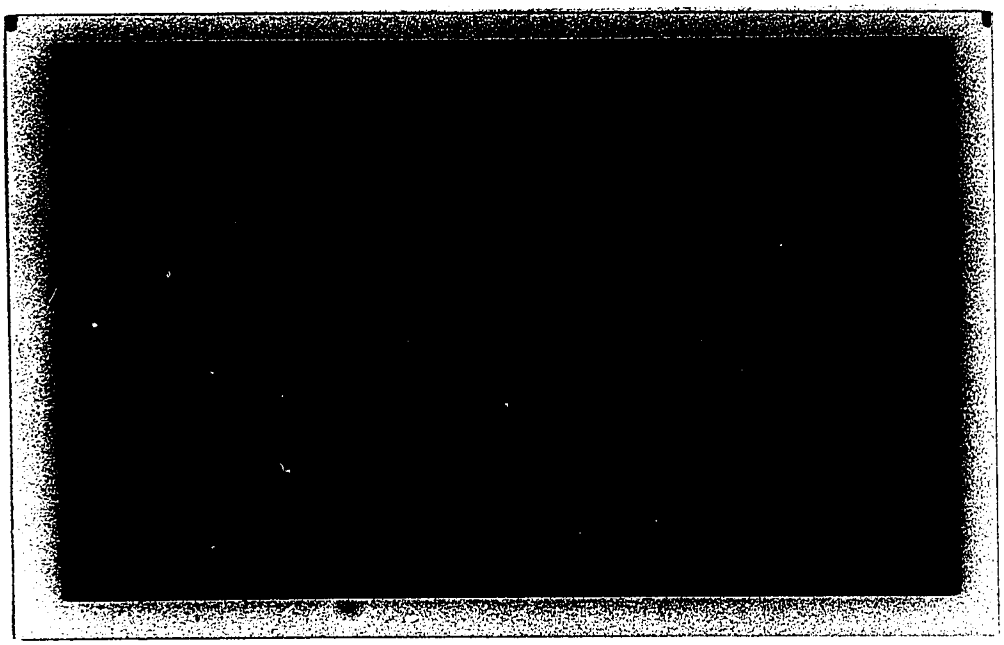

Figure 4.5. Continuous Surface Ground Plane Disk and Four Radial Wire Models.

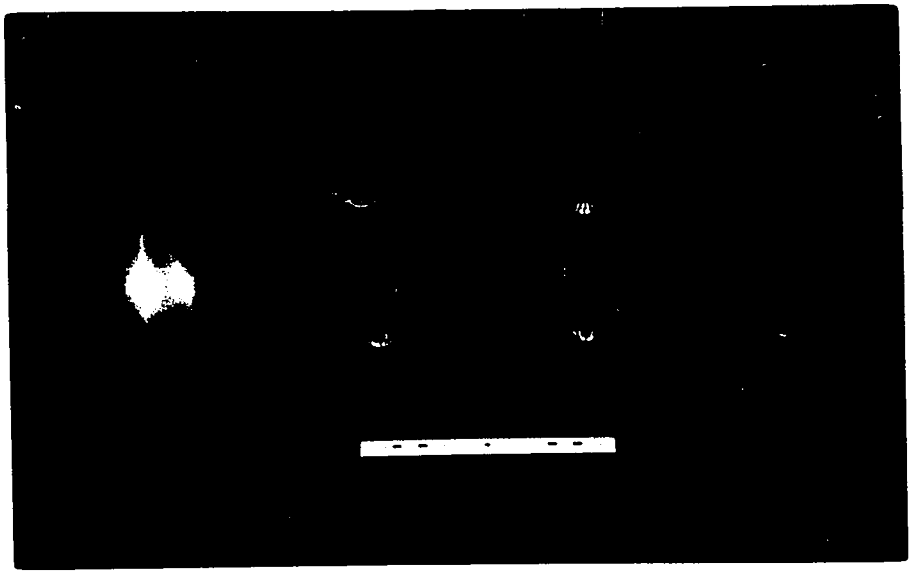

Figure 4.4. Solid Sphere and Three Wire Grid (32, 24, 16) Meridians with Mounted Monopoles.

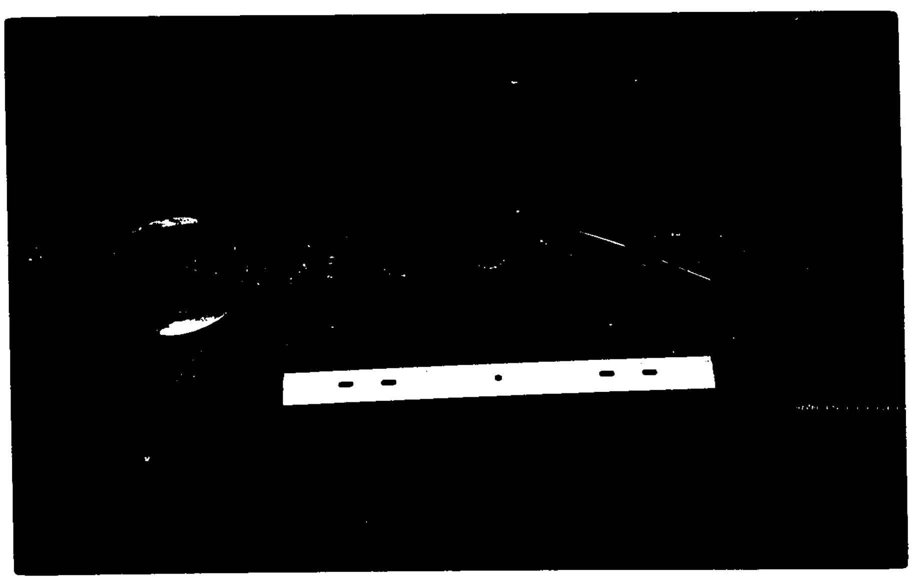

Figure 4.5. Continuous Surface Ground Plane Disk and Four Radial Wire Models.

were required, the cylinders were covered by aluminum foil. The wire grid structures were made by pasting strips of self-adhesive thin copper tape on the surface of the cylinders parallel to their axes. Strips of 0.3 cm width were used. At 1000 MHZ, the cylinders would have diameters of $\lambda/6$ and $\lambda/3$, respectively. Four strips were placed on the smaller diameter cylinder, and six strips on the longer cylinder. A balanced dipole antenna was mounted axially parallel on the side of each cylinder by means of a rigid coaxial cable. The unbalance - to - balance transformation from the coaxial cable to the dipole was made using $\frac{\lambda}{4}$ slots following similar designs by Kubina [84]. Each dipole antenna had a height of a half wavelength at 1000 MHZ, and was constructed from a thin silver-copper alloy wire of about 36 mils in diameter.

4.3 (d) Corner Reflector Antenna

The corner reflector antenna was modeled using acrylic plastic plates for the fundamental structure. The reflector walls were hinged at the corner and their angular position determined by a protractor scale on a supporting base plate. The dipole antenna was similar to the one used in the cylindrical mast case both in its construction and mounting. The reflector height (H) was designed to be $1.0\,\lambda$ near 1000 MHZ, and two side widths (S) were chosen : $0.5\,\lambda$ and $1.0\,\lambda$. Again, copper tape strips about 0.6 cm wide were used to model the grids and aluminum foil used to obtain continuous surfaces. The half-wave dipole was mounted symmetrically at a distance of $0.25\,\lambda$ from the corner line.

4.3 (e) Cylinder with Short Radial Dipole

The thicker styrofoam cylinder with six strips described above was also used to model a finite cylinder with a radial dipole on its centre. Circumferential strips were added as described in Chapter III taking due care to obtain adequate bonding at the junctions. The radial dipole used was the OSM 204CC Omni Spectra short antenna .

4.3 (f) Thin Wire Structure (Helicopter Tail Section) with Radial Dipole

From the design and construction point of view, the helicopter tail section was the most difficult to model. As shown in Figure 4.6, the truss members have many junctions. These had to be dressed to ensure permanent contacts. Those points at which the junctions tended to become loose due to structural stress during pattern scanning were carefully reinforced with the adhesive copper tape material. Most of the wires used in the structure were brass of 1/16 inches in diameter, but the supporting rod was 1 / 4 inch in diameter. Ath the tail end, there were also segments of 1 / 8 inch diameter. Rotor blades were modeled from thin brass sheets of 9 / 16 inch width. The OSM 204CC Omni Spectra short antenna was used for testing and preliminary measurements. In the final measurements, it was replaced by a longer dipole of about 0.2 λ near 675 MHZ. The significant electrical dimensions of the structure have already been given in Figure 3.31. Again, by covering the structure with aluminum foil, a continuous conducting surface was obtained.

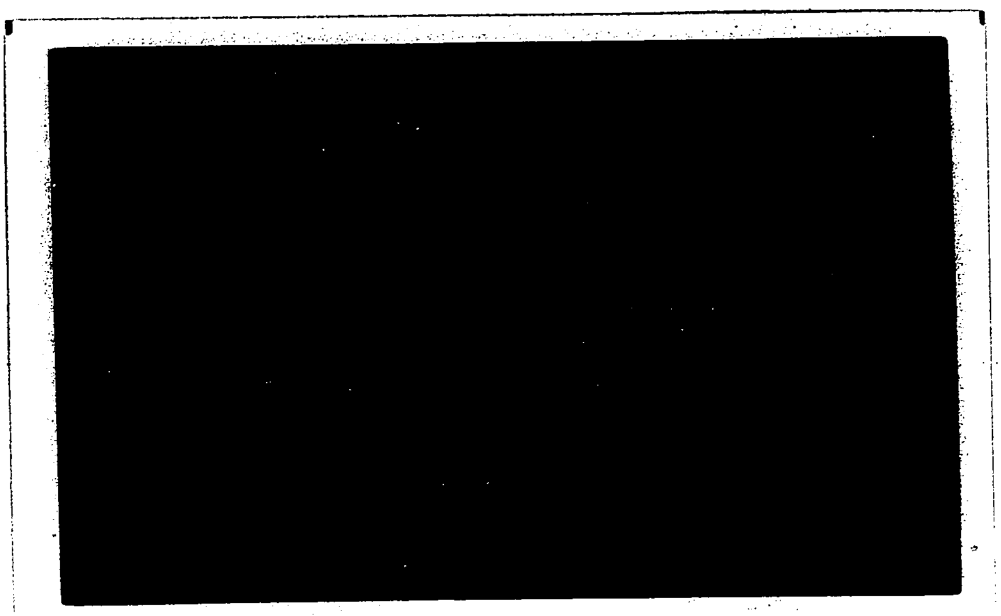

Figure 4.6. Thin Wire Structure (Helicopter Tail Section) with Radial Dipole.

4.3 (f) Thin Wire Structure (Helicopter Tail Section) with Radial Dipole

From the design and construction point of view, the helicopter tail section was the most difficult to model. As shown in Figure 4.6, the truss members have many junctions. These had to be dressed to ensure permanent contacts. Those points at which the junctions tended to become loose due to structural stress during pattern scanning were carefully reinforced with the adhesive copper tape material. Most of the wires used in the structure were brass of 1/16 inches in diameter, but the supporting rod was 1 / 4 inch in diameter. Ath the tail end, there were also segments of 1 / 8 inch diameter. Rotor blades were modeled from thin brass sheets of 9 / 16 inch width. The OSM 204CC Omni Spectra short antenna was used for testing and preliminary measurements. In the final measurements, it was replaced by a longer dipole of about 0.2 λ near 675 MHZ. The significant electrical dimensions of the structure have already been given in Figure 3.31. Again, by covering the structure with aluminum foil, a continuous conducting surface was obtained.

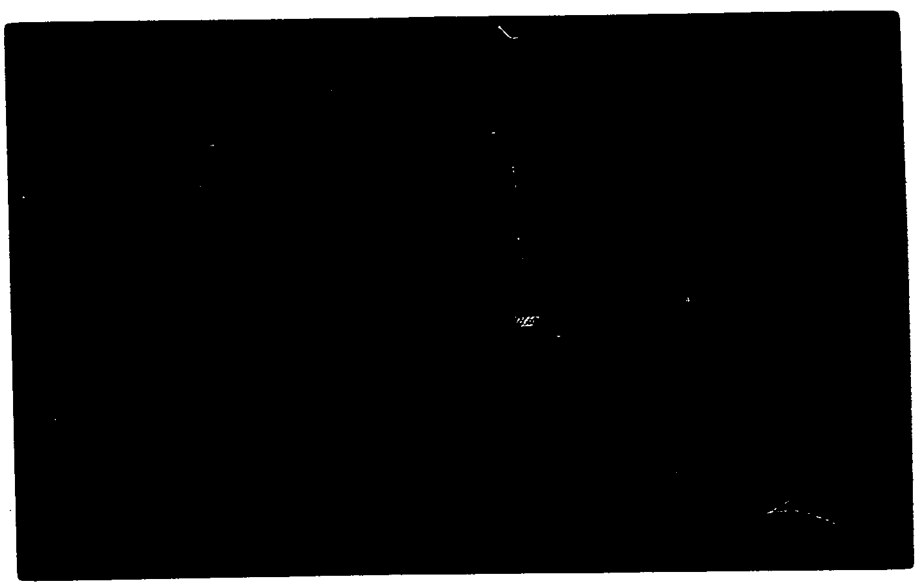

Figure 4.6. Thin Wire Structure (Helicopter Tail Section) with Radial Dipole.

In addition to the computational study, a motivation for constructing this structure was to make preliminary studies of rotor modulation effects on a scaled model (1 : 20) of a Bell 47 G - 2 A helicopter. A further and more extensive study of the problem has been made for a complete helicopter model by Kubina [84].

4.4 Radiation Pattern Measurements

The basic considerations of type of pattern and polarizations, the general measurement procedure, and finally the radiation pattern measurements for the six structures are to be considered in this section.

4.4.1 Basic Considerations : Type of Patterns, Coordinate System, and Polarization Component

It is essential that the type of radiation patterns measured, the coordinate system used, and the polarization components be clearly identified from the outset.

Type of Patterns

The only concern in the present experimental work has been the measurement of electric field strength patterns. In one or two cases, power patterns were also taken. Some attention was also given to phase behaviour.

Coordinate System

The two arches in the anechoic chamber shown in Figure 4.1 have as a common centre a point on the axis of the antenna turntable. The usual spherical coordinate system shown in Figure 4.7 is therefore defined at this centre point as the origin [41], [88]. While the origin was fixed, the coordinate axes however were occasionally rotated to fit a particular antenna structure and mounting. The angular coordinates - elevation angle θ, and azimuth angle φ are the only significant ones since the pattern measurements were made in far field regions following the Fresnel - zone criterion

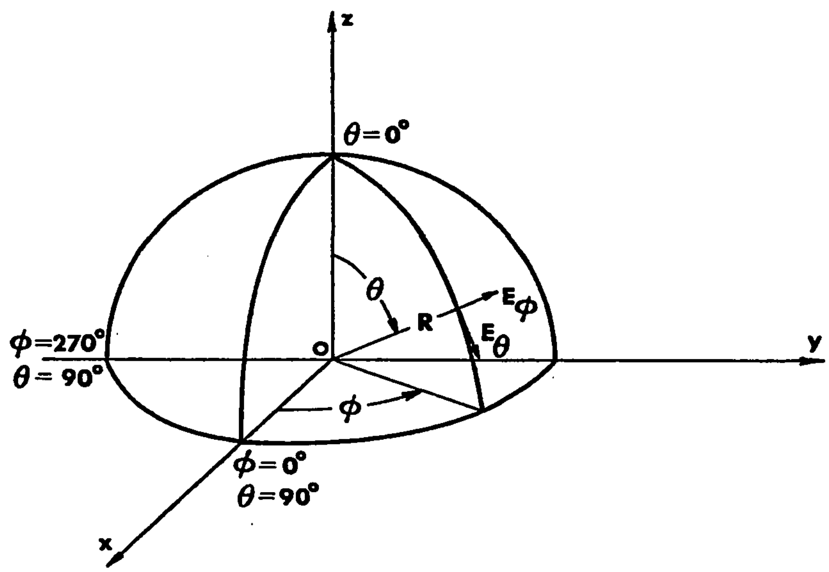

Figure 4.7. System of Spherical Coordinates used in Radiation Pattern Measurement.

$$R \geq 2D^2/\lambda \tag{4.1}$$

where D was taken as the largest dimension of each structure.

Polarization

At the observation point (R, θ, φ) shown in Figure 4.7, the electric field in general was considered to be elliptically polarized with components E_θ and E_φ. Hence, whenever necessary or possible, E_θ versus φ, or E_φ versus φ were measured for various θ - principal plane cuts. It will be indicated below how this was done by mounting a probe dipole in one or two orientations. Other measurements made were, E_θ versus θ, and E_φ versus φ for different φ - plane cuts.

4.4.2 Basic Measurement Procedure

The method of measurement discussed below was developed by Kubina [84]. Considerable care and effort is needed in such measurements to obtain dependable operation of the system and reliable results. The following is an outline of the essential adjustments and operating procedures.

The equipment schematic given in Figure 4.3 has the essential components of apparatus for antenna pattern determination. When a vector voltmeter is used a CW signal is required and since a phase measurement is also involved, a reference signal channel is required. Signal purity, amplitude and frequency stability are monitored by a spectrum analyzer, power meter and frequency counter. Amplitude stability was continuously monitored.

Unlike usual outdoor range procedures, the antenna under test was energized. The measuring probe was an E - type dipole (approximately $1/2\ \lambda$ or less). The analog signal output from the vector voltmeter was recorded on an X - Y plotter arranged to operate as a polar plotter. This was achieved by driving a sine-cosine function generator by the vector-voltmeter output and a φ position signal from the azimuth rotator, thus generating $V \cos \varphi$ and $V \sin \varphi$ serving as the X and Y inputs to the plotter. A rectangular coordinate pattern on a strip chart recorder was also recorded simultaneously. Since the patterns measured were to be normalized for comparison with computed patterns, no attempt was made to calibrate the voltmeter and the powermeter, although the signal field strength was monitored.

Rotation of the antenna mount was physically possible only in the horizontal plane about a vertical axis. However, as indicated earlier, by re-defining the proper coordinate system and also by properly orienting the dipole probe, either E_θ versus θ, or E_θ versus φ and E_φ versus φ could be measured, depending on the antenna structure. For each pattern scan, the positioning of the radiating structure, probe alignment, and the compass zero settings were carefully determined. Azimuth position of the rotator was indicated on the strip chart recordings by markers generated in synchronism with the rotator position in order to provide position calibration.

Point-by-point measurements were attempted for some structures with the probe mounted on the inner arch. However, because of difficulties involved in changing the probe position, and the recording of the output data, this tedious procedure was of necessity avoided as much as possible.

4.4.3 Pattern Measurements

Patterns of six antenna systems were measured using the general procedure outlined above. Specific details concerning the mounting of each antenna and a qualitative appraisal of the influence of absorber positioning are now discussed. A summary of the pattern measurements made is presented in tabular form.

4.4.3 (a) Antenna Mounting and the Measurements Made

Table 4.1, below lists the antenna models whose patterns were measured, the significant dimensions, the field components and the coordinates within which they were studied.

The coordinates used and the planar cuts in which the patterns were measured, determined in each case the specific geometric form of the mounting to be used and the position of the antenna coordinates relative to the rotator and probe coordinates. For example in the case of the monopole on a sphere the sphere was mounted with the monopole axis either colinear with or perpendicular to the rotator axis. In each mounting case, however special care had to be taken so that the mechanical structure used would be sufficiently rigid and accurate to ensure correct positioning of the model's coordinates relative to the rotator and measuring probe without disturbing the model's impedance structure. In addition it is essential that the mounting should not disturb the electrical structure of the model. Use of dielectric materials is thus indicated wherever possible, but as sparingly, since even with dielectric structures, scattering effects will be present [89]. Furthermore, a connecting cable is required in most cases unless the antenna is large enough to contain a small battery operated service. A self-contained source however makes phase measurements difficult since provision of a reference signal then requires a high resistance cable or a not too reliable second measuring probe, hopefully located in an uncarrying portion of the field.

The above mentioned mounting problems thus result in design compromises among the three mutually contradictory requirements of mechanical mounting, electrical environment and instrumental arrangement. The materials used for the resulting mountings were either PVC or phenolic plastic forms. In the above mentioned mounting

TABLE 4.1.

SUMMARY OF PATTERN MEASUREMENTS

	ANTENNA STRUCTURE: CONTINUOUS SURFACE	ANTENNA STRUCTURE: WIRE-GRID MODEL	SIGNIFICANT ELECTRICAL DIMENSIONS	FIELD COMPONENTS MEASURED	PARTICULAR DETAILS
1	$\lambda/4$ Monopole mounted on sphere of radius R_s	16, 24, 32 Meridian wires	(a) $R_s \approx \lambda/4$ (b) $R_s \approx 5\lambda/16$	E_θ versus θ	For bronze sphere, pattern measurements made with external source and self-contained source.
2	0.166λ monopole mounted on disk of radius R_d	8, 12, 16, 24 Radial wires	$R_d \approx 0.5\lambda$	E_θ versus θ	External source. Influence of circular (ring) bonding wires on wire-grid modeling also investigated.
3*	Dipole Antenna of height h_d mounted axially at a distance S from the surface of a cylindrical mast of height h_c and diameter D.	4 axial thin copper strips	(a) $D = 0.126\lambda$ $h_c \approx 0.76\lambda$, $h_d \approx 0.38\lambda$	E_θ versus φ	External source. $S = 0.755\lambda$
			(b) $D = 0.167\lambda$ $h_c \approx 1.0\lambda$ $h_d \approx 0.5\lambda$	E_θ versus φ	External source. $S = 0.368\lambda$
		6 axial thin copper strips	(c) $D = 0.33\lambda$ $h_c \approx 1.0\lambda$ $h_d \approx 0.5\lambda$		External source. $S = 0.28\lambda$
			(d) $D = 0.202\lambda$ $h_c \approx 0.6\lambda$ $h_d \approx 0.3\lambda$	E_θ versus φ	External source. $S = 0.686\lambda$
			(e) $D = 0.28\lambda$ $h_c \approx 0.82\lambda$ $h_d \approx 0.41\lambda$	E_θ versus φ	External source. $S = 0.75\lambda$
			(f) $D = 0.33\lambda$ $h_c \approx 1.0\lambda$ $h_d \approx 0.5\lambda$	E_θ versus φ	External source. $S = 0.914\lambda$
4*	Corner Reflector Antenna with 0.5λ dipole mounted 0.25λ from apex of reflector of width S and height H, and corner angle β	9 thin copper strips each 0.6 mm wide ($\approx 0.02\lambda$)	$S \approx 0.5\lambda$ $H \approx 1.0\lambda$	E_θ versus φ	External source. $\beta = 60^\circ, 90^\circ, 120^\circ, 130^\circ$
				E_θ versus θ ($\varphi = 0^\circ$)	$\beta = 90^\circ, 130^\circ$
		17 thin copper strips	$S \approx 1.0\lambda$ $H \approx 1.0\lambda$	E_θ versus φ	$\beta = 60^\circ, 90^\circ, 110^\circ, 120^\circ$
				E_θ versus θ ($\varphi = 0^\circ$)	$\beta = 90^\circ, 110^\circ$
5*	Radial dipole mounted on a cylinder of diameter d and length l	6 axial thin copper strips ; 7, 9 circular aluminum foil strips	$d \approx 0.21\lambda$ $l \approx 0.61\lambda$	E_θ versus θ ($\varphi = 0^\circ$)	External source. Precautions were taken to maintain good electrical contacts at the junctions of the axial and circular strips.
6**	Radial Dipole on "helicopter tail structure"	Structure already in wire-grid form	Dimensions given in Figure 3.31	E_θ versus φ E_φ versus φ	External source. $\theta = 60^\circ, 70^\circ, 80^\circ, 90^\circ, 100^\circ$ Three basic measurements (a) without rotor blades, (b) with rotor blades in parallel (i.e. to axis of structure) position, (c) with rotor blades in perpendicular position.

* Measurements repeated with structures covered with aluminum foil.

** Measurements partially repeated with structures covered with aluminum foil.

problems the most serious one is that arising from the presence of the exposed cable leading to the model. Typical mountings for the short monopole placed on radial ground wires and for the mast-supported dipole are shown in Figures 4.8 and 4.9 respectively.

It is well-known that in pattern measurements than the exposed cable does introduce pattern distortions [90], [91]. Thus the general practice is to have such cable covered by absorber and located to minimize its perturbing effects. Of the six structures considered here, the sphere grids, the thin wire structure, and the disk had portions of cables exposed near their antenna base. In the latter case, it was a rigid coaxial line, and the only thing possible was to cover it with an absorber. In the case of the helicopter tail section, it was possible by proper design to place the cable inside the relatively large brass rod (see Figure 4.6). For the spherical grids, the cable was not taken through the plexiglass tube (Figure 4.4), but along one of the wire grid meridians. These precautions were part of the experimental model design, and their effectiveness confirmed by extensive preliminary testing.

An attractive method of avoiding feed cable interference would be by using a self-contained source operated by a battery inside the model. However, in the case of the small scale antenna systems, this is not always possible. In addition unless special provisions are made (which again introduce new metal structures), the measurement of phase is precluded. Consequently, this technique was limited to the solid spherical structure.

4.4.3 (b) Anechoic Chamber Characteristics and Performance

The dimensions and basic layout of the anechoic room are shown in Figure 4.10. The shape and arrangement were chosen to accommodate a centrally located model, rotatable in azimuth, while allowing three dimensional positioning of the measuring probe as well. The location of the chamber on a building roof, its shape and size, its "open sky" (with removable weatherproof radome) feature were chosen to maximize the enclosed volume while minimizing costs. The detailed design and proof of performance tests are described elsewhere [84]. The 'free-space' region available and the 'quiet zone' re-

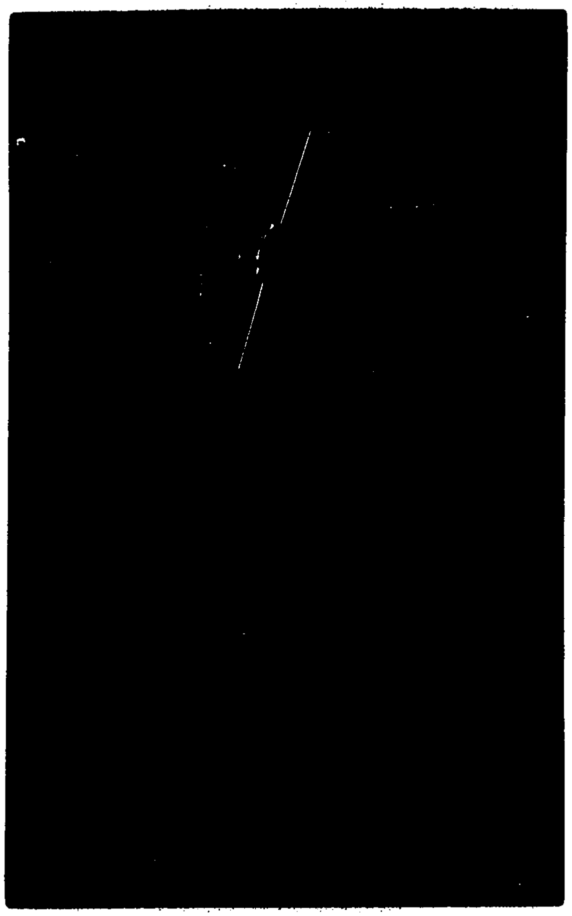

Figure 4.8. Mounting of Short Monopole on Radial Ground Wires for Pattern Measurement.

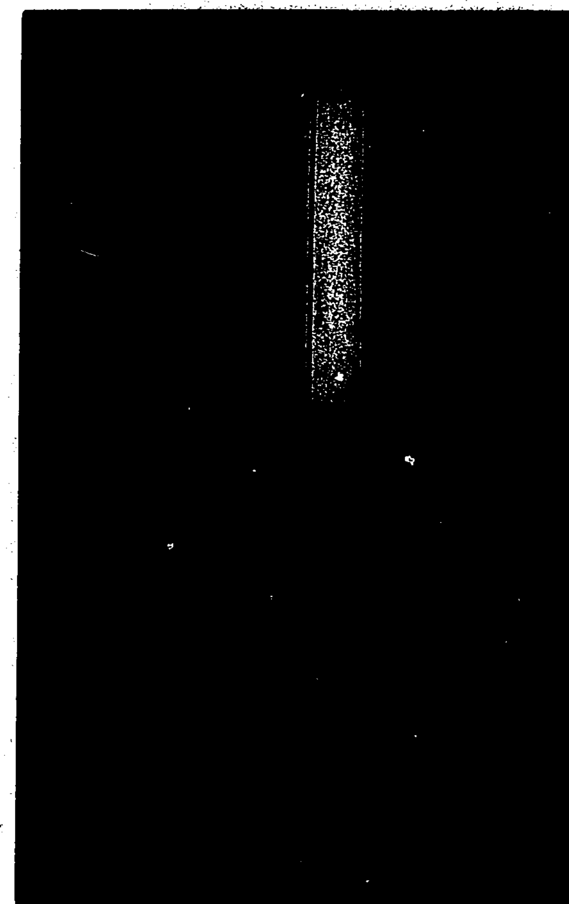

Figure 4.9. Mounting of Mast-Supported Dipole for Pattern Measurement.

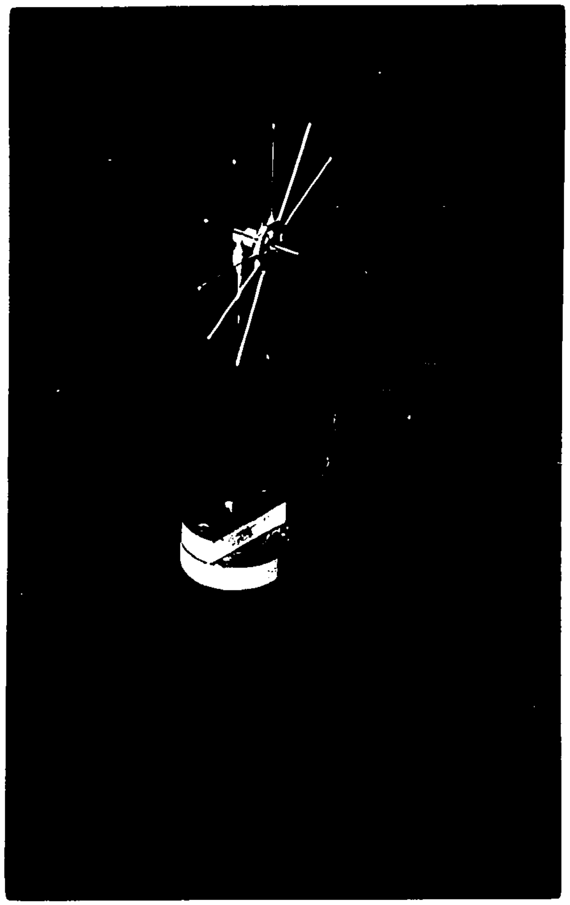

Figure 4.8. Mounting of Short Monopole on Radial Ground Wires for Pattern Measurement.

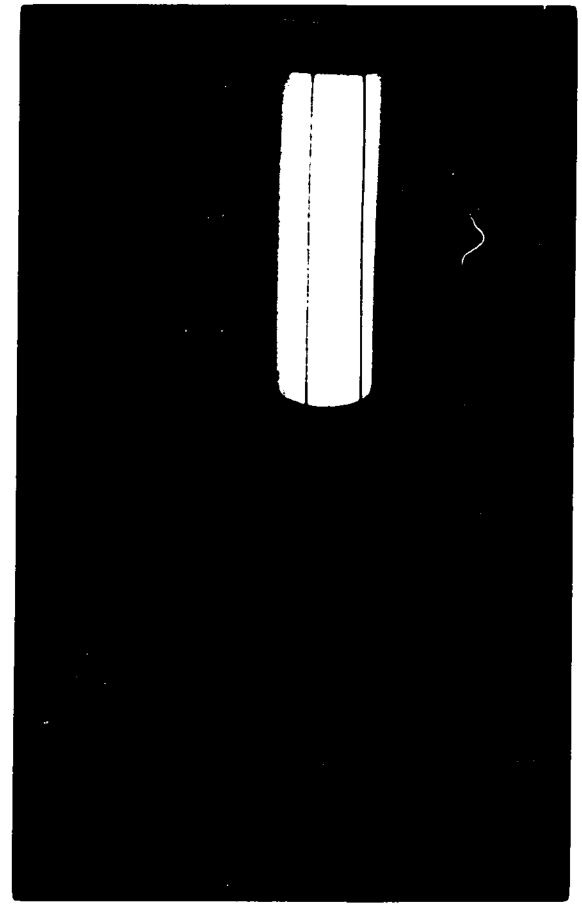

Figure 4.9. Mounting of Mast-Supported Dipole for Pattern Measurement.

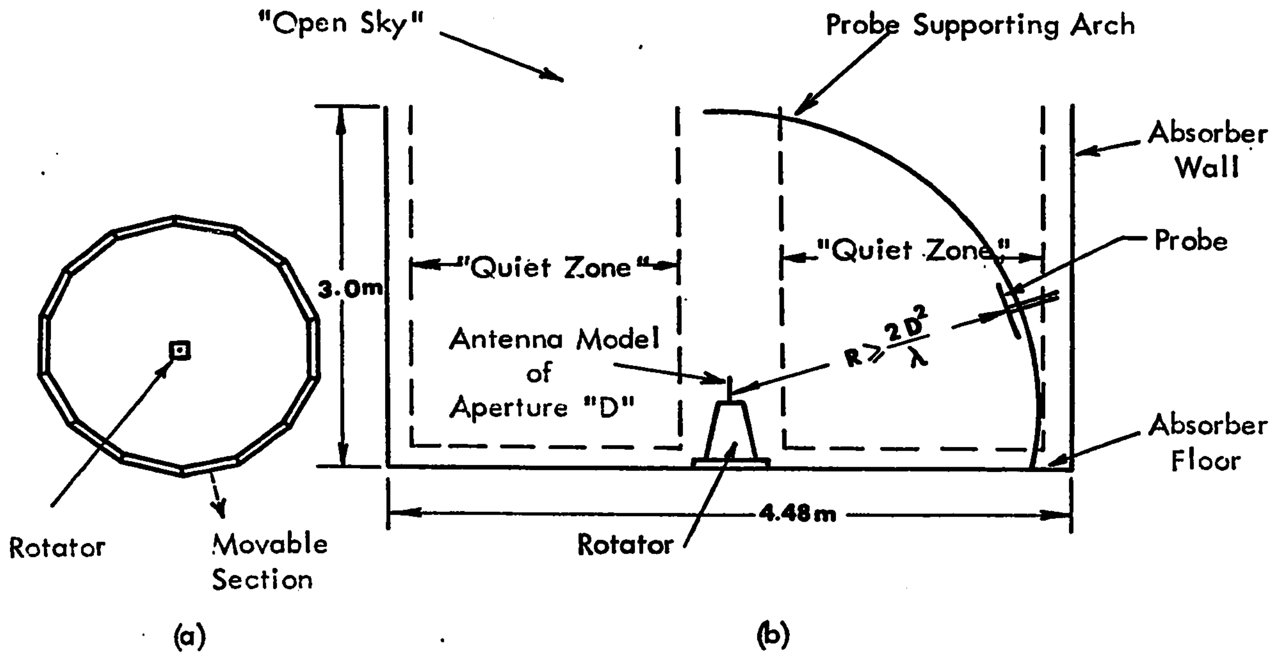

Figure 4.10. Basic Layout of Anechoic Room.
(a) Top View, (b) Enlarged Vertical Section.

quirements were sufficient for the measurements mode. A telling check on the room performance was made for some test models which were also measured on a full scale open air antenna range (Canadair Microwave Antenna Range, Montreal) giving identical results [84].

Some interesting difficulties which are worthy of note were encountered however, which might be attributed to the anechoic room and the location of absorber material, especially on the floor.

The first difficulty relates to weather during heavy rainfall. Inconsistencies developed in some patterns and 'noisy' patterns would result. The root cause of this was not ultimately diagnosed. However, the trouble departed with clear dry weather. Suspicion is directed however to the 'radome' cover and to the effect of air moisture on the absorber. A second noteworthy difficulty was one whose symptoms were lack of repeatability and the appearance of dissymmetry (even for clearly symmetrical cases) in the case of some measurements especially those made in the 600 - 700 MHz range. Eventually the distortions were traced to some absorber material laid on the room floor which was inappropriately placed. Relocating and rearranging of the floor absorbers eventually yielded satisfactory results. While there appeared to be no obvious systematic feature to this problem, it was found that essentially random positioning of the absorber was the best.

CHAPTER V

DISCUSSION OF COMPUTED AND MEASURED PATTERNS

5.1 Introduction

The wire-grid modeling method was applied in Chapter III to compute current distributions as a first step in the determination of radiation patterns of the antenna structures considered. The previous chapter described the experimental procedures used for pattern measurements. This chapter contains a systematic presentation and a comparative evaluation of the computed and experimental patterns.

The scope of the discussion will be described further on. However, some additional details about the radiation field computation scheme are first necessary. After the approximate current distribution is computed for a given antenna system, the E_θ and E_φ patterns are determined using (2.93) and (2.94), respectively. A flow diagram for the computation routine is illustrated in Figure 5.1. First the principal-plane cuts are chosen, the current distribution data is supplied, and the pattern is then calculated. The pattern can then be normalized and plotted directly in rectangular coordinates using a line printer. If the resulting pattern is found to differ significantly from a known or an experimentally determined pattern, the complete computation scheme, including the evaluation of the current distribution is re-checked, as indicated by the dotted line.

The significant features of the computed and measured patterns are discussed in two main stages. First the computed results are considered. The aim here is to demonstrate the logical steps involved in developing the modeling procedure. The steps are first, the testing of the computation program on simple structures, secondly the study of the dependence of the pattern on the number of current elements, and finally the application to the analysis of more complicated structures. In the second stage the measured and computed patterns are compared. There are four subsections. First examples of fields which illustrate the characteristics of the anechoic chamber are considered. Next,

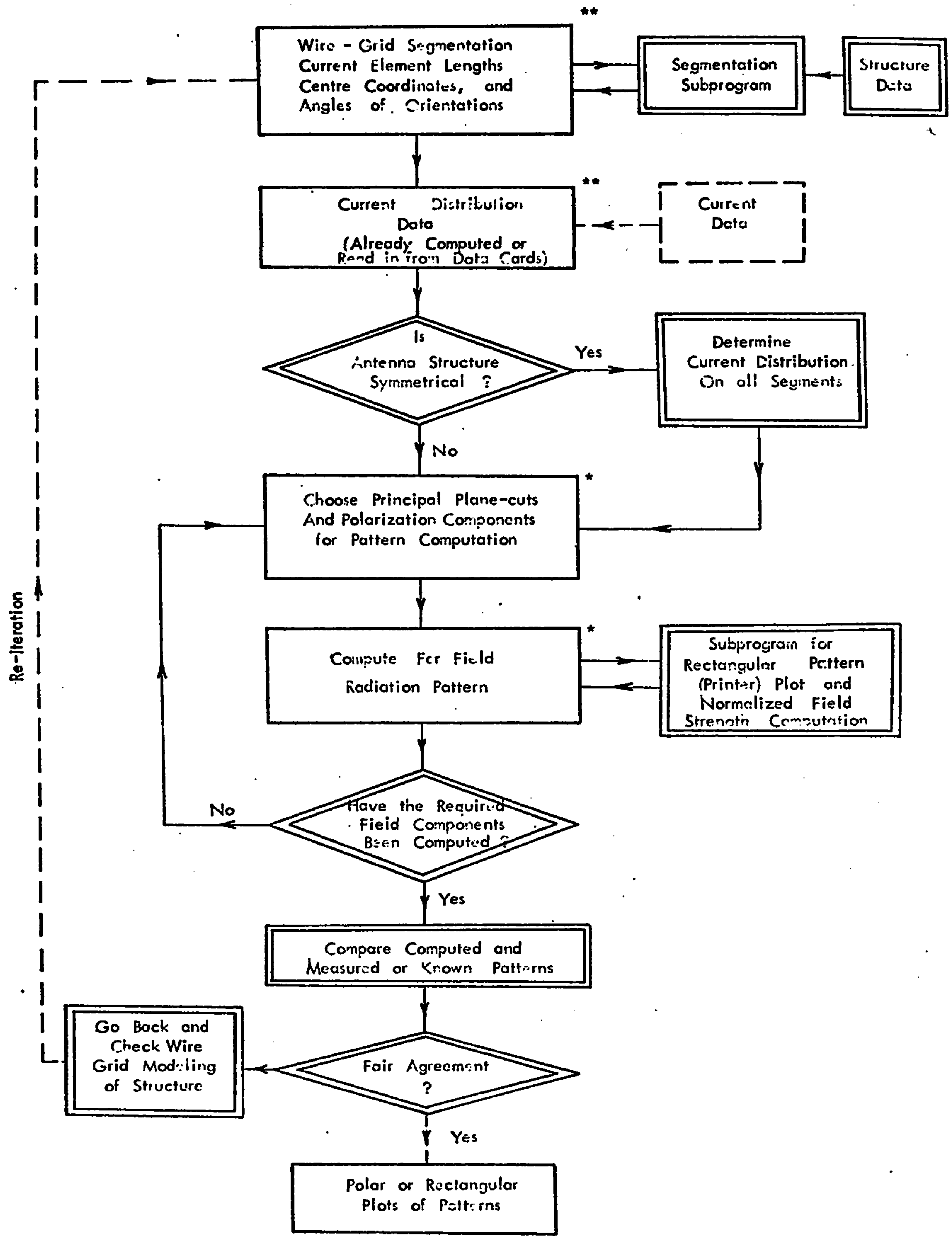

Figure 5.1. Program for Radiation Pattern Computation. Basic Program adopted from Reference [56] with some Minor (*) and Major (**) changes.

some discussion is devoted to the equivalence of continuous conducting surfaces and their wire-grid models, thus providing an experimental validation for the wire modeling procedures described earlier. Then the influence of the wire radius parameter on pattern computation is examined with reference to the short monopole mounted on twelve or sixteen radial ground wires. The final section makes direct comparison of computer and measured patterns both for wire-grid and continuous surfaces in the case of four antenna structures, namely :

(i) sphere-mounted monopole,
(ii) mast-mounted dipole,
(iii) corner-reflector antenna,
(iv) radial dipole mounted on a helicopter tail section.

While it will be found that the comparisons are satisfactory on the whole, patterns for which disagreements were noted are also cited. The causes of the discrepancies may be attributed either to the inadequacy of computational models or to basic measurement constraints.

5.2 Discussion of Computed Patterns

5.2.1 Testing of Computation Scheme

As summarized in Table 3.1, the main object in carrying out the extensive current computations for a $1/4\,\lambda$ monopole mounted on different sphere models was to establish the validity of the assumptions employed (e.g. source representation), and also to test the general computation scheme. Figure 5.2 shows the radiation patterns (relative power) on a rectangular plot for sphere radii of $\lambda/8$ and $\lambda/4$, respectively. The agreement of the wire-grid model results is very good with those published by Tesche and Neurether [49] for the smaller sphere, and reasonably fair for the larger radius except in the null region. * Both finite - width gap and magnetic frill source representations were tested with the latter sphere radius. As discussed earlier, since the current distributions were found to differ by a constant multiplying factor, the normalized patterns were also identical.

---

* Patterns given in Reference [49] have in turn been found to agree well with computations described in Reference [54] .

5.2.2 Influence of Current Elements on the Computed Patterns

In seeking more 'correct' wire-grid models, a systematic search was conducted to determine the influence of the number of current elements used in the wire modeling process. As described in Chapter III the number of segments and wires in the grid used in computations were varied according to the following tests :

(a) the number of wires in the grid representing the "stationary lines of flow" and the number of segments into which each wire was divided were varied ,

(b) the number of wires in the grid was varied, but the number of segments into which each wire was divided was held fixed ,

(c) the number of wires in the grid was kept constant, but the segment length distribution was varied.

Figure 5.3 illustrates the convergence in the minimum region of the radiation pattern for the $1/4\,\lambda$ monopole mounted one of the spheres ($R_s = \lambda/4$) mentioned above. The four different patterns shown, as listed in Table 3.1 are for the sphere modeled, by 16, 24, 24 and 32 stationary lines of flow, and with the meridians divided into 16, 16, 25 and 25 segments, respectively. It is notable that in this test the resulting pattern in each case was not changed significantly even when the number of elements was greatly increased from 256 to 800 .

For the second test the variation in the radiation pattern of the disk-mounted monopole was investigated. Patterns are shown in Figure 5.4 for four different numbers of radial wires, and an experimentally measured pattern for a continuous disk is included as a reference. In progressing from eight to twenty-four wires, it can be seen that in the minimum region, the computed pattern approaches the reference pattern gradually. However, it is significant to observe that the patterns in the upper θ region ($\theta < 80$) practically coincide with each other. One possible explanation that can be put forward is that in this region, the current distribution on the monopole dominates the radiated field, whereas in the region below the plane of the radial wires the monopole is largely screened off. Thus as more radial wires are added to simulate the ground disk, the more effective the screening becomes, and hence the deeper the minimum becomes in the computed pattern.

Similar computations were carried out for the mast-mounted dipole where the number of current filaments modeling the cylindrical supports was varied from 4 to 6 for a cylinder diameter of $\lambda/8$, and from 6 to 8 for cylinder diameters of $\lambda/4$ and $\lambda/2$. Typical patterns are shown in Figures 5.5, 5.6 and 5.7, for various separation distances of the dipole antenna from the cylindrical surfaces. In each case it is seen that the patterns are very close to each other, and thus the modeling criteria which were postulated in Chapter III for this antenna structure appear justified. However, further justification is needed to substantiate the choice between 4 or 6 strips, and 6 or 8 strips to represent the mast. This will be done after the experimental patterns have been presented.

Another structure that was found well-suited for the above testing of the influence of the number of segments on computed patterns, was the corner reflector antenna. In Figures 5.8 and 5.9 are shown the horizontal (H - plane) and the vertical (E - plane) patterns of a frame which is $1.0\,\lambda$ wide and $1.0\,\lambda$ high with a corner angle of 110°, and a half-wave dipole antenna placed at $0.25\,\lambda$ from the corner edge. The computations were carried out for 17 and 21 current filaments, respectively, modeling the reflecting sides, and experimental patterns have been taken from the work of Wilson and Cottony [78] for reference. It can be seen that for both polarization components the computed patterns are almost identical within a span of 180°. The agreement with the reference patterns is quite satisfactory. For the E - plane field, the computed patterns show deep minimum at $\theta' = 90^\circ$ on both sides of the centre beam (i.e. near either end of the dipole antenna). Outside this range the discrepancies in both polarizations from the chosen reference values grow wider. The above computations were repeated for a reflector of the same height, but $0.5\,\lambda$ wide, with corner angle of 130°, with the dipole antenna positioned at $0.2\,\lambda$ from the corner edge. Here the number of current filaments used was 9 and 11, respectively, and once again comparisons are made for the two polarization components (H - and E - planes) in Figures 5.10 and 5.11. The general observations already made also apply here, and it can be seen that the slight increase in the number of current filaments causes the computed patterns to move towards the given references. Pattern measurements were carried out in this study for the $1.0\,\lambda$ -

by $-1.0\,\lambda$ structure using 17 filaments and continuous aluminum surfaces for the reflecting sides, as described in the previous chapter. However, because the dimensions of the reflector were too large to meet the far-zone condition (Equation (4.1)) with respect to the probe position in the anechoic chamber, differences in levels were found although the basic pattern features were very similar. Far better agreement between computed and measured patterns was obtained for the smaller reflector (but with the dipole antenna placed at $0.25\,\lambda$ from the corner) as discussed later in Section 5.3.4.

The third test, that of varying the segment distribution was used for the mast-supported and corner reflector antenna. The number of filaments modeling the surfaces was fixed, and the segmentation distribution was varied. In all the computations, however the resulting patterns were so similar to those shown in Figures 5.5, 5.6 and 5.7, and to those in Figures 5.8 to 5.11, that the actual results are not presented. The results were predictable because, beyond the basic requirement that a current segment length be kept within $0.1\,\lambda$, the fineness of the segmentation can strongly affect the accuracy of the segment current values, but the far field is not appreciably changed. Thus the influence of the number of current elements on radiation patterns as described in Chapter III has been found to depend more on the number of wire grids used to replace the current paths rather than on the fineness of segmentation. This is of course intuitively evident since a given continuous surface would be more closely approximated as the number of wires is increased.

5.2.3 Radiation Patterns of Radial Dipoles Mounted on Finite Length Cylinders

Patterns are presented here for radial dipoles with or without a parasitic element placed symmetrically and asymmetrically on finite cylinders. In Figures 5.12 to 5.15 are shown four principal-plane cut patterns for E_θ versus θ (in the $x-z$ plane), E_θ versus θ (in the $y-z$ plane), E_θ versus φ (in the $x-y$ plane), and E_φ versus φ ($x-y$ plane) due to a centrally-mounted radial dipole on a uniform cylinder $0.48\,\lambda$ long and with a circumference of $0.36\,\lambda$ (or diameter of $0.115\,\lambda$). As pointed out earlier, the dimensions were chosen to make comparisons possible with similar results computed by Goldhirsh and others [50] using the surface element technique. In the latter work, the two end faces of the cylinder have been included in the modeling scheme. However, it appears that the radial currents on these faces were neglected in the pattern computations since it is indicated that the axial currents on the ends of the cylinder were found to vanish. Thus since no radial currents were included in the present wire-grid model, the comparisons made here are valid. It is encouraging to note that the agreements are very close.

For the same cylinder length, but a diameter of 0.25λ, the computations were repeated, and the resulting patterns are shown in Figures 5.16 to 5.19. A pattern given by Wait [40] for a radial dipole mounted on an infinite cylinder but of the same diameter is also plotted in Figure 5.16. It can be seen that the agreement is quite good in the shadow region, but only fair in the front side for $\theta \leq 90^\circ$. Nevertheless in comparison with Figure 5.12 where the E_θ versus θ pattern is essentially similar to the basic pattern of an isolated dipole, the influence of the cylinder diameter is clearly indicated by both patterns shown in Figure 5.16 in that the maximum field strength is shifted below the $\theta = 90^\circ$ plane. The E_θ versus φ pattern (Figure 5.18), which is basically uniform as in Figure 5.14, appears to unaffected by the diameter of the cylinder. Similar observations can be made about the E_φ versus φ patterns in Figures 5.15 and 5.19.

Mounting two radial dipoles symmetrically on the above cylinder predictably differs from the single radial dipole patterns as illustrated in Figures 5.20 (E_θ versus θ, $x-z$ plane), 5.21 (E_θ versus θ, $y-z$ plane), and 5.22 (E_φ versus φ, $x-y$ plane) viz Figures 5.16, 5.17 and 5.19. As can be shown from symmetry considerations, the E_θ versus φ pattern in the $x-y$ plane vanishes, and this can also be seen from Figure 5.20 where once again a known pattern has been superimposed [40]. Since E_θ versus θ patterns in both the $x-z$ and $y-z$ planes are similar, it is obvious that there will be omnidirectionality in the horizontal (E_θ versus φ) pattern for planes other than $\theta = 90^\circ$. However the E_φ versus φ pattern given in Figure 5.22 does not differ in shape from the one given earlier for the single radial dipole (Figure 5.19).

The above series of patterns were calculated mainly as additional tests for the internal consistency of the wire-grid modeling method as applied in this study. As described previously, the relatively simple configuration just considered was modified by replacing one dipole by a parasitic stub, and also by moving the dipole and the stub to one end of the cylinder and lastly to the large end of a truncated cone. Three separate sets of patterns are presented in pairs to bring out the modeling features discussed in the computation of current distribution for the various structures illustrated in Figures 3.32 (c) to 3.32 (f). First patterns in four principal-plane cuts are compared in Figures 5.23 to 5.26 for the case of the radial dipole and the stub mounted in two different positions : one at the centre of the cylinder, and the other at the right end of the cylinder. Comparisons are made with previous patterns (Figures 5.16 to 5.19) given for the single dipole. Consider first the centrally mounted case; there are differences in the E_θ versus θ patterns (Figures 5.23 and 5.24 compared with Figures 5.16 and 5.17). It is interesting to observe on the other hand that the patterns in the horizontal planes (E_θ versus φ : Figure 5.25 viz Figure 5.18, E_φ versus φ : Figure 5.26 viz Figure 5.19) are very similar. Thus the presence of the parasitic stub affects mainly the vertical plane patterns. For the second antenna with parasitic element location, the E_θ versus θ pattern in the x - z plane (Figure 5.23) is still symmetrical, but is predictably asymmetrical in the y - z plane (Figure 5.24). Both horizontal patterns (E_θ versus φ in Figure 5.25, E_φ versus φ in Figure 5.26) though symmetrical about the axis of the cylinder are now radically changed. It is to be noted that the non-omnidirectionality of the E_θ versus φ pattern is expected from antenna geometry considerations.

The next group of patterns given in Figures 5.27 to 5.30 refer to two of the other antenna configurations illustrated in Figure 3.32. In this series, the situations considered consisted of the cylinder with additional current lines placed across its diameter at both ends, and the case of the radial dipole with stub mounted on the large end of the cone with additional current lines placed in line with the dipole across its diameter. While the patterns are fairly similar in Figures 5.27 (E_θ versus θ, x - z plane), and 5.29 (E_θ versus φ, x - y plane), the other patterns in Figures 5.28 and 5.30 are markedly different. As it will be seen later, the cylinder was actually found to be a closer approximation to the helicopter tail section than the cone. However, it is important to note that even though the cone surface represents a far more idealized model for this structure, its

E_θ horizontal pattern (Figure 5.29) still has the general characteristics exhibited by the corresponding pattern for the cylindrical surface.

Finally, in the third set of patterns, Figures 5.31 to 5.38, comparisons are made of the E_θ versus φ' and E_φ versus φ' patterns for the cylinder configuration just described, and the same cylinder with a parasitic current line parallel to the cylinder axis attached to the stub. The patterns are given for four θ - plane cuts : $\theta = 60^\circ, 70^\circ, 80^\circ$ and 90°. While the E_φ versus φ' patterns remain essentially the same, the E_θ versus φ' pattern approaches omnidirectionality as θ is gradually increased from the radial dipole side to the shadow region. The presence of the horizontal wire affects the patterns, but its influence appears also to be a function of θ. For example at $\theta = 70^\circ$ (Figure 5.33), there is a maximum difference between the two to polarizations of about 2 dB whereas at $\theta = 90^\circ$ Figure 5.37), the difference is less than .2 dB. The differences in the E_φ components appear to widen in the front region ($\varphi' \leq 90$, and $\varphi' \geq 270$) as θ is increased. However, the point of interest in the above series of patterns has been focused mainly on their basic features. It will be shown later how useful they were in predicting the radiation fields for the short monopole mounted on the approximated helicopter tail section.

5.3 Measured and Computed Patterns

In the preceding section, emphasis was placed on demonstrating the consistency and general applicability of the source representations and modeling procedures in terms of various antenna systems. Radiation patterns which confirm more directly the modeling procedures used in Chapter III will now be examined. The discussion is centred around the experimentally measured patterns for the antenna models described in Chapter IV in comparison with the computed patterns. Both the measured and computed results will be found to have a special contribution to make to the understanding of the wire-grid modeling method.

5.3.1 Testing of Chamber Characteristics

As in the computational part of this study, the monopole-sphere structure was useful also for the experimental testing of the anechoic chamber. Experimental polar plots of E_θ versus φ amplitude and phase are shown in Figure 5.39 and both are effectively omnidirectional. The phase pattern given above was useful in establishing the essentially uniform characteristics that are required of a free-space room. Next an E_θ versus θ amplitude pattern which was obtained with the battery-operated self-contained source inside the sphere is shown in Figure 5.40. Again, this result illustrates the degree of symmetry that could be attained to ensure the validity of the experimental patterns and the measurement methods as described in Chapter IV. The measurements were repeated for different probe angular positions, and the same degrees of symmetry and uniformity were noted.

5.3.2 Experimental Validation of the Wire-Grid Modeling Procedures Proposed in the Computational Study

Measured patterns for the disk-mounted monopole together with patterns for the same monopole mounted on 8, 12 and 16 radial wires, respectively, are shown in Figure 5.41. The wires were bonded on their periphery by circular rings. In Figure 5.42, similar patterns are illustrated but with the rings removed. The main question of interest is as to which wire-grid modeling procedure is 'correct'. If one of the models were to be based on the location of the stationary lines of flow on the continuous surface, then the presence of the outer ring is actually unnecessary. This is simply because the flow of circulatory currents on the edge of the continuous disk cannot be justified on physical grounds. That this observation is plausible is clearly illustrated by examining the two sets of patterns. In Figure 5.42, the pattern for the 16 radial wires (ring removed) practically coincides with that of the solid disk, and even the 12 and 8 radial wires appear also to be very close models. On the other hand, while its influence on the main beam is minimal, the presence of the ring changes noticeably the pattern in the minimum region. This is true not only for the case of the 8 radial wires which exhibits a deep minimum, but also in the case of the 16 radial wires. It is therefore felt that the above patterns can serve as a good experimental validation of the first important step in the wire-grid modeling procedure, namely : that the wire grids should only be placed along stationary lines of flow. The influence of increasing the number of wire grids is also predictable in that the pattern of the continuous disk is rapidly approached. By referring back to Figure 5.4, it can be noted that the improvement in the patterns for the three experimental radial wire models is interestingly faster than that for the computed patterns when the number is increased from 8 to 12 and then to 16. Thus while the modeling procedures are being validated, the accuracy of the computational results are tested also. For the monopole mounted on the radial wires, more weight is given to the experimental patterns. This is not necessarily so for the other structures as described later.

The sphere models (i.e., the 16, 24, 32 meridians, and the solid sphere) led again to pattern comparisons somewhat similar to the above ones. However, the most critical test for using stationary lines of flow as a basis for wire modeling in the present study was the case of the finite cylinder with a radial dipole mounted on its surface. A computed E_θ versus θ pattern (in the $x-z$ plane) is compared in Figure 5.43 with experimental patterns obtained for a continuous surface, and a wire-grid model consisting of axial and circumferential strips. For the three curves, the nulls and maximum points are indicated to be basically in the same positions. On the whole, close agreements can be seen, although a maximum difference of the order of 3 - 4 dB is noted in the front region. Still, the patterns as presented provide a strong experimental validation for the conclusion made earlier that as a working rule one should attempt to predict carefully the components of the surface current distribution on a given antenna configuration before applying the numerical procedure.

5.3.3 Influence of the Wire Radius Parameter

The patterns illustrated in Figures 5.44 and 5.45 are directly related to the current values given in Tables 3.3 (a) and 3.3 (b) earlier where an indication of the influence of the wire radius parameter on current computations was sought. In both cases, four patterns, three computed and one experimental, are compared for a short monopole mounted on 12 and 16 radial wires, respectively. The three computed patterns in each figure are denoted by A, B, and C and the experimental ones by D. Each pattern was computed with a current distribution obtained using a different value of wire radius in the impedance matrix equations of (2.80). The resulting patterns are seen to be affected by the value of wire radius employed for the three separate cases since they are all visibly different in the region $50^\circ \leq \theta \leq 145^\circ$. Thus the significance of the wire radius parameter which was only qualitatively established in the problem formulation part of Chapter III can now be discussed more specifically.

The important question is, how to determine the pattern which is closest to the experimental pattern, and thence to show which value of wire radius is most appropriate. A close examination of the two sets of patterns (i.e. both in Figures 5.46 and 5.47) is needed. Curves are shown for the following three radius values :

(i)	a	=	$0.00104\ \lambda$	(Pattern A)
(ii)	a	=	$0.00182\ \lambda$	(Pattern B)
(iii)	a	=	$0.00564\ \lambda$	(Pattern C)

The third value above corresponds to the physical wire dimension of the radials in the experimental models shown in Figure 4.5. Calculations were made for a fourth value, $a = 0.0078\ \lambda$; however, the resulting curve for this large radius is similar to curve C.

The three computed patterns in Figure 5.44 may be compared with the experimental pattern on the basis of the basic pattern features such as the main beams, nulls, minima, side lobes. It can be easily seen all are essentially of the same shape. However, Pattern A (i.e. the one for the thinnest wires) is clearly far removed from the experimental curve except for low values of θ. Thus the choice is to be made between curves B and C. On the main beam side, if the greatest discrepancies are considered, curve B is about 1.3 dB below D (at $\theta = 95^\circ$), whereas C is about 1.4 dB above D (at $\theta = 120^\circ$). Near the minimum and minor lobe regions B appears also to be closer to D than C. However, since the current distributions employed in the pattern computations are in any case approximate, a fair agreement between computed and measured patterns can only be achieved in the main beam region and at the nulls [58]. Based on this consideration, it is thus argued that pattern C is the closest to the experimental one. On the other hand, curve B shows better agreement in the side lobe region.

Similar observations can be made for the patterns given in Figure 5.45. Since the value of the wire radius appears to affect the results in the same manner as in the previous ones, this suggests that its influence is independent of the number of wires used in the grid, or possibly the shape of the antenna structure. As stated earlier in connection with the current computation schemes, the general conclusion drawn was therefore to take into consideration the actual physical wire sizes in computing current distributions on wire-grid structures. Clearly a mathematical technique, such as the least squares curve fitting method could have been used as a basis of comparison for the above curves. Such a statistical comparison however would not be necessarily as useful qualitatively as the one used above, which is based on basic antenna pattern features.

The above observations emphasize the question "how thin should the wires be ?" when a given continuous antenna surface is replaced by an equivalent wire-grid body. Or equivalently, can there be a certain 'correct' order of magnitude to be assigned to the wire radius value ? This question is fundamental to the whole wire-grid method of analysis of antenna systems. Moreover, since the results of this study have also demonstrated that thin strips are equally useful, possibly more useful than circular thin wires in wire modeling procedures, then the problem becomes even more complicated. In fact, the question posed above should be re-phrased to read : " what is the largest cross-sectional dimension that the wires (elliptical, circular, flat) should have in a grid model of an antenna structure ? " Although no direct answer has yet been provided, nevertheless the results suggest a need for further examination of this aspect of the wire-modeling procedure.

In closing, it should be pointed out that although the influence of the wire radius parameter has been demonstrated by the results of this study, it is still significant that a thin wire must be assumed for linear antennas. In the standard field formulations, the thinness is purposely introduced or assumed so as to justify the classical sinusoidal current distribution, or to simplify the solutions derived from Hallén's or Pocklington's integral equations. The results of the present study appear, however, to modify this assum- slightly in that the value of " a " in the fundamental integral equation given in (2.19) should not be arbitrarily chosen to be very small. Such a step might lead to the calculation of incorrect patterns. However, this does not mean that the use of finite wire radius values will automatically yield correct far fields since there might be other equally important factors (e.g. mathematical approximation, segmentation and modeling procedures) that would also have to be taken into consideration, as will be shown by some of the results discussed below.

5.3.4 Comparison of Computed and Measured Patterns

This section presents a broader comparison of computed and experimental results, using four antenna structures which differ widely in terms of electrical dimensions, location of sources, geometrical shape and complexity. Patterns for the sphere-mounted monopole are once again considered followed by an examination of the mast-mounted dipole, then the patterns for the corner reflector are presented and lastly, the elliptical polarization components (E_θ and E_φ) of the far fields for a monopole mounted on the helicopter tail section are discussed for a number of θ - plane cuts.

5.3.4 (a) Sphere-Mounted Monopole

Figures 5.46, 5.47 and 5.48 illustrate how the sphere radius affects the E_θ versus θ patterns for the $1/4\ \lambda$ monopole mounted on the 32-meridian sphere model. The agreement is good in terms of the main beams' side lobe, minima and nulls. It can be noted that as the radius is increased, the minimum region in the centre of the beam tends to move towards $\theta = 180^\circ$, and at the same time the main lobe moves towards the region $\theta > 90^\circ$. Thus in the limit of a large sphere radius, the case of a monopole mounted on an infinite disk would be approached.

5.3.4 (b) Mast-Mounted Dipole Antenna

For the dipole antennas mounted on the cylindrical masts with varying diameters and for different antenna positions, six groups of E_θ versus φ patterns are given in Figures 5.49 to 5.54. First experimental and numerical patterns are compared in Figure 5.49 with commercially available data [77]. The same basic pattern shapes including the locations of both major and secondary lobes are apparent in each curve although discrepancies are noted in the field strengths. Better agreements between computed and measured patterns are indicated in Figure 5.50 where two experimental curves (one for continuous surface and the other for a wire-grid model with six strips) are compared with a numerical result. Next, two computed patterns (one with six strips, and the other with eight strips) are compared in Figure 5.51. The influence of using an increased number of current paths in the computation scheme can be noted in the forward region. The remaining three groups of patterns provide further illustration for the validity of the computational models. There is, however, one noticeable aspect in the above patterns with the exception of those shown in Figure 5.50. It is that, although the pattern features are similar, nevertheless, the experimental and calculated radiation fields are shifted from each other by appreciable offsets which range from about 3 dB (Figures 5.49 and 5.54) to about 1.3 dB (Figure 5.53). This then suggests the need to either re-examine the accuracy of the wire-grid modeling procedure for this antenna structure, or the dependability of the experimental procedure. As discussed earlier in the problem formulation part of Chapter III, one would intuitively expect to find more current paths on the surface near the dipole antenna and fewer on the back side of the cylinder. However, to simplify the coordinate segmentation scheme, the current filaments were purposely placed at equal intervals around the periphery of each cylinder. Even then, the proposed wire-grid models have been shown to be equivalent to the continuous surfaces as demonstrated particularly by the patterns given in Figures 5.52 and 5.53. Thus the reason behind the offsets must lie elsewhere. Since the measured pattern is bodily shifted along the dipole axis with reference to the computed one the appropriate questions to ask are :

(i) where is the actual axis of symmetry ?

(ii) where is the phase centre ?

In the far field computations, these factors are not critical. However, in the experimental arrangement since at $\varphi = 0^{\circ}$ the antenna is nearer to the probe than the cylinder, and farthesr at $\varphi = 180^{\circ}$, the choice of the axis of rotation could conceivable have a bearing on the measured patterns. Nevertheless, the experimental patterns serve a useful purpose by providing an independent validity check for the computed patterns. They also establish more firmly the wire modeling procedure proposed in Chapter III where the number of axial strips used to model a given cylindrical mast was indicated to be dependent on its diameter.

5.3.4 (c) Measured and Computed Patterns for Corner Reflector Antenna

Computed patterns for typical finite corner reflectors have already been considered in Figures 5.8 to 5.11 in which published measured values were used for comparison. These are now supplemented by five additional ones shown in Figures 5.55 to 5.59 in which three H - plane and two E - plane patterns are included. In the latter patterns (Figures 5.57 and 5.59), the minor irregularities of the experimental pattern are due to the fact that the measurements were carried out by a point - by - point method. The agreement between the computed and measured patterns is better than 1 dB within the half-power region of the main beam, and the maximum discrepancy in the back lobe (see Figure 5.55) is about 3 dB. It is important to note that the corner angles indicated in these patterns and in the previous ones are not necessarily sub-multiples of 180°. The close agreement between the experimental and computed fields therefore demonstrates the fact that the wire-grid method of analysis can be applied to such relatively simple and finite antenna structures as the corner reflector that hitherto could be studied using either greatly simplified approximations (e.g. image theory methods) or complex mathematical formulations (e.g. geometric diffraction techniques).

5.3.4 (d) Measured and Computed Patterns for the Short Monopole Mounted on the Thin Wire Structure

The final series of patterns, presented in Figures 5.60 - 5.75, are for a short monopole mounted on the helicopter tail section. The first eight patterns (E_θ versus φ : Figures 5.60 to 5.63, and E versus φ : Figures 5.64 to 5.67) shown were obtained for the basic wire structure without the rotor blades. The principal - plane cuts considered are $\theta = 60^\circ$, 70°, 80°, and 90°. The remaining radiation fields demonstrate the influence of the rotor blades (mainly on the E_θ component) when they are placed parallel (as shown in Figure 4.6) or perpendicular with respect to the axis of the wire structure. For the latter patterns, the E_θ and E_φ components were obtained for $\theta = 80^\circ$ and 90°. Patterns were also measured for the structure covered with aluminum foil. The complete set of patterns is noteworthy for two reasons :

(i) Both polarization components (E_θ versus φ and E_ϕ versus φ were predicted by the patterns shown earlier (Figures 5.31 - 5.38) for the radial dipole mounted at one end of a finite cylinder.

(ii) Although the basic feature of the computed and measured patterns were found to be the same, still the differences, especially in the E_θ polarizations, are relatively large.

The first observation suggests the possibility that, right from the start, the arbitrary thin wire structure could actually have been replaced completely by the smooth continuous surface shown in Figure 3.32 (g) . This would have meant that instead of reading coordinate segmentation data from a drawing into the current or pattern computation programs, one could have used a simple segmentation subroutine as was done in the case of the other simpler antenna bodies. Thus many sources of error which were encountered in the study could have been partially eliminated. In fact, this alternative route is clearly validated by the patterns given in Figures 5.61, 5.62, and 5.63 where, in each case, two experimental patterns - one for the thin wire structure, and the other for the body covered with aluminum foil, are illustrated. The reason why this simplified approach was not followed was simply that it could not be predicted in advance. It became apparent only after the series of cylinders with the radial dipoles were successfully modeled, and also after the experimental patterns for the helicopter tail section were obtained.

On the other hand, the fact that the differences between the computed and measured patterns are seen to be relatively large (in some cases, greater than 6 dB as can be noted from Figures 5.68 and 5.72) strongly implies that either the measurements or the corresponding computations require more detailed re-consideration. The experimental patterns were repeated with considerable care and the same results were obtained. It can be concluded that the computed patterns suffer from over simplification of the computational model.

There were a number of factors which led to this conclusion. First and foremost, to keep the size of the structure impedance matrix within a tolerable core memory requirement (about 300 k), some wire segments had to be omitted in the current computation schemes. The elimination process, as indicated earlier, involved some guesswork. Because of computational costs, repeating such a procedure more than once by varying the locations of the omitted segments was restricted to very few runs. Thus this source of error was unavoidable.

A second source of error may be related to the coordinate segmentation data which had to be prepared from a drawing. However, in this case the errors introduced would be mainly of second order. The wire radius parameter is another possible factor. Although great care was taken to assign to the various current elements their physical wire radii, one gross assumption was made about the thick rod A - B in Figure 3.31 as being sufficiently thin, and thus the current flowing on its surface uniformly distributed around its circumference. This was suspected to be a questionable assumption, and since the rod is in the vicinity of the source and the monopole, a refinement in its modeling would have had a noticeable influence on the resulting approximate current distribution and hence on the computed pattern. A better modeling procedure would have been to split the rod into two or three thinner filaments. This technique was used in the case of the mast-mounted dipole and also was found to be useful in a similar study [84].

Finally, a major simplification which may contribute to the difference between the computed and experimental data is that of ignoring the problem of current element junctions. As briefly mentioned in the problem formulation part of Chapter III, this question was set aside and continues to form one of the limitations of the modeling technique as used here. The thin wire structure as seen from Figures 3.31 and 4.6, is inherently characterized by many junction points. However, because of computational complexities, the junctions were necessarily ignored.

After explaining why the above mentioned discrepancies may occur it should, however, be repeated that the agreement is fairly satisfactory in both the E_θ and E_φ components. For the E_φ patterns, all the nulls, minor and major lobes are substantially confirmed by the experimental patterns although there appear to be some angular shifts

(of the order of 15^{o}) in the location of the major lobes. It should also be emphasized that the two questions that were raised in discussing the patterns for the mast-mounted dipole (i.e. about axis of symmetry and location of centre of phase) are equally applicable to the present series of patterns. Thus between the two possible extremes, that is sources of error due to computational modeling on the one hand, and experimental validity on the other, it is concluded that the computed and measured patterns are sufficiently meaningful to confirm the validity of the computational procedures used. The application of the wire-grid modeling method to this complex structure, therefore demonstrates the utility of the method, and as described earlier in Chapter III and also in the following chapter, important guidelines to the effective use of the technique have been established.

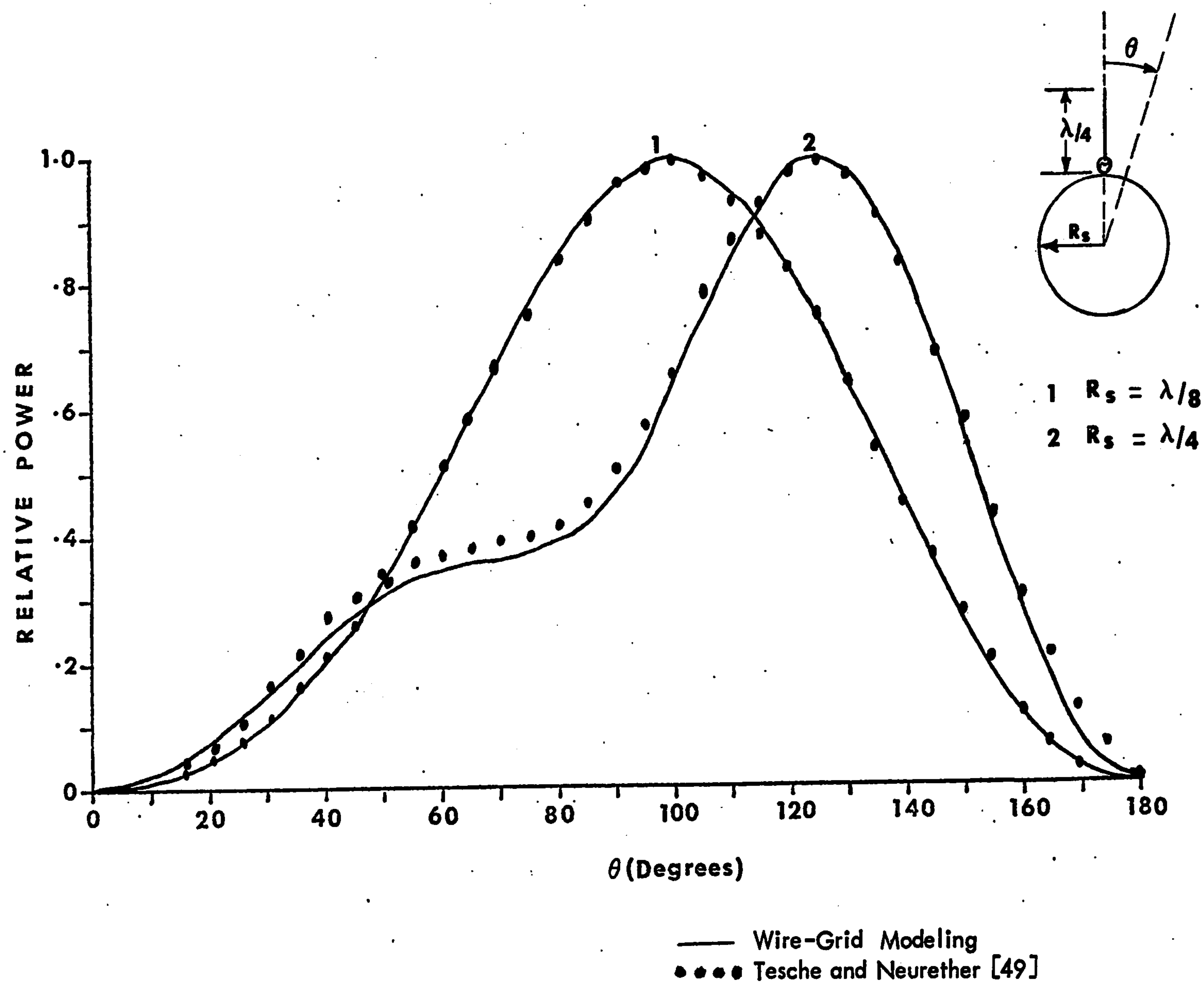

Figure 5.2. Computed Radiation Pattern for Sphere-mounted Monopole for Testing of Wire-Grid Modeling and Computation Scheme.

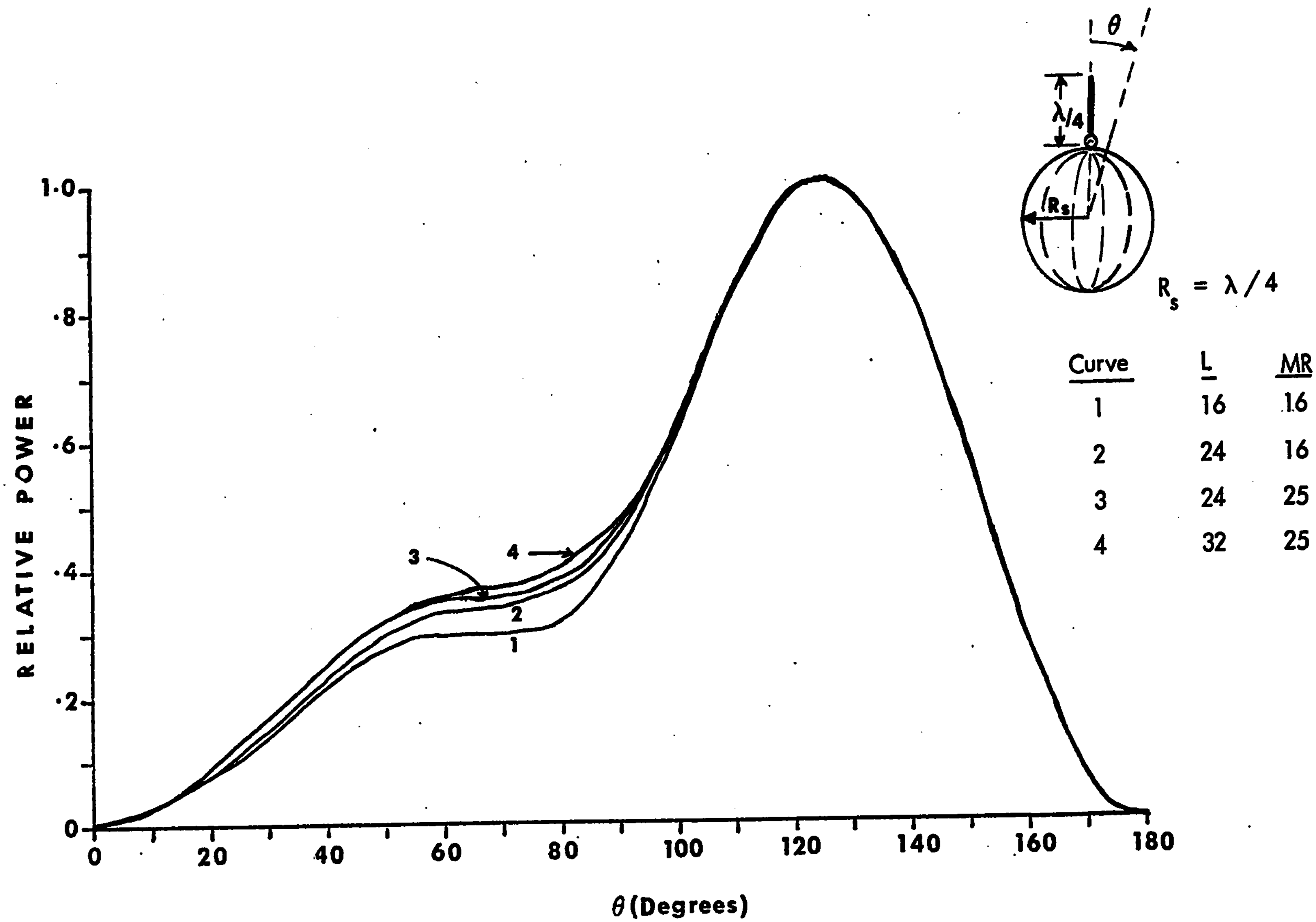

Figure 5.3. Sphere-mounted Monopole : Study of Influence of Fineness of Segmentation on Computed Pattern.
Note : L = Number of Meridians used for Wire-Modeling of Sphere.
MR = Number of Segments in each Meridian.

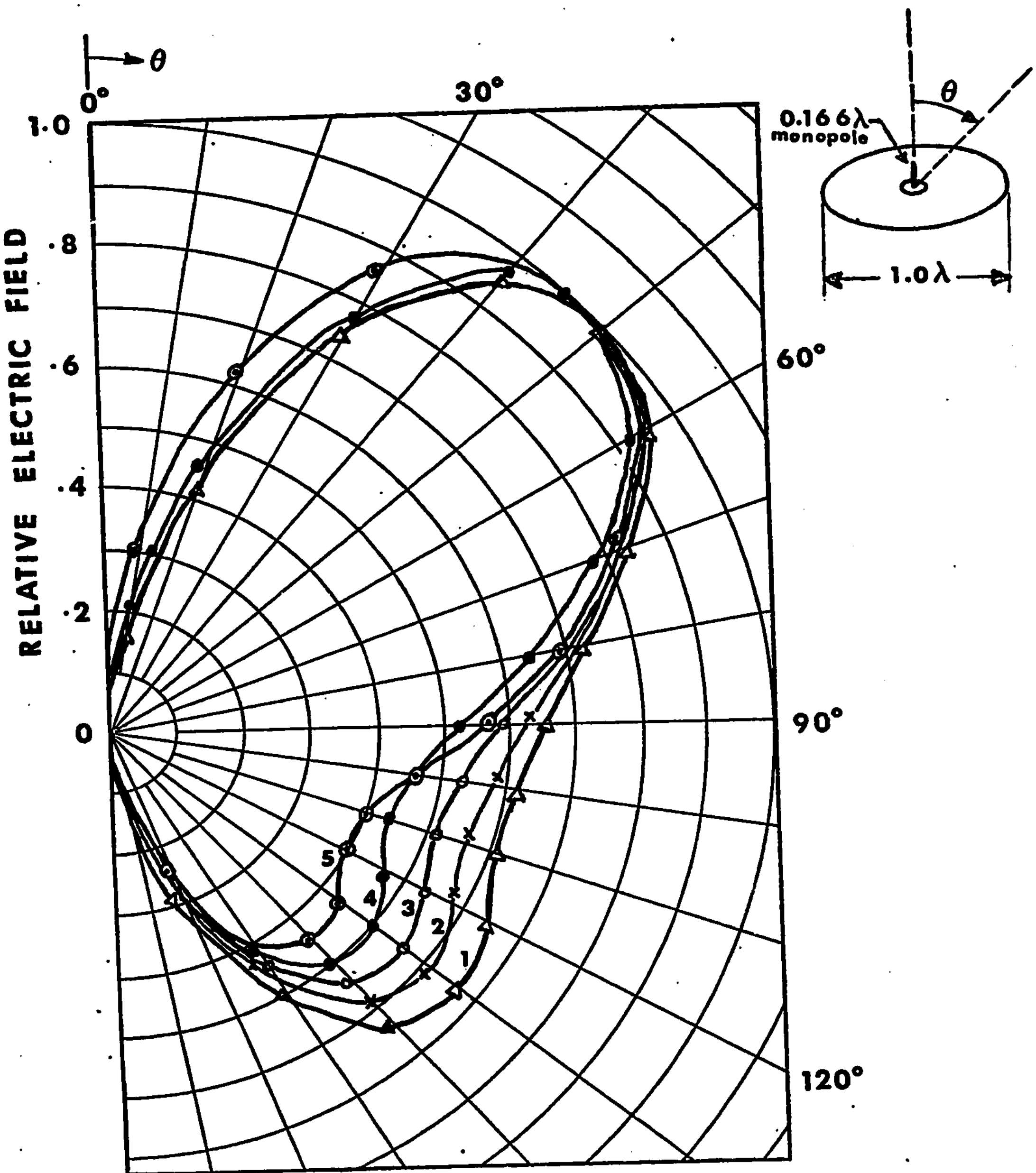

Curve		No. of Radial Wires
1	—△—△—	8
2	—×—×—	12
3	—o—o—	16
4	—•—•—	24
5	—⊙—⊙—	EXPERIMENTAL FOR CONTINUOUS DISK

Note : Curves 2 and 3 lie between Curves 1 and 4 in the $0^\circ \leq \theta \leq 50^\circ$ Region.

Figure 5.4. Computed Patterns E_θ vs θ for Short Monopole Mounted on different Number of Radial Ground Wires. Experimental Pattern also shown for Monopole Mounted on a Continuous Disk.

Figures 5.5. to 5.7. Computed E_θ vs φ (H - plane) Pattern (Relative Electric Field) for Dipole Antenna Mounted on the Side of a Cylinder Support.

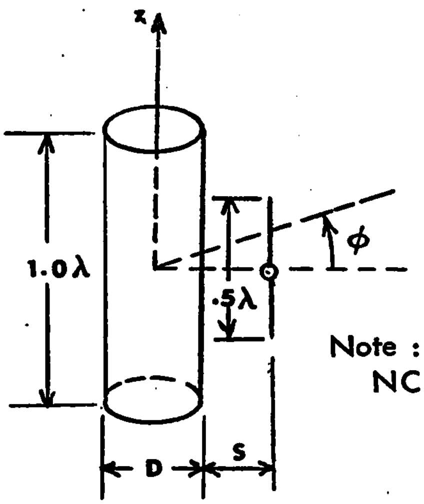

Note : Additional Parameter
NC = NO. OF WIRES USED IN WIRE-GRID MODELING OF CYLINDER.

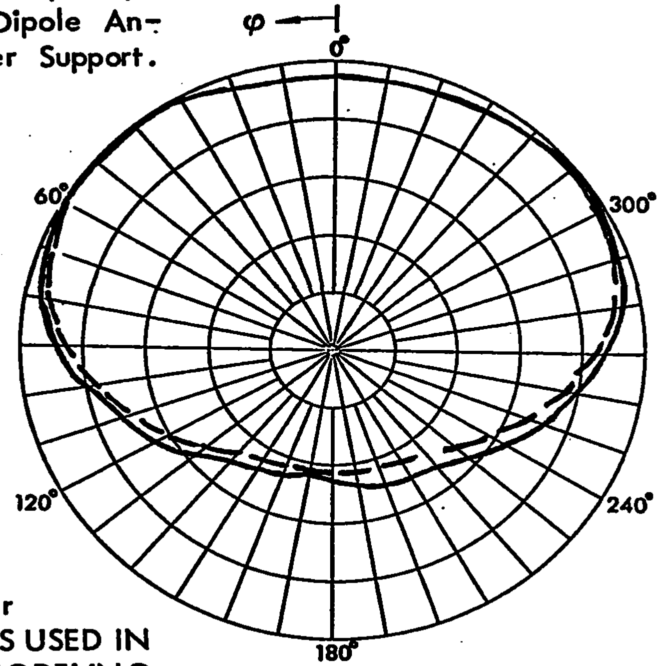

——— NC = 4
– – – NC = 6

Figure 5.5. D = λ/8, S = λ/4.

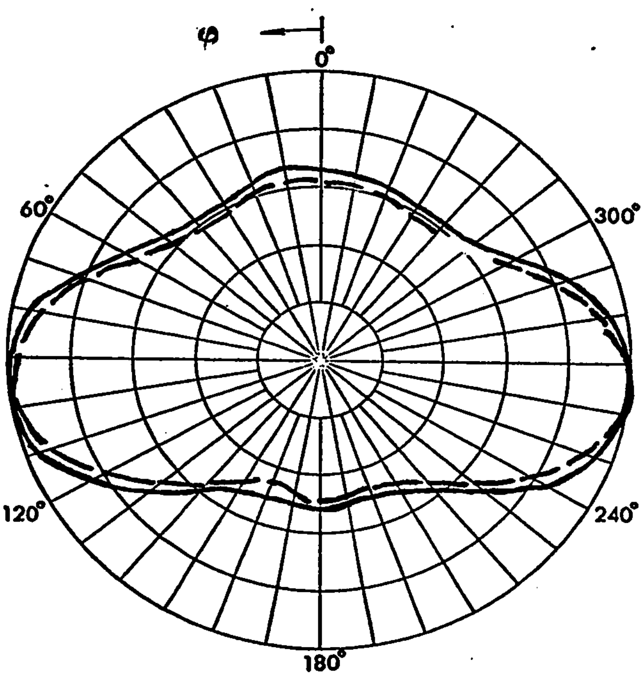

– – – NC = 6
——— NC = 8

Figure 5.6. D = λ/4, S = λ/2 .

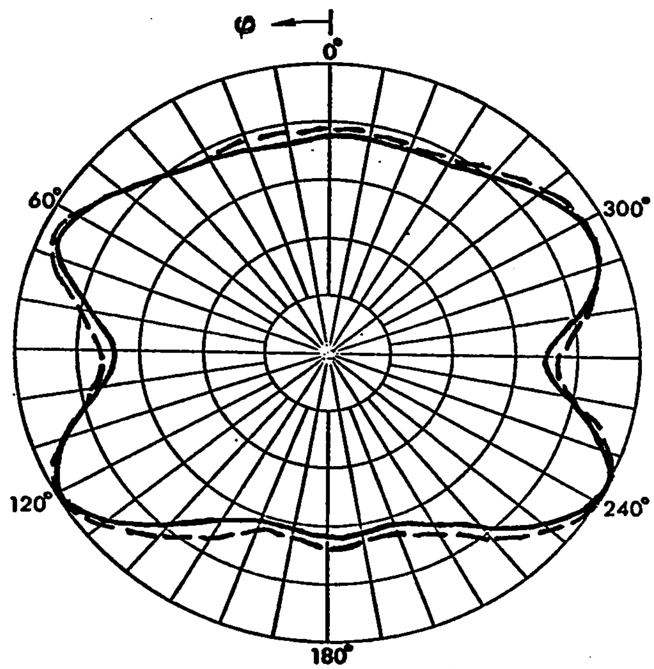

——— NC = 6
– – – NC = 8

Figure 5.7. D = λ/2, S = λ .

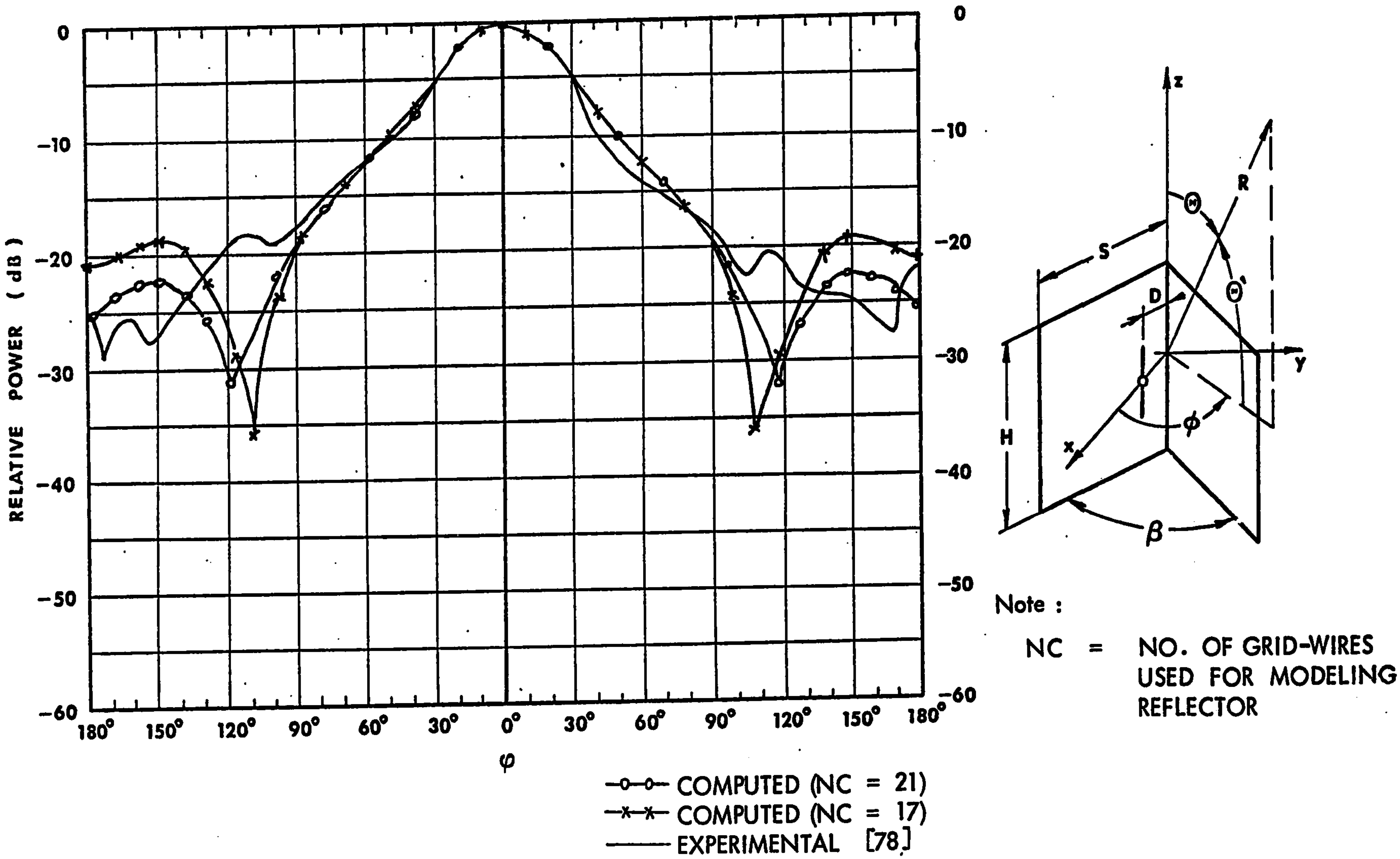

Figure 5.8. E_θ vs φ (H - plane) for Corner Reflector with H = S = 1.0 λ, β' = 110°, D = 0.25 λ.

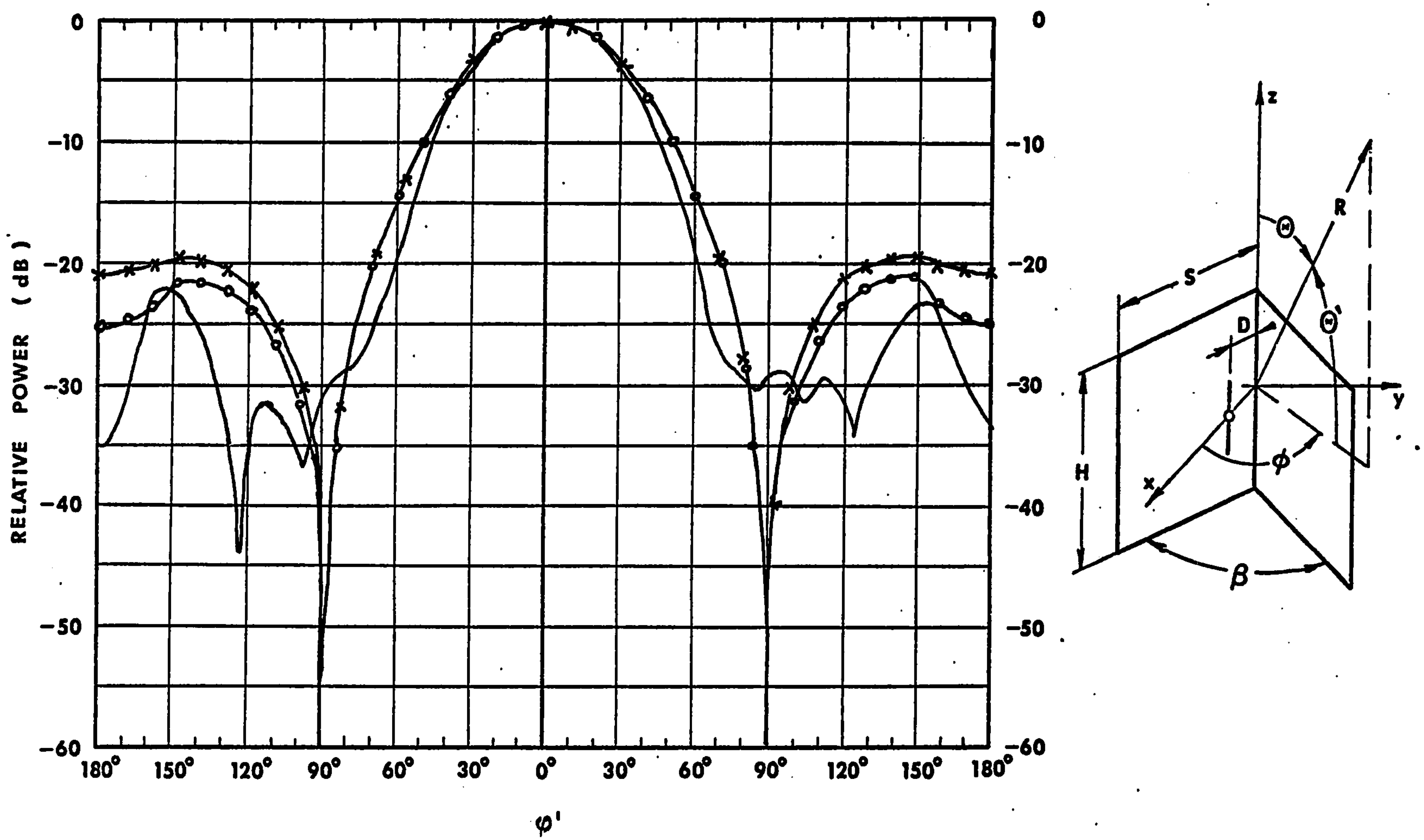

Figure 5.9. E_{θ} vs θ' (E-plane) for Corner Reflector with $H = S = 1.0\,\lambda$, $\beta' = 110^{\circ}$, $D = 0.25\,\lambda$.

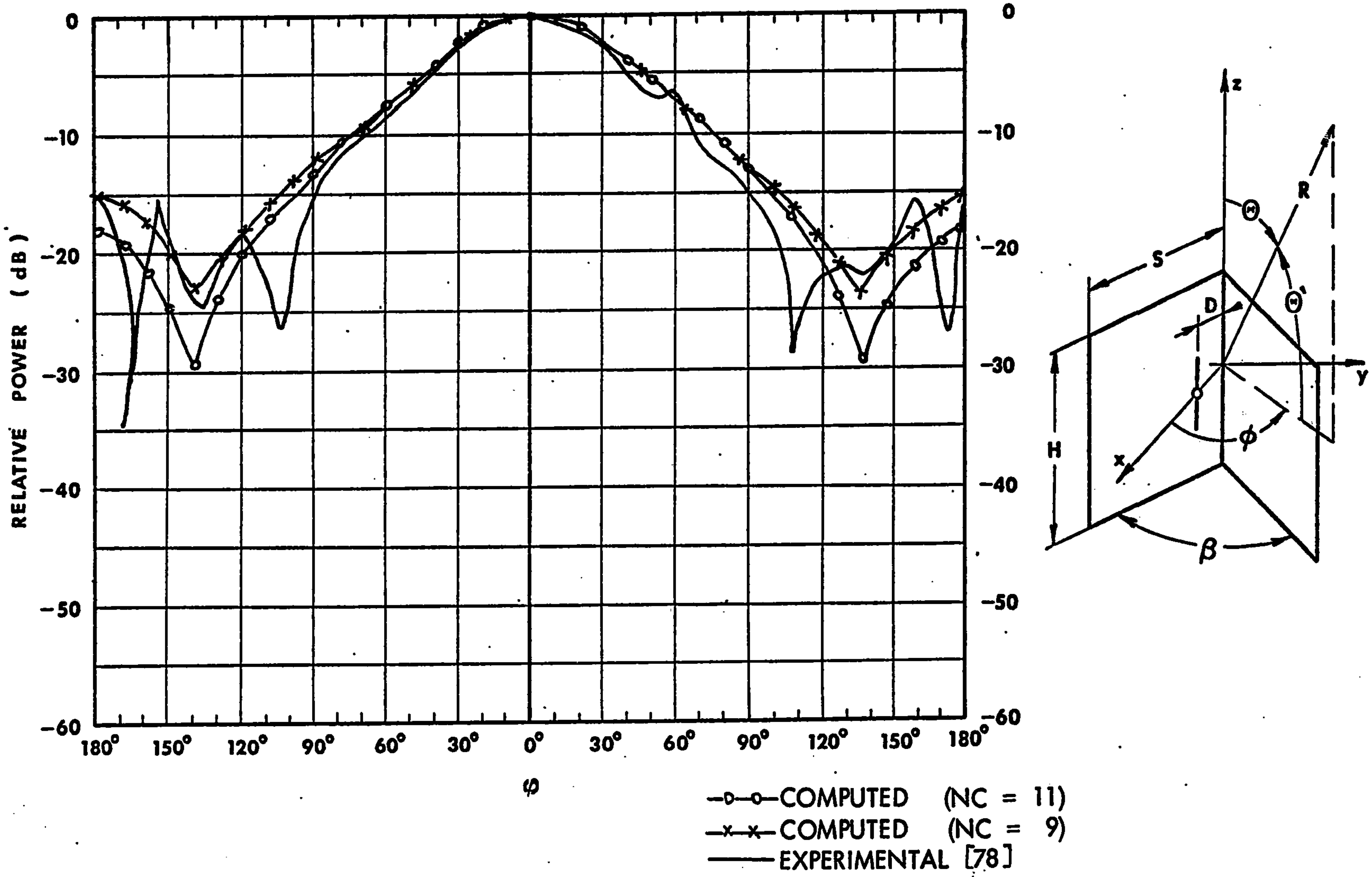

Figure 5.10. E_θ vs φ for Corner Reflector Antenna with $H = 1.0\,\lambda$, $S = 0.5\,\lambda$, $\beta' = 130^\circ$, $D = 0.2\lambda$.

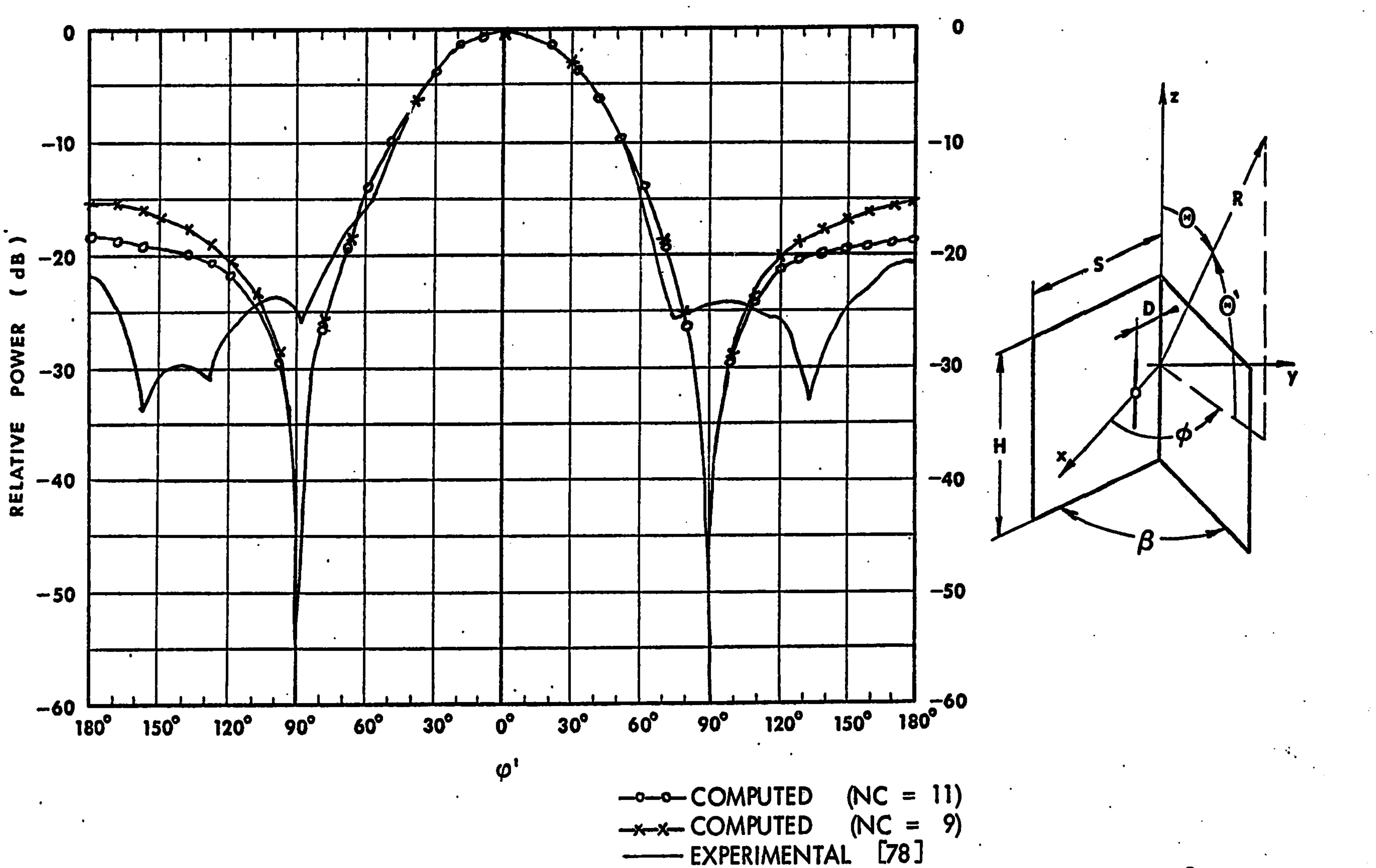

Figure 5.11 E_θ vs θ' (E-plane) for Corner Reflector Antenna with $H = 1.0\,\lambda$, $S = 0.5\,\lambda$, $\beta' = 130°$ and $D = 0.2\lambda$.

Figures 5.12 to 5.19: Computed Patterns for Radial Dipole Mounted on Finite Cylinders.

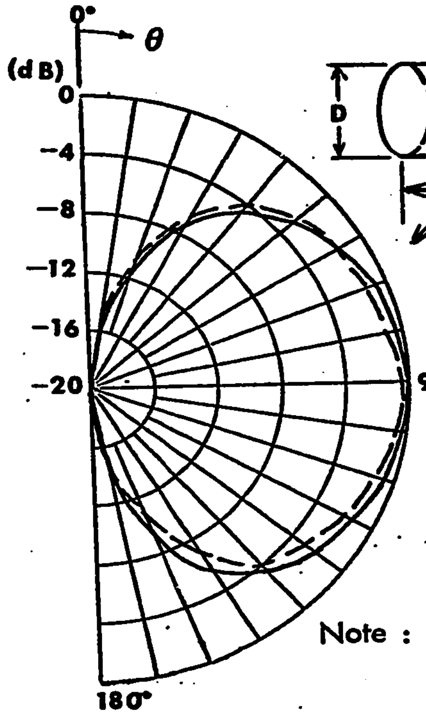

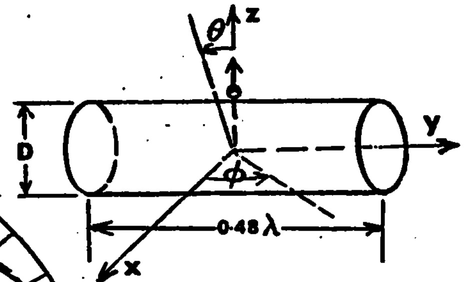

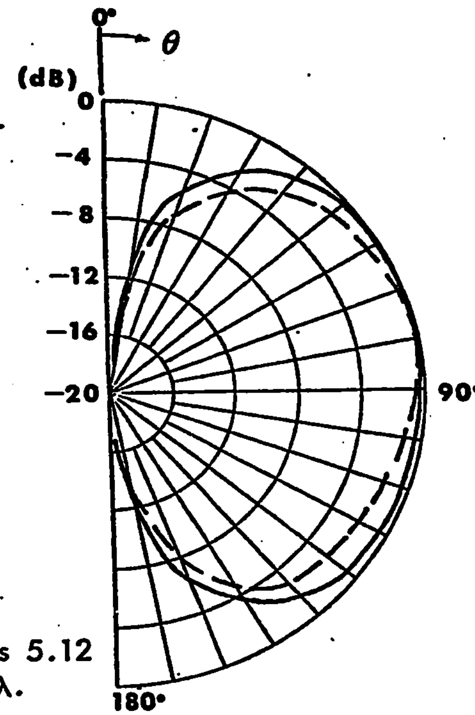

Note : For Patterns in Figures 5.12 to 5.15, D = 0.115 λ.

Figure 5.12. E_θ vs θ, x − z plane.

Figure 5.13. E_θ vs θ, y − z plane.

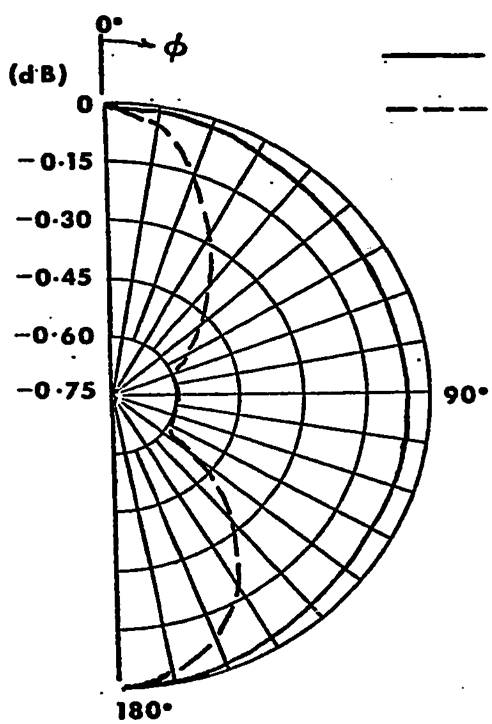

——— WIRE-GRID MODELING

– – – SURFACE ELEMENT METHOD [50]

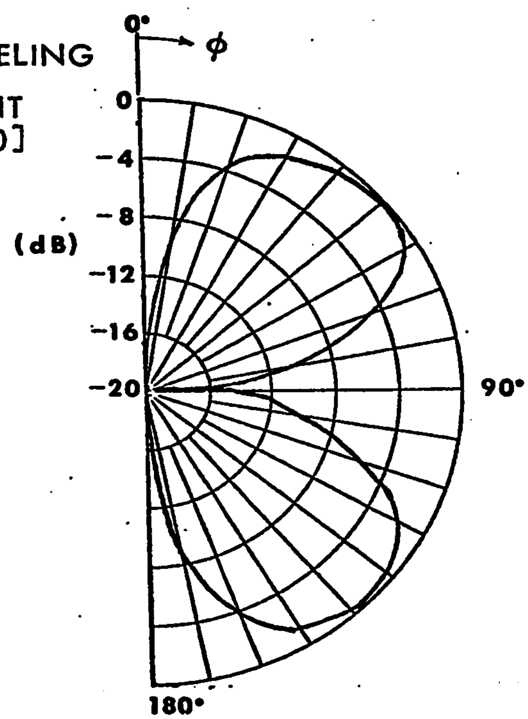

Figure 5.14. E_θ vs φ, x − y plane.

Figure 5.15. E_φ vs φ, x − y plane.

Note : For Patterns (Relative Electric Field) shown in Figures 5.16 to 5.19, D = 0.25 λ .

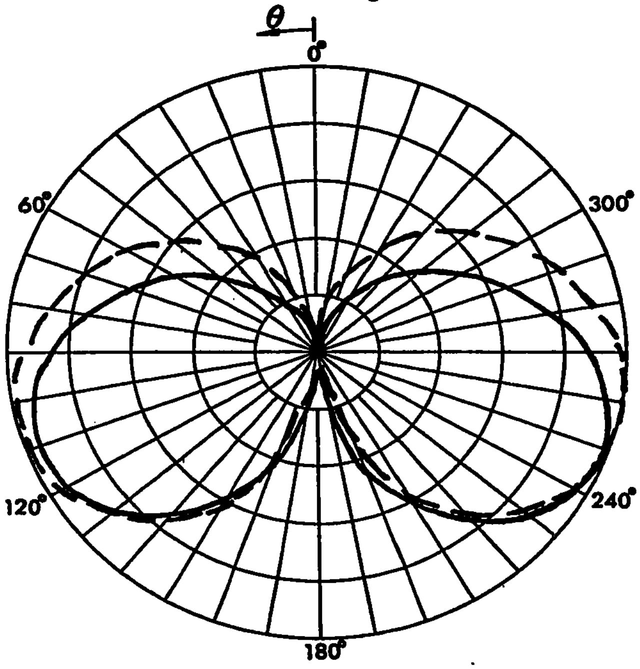

Figure 5.16. E_θ vs θ, x - z plane.

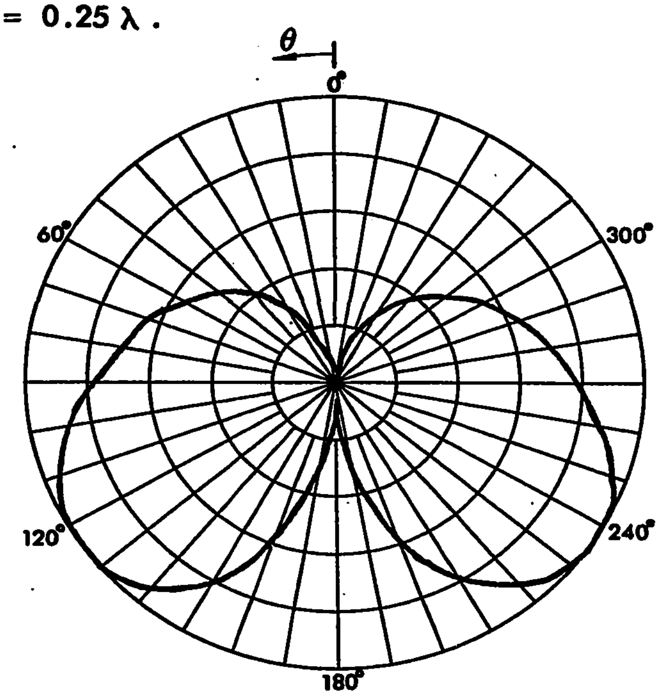

Figure 5.17. E_θ vs θ, y - z plane.

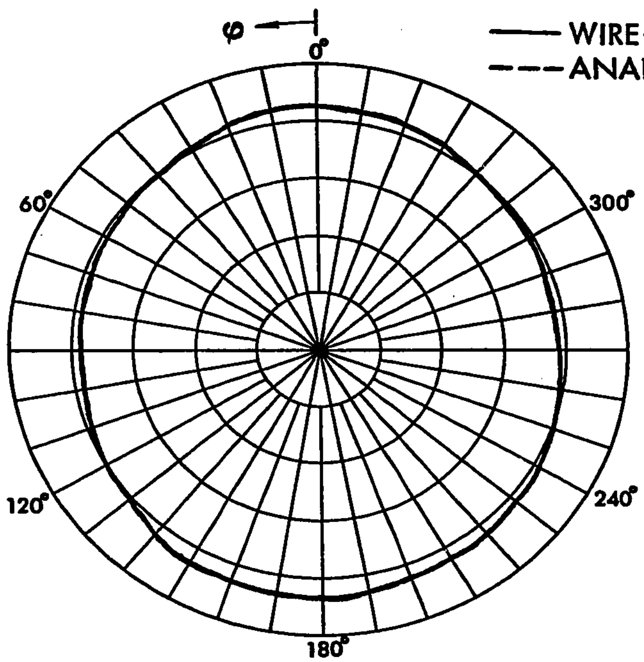

Figure 5.18. E_θ vs φ , x - y plane.

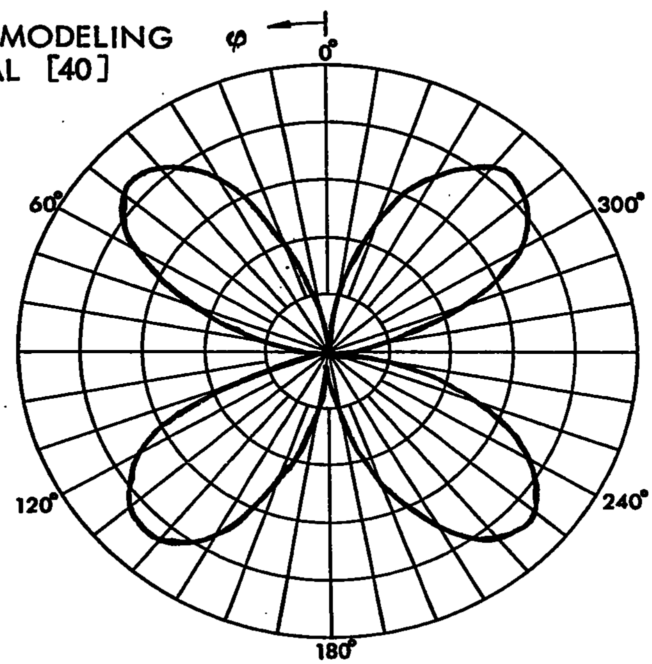

Figure 5.19. E_φ vs φ , x - y plane.

Figure 5.20 to 5.22 : Computed Radiation Patterns (Relative Electric Field for Two Radial Dipoles Symmetrically mounted on a Finite Cylinder.

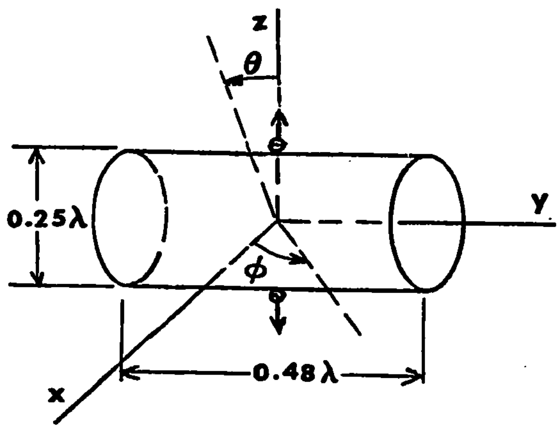

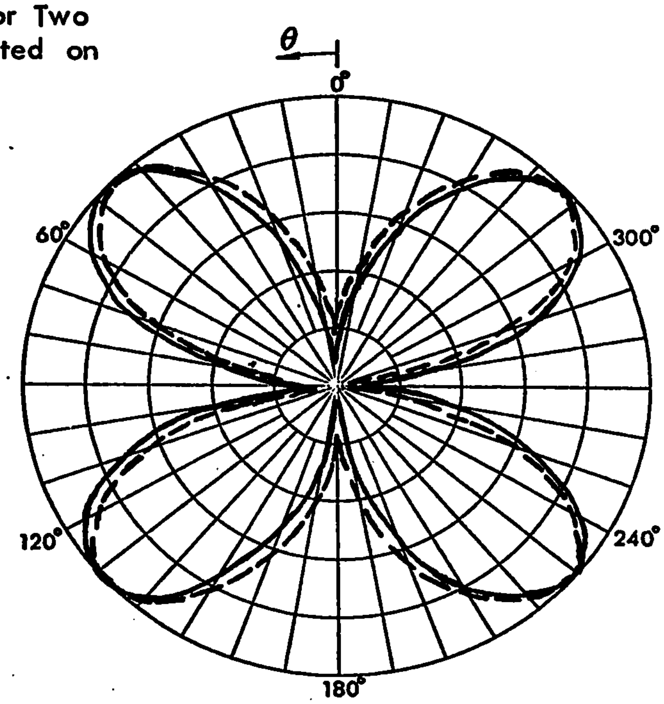

—— COMPUTED

---ANALYTICAL [40]

Figure 5.20. E_θ vs θ, x - z plane.

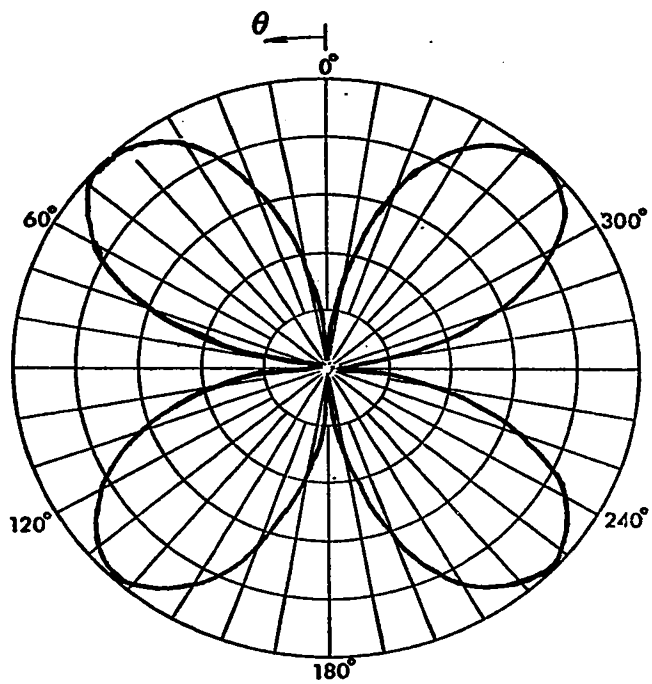

Figure 5.21. E_θ vs θ, y - z plane.

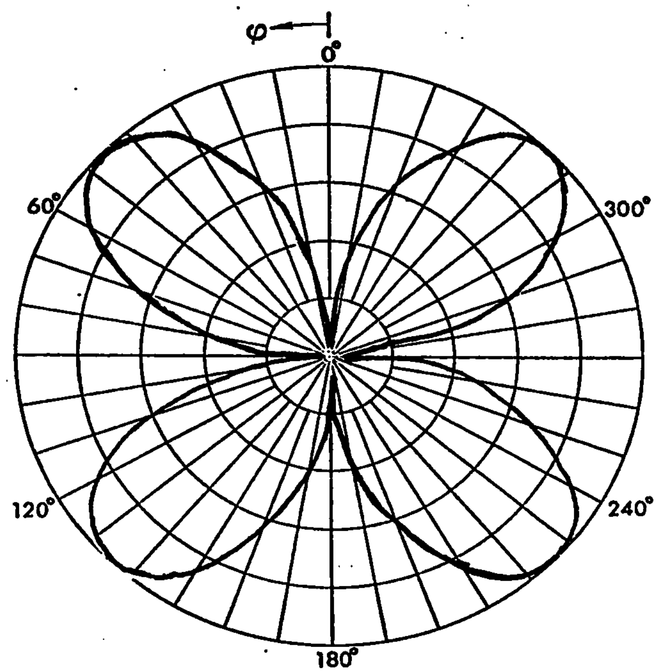

Figure 5.22. E_φ vs φ, x - y plane.

Figure 5.23 to 5.26. Comparison of Computed Patterns for a Radial Dipole and a Radial Parasitic Element mounted on Finite Cylinder as shown in Figures 3.32 (c) and 3.32 (d), respectively.

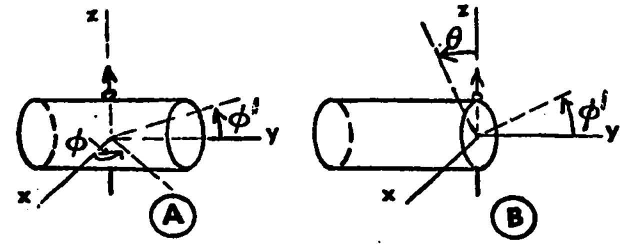

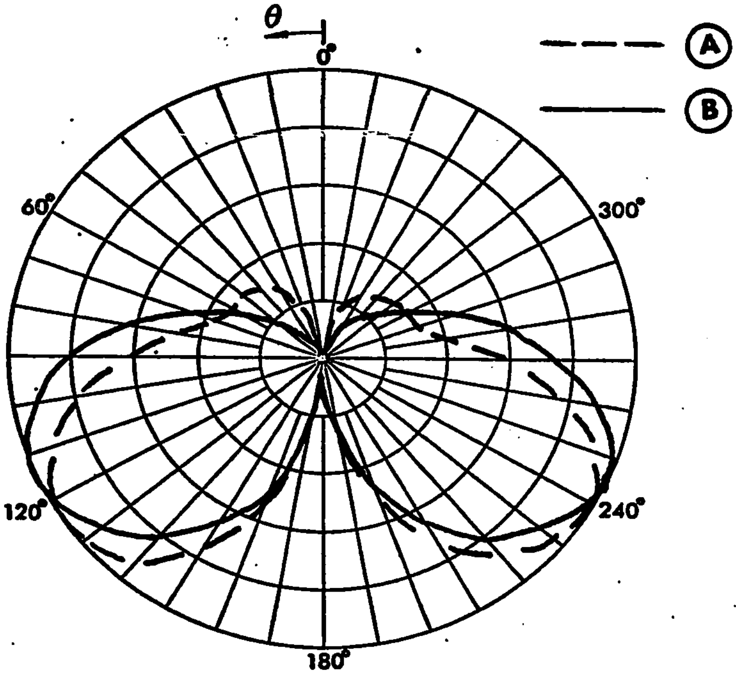

Figure 5.23. E_θ vs θ, x - z plane.

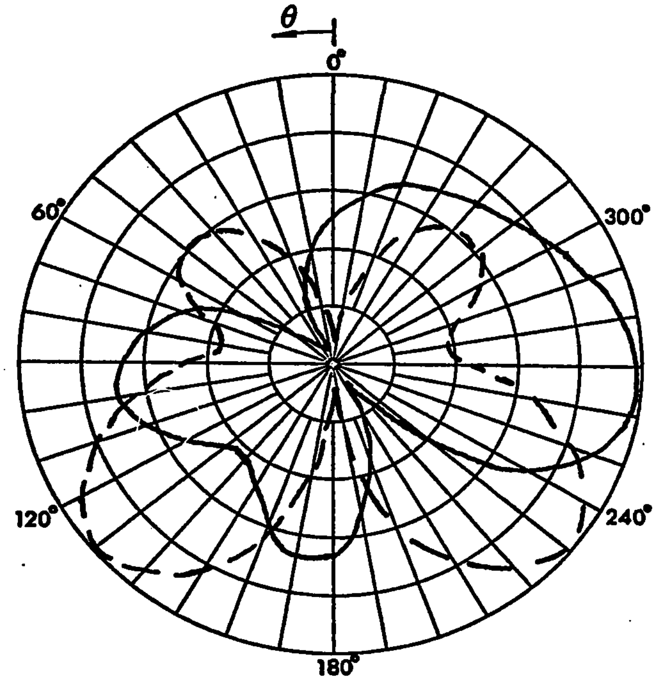

Figure 5.24. E_θ vs θ, y - z plane.

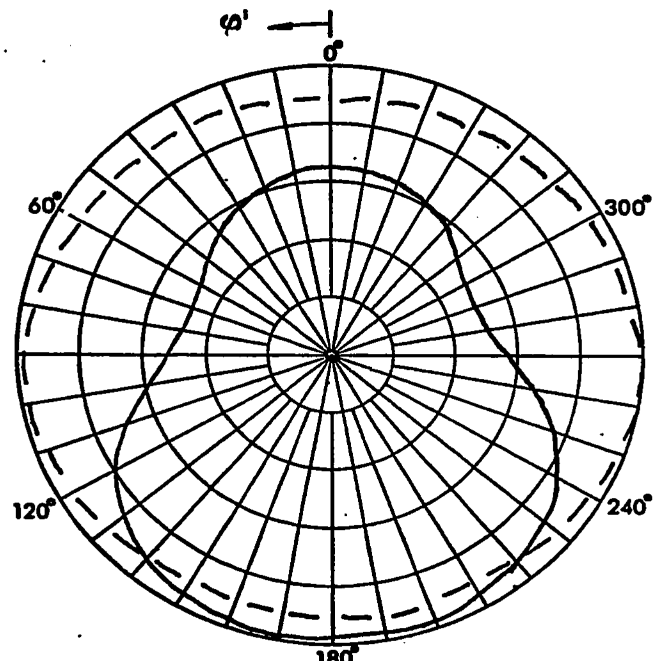

Figure 5.25. E_θ vs φ', x - y plane.

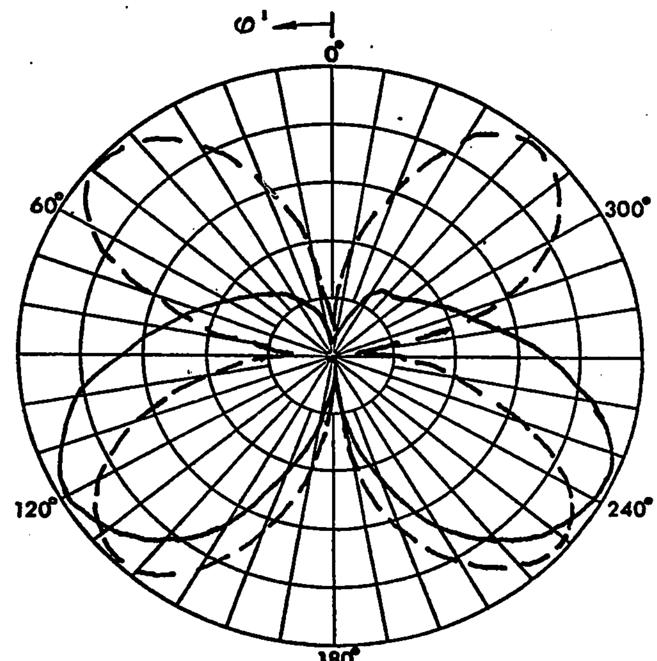

Figure 5.25. E_φ vs φ', x - y plane.

Note : φ' = 0 corresponds to axis of Cylinder (or to φ = 90°) .

Figures 5.27 to 5.30. Comparison of Computed Patterns for Antenna Structures shown in Figures 3.32 (e) and 3.32 (f).

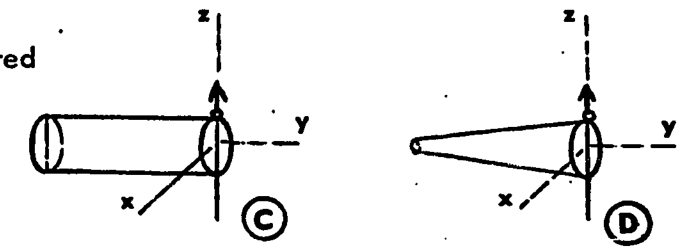

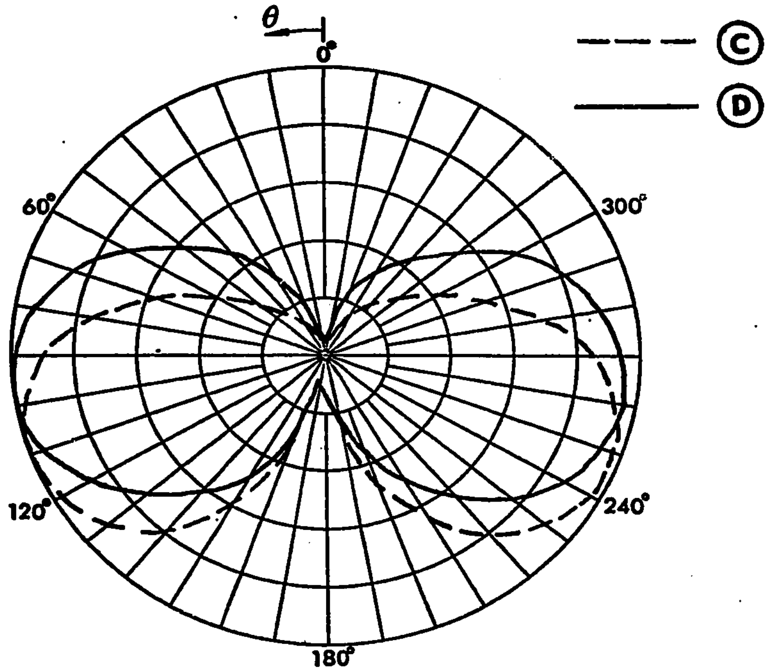

Figure 5.27. E_θ vs θ, x – z plane.

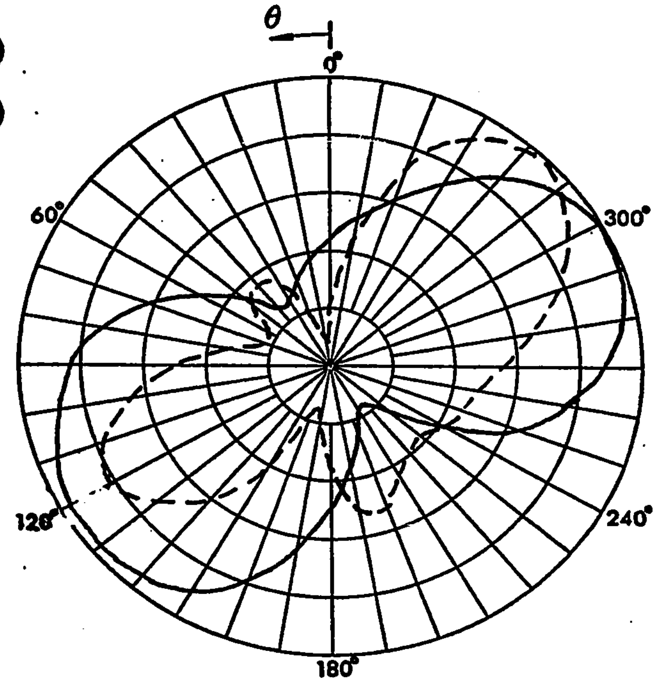

Figure 5.28. E_θ vs θ, y – z plane.

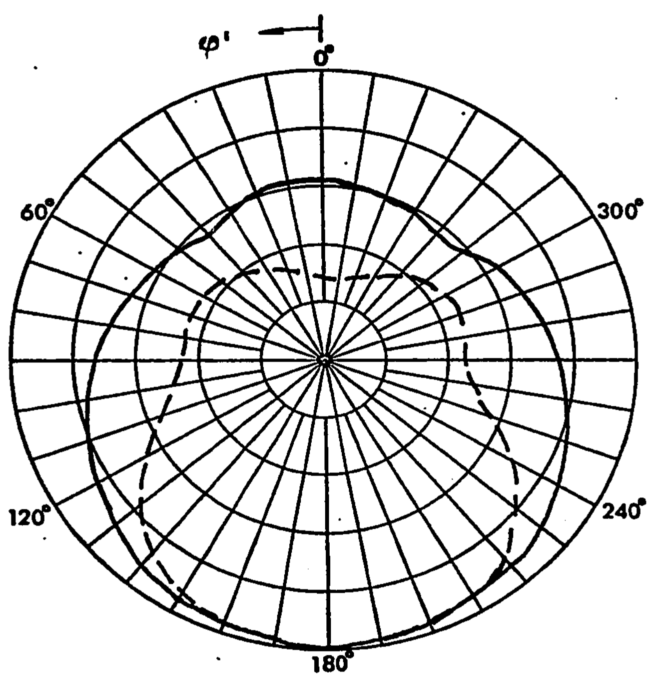

Figure 5.29. E_θ vs φ' , x – y plane.

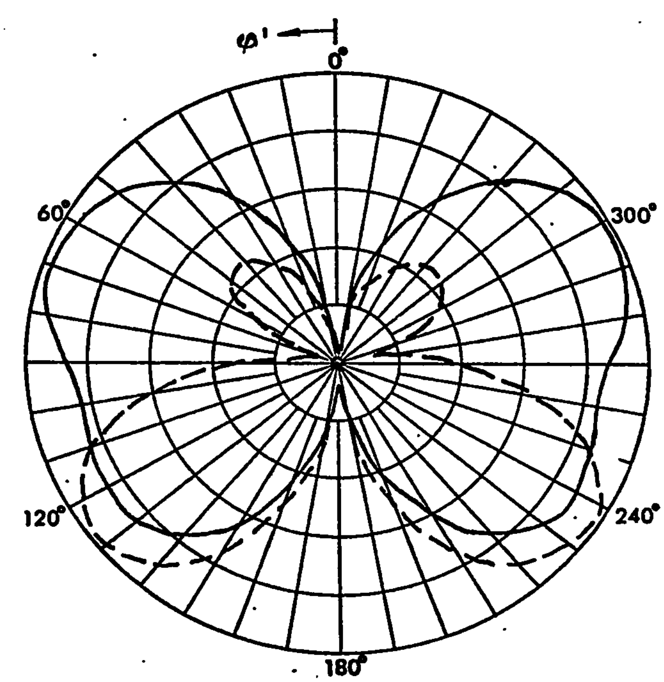

Figure 5.30. E_φ vs φ', x – y plane.

Note : $\varphi' = 0$ corresponds to axis of Cylinder or Cone (or to $\varphi = 90°$).

Figures 5.31 to 5.38. Comparisons of computed Patterns (at Different θ – plane Cuts) for Antenna Structures shown in Figures 3.32 (e) and 3.38 .

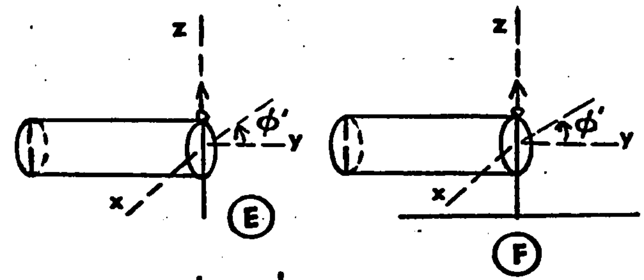

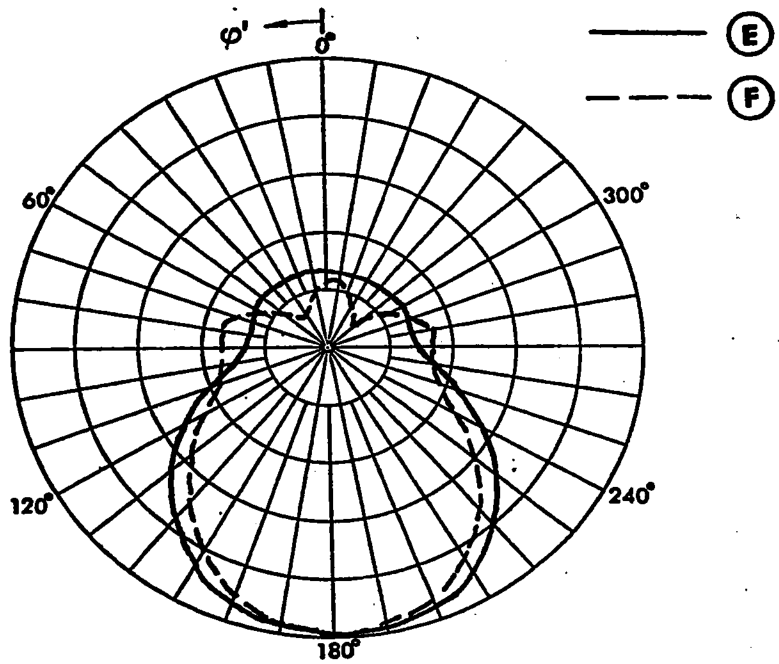

Figure 5.31. E_θ vs φ' , $\theta = 60^\circ$

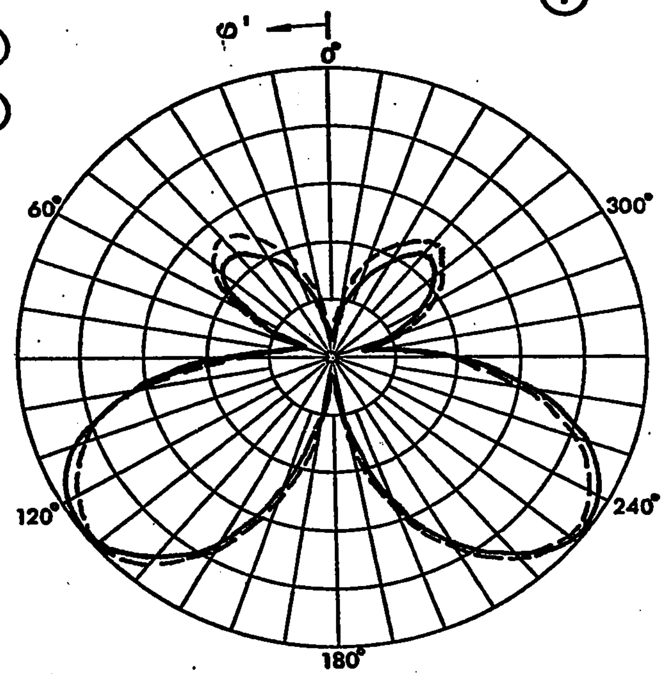

Figure 5.32. E_φ vs φ', $\theta = 60^\circ$.

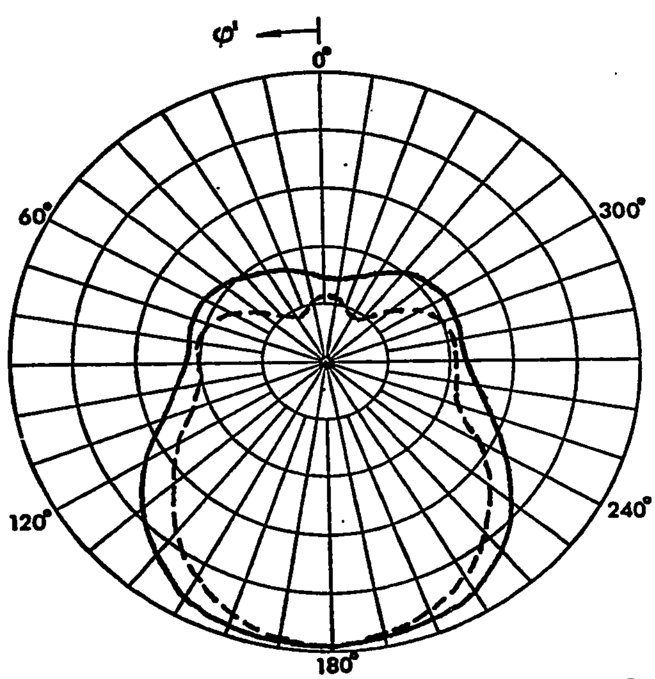

Figure 5.33. E_θ vs φ' , $\theta = 70^\circ$.

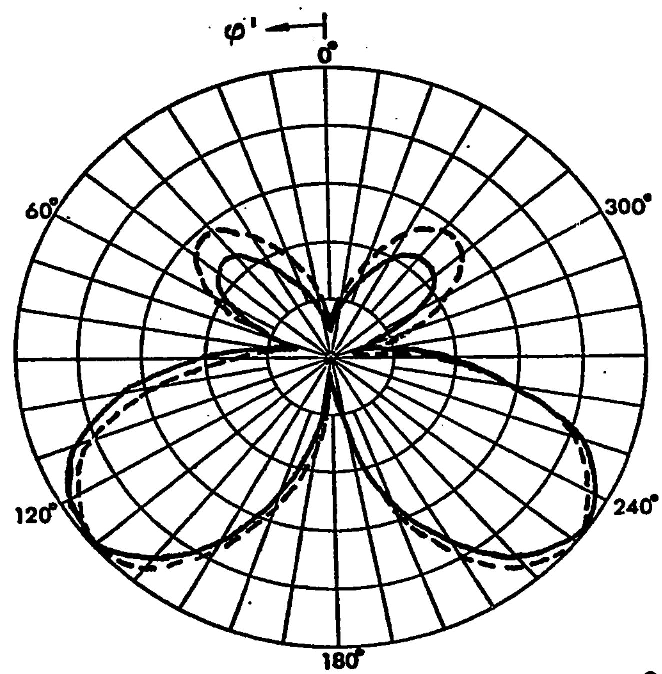

Figure 5.34. E_φ vs φ' , $\theta = 70^\circ$.

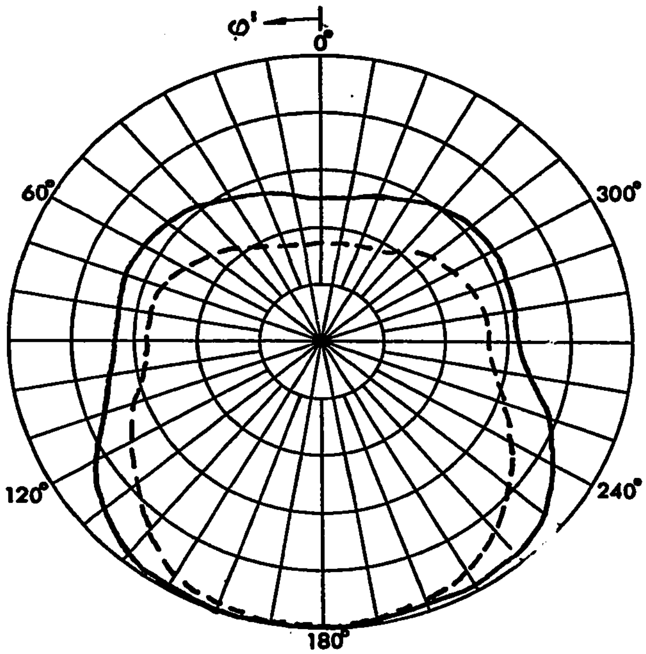

Figure 5.35. E_θ vs φ', $\theta = 80°$.

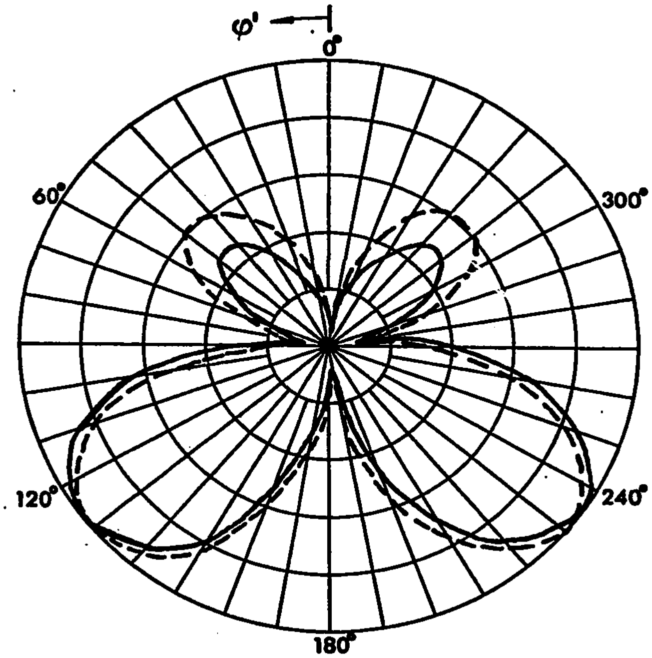

Figure 5.36. E_φ vs φ', $\theta = 80°$.

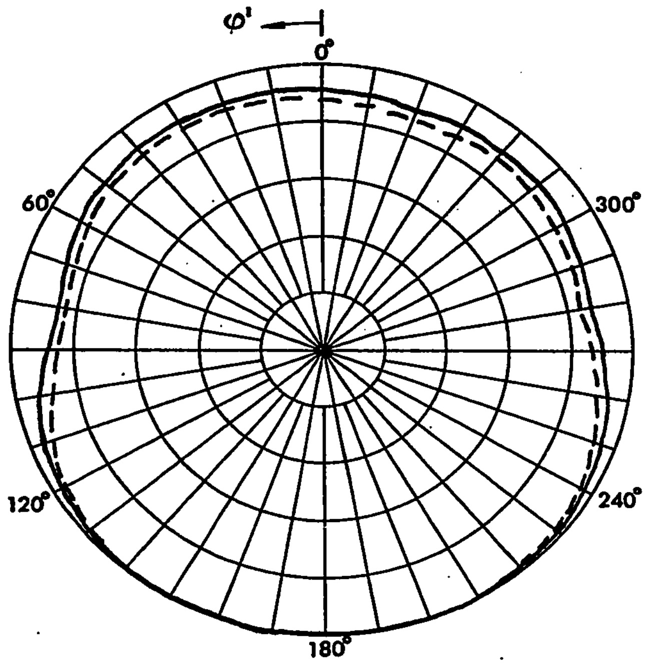

Figure 5.37. E_θ vs φ', $\theta = 90°$.

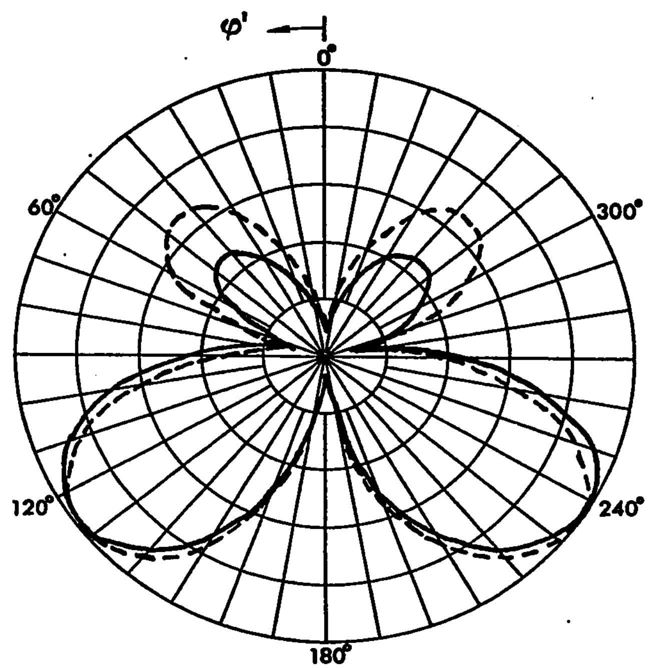

Figure 5.38. E_φ vs φ', $\theta = 90°$.

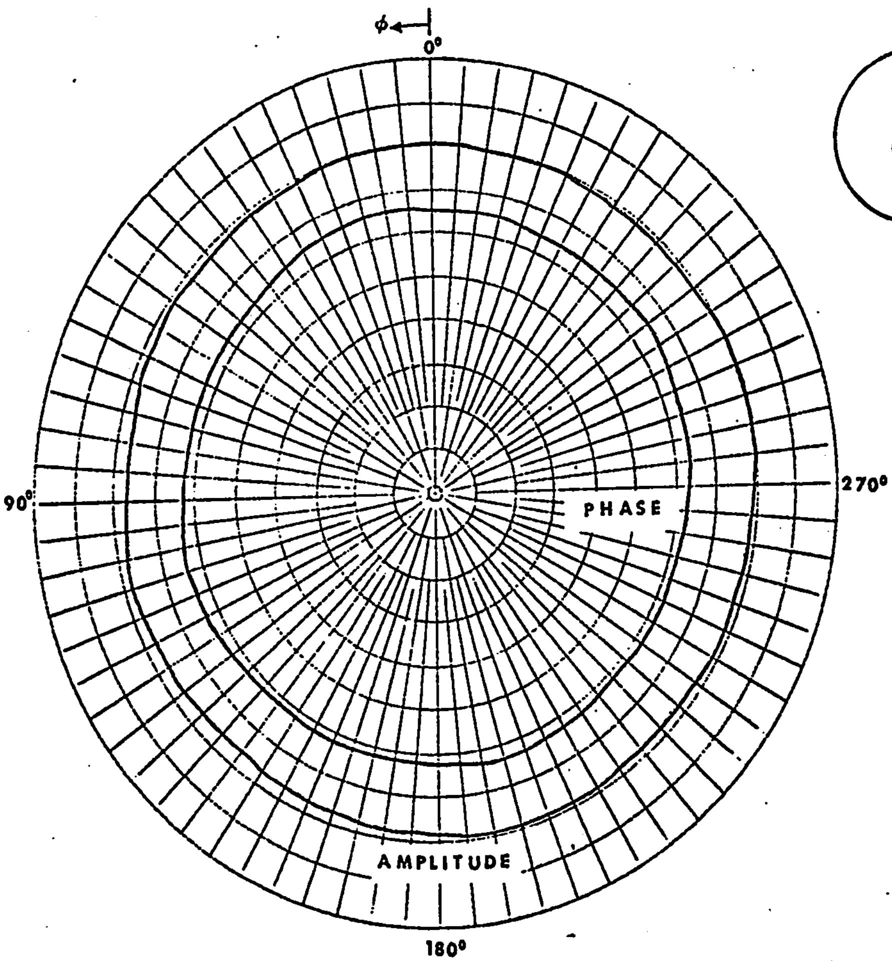

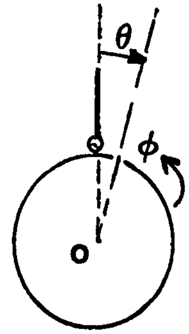

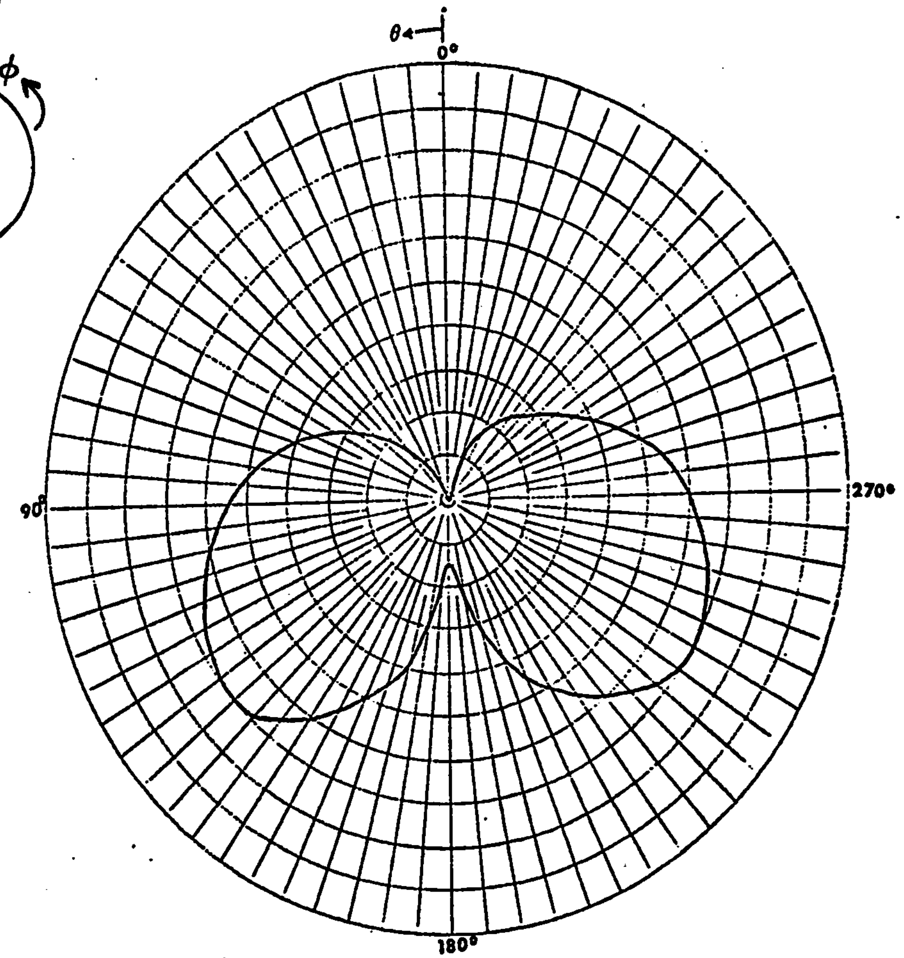

Figure 5.39. Testing of Anechoic Chamber Performance : Measured E_θ vs φ Amplitude and Phase Patterns for Sphere.mounted Monopole. (External source used to Energize the Monopole).

Figure 5.40. Testing of Anechoic Chamber : Measured E_θ vs θ Pattern (Amplitude) for Sphere-mounted Monopole. (Battery-operated source used to energize the Monopole).

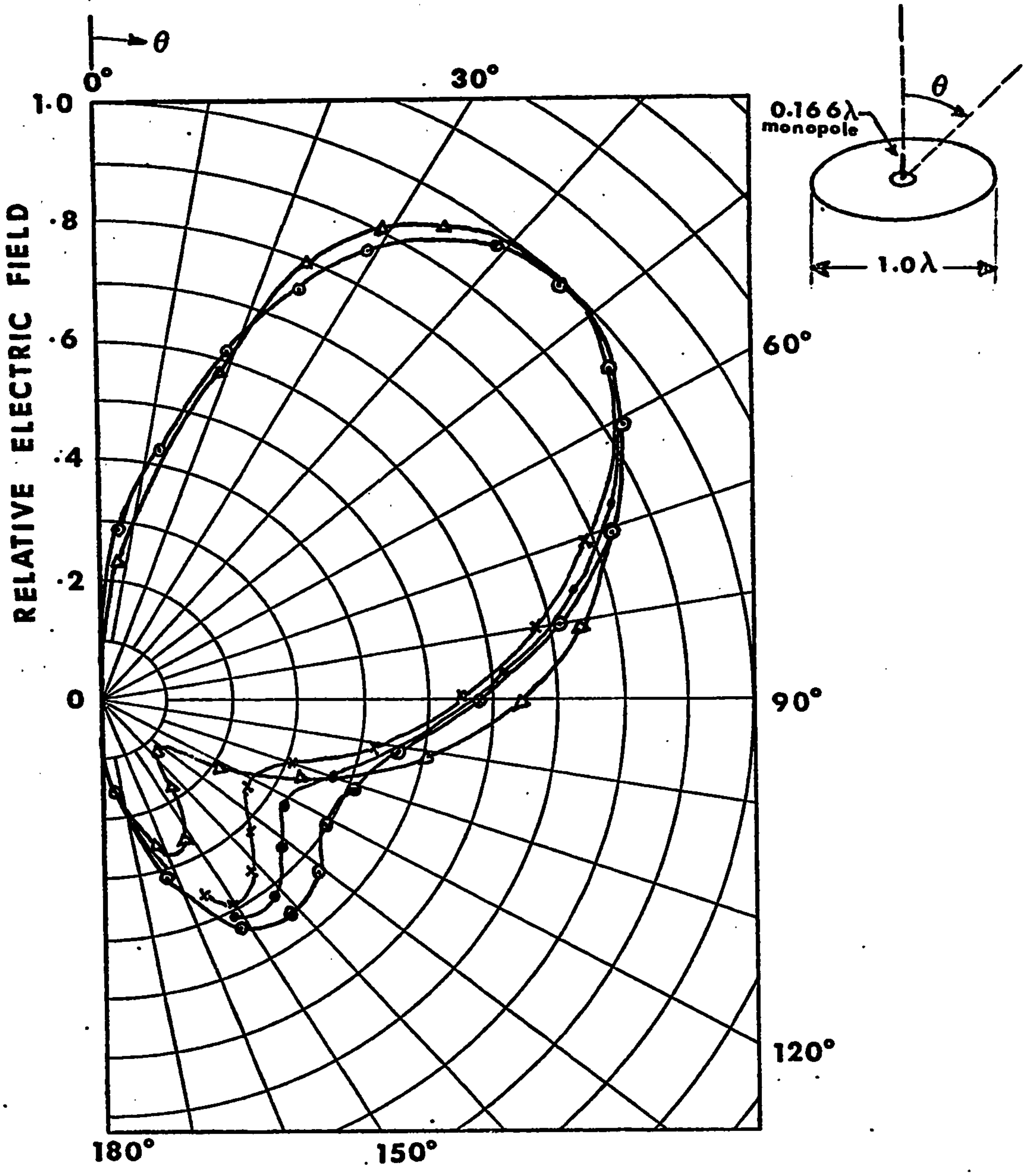

Curve	No. of Radial Wires
—△—△—	8
× × ×	12
• • •	16
—⊙—⊙—	CONTINUOUS DISK (EXPT.)

Figure 5.41. E_θ vs θ Measured Patterns for Short Monopole Mounted on Different Radial Wires Bonded by Thin Wire Rings. Pattern for Continuous Disk also included.

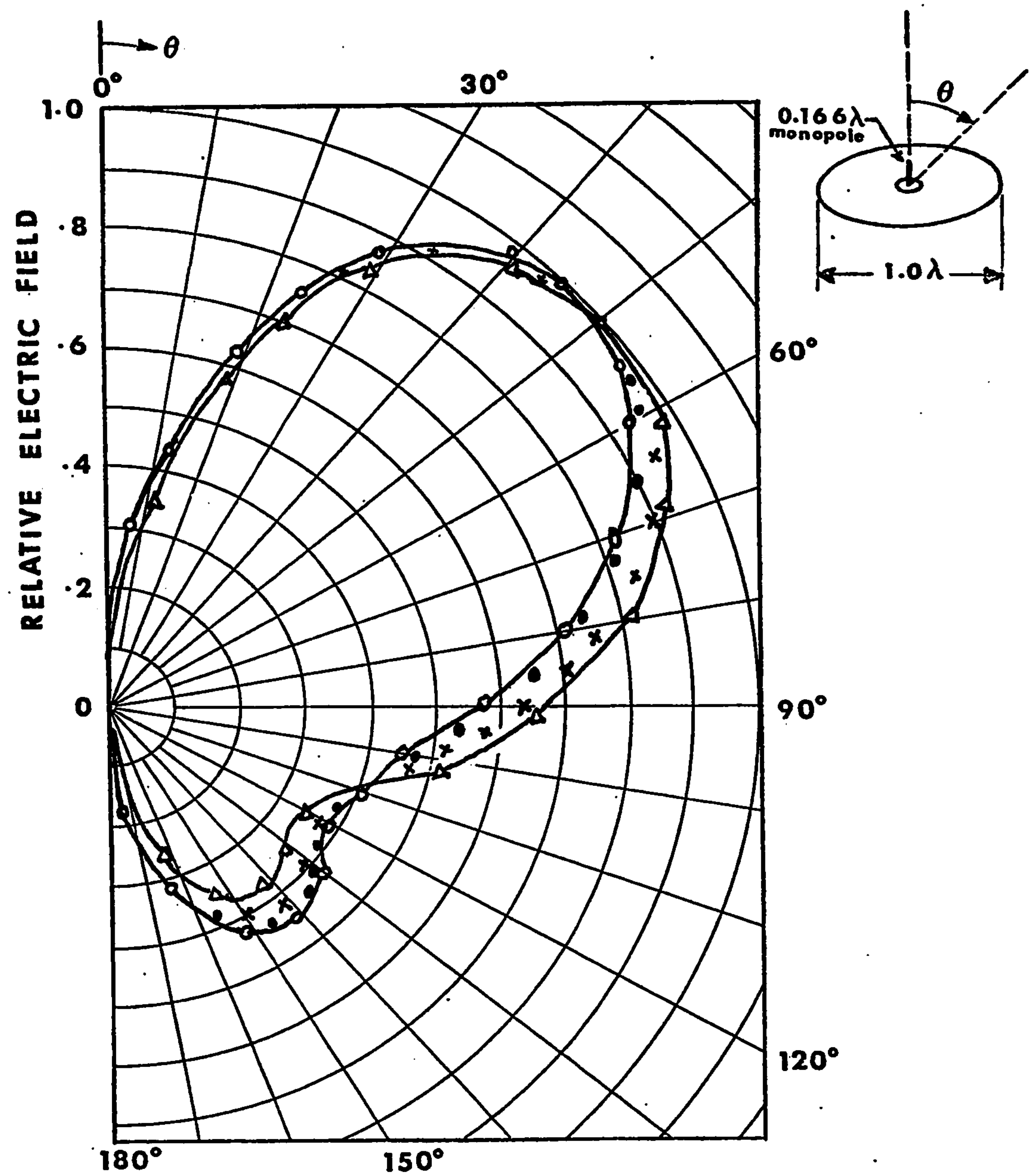

Curve	No. of Radial Wires
—△—△—	8
× × ×	12
• • •	16
—o—o—	CONTINUOUS DISK (EXPT.)

Figure 5.42. E_θ vs θ Measured Patterns for Short Monopole on Radial Ground Wires with the Bonding Rings removed.

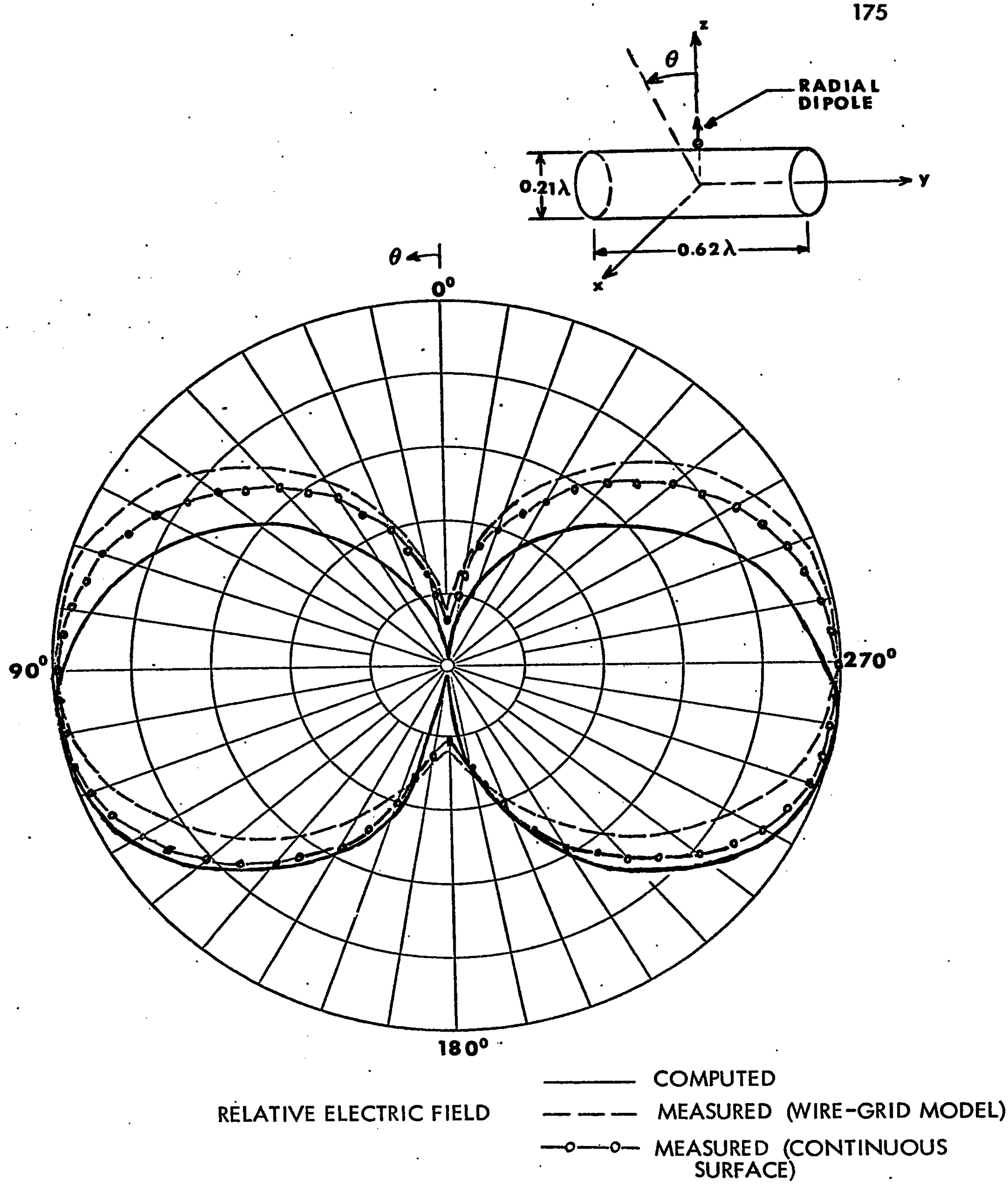

Figure 5.43. E_θ vs θ (x - z plane) for Radial Dipole Mounted Symmetrically on a Finite Cylinder.

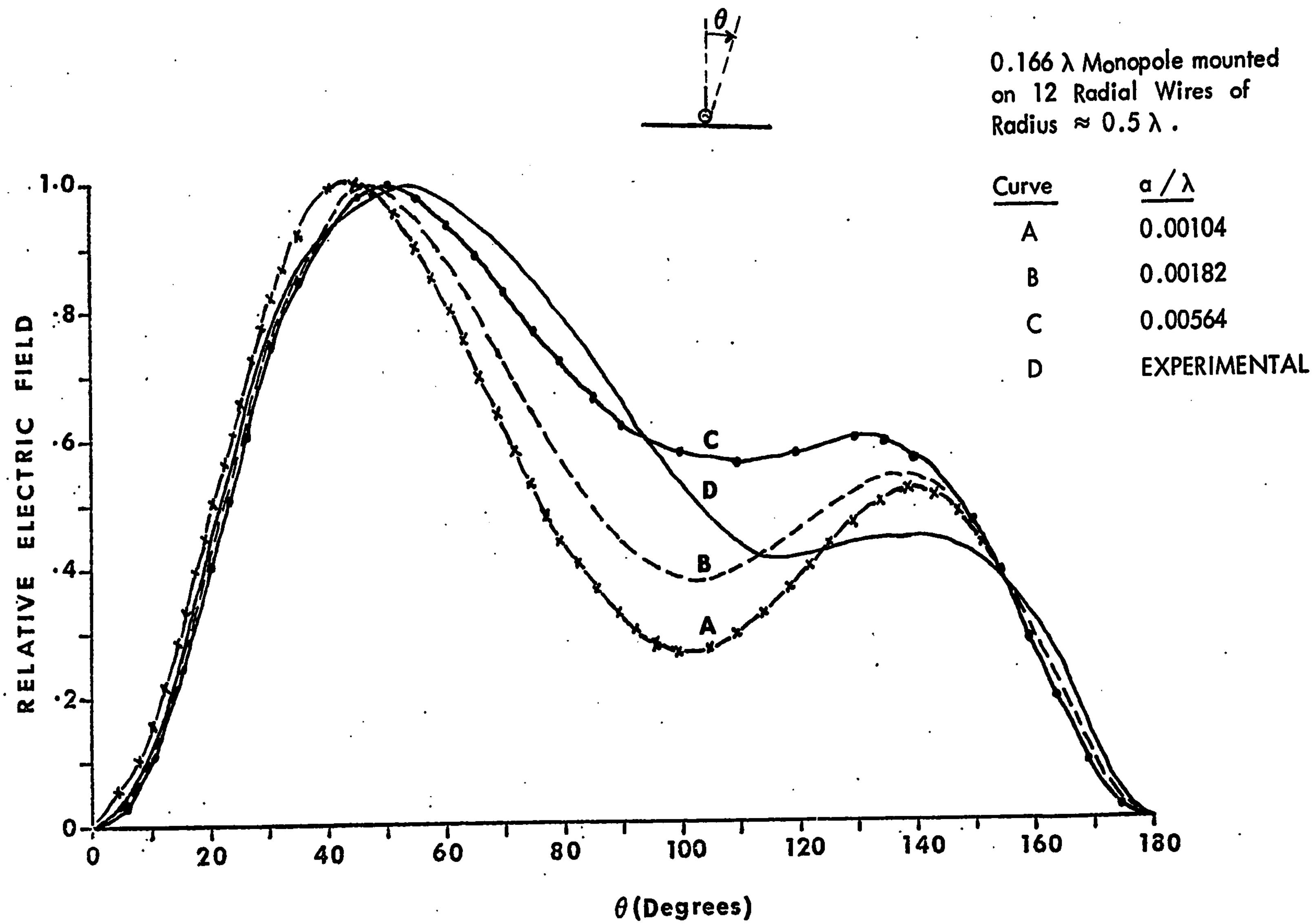

Figure 5.44. Short Monopole mounted on 12 Radial Ground Wires : Study of Influence of Wire Radius Parameter "a" .

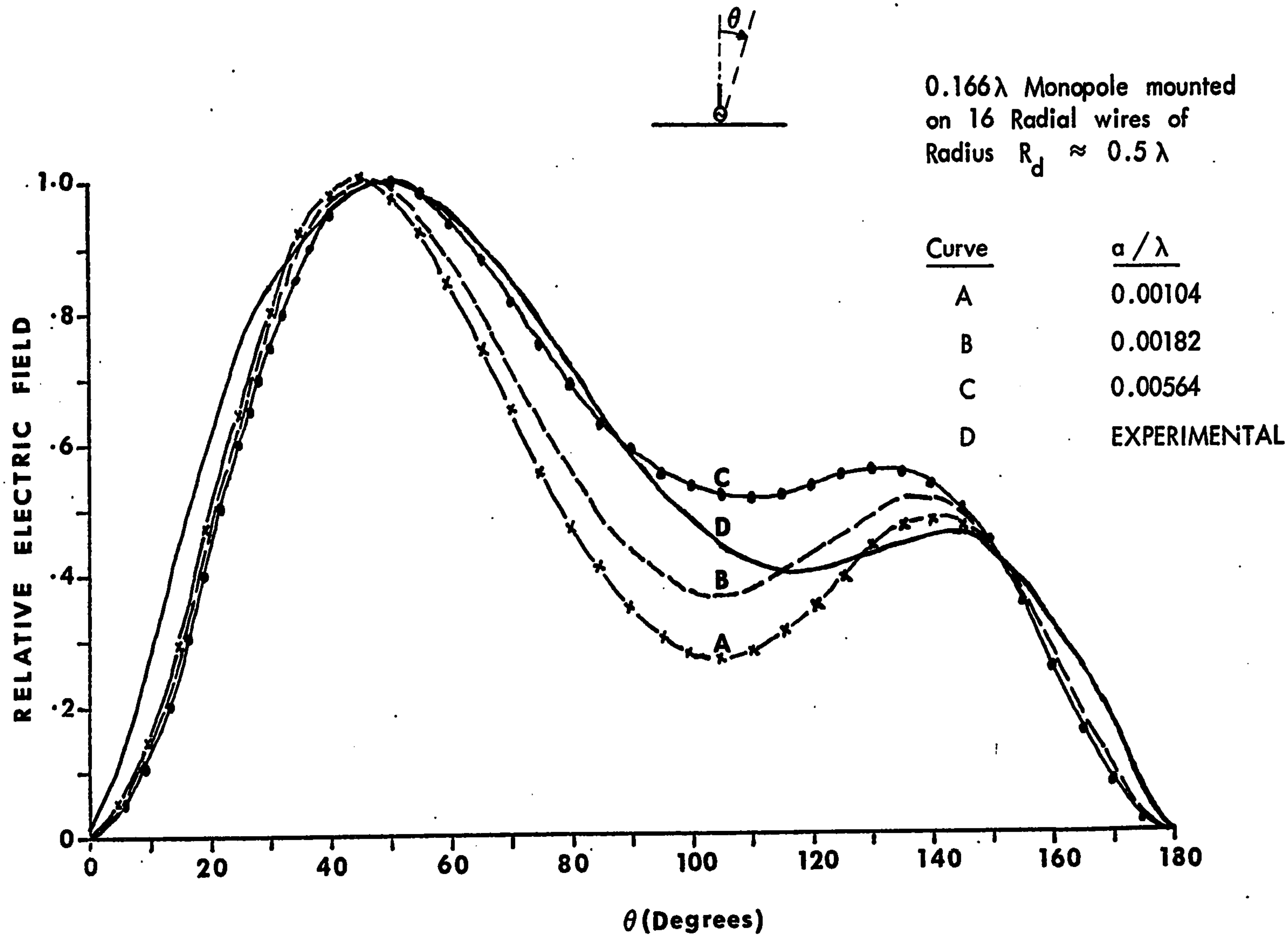

Figure 5.45. Short Monopole mounted on 16 Radial Ground Wires.
Study of Influence of Wire Radius Parameter "a" on Pattern Computation.

Figures 5.46 to 5.48

Computed and Measured E_θ vs θ Patterns (Relative Electric Field) for Monopole mounted on 32 - Wire-Grid Model of Sphere

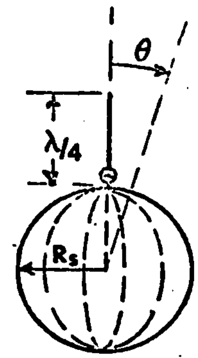

——— Computed

– – – Measured

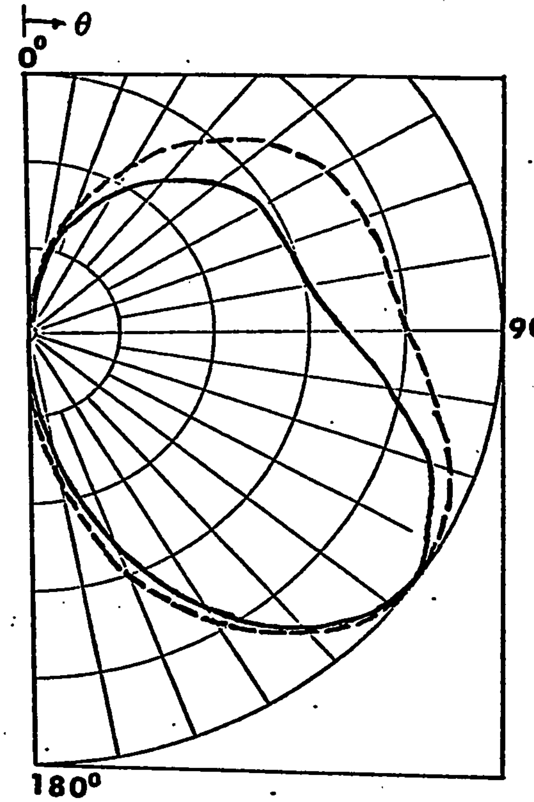

Figure 5.46. $R_s = \lambda/4$.

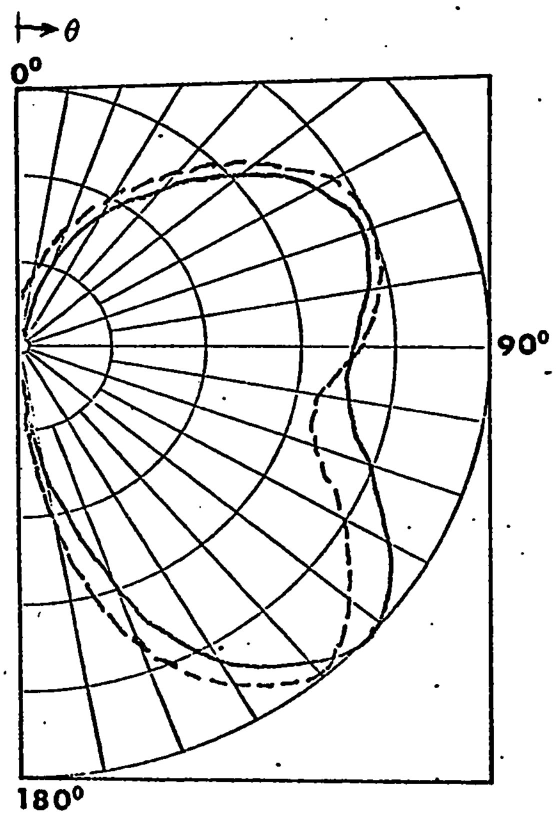

Figure 5.47. $R_s = 5\lambda/16$.

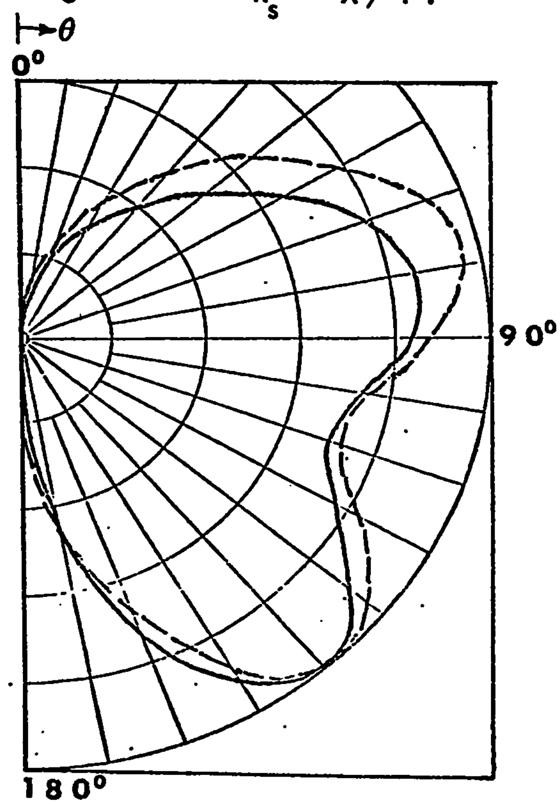

Figure 5.48. $R_s = 3\lambda/8$.

Figure 5.49 to 5.54. E_θ vs φ Computed and Measured Patterns (Relative Electric Field) for Dipole Antenna mounted on the Side of a Supporting Cylinder.

Note :

(1) Additional Parameters :

NC = NO. OF WIRES USED IN COMPUTATIONAL MODELING OF CYLINDER.

NE = NO. OF WIRES USED IN EXPERIMENTAL MODELING OF CYLINDER.

(2) Abbreviations :

WGM = WIRE-GRID MODELING

CSM = CONTINUOUS SURFACE MODEL

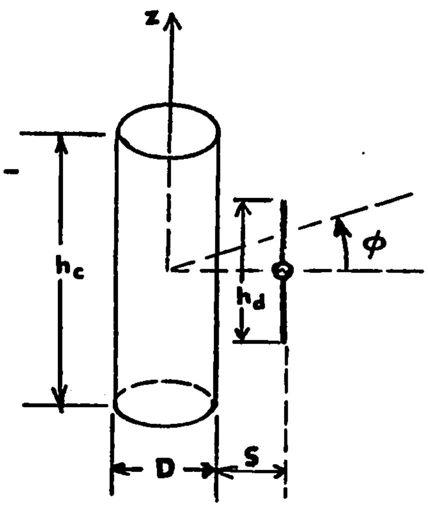

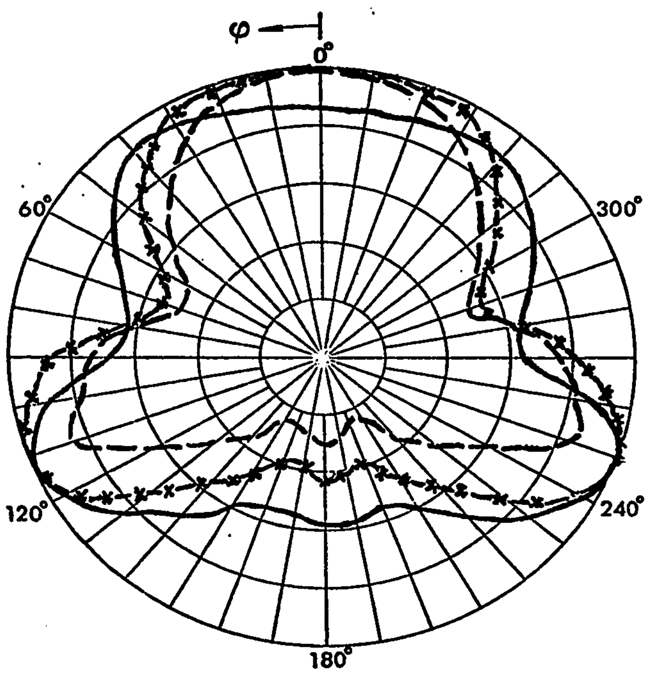

——— COMPUTED (NC = 6)
– – – EXPERIMENTAL (WGM, NE = 6)
–x–x– DATA FROM REF . [77]

Figure 5.49. $D = 0.28\lambda$, $h_c = 0.823\lambda$. $S = 0.75\lambda$, $h_d = 0.414\lambda$.

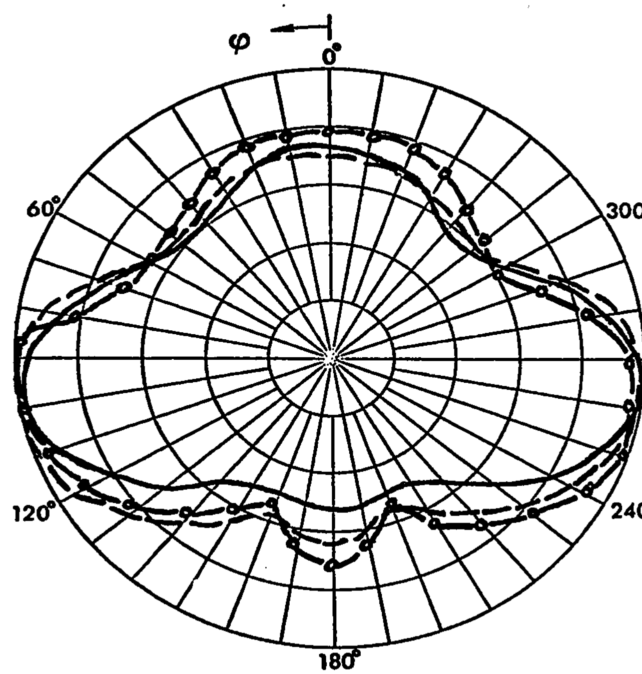

——— COMPUTED (NC = 6)
– – – EXPERIMENTAL (WGM, NE = 6)
–o–o– EXPERIMENTAL (CSM)

Figure 5.50. $D = 0.202\lambda$, $S = 0.55\lambda$. $h_c = 0.63\lambda$, $h_d = 0.3\lambda$.

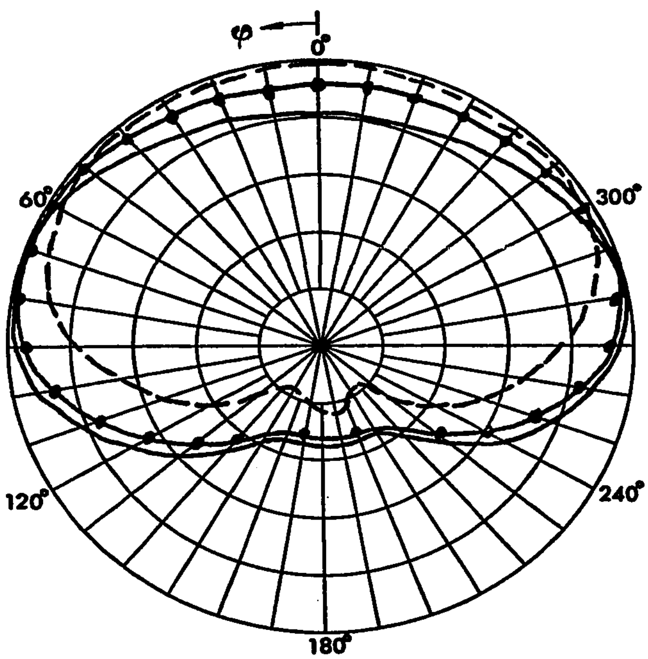

——— COMPUTED (NC = 6)
—●—●— COMPUTED (NC = 8)
– – – EXPERIMENTAL (WGM, NE=6)

Figure 5.51. $D = 0.33\lambda$, $S = 0.28\lambda$. $h_c = 1.0\lambda$, $h_d = 0.5\lambda$.

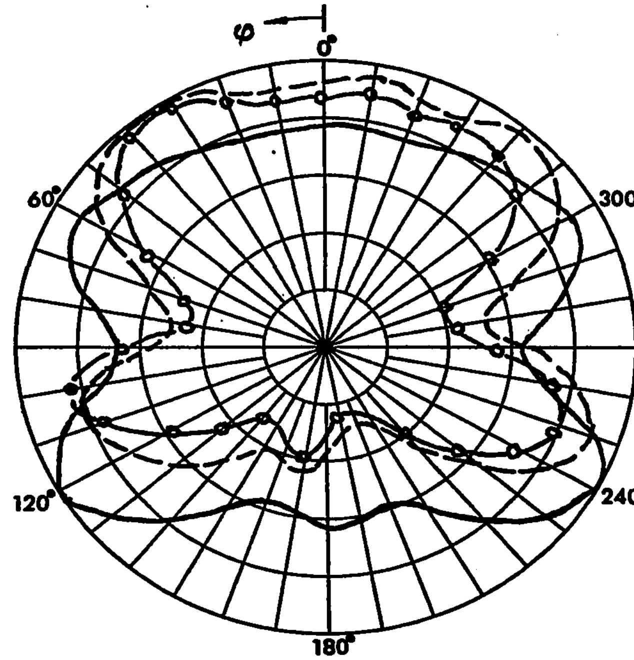

——— COMPUTED (NC = 6)
– – – EXPERIMENTAL (WGM, NE = 6)
—o—o— EXPERIMENTAL (CSM)

Figure 5.52. $D = 0.33\lambda$, $S = 0.914\lambda$. $h_c = 1.0\lambda$, $h_d = 0.5\lambda$

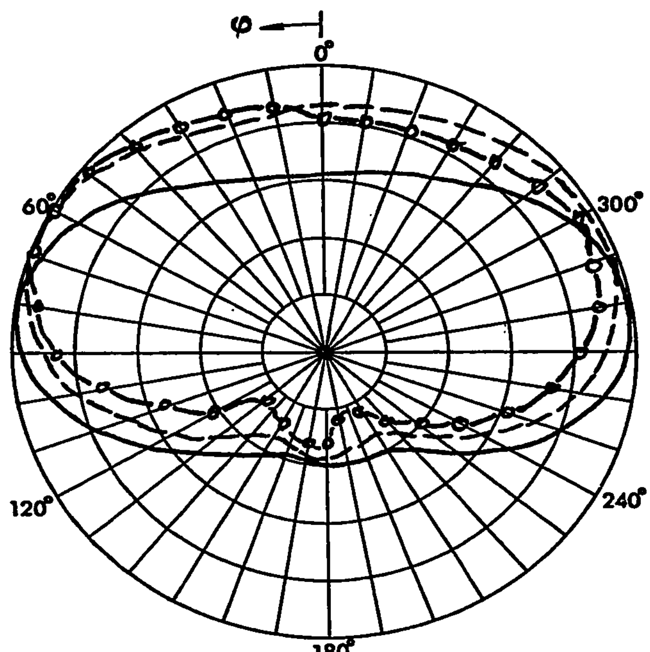

——— COMPUTED (NC = 4)
– – – EXPERIMENTAL (WGM, NE = 4)
—o—o— EXPERIMENTAL (CSM)

Figure 5.53. $D = \lambda/6$, $S = 0.368\lambda$. $h_c = 1.0\lambda$, $h_d = 0.5\lambda$.

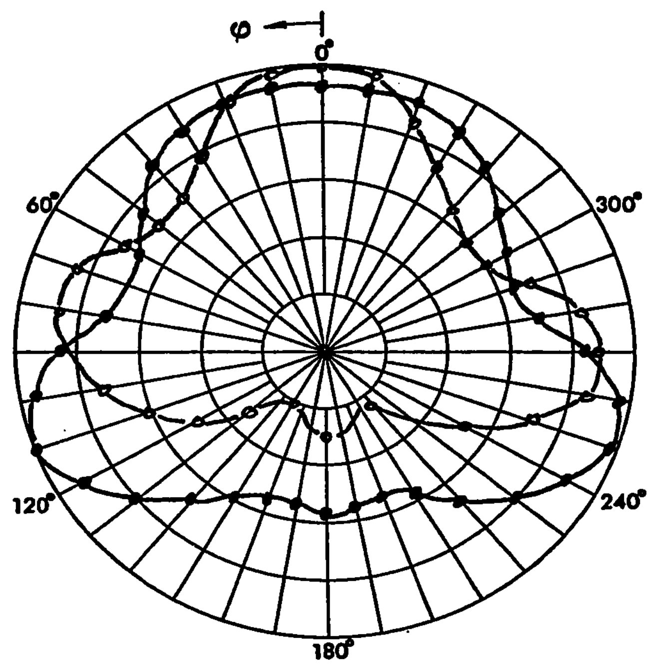

—●—●— COMPUTED (NC = 8)
—o—o— EXPERIMENTAL (CSM)

Figure 5.54. $D = 0.257\lambda$, $S = 0.69\lambda$. $h_c = 0.823\lambda$, $h_d = 0.38\lambda$.

Figures 5.55 to 5.59. Computed and Measured H-plane and E-plane Patterns (Relative Electric Field) for a Finite Corner Reflector) with

Height ,	H	=	1.0 λ
Width ,	S	=	0.5 λ
Distance,	D	=	0.25 λ

Note : Symbols NC, NE, WGM and CSM as defined on page 179 are also used here.

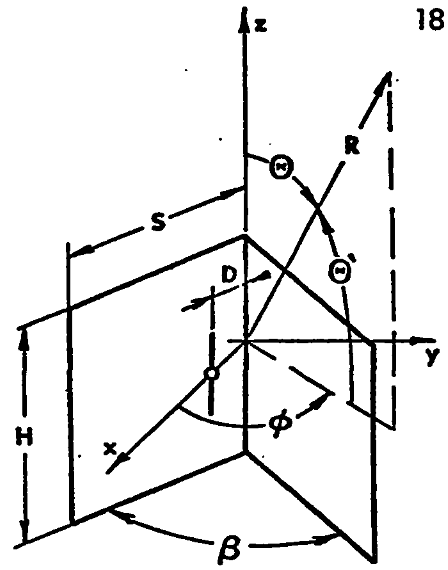

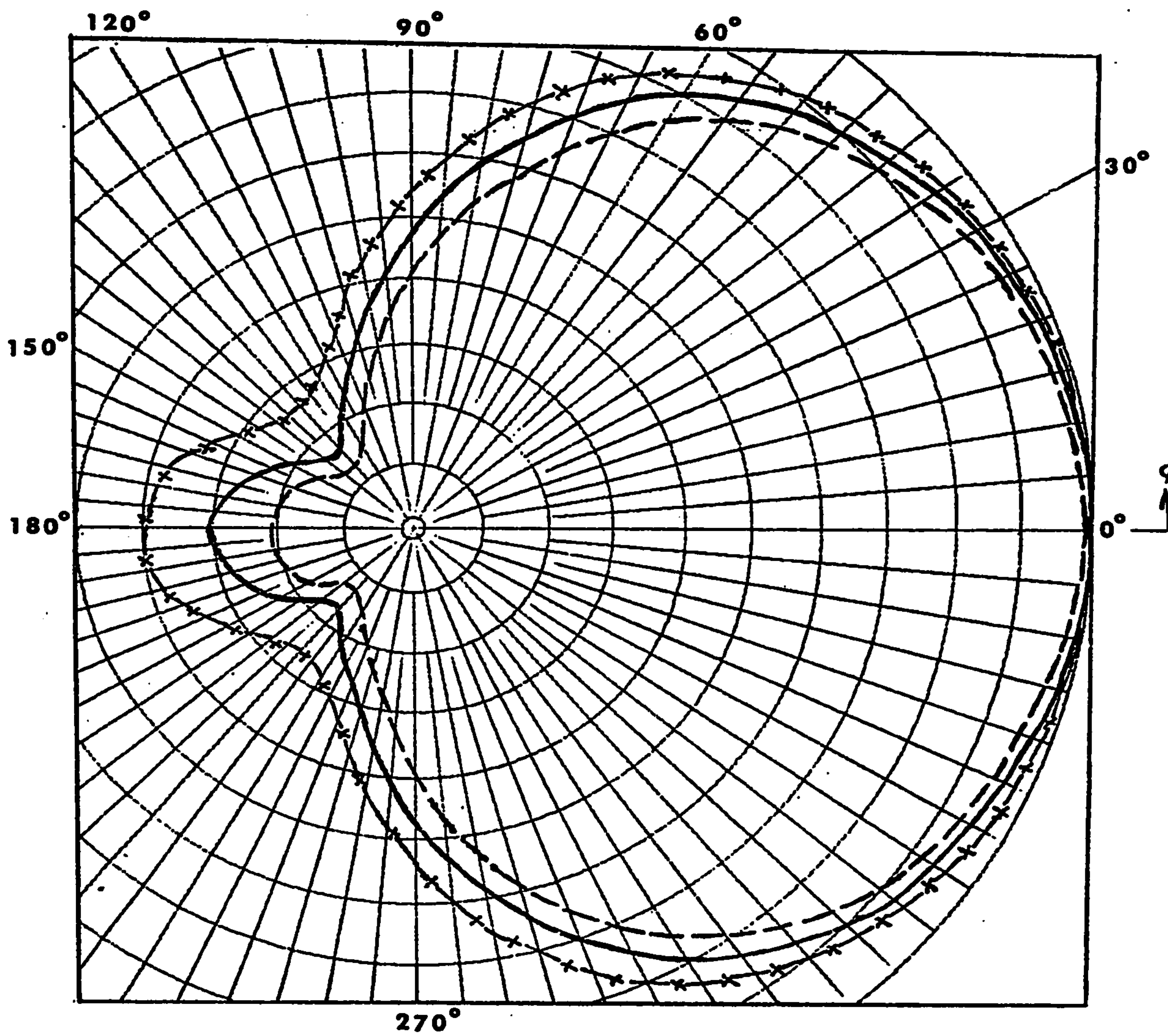

—x—x—COMPUTED (NC = 9). ——— COMPUTED (NC = 11), – – – EXPERIMENTAL (WGM, NE=9).

Figure 5.55. E_θ vs ϕ (H - plane) for β = 60°.

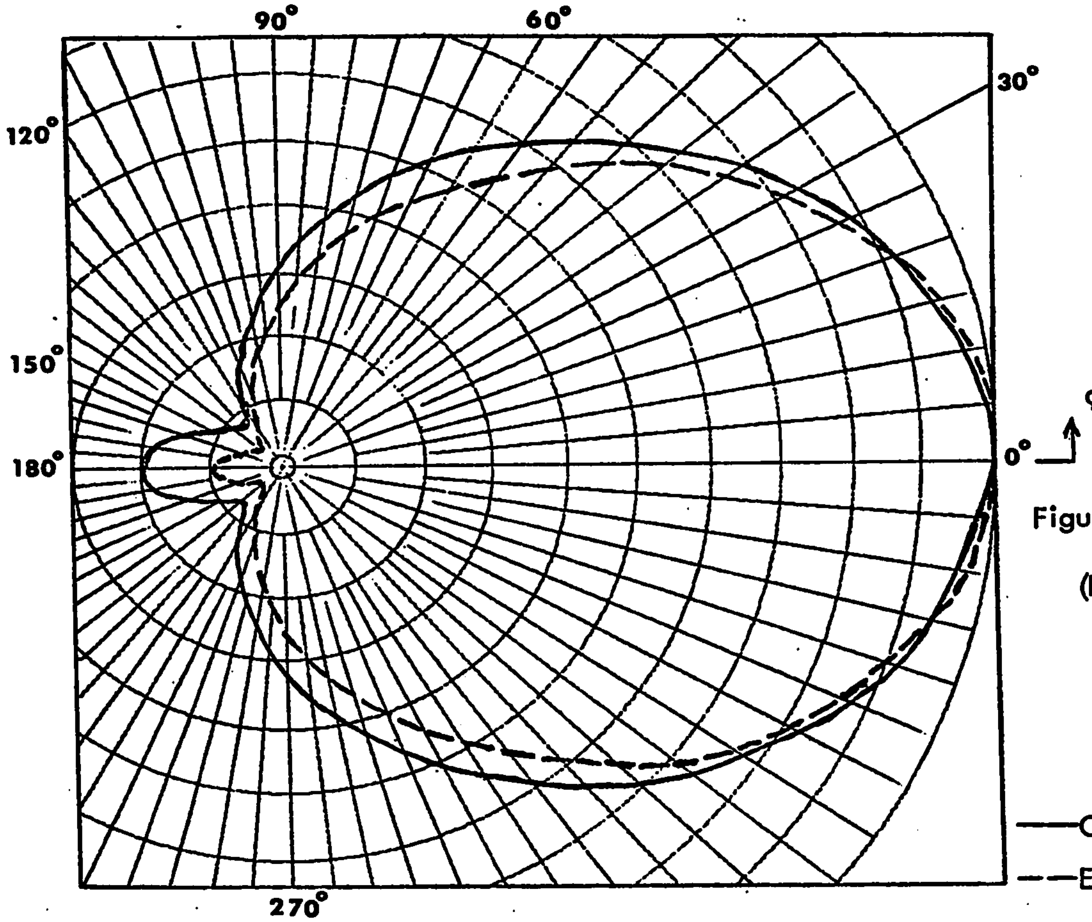

Figure 5.56. E_θ vs φ (H-plane) for $\beta = 90^\circ$.

——COMPUTED (NC = 9).
– – –EXPERIMENTAL (WGM, NE = 9).
–o–o–EXPERIMENTAL (CSM).

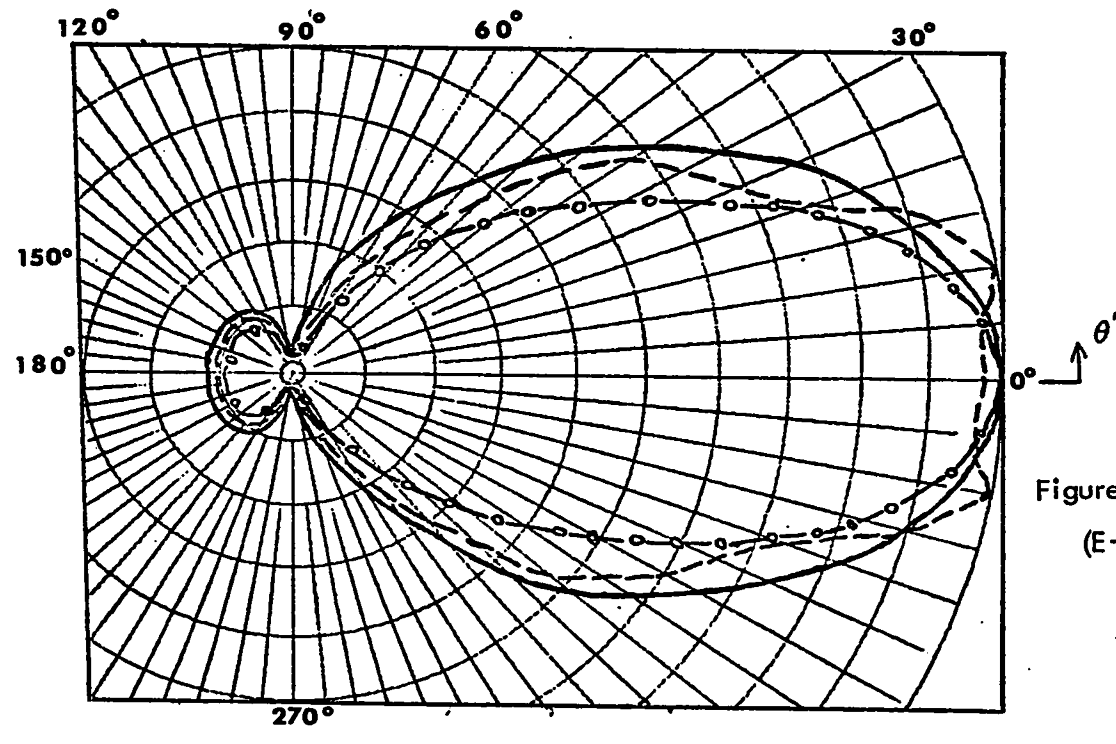

Figure 5.57. E_θ vs θ' (E-plane) for $\beta = 90^\circ$.

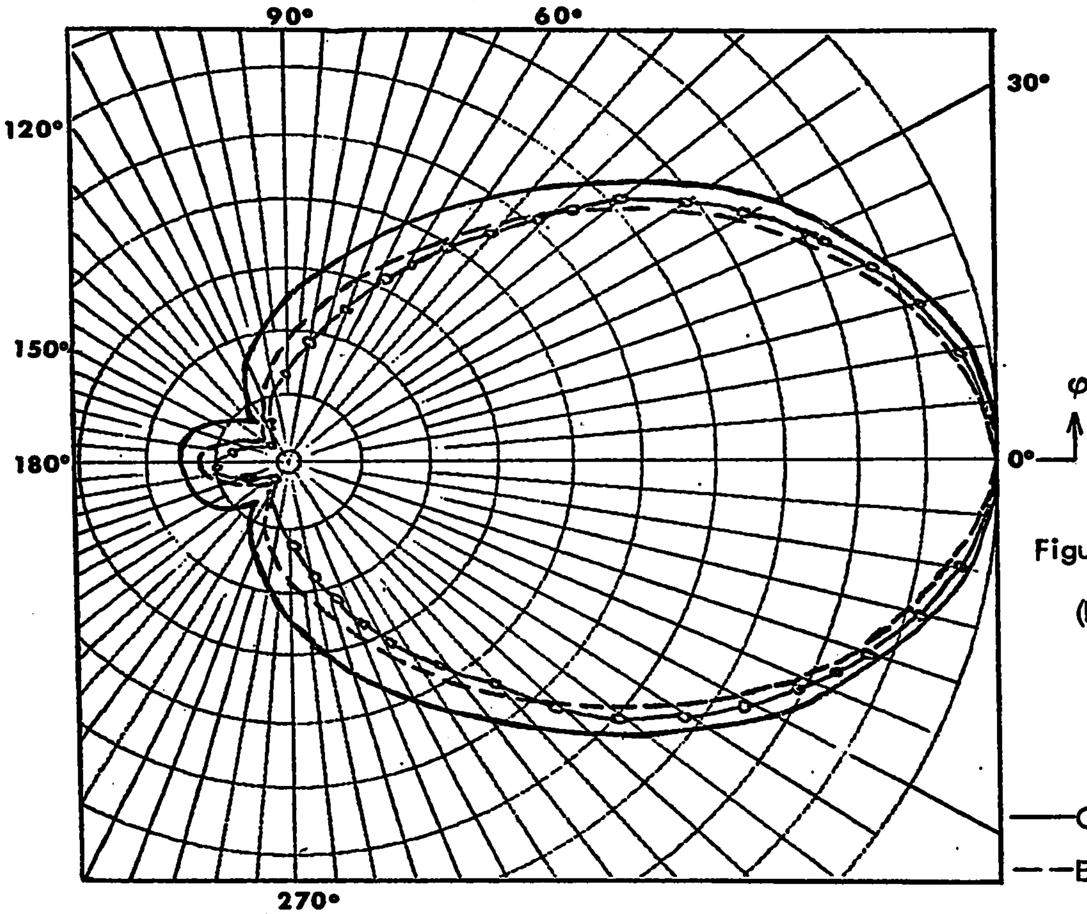

Figure 5.58. E_θ vs φ (H-plane) for $\beta = 130°$.

——COMPUTED (NC = 9) .
– –EXPERIMENTAL (WGM , NE = 9) .
-o-o-EXPERIMENTAL (CSM) .

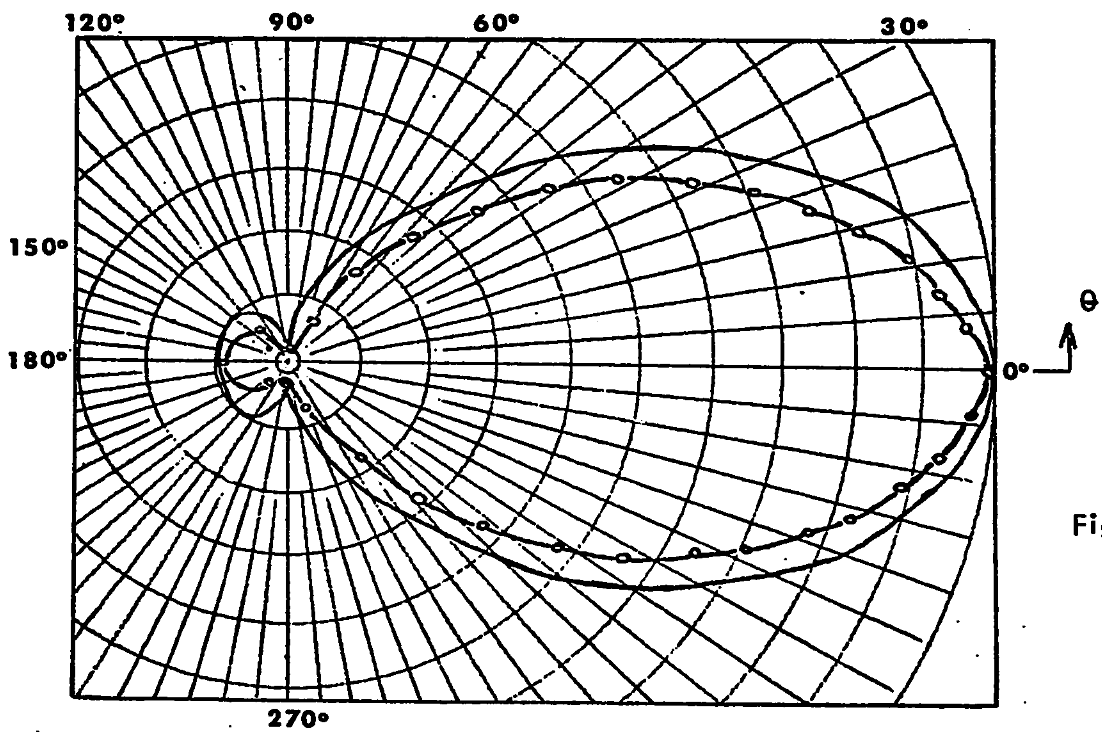

Figure 5.59. E_θ vs θ' (E-plane) for $\beta = 130°$.

Figures 5.60 to 5.75

Computed and Measured Patterns (Relative Electric Field) for Thin Wire Structure.

Note :

WOR = Without Rotor Blades.
WRL = With Rotor Blades Parallel.
WRR = With Rotor Blades Perpendicular.

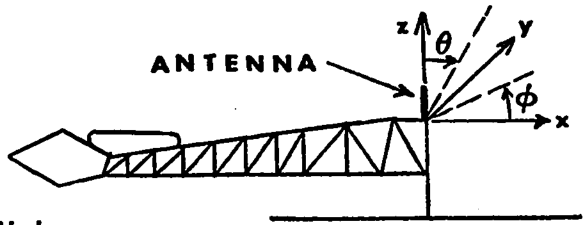

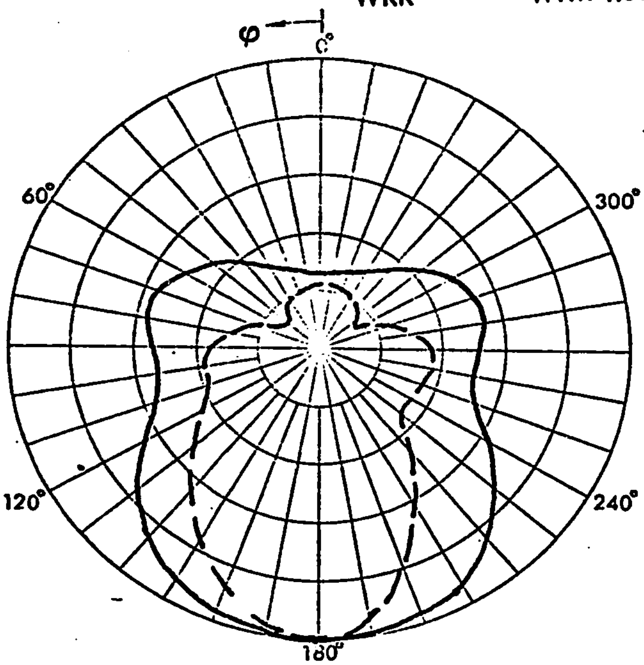

Figure 5.60. E_θ vs φ, $\theta = 60°$ (WOR)

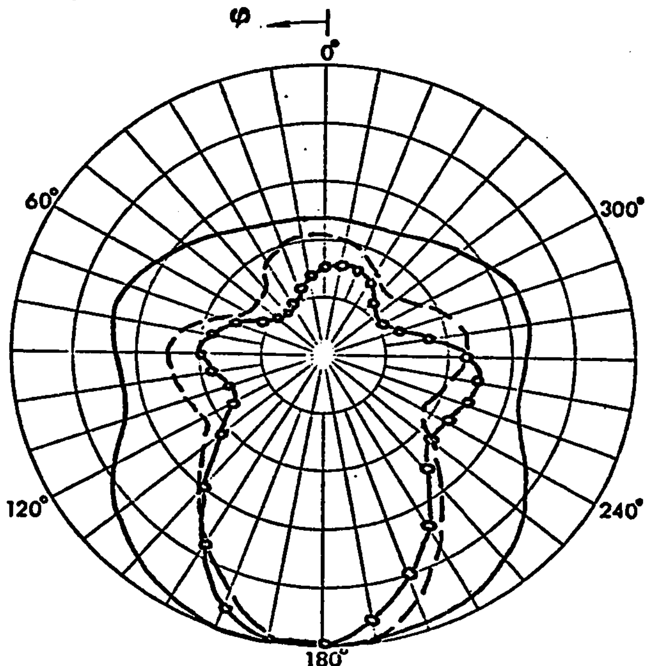

Figure 5.61. E_θ vs φ, $\theta = 70°$ (WOR)

Computed
Measured (Wire-Grid)
Measured (Cont.)

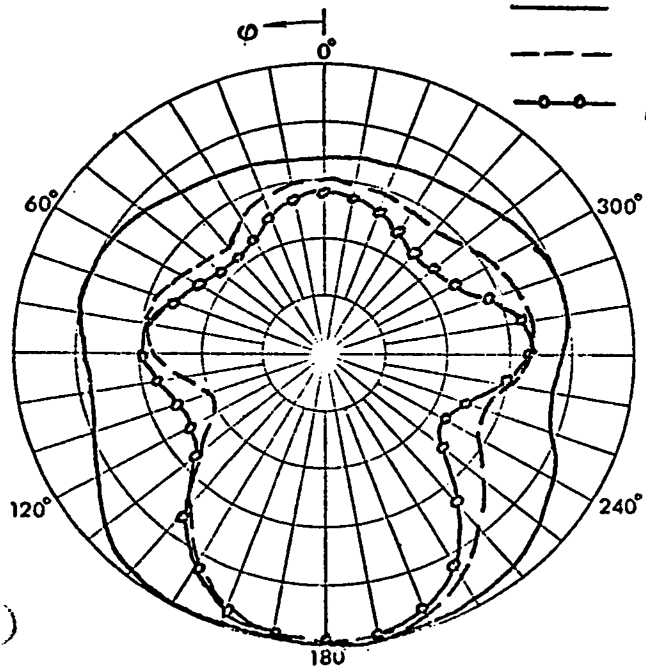

Figure 5.62. E_θ vs φ, $\theta = 80°$ (WOR)

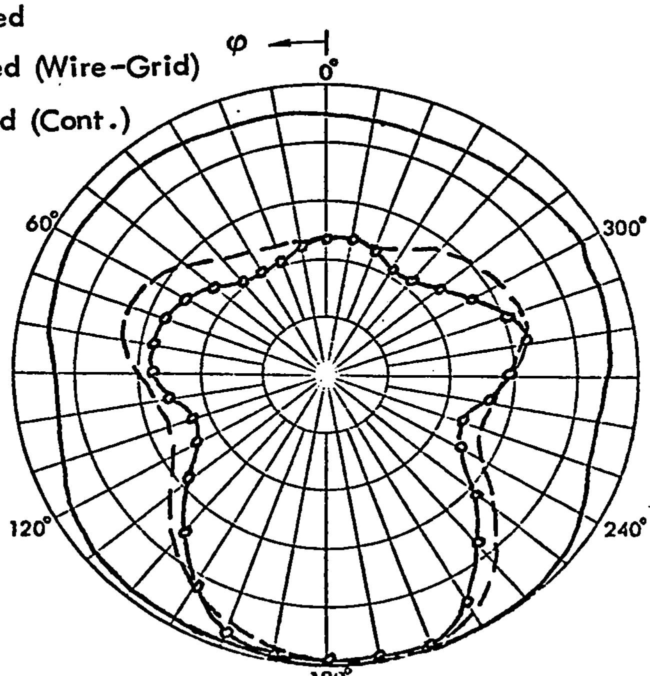

Figure 5.63. E_θ vs φ, $\theta = 90°$ (WOR)

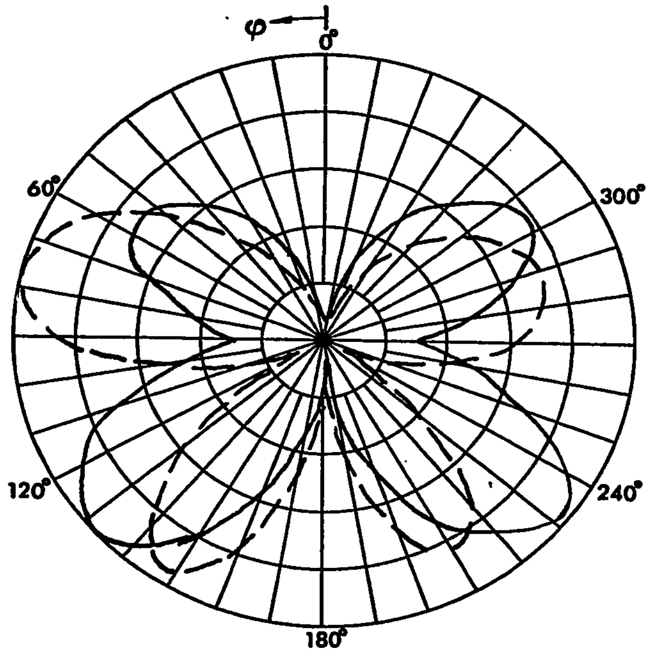

Figure 5.64. E_φ vs φ, $\theta = 60^\circ$ (WOR)

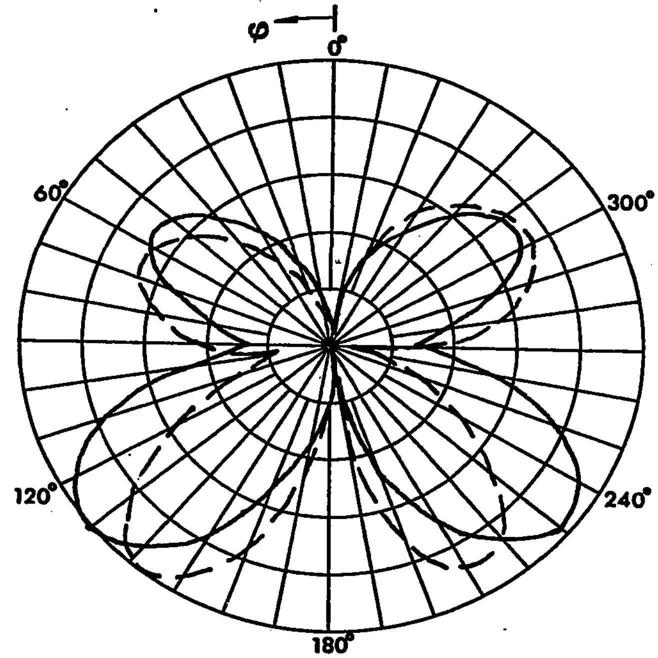

Figure 5.65. E_φ vs φ, $\theta = 70^\circ$ (WOR)

——— Computed
– – – Measured

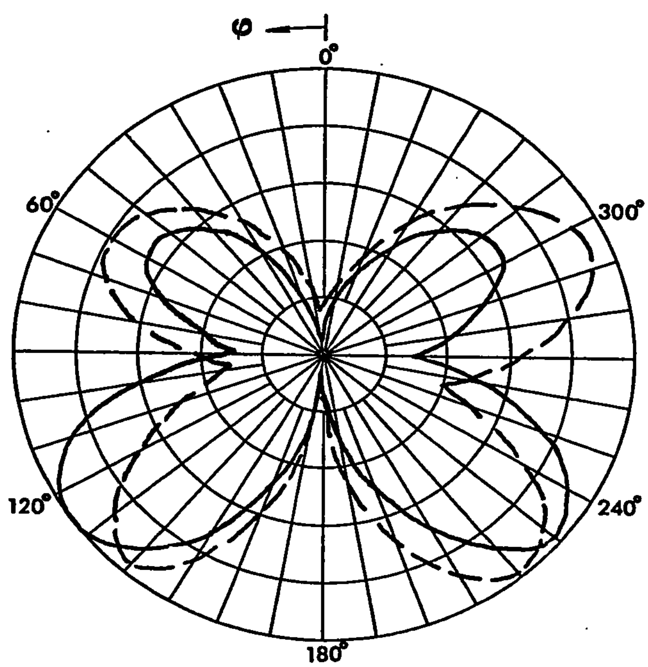

Figure 5.66. E_φ vs φ, $\theta = 80^\circ$ (WOR)

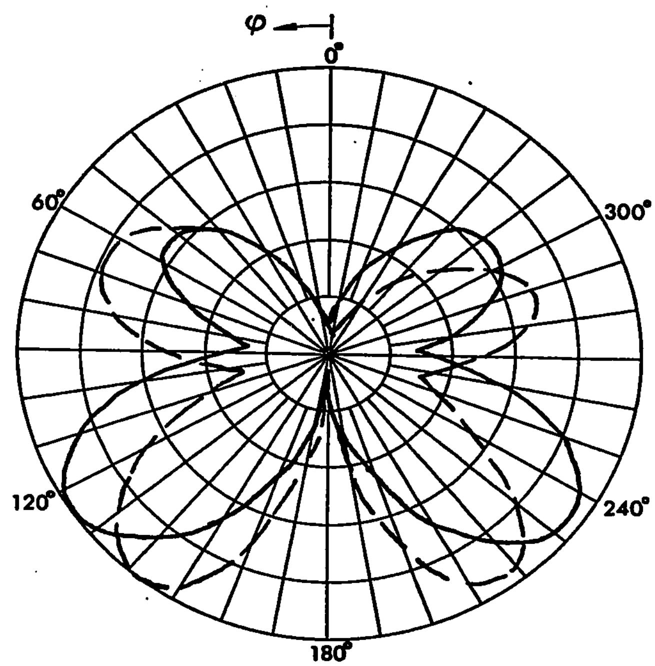

Figure 5.67. E_φ vs φ, $\theta = 90^\circ$ (WOR)

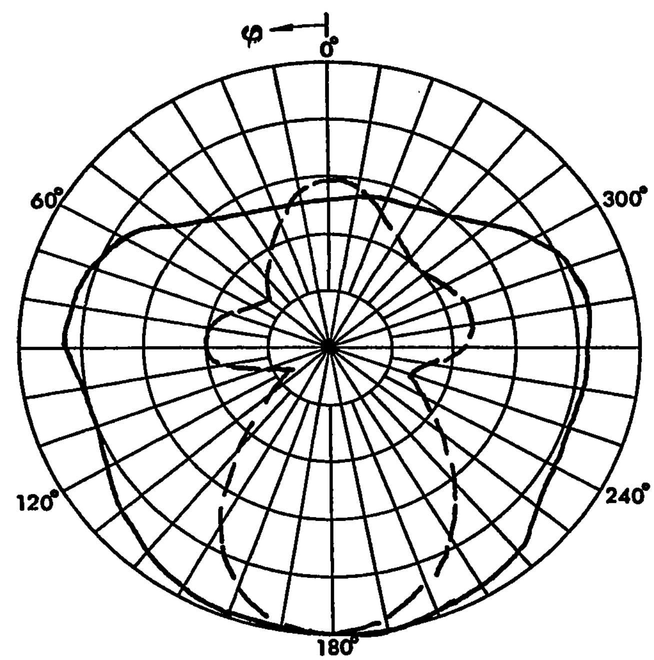

Figure 5.68. E_θ vs φ , $\theta = 80^\circ$ (WRR)

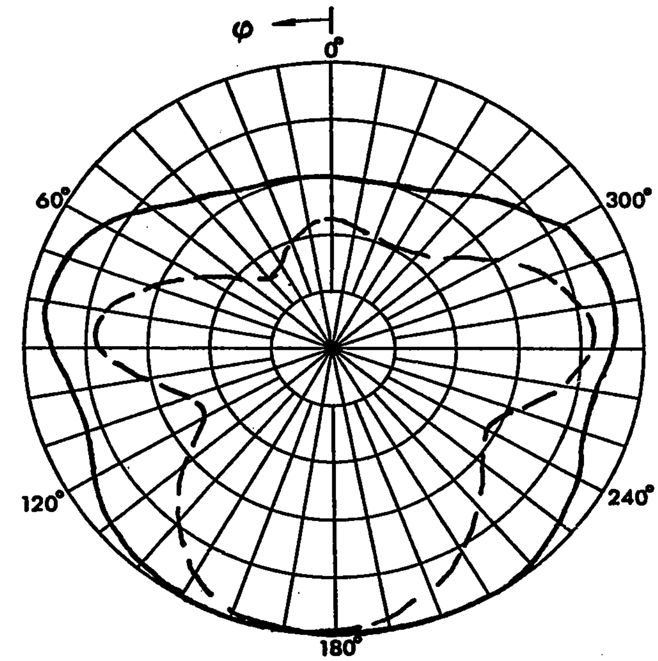

Figure 5.69. E_θ vs φ , $\theta = 80^\circ$ (WRL)

——— Computed

– – – Measured

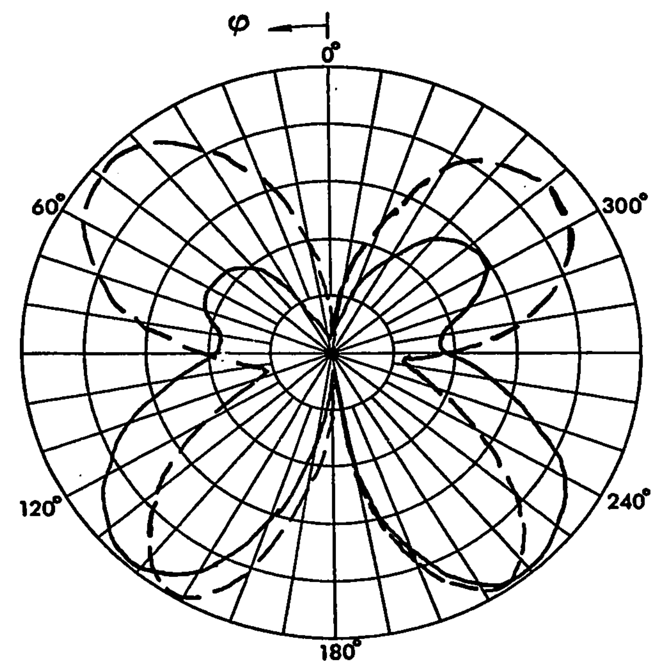

Figure 5.70. E_φ vs φ , $\theta = 80^\circ$ (WRR)

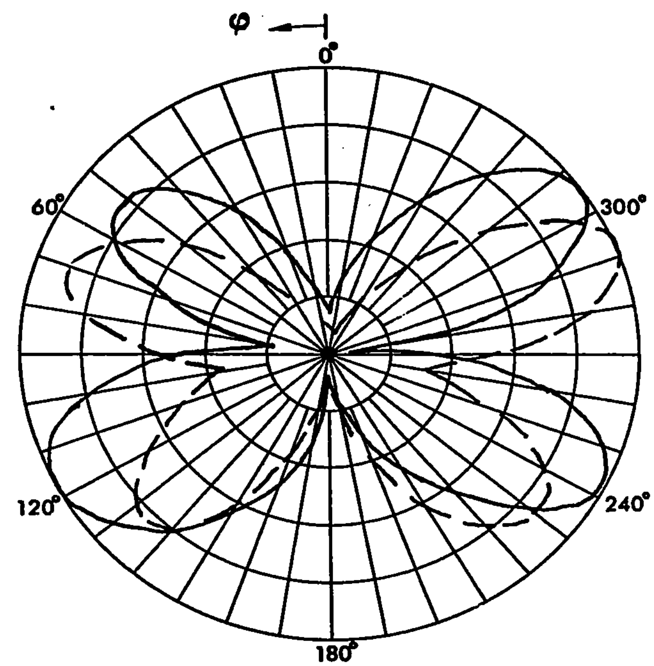

Figure 5.71. E_φ vs φ, $\theta = 80^\circ$ (WRL)

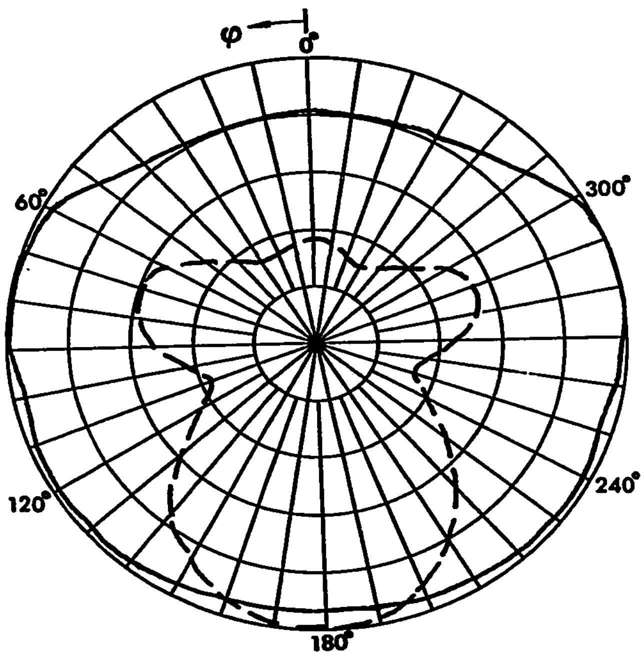

Figure 5.72. E_θ vs φ, $\theta = 90°$ (WRR)

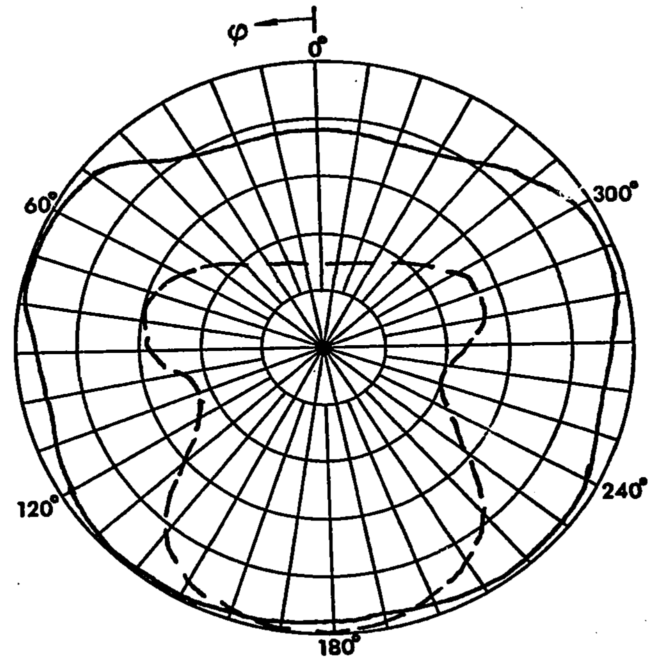

Figure 5.73. E_θ vs φ, $\theta = 90°$ (WRL)

——— Computed
— — — Measured

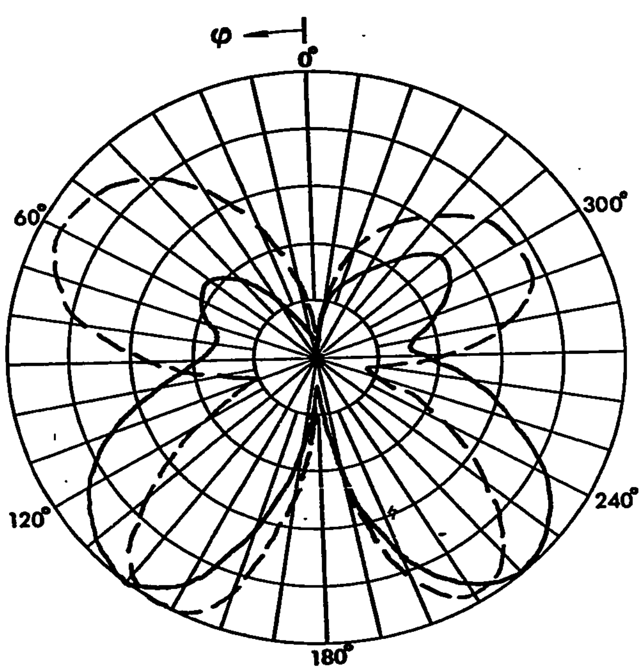

Figure 5.74. E_φ vs φ, $\theta = 90°$ (WRR)

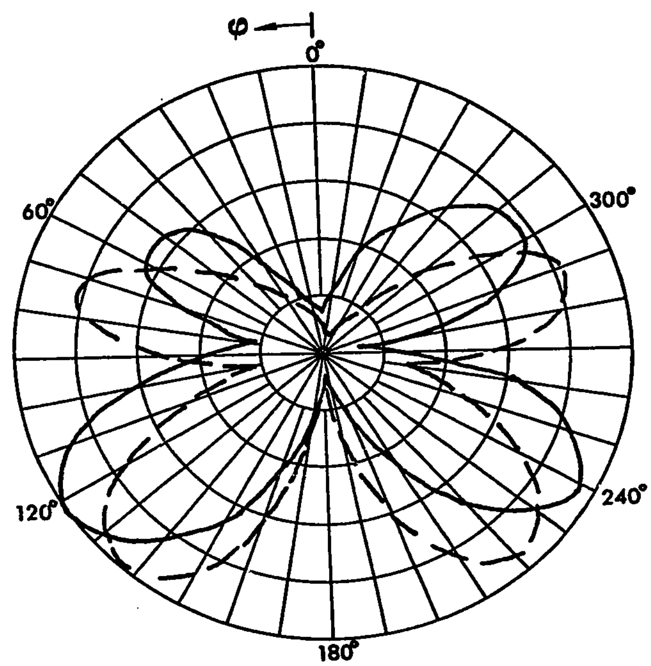

Figure 5.75. E_φ vs φ, $\theta = 90°$ (WRL)

CHAPTER VI

CONCLUSIONS

The central objective of this study was to apply the wire-grid method of analysis systematically to linear antennas mounted near conducting bodies, with the broad aim of establishing guidelines both for the formulation of the wire-grid models and for the structuring of the computational process.

The computational analysis of the antenna systems studied and the accompanying experimental measurements have yielded results which are generally in good agreement. The important findings and conclusions based on this investigation are as follows :

(a) The study was started on the basis of the concepts, methods, and assumptions of linear antenna theory using Pocklington's integral equation as the fundamental formulation. The problem of the excitation source representation was given special attention. In seeking computational models for the sources, recourse was had to classical studies of straight wire antennas. The models used were either the finite-width gap or the magnetic frill current source. While these models have been exploited in a restricted form by others in the case of simple wire antennas, it is claimed that the results reported in this study demonstrate the effectiveness of the adaptation of these source models to complex three-dimensional antenna structure. Detailed computations of current distributions have shown the two source representations to be equally useful for far field patterns. It should be noted that some formal representation of the source is essential to make the use of the wire-grid technique possible for the analysis of the type of antenna systems considered in this work.

(b) The basic computational approximations used and numerical procedures followed have been developed elsewhere. However, much effort was expended on the general structuring of the computations into self-contained schemes. Particular attention was given to the the evaluation of "impedance" matrices and their solution using a standard matrix elimination method.

(c) In applying the wire-grid analysis method to linear antennas near conducting bodies, considerable insight has been gained for developing a modeling procedure on a sound physical basis. Unlike applications to scattering by conducting bodies where mesh size is the starting criterion for correct modeling, the present study has emphasized the concept of stationary lines of flow as the basis of wire-grid modeling. It has been demonstrated that this approach removes considerable doubt about the location of the thin wires needed to model a given continuous surface. Although the concept has been known in antenna analysis and commonly used in engineering designs (e.g. grid-like corner reflector antennas), its usefulness in current distribution computation has been recognized only in this study. The validity of this approach has been demonstrated by the computed and measured results.

(d) The stationary line of flow approach has been applied to specific antenna systems and modeling and segmentation details have been developed for them. Depending on antenna location and configuration of the supporting surface, two general cases have been considered:

(i) bodies in which the surface currents have a single common vectorial orientation, and

(ii) bodies in which, surface elements need to be considered in terms of two or more orientations.

It has been shown that each antenna structure needs an appropriate segmentation scheme before it becomes amenable to current and pattern computations. The possibility of achieving programming efficiency in current computations using symmetry has been demonstrated. Computation of radiation patterns has re-emphasized the sufficiency of the point-matching method for far field calculations.

(e) Modeling criteria have been established for specifying the number of paths to be used for the different antenna configurations and have been corroborated experimentally. Segmentation procedures have also been developed and tested by comparing calculated, measured or known patterns. The influence of the number of wire elements used in a given computation has been shown to depend more on the number of current paths included in the wire model rather than on the fineness of segmentation provided that a certain upper limit of size is not exceeded.

(f) An important insight has been gained into the influence of the wire-radius parameter for antenna structures already in a wire-grid form. The conclusion is drawn that in applying the wire-grid technique to such structures, the physical wire radius values must be taken into consideration. This conclusion would not have been reached without the availability of experimental results.

(g) The experimental work has emphasized two special aspects of the wire-modeling process :

(i) the use of narrow strips in place of thin circular cross section wires,

(ii) the replacement of grid-like structures by continuous surfaces.

In the first case it was found that narrow flat strips are as useful as round wires. In the second case, which experimentally is a reversal of the numerical modeling procedure, results were obtained which were essentially identical for grid or continuous surface models, thus giving substantial credibility to the wire-grid modeling concept.

It must also be emphasized that at this stage of development of the wire-grid modeling technique, experimental measurement still serves a function more crucial than mere corroboration of the calculations. Experimentation on models in this investigation served as an essential factor in helping to develop insight into the numerical technique. It helped to reduce expensive or even misleading "iterations" or trial computations by a considerable amount and contributed substantially to the development of the "correct" models.

(h) Two major sources of error were encountered in the computational procedures :

(i) errors due to coordinate segmentation subprograms, and

(ii) errors in the computation of "network impedance" elements.

Even after the wire modeling approximations were satisfactorily established, it was sometimes found in preliminary test runs that some minor detail in the segmentation scehme would cause major errors. As an example, the centre coordinates of the current elements might be evaluated correctly, but the angular orientation would differ from the assumed direction of the stationary current lines, thus leading to wrong results. Such errors are further aggravated by the computer's ready ability to produce an output that may either be relevant or meaningless. Similarly, serious errors in impedance computation were noted under conditions for which program debugging was very difficult. This kind of situation occurred particularly for antennas with geometrical symmetry. In the reduction of an impedance matrix,it was found essential for the compact impedance structure to give results identical to those given by the complete matrix. The fact that there is symmetry in a current distribution can be seen easily enough heuristically, but to program the appropriate structure data correctly, great care is needed in the arrangement of the unique current elements.

In summarizing the above observations it can be concluded that the wire-grid method of analysis has a wide range of applicability provided that careful attention is given to the "correct" modeling, coordinate segmentation, source representation and computational structuring. It is in fact difficult to find other alternative methods amongst those discussed in the introductory chapter which would have as powerful a scope of application, except possibly the surface element method, which is of the same generic family.

The modeling procedures evolved in the present investigation are adaptable to a wide variety of specific antenna problems and a series of procedural guidelines have become apparent as described in the body of the thesis. These guidelines relate in particular to :

1. Correct source representation and location.
2. Use of the stationary current flow concept for the modeling of the wire grid.
3. The choice of segmentation and structuring of the computation process.
4. The use of a finite radius for the wire elements.

In addition to the above conclusions, the results of the study suggest further areas for research. These are as follows :

(a) It has been demonstrated that thin circular wires or thin filament strips can be used to make experimental wire-grid models of antenna surfaces. From a physical point of view, the wires representing a surface structure actually should be strips. If this can be achieved, then by adjusting the width of the strips the procedure could possibly be made to approximate the surface element modeling technique. However, this would first require a fundamental restatement of the basic integral equation formulation.

(b) The influence of the wire radius parameter for circular wires had been established for grid-like structures. It is suggested that its influence on the accuracy of the wire modeling process for a continuous surface be explored further. This might be done by reassessing the assumption made about the current distribution being uniformly distributed around the periphery of a thin cylindrical current element especially in the presence of nearby elements.

(c) The comparisons between computed and measured patterns have shown that the agreements were fairly good for those structures which were modeled by wire grids with few junctions. However, in the case of the thin wire structure approximating the tail section of a helicopter, many junctions were part of the structure, and the pattern agreements were found to be rather unsatisfactory in the detail. It is suggested that Kirchhoff's junction condition may have to be satisfied for this type of structure even though in other structures this condition was up till now successfully neglected. Investigation in this area no matter how difficult might make the wire-modeling technique more rigorously complete.

(d) It has been stated and implicitly assumed that the antenna structures studied had finite electrical dimensions. It would be of considerable interest to make a systematic search for the "finiteness" of the boundary beyond which the wire modeling technique might become inappropriate. The bounds to the technique may arise from considerations of either computational capacity limitations or from the existence of other analytical methods which may be more pertinent to larger size systems.

(e) Finally, it is recommended that a systematic application of the surface element method be examined in a manner similar to that undertaken in the present investigation. Such a study might hopefully bring out further additional insight which would supplement the conclusions reached in this work.

In summary, although the precise formulation of a set of "canonic" rules has yet to be attained, it is contended that important guidelines for the use of the wire-grid method of analysis have emerged from the study. The application of the technique for determination of patterns of practical antenna systems which hitherto were mainly attainable only by scaled or actual size measurements, or by approximate analysis, is firmly established.

Furthermore even if generalized canonic theorems should prove to be unattainable, a systematic development of wire-grid models for the frequently used antenna configurations, organized in an encyclopaedic manner, along with programming and computational details, could be envisaged. Such a compendium is possible and would be a powerful research and design tool, since once a wire grid model for a particular antenna form is established and proven, it can be used exhaustively to investigate and optimize the antenna system in terms of its various parameters.

REFERENCES

[1] J. Aharoni, Antennae : An Introduction to Their Theory. Oxford, England : Clarendon Press, 1946.

[2] S.A. Schelkunoff, Advanced Antenna Theory. New York : John Wiley and Sons, 1952.

[3] L.J. Chu and J.A. Stratton, "Steady-state solutions of electromagnetic field problems : III Forced oscillations of a prolate spheroid," J. Appl. Phys., vol. 12, pp. 241 - 248, March 1941.

[4] H. Margenau and G.M. Murphy, The Mathematics of Physics and Chemistry. Princeton : D. Van Nostrand, Second Edition, 1956.

[5] S.S. Schelkunoff, "Theory of antennas of arbitrary shape and size," Proc. IRE, vol. 29, pp. 493 - 521, September 1941.

[6] P.S. Carter, "Circuit relations in radiating systems and applications to antenna problems," Proc. IRE, vol. 20, pp. 1004 - 1041, June 1932.

[7] G.H. Brown, "Directional Antennas," Proc. IRE, vol. 25, pp. 79 - 145, January 1937.

[8] H.C. Pocklington, "Electrical oscillations in wire," Camb. Phil. Soc. Proc., 9, pp. 324 - 332, 1897.

[9] J.D. Kraus, Antennas. New York : McGraw-Hill, 1950.

[10] E.A. Laport, Radio Antenna Engineering. New York : McGraw-Hill, 1952.

[11] E.A. Wolff, Antenna Analysis. New York : John Wiley and Sons, 1966.

[12] E. Hallen, "Theoretical investigation into transmitting and receiving antennae," Nova Acta Regiae Sco. Sci. Upsaliensis, Ser. 4, vol. 2, p. 1, 1938.

[13] R. King and D. Middleton, "The cylinfrical antenna : current and impedance," Quart. Appl. Math., vol. 3, pp. 302 - 335, 1946.

[14] R.W.P. King, The Theory of Linear Antennas. Cambridge, Mass. : Harvard University Press, 1956.

[15] R.E. Collin and F.J. Zucker, Antenna Theory, Pt. I. New York : McGraw-Hill, 1969.

[16] R.W.P. King and C.W. Harrison, Jr. Antennas and Waves : A Modern Approach. Cambridge, Mass. : The M.I.T. Press, 1969.

[17] G.L. Albert and J.L. Synge, "The general problem of antenna radiation and the fundamental integral equation, with application to an antenna of revolution Part I," Quart. Appl. Math., vol. 5, pp. 117 - 131, 1948.

- also J.L. Synge, "The general problem of antenna radiation and the fundamental integral equation, with application to an antenna of revolution Part II," Quart. Appl. Math., vol. 5, pp. 133 - 156, 1948.

[18] K.K. Mei, "On the integral equations of thin wire antennas," IEEE Trans. Antennas Propagat., vol. AP-13, pp. 374 - 378, May 1965.

[19] Y.S. Yeh and K.K. Mei, "Theory of conical and equiangular-spiral antennas, Part I - Numerical techniques, "IEEE Trans. Antennas Propagat., vol. AP-15, pp. 634 - 639, September 1967.

[20] R.F. Harrington, "Matrix methods for field problems," Proc. IEEE, vol. 55, pp. 136 - 149, February 1967.

[21] R. F. Harrington, Field Computation by Moment Methods. New York : Macmillan, 1968.

[22] D. Popović, "Polynomial approximation of current along thin symmetrical dipoles," Proc. IEE (London), vol. 117. pp. 873 - 878, May 1970.

[23] R.F. Harrington and S.R. Mautz, "Straight wires with arbitrary excitation and loading," IEEE Trans. Antennas Propagat., vol. AP-15, pp. 502 - 515, July 1967.

[24] G.A. Thiele, "Calculation of the current on a thin linear antenna," IEEE Trans. Antennas and Propagat. (Commun.), vol. AP-14, 648 - 649, September 1966.

[25] A. Leitner and R.D. Spence, "Effect of a circular ground plane on antenna radiation," J. Appl. Phys., vol. 21, pp. 1001 - 1006, October 1950.

[26] J.E. Storer, "The radiation pattern of an antenna over a circular ground screen," J. Appl. Phys., vol. 23, pp. 558 - 593, May 1952.

[27] A.S. Meier and W.P. Summers, "Measured impedances of vertical antennas over finite ground planes," Proc. IRE, vol. 37, pp. 609-616, June 1949.

[28] J.E. Storer, "The impedance of an antenna over a large circular screen," J. Appl. Phys., vol. 22, pp. 1058 - 1066, August 1951.

[29] G. Bekefi, "The impedance of an antenna above a circular ground plate laid upon a plane earth," Can. Jour. Phys., vol. 32, pp. 205 - 222, March 1954.

[30] J.D. Kraus, "The corner reflector antenna," Proc. IRE, vol. 28, pp. 513 - 519, November 1940.

[31] E.B. Moullin, Radio Aerials. Oxford, England : Clarendon Press, 1949.

[32] J.R. Wait, "On the theory of an antenna with an infintie corner reflector," Can. J. Phys., vol. 32, pp. 365 - 37p, May 1954.

[33] Y. Ohba, "On the radiation pattern of a corner reflector finite in width," IEEE Trans. Antennas Propagat., vol. AP-11, pp. 127 - 132, March 1963.

[34] C.H. Papas and Ronald King, "Surface currents on a conducting sphere excited by a dipole," J. Appl. Phys., vol. 19, pp. 808 - 816, September 1948.

[35] R.F. Harrington, Time-Harmonic Electromagnetic Fields. New York : McGraw-Hill, 1961 .

[36] P.S. Carter, "Antenna arrays around cylinders," Proc. IRE, vol. 31, pp. 671 - 693, December 1943.

[37] G. Sinclair, "The patterns of antennas located near cylinders of elliptical cross section," Proc. IRE, vol. 39, pp. 660 - 668, 1951.

[38] W.S. Lucke, "Electric dipoles in the presence of elliptic and circular cylinders," J. Appl. Phys., vol. 22, pp. 14 - 19, January 1952.

[39] P. Knight, "Methods of calculating of the horizontal radiation patterns of dipole arrays around a support mast," Proc. IEE (London), vol. 105, Part B, pp. 548 - 554, November 1958.

[40] J.R . Wait, Electromagnetic Radiation fron Cylindrical Structures. New York : Pergamon, 1959.

[41] G. Sinclair, E.C. Jordan, and E.W. Vaughan, "Measurement of aircraft-antenna patterns using models," Proc. IRE, vol. 35, pp. 1451 - 1462, December 1947.

[42] G. Sinclair, "Theory of models of electromagentic systems," Proc. IRE, vol. 36, pp. 1364 - 1369, November 1948.

[43] J.V.N. Granger and T. Morita, "Radio - frequency current distributions on aircraft structures," Proc. IRE, vol. 39, pp. 932 - 938, August 1951.

[44] J.Y. Wong and J.C. Barnes, "Design and construction of a pattern range for testing high frequency shipborne antennas," Trans. Eng. Inst. Can., vol. 2, pp. 15 - 21, January 1958.

[45] H. Jasik (ed.), Antenna Engineering Handbook. New York : McGraw-Hill, 1961.

[46] C.A. Balanis, "Radiation characteristics of curremt elements neae a finite-length cylinder," IEEE Trans. Antennas Propagat., vol. AP-18, pp. 352 - 359, May 1970 .

[47] A.J. Poggio and E.K. Miller, "Integral equation solutions of three-dimensional scattering problems," Computer Techniques for Electromagnetics and Antennas, Part 2. R. Mittra (ed.), University of Illinois, October 1970.

[48] F.K. Oshiro and K.M. Mitzner, "Digital Computer solution of three - dimensional scattering problems," Presented at 1967 IEEE International Antennas and Propagation Symposium. Ann Arbor, October 1967. Summary published in the Symposium Digest, pp. 257 - 263.

[49] F.M. Tesche and A.R. Neureuther, "Radiation patterns for two monopoles on a perfectly conducting sphere," IEEE Trans. Antennas Propagat. (Commun.), vol. AP -18, pp. 692 - 694, September 1970.

[50] J. Goldhirsh, D.L. Knepp, and R.J. Doviak, "Radiation from a dipole near a conducting cylinder of finite length," IEEE Trans. Antennas Propagat., vol. AP - 18, pp. 96 - 105, August 1970.

[51] J.H. Richmond, " A wire-grid model for scattering by conducting bodies," IEEE Trans. Antennas Propagat., vol. AP - 14, pp. 782 - 786, November 1966.

[52] E.K. Miller, J.B. Morton, G.M. Pjerrou, and B.J. Maxum, "Numerical analysis of aircraft antennas," Proc. of Conf. on Environmental Effects on Antenna Performance, vol. I, edited by J.R. Wait, 1969, pp. 55 - 58.

[53] G. A. Thiele, M. Travicso - Diaz, and H.S. Jones, "Radiation of a monopole antenna on the base of a conical structure," Proc. of Con. on Environmental Effects on Antenna Performance, vol. I, edited by J.R. Wait, October 1969.

[54] D.A. Bolle and M.D. Morganstern, "Monopole and conic antennas on spherical vehicles," IEEE Trans. Antennas Propagat., vol. AP-17, pp. 477 - 484, July 1969.

[55] L.L. Tsai, "Analysis and measurement of a dipole antenna mounted symmetrically on a conducting sphere or cylinder," Ph.D. dissertation, The Ohio State University, Columbus, Ohio, 1970.

[56] G.A. Thiele, "Wire antennas," Computer Techniques for Electromagnetics and Antennas, Part I. R. Mittra (ed.), University of Illinois, 1970.

[57] CRC Standard Mathematical Tables. Clevland, Ohio : The Chemical Rubber Co., Eighteenth Edition, 1970, p. 368.

[58] S.A. Schelkunoff and H.T. Friis, Antennas : Theory and Practice. New York : John Wiley and Sons, 1952.

[59] J. Mathews and R.L. Walker, Mathematical Methods of Physics. New York : W.A. Benjamin, 1965.

[60] S.H. Lee and K.K. Mei, "Analysis of zig-zag antennas," IEEE Trans. Antennas and Propagat., vol. AP - 18, pp. 760 - 764, November 1970.

[61] A. Ralston, A First Course In Numerical Analysis. New York : McGraw-Hill, 1965.

[62] L. Infeld, "The influence of the width of the gap upon the theory of antennas," Quart. Appl. Math., vol. 5, pp. 113 - 131, 1947.

[63] Y.M. Chen and J.B. Keller, "Current on and input impedance of a cylindrical antenna," J. Res. NBS., vol. 66D, pp. 15 - 31, January 1962.

[64] R.W.P. King and T.T. Wu, "The thick tubular transmitting antenna," Radio Sci., vol. 2, pp. 1061 - 1065, September 1967.

[65] D.V. Otto, "The admittance of cylindrical antennas driven from a coaxial line," Radio Sci., vol. 2, pp. 1031 - 1042, September 1967.

[66] D.V. Otto, "A note on the mathematical representation of the source for tubular transmitting antennas," Radio Sci., vol. 3, pp. 862 - 863, August 1968.

- also, Ronald W.P. King and Tsui Tsun Wu, "A comment on 'A note on the mathematical representation of the source for tubular transmitting antennas' by D.V. Otto", Radio Sci., vol. 3, pp. 864 - 865, August 1968.

[67] D.C. Chang, "On the electrically thick monopole, Part I : theoretical solution," IEEE Trans. Antennas Propagat., vol. AP - 16, pp. 58 - 64, January 1968.

[68] J.B. Andersen, "Admittance of infinite and finite cylindrical metallic antenna," Radio Sci., vol. 3, pp. 607 - 621, June 1968.

[69] S.A. Schelkunoff, "A general radiation formula," Proc. IRE, vol. 27, pp. 660 - 666, October 1939.

[70] S.W. Maley and R. J. King, "Impedance of a monopole antenna with radial-wire ground system on an imperfectly conducting half space, Part I," J. Res. NBS., vol. 66 D, pp. 175 - 180, March 1962 .

[71] W. L. Weeks, Electromagnetic Theory for Engineering Applications. New York : John Wiley and Sons, 1964.

[72] R.W. P. King, Electromagnetic Engineering, vol. I. New York : McGraw - Hill, 1945.

[73] R.F. Harrington and J. Mautz, "Matrix methods for solving field problems, vol. II - Computations for linear wire antennas and scatterers," Technical Report No. RADC - TR - 66 - 351, Syracuse University, August 1966.

[74] R.L. Tanner and M.G. Andreasen, "A wire-grid lens of wide application, Part II, Wave - propagation properties of a pair of wire grids with square, hexagonal or triangular mesh," IRE Trans. Antennas Propagat., vol. AP-10, pp. 416 - 429, July 1962.

[75] E. K. Miller, G. J. Burke, and E.S. Selden : "Accuracy-modeling guidelines for integral-equation evaluation of thin-wire scattering," IEEE Trans. Antennas Propagat. (Commun.), vol. AP-19, pp. 534 - 536, July 1971.

[76] D.D. McCracken, Fortran with Engineering Applications. New York : John Wiley and Sons, 1967.

[77] Phelps Dodge Communications Company, "Side - mounted base station omnidirectional antennas," Communication Antenna Systems. Catalog No. 667, pp. 59 - 61, 1970.

[78] A.C. Wilson and H.V. Cottony, "Radiation patterns of finite-size corner reflector antennas," IRE Trans. Antennas Propagat., vol. AP - 8, pp. 144 - 156, March 1960 .

[79] E.F. Harris, "An experimental investigation of the corner-reflector antenna," Proc. IRE, vol. 41, pp. 645 - 651, May 1953.

- also E.F. Harris, "Corner-reflector antennas," Chapter II, Reference [45] .

[80] H.H. Kuehl, "Radiation from a radial electric dipole near a long finite circular cylinder," IRE Trans. Antennas Propagat., vol. AP – 9, pp. 546 – 553, November 1961 .

[81] J.R. Wait and K. Okashimo, "Patterns of stub antennas on cylindrical (and semi-cylindrical) surfaces," Can. J. Phys., vol. 34, pp. 190 – 202, February 1956.

[82] S.J. Kubina, T.J.F. Pavlasek, and W. Wolde-Ghiorgis, "Applications of numerical techniques to the design of vehicle antennas," Conference Digest, pp. 58 – 59, International Electrical, Electronic Conference, Toronto, Ontario, October 1971.

[83] T.J.F. Pavlasek, S.J. Kubina, and W. Wolde-Chiorgis, "Influence of time-varying geometry on H.F. Antennas," Supplementary Report, D.R.B. Grant No. 5540 – 32, Department of Electrical Engineering, McGill University, Montreal, Québec, October 1971 .

[84] S.J. Kubina, "Radiation characteristics of vehicle antennas – towards a comprehensive methodology," Ph.D. Dissertation (in preparation), Department of Electrical Engineering, McGill University, Montreal, Québec, 1972.

[85] T.J.F. Pavlasek and S.J. Kubina, "Influence of time-varying geometry on H. F. antennas," Annual Report 1967, D.R.B., Grant No. 5540 – 32, Department of Electrical Engineering, McGill University, Montreal, Québec.

[86] T.J.F. Pavlasek and S.J. Kubina, "Influence of time-varying geometry on H.F. antennas," Annual Report 1968, D.R.B. Grant No. 5540-32, Department of Electrical Engineering, McGill University, Montreal, Québec.

[87] T.J.F. Pavlasek and S.J. Kubina, "Influence of time-varying geometry on H.F. antennas," Annual Report 1969, D.R.B. Grant No. 5540 – 32, Department of Electrical Engineering, McGill University, Montreal, Québec.

[88] "IEEE Test Procedure for Antennas, Number 149 (Revision of 48 IRE 2S2) January, 1965, " IEEE Trans. Antennas Propagat., vol. AP – 13, pp. 437 – 466, May 1965 .

[89] E. K. Miller, G.F. Burke, B.J. Maxum, G.M. Pjerrou, "Radar cross section of a long wire," IEEE Trans. Antennas and Propagat. (Commun.), vol. AP - 17 , pp. 381 - 384. May 1969.

[90] Harvard Radio Res. Lab. Staff, Very High-Frequency Techniques : vol. 1, Chapter 2. New York : McGraw-Hill, 1947.

[91] G.D. Monteath and P. Knight, "The performance of a balanced aerial when connected directly to a coaxial cable," Proc. IEE (London), vol. 107, Part B, pp. 21 - 25, January 1960.

APPENDIX A

USE OF SINUSOIDAL INTERPOLATION AS BASIS FUNCTIONS

The computational complexities involved in using higher order basis functions to approximate segment currents on thin wire structures can be illustrated for the sinusoidal interpolation function given in (2.46). Consider a centre fed thin linear antenna which is divided into N current elements for current computation using Hallén's integral equation. The formulation is given commonly in the form

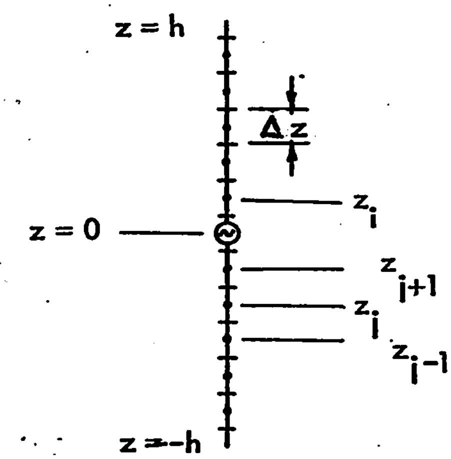

Figure A.1. Segmentation of a Straight Antenna for Current Computation.

$$\int_{-h}^{h} I(z')\, G(z, z')\, dz' = B \cos kz + \frac{jV}{2Z_o} \sin k|z| \qquad \text{(A.1)}$$

where $I(z')$ denotes the current distribution, $G(z, z')$ is the usual Green's function given in (2.16), V is the complex amplitude of the excitation voltage, Z_o is the free space impedance, and B is an unknown coefficient to be determined using the end conditions [14].

$$I(h) = I(-h) \qquad \text{(A.2)}$$

Applying the collocation method to the above equation yields [18]

$$\sum_{j=1}^{N} \int_{\Delta z_j} I_j(z')\, G(z_i, z')\, dz' = B \cos k z_i + \frac{jV}{2 Z_o} \sin k\, l\, z_i) \qquad \text{(A.3)}$$

To simplify the discussion, the segmentation can be chosen to be uniform, i.e.

$$z_{i+1} - z_i = z_i - z_{i-1} = \Delta z_i \qquad \text{(A.4)}$$

where z_{i-1}, z_i, and z_{i+1} are centre coordinates of three neighbouring segments as shown in Figure A.1. Along the i^{th} segment centred about z_i, it has been shown [19] that for faster convergence (i.e. with fewer segments), the current can be approximated by (2.46) which can be re-written in the form

$$\begin{aligned} I_i(z') &= A_i + B_i \sin k\,(z' - z_i) + C_i \cos k\,(z' - z_i) \qquad \text{(A.5)} \\ &\qquad \text{for } z' \text{ in } \Delta z_i \\ &= 0 \text{ otherwise} \end{aligned}$$

in which A_i, B_i, C_i are unknown coefficients. Let I_{i-1}, I_i, and I_{i+1} be the current values at z_{i-1}, z_i and z_{i+1}, respectively. Then, by matching the current distribution at the three neighbouring points, the following expressions are obtained :

$$I_{i-1} = A_n - B_i \sin k\ d_{i-1} + C_i \cos\ d_{i-1} \qquad \text{(A.6)}$$

$$I_i = A_i + C_i \qquad \text{(A.7)}$$

and where

$$I_{i+1} = A_i + B_i \sin k\ d_{i+1} + C_i \cos k\ d_{i+1} \qquad \text{(A.8)}$$

$$d_{i-1} = z_i - z_{i-1} = \Delta z \qquad \text{(A.9)}$$

and

$$d_{i+1} = z_{i+1} - z_i = \Delta z \tag{A.10}$$

Defining

$$p = \sin k \Delta z \tag{A.11}$$

$$q = \cos k \Delta z \tag{A.12}$$

then the three unknown coefficients can be expressed as follows:

$$A_i = \frac{I_{i-1} - 2q I_i + I_{i+1}}{2(1-q)} \tag{A.13}$$

$$B_i = \frac{-I_{i-1} + I_{i+1}}{2p} \tag{A.14}$$

and

$$C_i = \frac{-I_{i-1} + 2I_i - I_{i+1}}{2(1-q)} \tag{A.15}$$

Thus the above expressions can be substituted into (A.3), and the impedance matrix coefficient for the unknown current distribution determined. However, it is apparent that the integrations have now become much more involved than was the case with pulse basis functions.

APPENDIX B

FIELD COMPUTATIONS WITH A MAGNETIC FRILL SOURCE MODEL

As stated in (2.66), the magnetic current density $\overline{M}$ gives rise to an electric vector potential from which the electric field $\overline{E}^i$ is to be derived according to (2.69). For a monopole mounted on a plane conducting disk, it has been shown elsewhere [56] that the space surrounding the frill source (see Figure 2.7) can be divided into three regions :

(i) Near field region in which elliptic integral evaluation is involved ;

(ii) Far field region in which closed form approximations are used ;

and

(iii) Axial field region, along the monopole axis, for which closed form field expressions are also obtained.

The boundary surface between the near and far field regions can be chosen judiciously depending on the accuracy required for the current values. Typically it can be located at a radius distance equal to five times the outer radius of the frill. If the observation point is placed in the x - z plane, then from (2.66)

$$r_o = [z^2 + \rho^2 + \rho'^2 - 2\rho\rho' \cos\varphi'] \tag{B.1}$$

and the electric vector potential would then be given by

$$F_\varphi = -\frac{\epsilon_o}{2\pi} \frac{1}{\ln\frac{b}{a}} \int_a^b \int_0^\pi \cos\varphi' \left(\frac{e^{-jkr_o}}{r_o}\right) d\varphi' \, d\rho' \tag{B.2}$$

where a and b are the inner and outer radii of the frill, respectively, and the excitation voltage is set at 1 volt . Because of symmetry it should be noted that integration in φ' is from 0 to π . It can be shown [55], [56] that for the near field region, $F\varphi$ can be written in the form

$$F_{\varphi} = -\frac{\epsilon_o}{2\pi} \cdot \frac{1}{\ln(\frac{b}{a})} \int_a^b \left[\frac{2}{r_1} K(\frac{\pi}{2}) p^2 + \int_0^{\pi} (\cos\varphi' \frac{e^{-jkr_o}}{r_o} - \frac{1}{r_o}) \, d\varphi' \right] d\rho' \tag{B.3}$$

where

$$r_1 = [z^2 + (\rho + \rho')^2] \tag{B.4}$$

$$p^2 = \frac{4\rho\rho'}{z^2 + (\rho + \rho')^2} \tag{B.5}$$

and $K(\frac{\pi}{2}; p^2)$ = complete elliptical integral of the first kind. Using the relations given in (2.71) and (2.72) for the E_z^i and E_p^i field components, integrations and differentiations can now be carried out numerically by means of (B.3). Simpson's rule can be used to perform the integrations, and Lagrange's three-point (equally-spaced abscissas) formula has been found to give sufficiently accurate partial differentials [56].

For the far field region, the approximation starts by setting

$$r_2 = [z^2 + \rho^2] \tag{B.6}$$

and then by taking r_o to be given by

$$r_o \approx r_2 + \frac{\rho'^2}{2r_2} - \frac{\rho\rho'\cos\varphi'}{r_2} \tag{B.7}$$

Thus

$$\frac{1}{r_o} \approx \frac{1}{r_2}\left[1 + \frac{\rho\rho'}{r_2^2}\cos\varphi' - \frac{\rho'^2}{2r_2^2} + \frac{\rho^2\rho'^2\cos 2\varphi'}{r_2^4} - \frac{\rho\rho'^3}{r_2^4}\cos\varphi' + \ldots\right] \tag{B.8}$$

Substitution of (B.8) into (B.2) yields

$$F_\varphi \approx -\frac{\epsilon_o}{2\pi}\frac{1}{\ln(\frac{b}{a})}\int_a^b\int_o^\pi \frac{1}{r^2}\left[1+\frac{\rho\rho'\cos\varphi'}{r_2^2}-\frac{\rho'^2}{2r_2^2}+\rho^2\rho'^2\frac{\cos^2\varphi'}{r_2^4}\right.$$

$$\left.-\frac{\rho\rho'^3\cos\varphi'}{r_2^4}\right]\cos\varphi' e^{-jkr_o}\,d\varphi'\,d\rho' \tag{B.9}$$

Integration with respect to φ' leads to zero, first and second order Bessel functions with $(\frac{k\rho\rho'}{r_2})$ argument. These can be approximated further by series expansions to give

$$F_\varphi \approx -\frac{\epsilon_o}{2\pi\ln(\frac{b}{a})}\frac{e^{-jkr_2}}{r_2}\int_a^b\left[\frac{j\pi k\rho\rho'}{2r_2}-\frac{j\pi k\rho\rho'^3}{4r_2^3}\right.$$

$$\left.+\frac{\pi\rho\rho'}{}\right]e^{-jk\rho'^2/2r_2}\,d\rho' \tag{B.10}$$

$$\approx \frac{\epsilon_o}{8\ln(\frac{b}{a})}(b^2-a^2)\frac{k\rho e^{-jkr_2}}{r_2}\left[\frac{1}{kr_2}+\frac{k(b^2+a^2)}{4r_2}\right.$$

$$\left.+j\left(1-\frac{b^2+a^2}{2r_2^2}\right)\right] \tag{B.11}$$

Finally expressions for E_z^i and E_ρ^i are obtained by partial differentiation. For the axial region, E_ρ^i is zero, and E_z^i is given by

$$\underset{\lim \rho\to 0}{E_z^i} = \lim_{\rho\to 0}\left[-\frac{1}{\epsilon_o}\frac{F_\varphi}{\rho}-\frac{1}{\epsilon_o}\frac{\partial F_\varphi}{\partial\rho}\right] \tag{B.12}$$

The final expression for E_z^i is given by

$$\underset{\lim \rho\to 0}{E_z^i} = \frac{1}{2\ln(\frac{b}{a})}\left[\frac{e^{-jkr_3}}{r_3}-\frac{e^{-jkr_4}}{r_4}\right] \tag{B.13}$$

where

$$r_3 = [z^2 + a^2] \qquad \text{(B.14)}$$

and

$$r_4 = [z^2 + b^2] \qquad \text{(B.15)}$$

Once E_z^i and E_ρ^i are known at the centre of a wire element excited by the frill source, the right hand side of (2.48b) can be determined using (2.73). In general the antenna configuration may consist of an arbitrary distribution of thin wires.

APPENDIX C

EVALUATION OF THE SELF-IMPEDANCE TERMS IN THE "NETWORK" EQUATIONS

The self impedance terms in (2.48b) are evaluated from approximate analytical expressions. This is first done by finding a finite series expansion for e^{-jkr} and the integrations are then carried out after separating the integral in (2.52) into real and imaginary parts. Consider an m^{th} segment of length s_m and radius a_m in a given distribution of cylindrical current elements.

Let

$$E_r = Re\,[\,Z'_{mm}\,] \tag{C.1}$$

$$E_i = Im\,[\,Z'_{mm}\,] \tag{C.2}$$

$$s = s_m \tag{C.3}$$

$$a = a_m \tag{C.4}$$

where, form (2.49), (2.52) and (2.17)

$$Z'_{mm} = \frac{-j}{4\pi\omega\,\epsilon_o} \int_{-s/2}^{s/2} [\,2\,r^2\,(1 + jkr) - a^2\,(3 + 3\,jkr) - k^2\,r^2\,]\,\frac{e^{-jkr}}{r^5}\,d\,z' \tag{C.5}$$

and by (2.16)

$$r = [\,z'^2 + a^2\,]^{1/2} \tag{C.6}$$

since $\rho = 0$ and $z = 0$. It is important to note that the self-impedance of element s_m is to be determined from its self-field evaluated along its axis (hence $\rho = 0$), and its centre-point (hence $z = 0$) as illustrated in Figure 2.1.

From (C.1), (C.2) and (C.5), and using a nine-term MacLaurin series expansion for e^{-jkr}, one obtains for the real part

$$E_r \approx -\frac{1}{4\pi\omega\epsilon_o}\int_{-s/2}^{s/2}\left[-\frac{2k^3}{3}+\frac{k^5a^2}{15}+(z'^2+a^2)\left(\frac{k^5}{15}-\frac{k^7a^2}{210}\right)\right]dz' \tag{C.7}$$

and the imaginary part becomes

$$E_i \approx -\frac{1}{4\pi\omega\epsilon_o}\int_{-s/2}^{s/2}\left[\frac{3a^2}{(z'^2+a^2)^{5/2}}+\frac{k^2a^2-4}{2(z'^2+a^2)^{3/2}}+\frac{k^4a^2-8k^2}{8(z'^2+a^2)^{1/2}}+\frac{(12k^4-k^6a^2)}{48}(z'^2+a^2)^{1/2}\right]dz' \tag{C.8}$$

While the integrations in (C.7) are straightforward, further re-arrangements are needed in (C.8). The final approximate expressions become

$$E_r \approx -\frac{\pi}{3}\cdot\frac{s}{\lambda}\left[2-\frac{a^2k^2}{3}+\frac{a^4k^4}{105}+\frac{r_t^2k^2}{210}(a^2k^2-14)\right] \tag{C.9}$$

and

$$E_i \approx -\frac{s}{2r_t\lambda}\left[\frac{1}{k^2r_t^2}+\frac{1}{2}+\frac{k^2r_t^2}{8}\left(1-\frac{k^2a^2}{8}\right)-\frac{k^4r_t^4}{288}\right] - \frac{1}{2\lambda}\left[1-\frac{k^2a^2}{4}+\frac{k^4a^4}{64}\right]\ln\left(\frac{1+\frac{s}{2r_t}}{1-s/2r_t}\right)] \tag{C.10}$$

where

$$r_t = [(s/2)^2+a^2]^{1/2} \tag{C.11}$$

It should be pointed out that there are notable differences in both E_r and E_i from the corresponding expressions given in Reference [56].

APPENDIX D

SEGMENTATION OF THE MERIDIANS IN WIRE-GRID MODEL OF SPHERE

Consider one typical meridian on the wire-grid model of the monopole sphere structure discussed in Section 3.3.

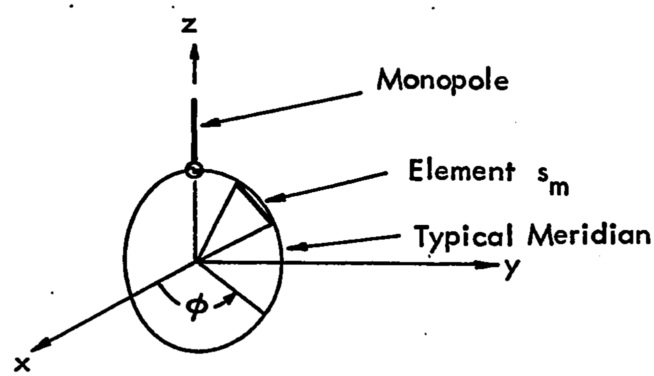

Figure D. 1 .

In Figure D.1 are shown the coordinates needed to specify uniquely the six segmentation parameters for the m^{th} element : the three centre coordinates (x_m, y_m, z_m), the length s_m and the angular orientations α_m and β_m . The meridian is re-drawn in Figure D. 2 in the φ plane.

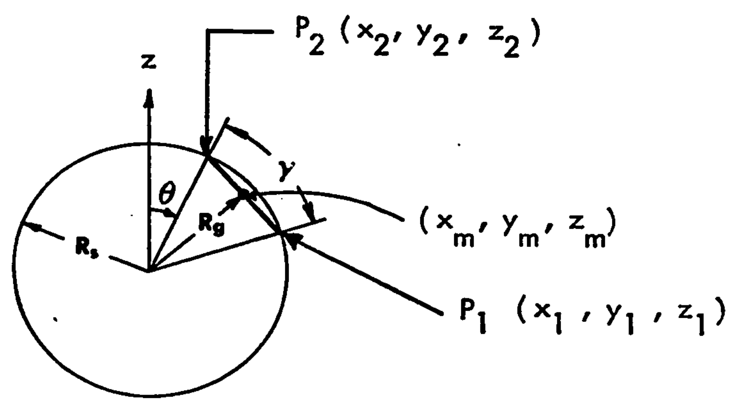

Figure D. 2 .

If θ, φ, γ and R_s are defined, then one obtains

$$R_g = R_s \cos(\gamma/2) \tag{D.1}$$

and therefore

$$x_m = R_g \sin(\theta + \gamma/2) \cos\varphi \tag{D.2}$$

$$y_m = R_g \sin(\theta + \gamma/2) \sin\varphi \tag{D.3}$$

$$z_m = R_g \cos(\theta + \gamma/2) \tag{D.4}$$

$$s_m = 2 R_s \sin(\gamma/2) \tag{D.5}$$

The β_m angular orientation is given by

$$\beta_m = \varphi \qquad \pi < \varphi < 2\pi \tag{D.6}$$

$$\beta_m = \varphi - \pi \qquad 0 \le \varphi \le \pi \tag{D.7}$$

The angle α_m is determined using the six coordinates $(x_2, y_2, z_2,)$ and $(x_1, y_1, z_1,)$ which can be expressed in terms of R_s and θ for the first set, and R_s and $\theta + \gamma$ for the second set as shown in (D.2), (D.3) and (D.4). To determine α_m, first let

$$\alpha' = \arctan\left(\frac{z_2 - z_1}{s_m}\right) \tag{D.8}$$

Then

$$\alpha_m = \alpha' \qquad -\frac{\pi}{2} \le \alpha' \le 0 \tag{D.9}$$

It should be noted that the segment angle γ is constant if the segmentation is uniform. If, on the other hand, the segmentation scheme involves putting finer segments near the monopole region and coarser ones near $\theta = 180^\circ$, then γ is appropriately incremented.

Segmentation schemes for other antenna structures studied in this work follow the above basic procedure in a similar manner.